



SAPIENZA  
UNIVERSITÀ DI ROMA

## Simplified Seismic Analysis of Straight Integral Frame-Abutment Bridges

Dipartimento di Ingegneria Strutturale e Geotecnica

Dottorato di Ricerca in Ingegneria Strutturale – XXXIV Ciclo

Candidate

Andrea Marchi

ID number 1463387

Thesis Advisor

Prof. Dr. Paolo Franchin

April 2022

Thesis defended on 23 May 2022  
in front of a Board of Examiners composed by:  
Prof. Stefano Aversa (chairman)  
Prof. Giuseppe Ricciardi  
Prof. Alberto Pavese

---

**Simplified Seismic Analysis of Straight Integral Frame-Abutment Bridges**

Ph.D. thesis. Sapienza – University of Rome

ISBN: 000000000-0

© 2022 Andrea Marchi. All rights reserved

This thesis has been typeset by L<sup>A</sup>T<sub>E</sub>X and the Sapthesis class.

Version: May 25, 2022

Author's email: [andrea.marchi@uniroma1.it](mailto:andrea.marchi@uniroma1.it)

*Dedicated to  
All professors that supports and supported me, my family and Francesca*





## Abstract

Since the second post-war period, Integral Abutment Bridges (IABs) have become widespread in the construction of overpasses in America and Europe, as they allow to save on the costs of inspection and maintenance of the bearings and deck joints. They are characterized by having an internal continuity constraint between abutments and deck. Their static and dynamic behavior is thus characterized by the strong interaction between structure and soil. Due to these structural characteristics, the analysis models cannot disregard the contribution of the surrounding soil non-linear behavior. While the latter can be modeled by means of a continuous medium with a non-linear constitutive law, such models are very complex and require specialized knowledge and skills beyond those of the average structural designer. The aim of this thesis is therefore the study of simplified two- and three-dimensional models for practice-oriented seismic analysis of integral abutment bridges.

The study focused first on a non-linear dynamic model where soil-structure interaction is modeled with non-linear Winkler springs. A comparison with a higher-order three-dimensional finite element model was performed, which allowed calibration and fine-tuning. The same non-linear dynamic model has been implemented both in **OpenSEES** and in **SAP2000**, in order to evaluate the sensitivity of the assessed system response to the limitations of commercial softwares and thus to highlight the practical applicability of the model for design. As a further step toward design, even more simplified static models, both non-linear and linear, were established and calibrated against the non-linear dynamic one. Finally the dynamic model was used to carry out a seismic risk analysis of archetypical overpasses with integral abutment on the Italian territory to quantify in probabilistic terms the better performance of these bridges with respect to bridges with traditional seat-type abutments.



## Acknowledgments

*Grateful thanks to Professor Dr. Paolo Franchin for his deep insight and support during my study.*

*Grateful thanks to Dr. Fabrizio Noto for providing materials, scripts and exchanging opinions.*

*Special Thanks to Mr. Domenico Gallese, Prof. Dr. Luigi Callisto and Dr. Davide Noé Gorini for the precious confrontation with their model.*

*Grateful thanks to the Reluis:RINTC project, in which this work has been included. Also thanks to the Eurocodes EN1998 revision task which introduced me to the topic.*

*Sincere thanks also to the external reviewers: Professor Dr. Fabio Biondini (Politecnico of Milan) and Professor Dr. Anastasios Sextos (University of Bristol).*



# Contents

<b>Contents</b>	<b>vii</b>
<b>Notation</b>	<b>xiii</b>
<b>1 Introduction</b>	<b>1</b>
1.1 Integral abutment bridges: evolution, advantages and current disadvantages . . . . .	1
1.2 Motivation and objectives . . . . .	6
<b>2 Literature review (state-of-art)</b>	<b>9</b>
2.1 Main behavior . . . . .	11
2.2 Secondary effects . . . . .	13
2.3 Current practices and applications . . . . .	14
2.4 Analysis models for IABs . . . . .	18
2.4.1 "Continuous" models . . . . .	19
2.4.2 "Discrete" models . . . . .	21
<b>3 Dynamic model</b>	<b>33</b>
3.1 Soil column elements . . . . .	34
3.1.1 Improved constitutive law for fine- and coarse-grained soils . . . . .	35
3.1.2 Calibration of geometric parameter $r$ . . . . .	38
3.2 Interface elements . . . . .	40
3.2.1 Stiffness . . . . .	41
3.2.2 Strength . . . . .	42
3.2.3 Vertical (shear) degree of freedom . . . . .	45
3.2.4 Bilateral interfaces . . . . .	48
3.2.5 Damping . . . . .	50
3.3 Base damper . . . . .	54
3.4 Construction stages . . . . .	55
3.5 Specific issues of platform-dependent implementations . . . . .	57
3.5.1 Soil-column elements . . . . .	57
3.5.2 Interface elements . . . . .	60
3.5.3 Base damper . . . . .	61
3.5.4 Structural elements . . . . .	61
3.5.5 Stages . . . . .	62
3.6 Sample model results . . . . .	64
3.6.1 Results for the construction stages and modal analysis . . . . .	64

3.6.2	Results for a sample motion . . . . .	67
3.7	Intensity measure and structural response correlation . . . . .	72
3.7.1	Ground motion selection . . . . .	72
3.7.2	Response parameters ( <i>EDP</i> ) considered . . . . .	74
3.7.3	Results in terms of correlation . . . . .	74
3.7.4	Analytical fit . . . . .	75
3.8	Parameters sensitivity . . . . .	77
3.8.1	Input and output parameters . . . . .	78
3.8.2	Results summary . . . . .	79
3.9	3D model . . . . .	80
3.9.1	Structure elements . . . . .	81
3.9.2	Interface elements . . . . .	82
3.9.3	Soil-column elements . . . . .	83
3.10	Limit skew angle for the applicability of the model . . . . .	84
<b>4</b>	<b>Comparison with a higher-order model</b>	<b>87</b>
4.1	Higher-order 3D FEM model . . . . .	87
4.2	Benchmark case . . . . .	88
4.2.1	Ground motions . . . . .	91
4.3	Analysis of construction stages . . . . .	91
4.4	Free-field site-response analysis . . . . .	92
4.5	Modal analysis . . . . .	95
4.6	Time series of the selected quantities . . . . .	97
4.7	Conclusions . . . . .	100
<b>5</b>	<b>Static models for design purposes</b>	<b>103</b>
5.1	Non-linear static model . . . . .	104
5.1.1	Static impedances . . . . .	105
5.1.2	Acceleration of the structural masses . . . . .	107
5.2	Linear static model . . . . .	107
5.3	Comparison with the non-linear dynamic model on the <i>Gatteo</i> case .	109
5.3.1	Evaluation of static impedances . . . . .	109
5.3.2	Seismic actions (equivalent lateral forces) . . . . .	110
5.3.3	Results . . . . .	112
5.4	Parametric study . . . . .	113
<b>6</b>	<b>Probabilistic seismic risk assessment</b>	<b>119</b>
6.1	Code conforming archetype bridge design . . . . .	123
6.1.1	Model for design . . . . .	123
6.1.2	Actions . . . . .	124
6.1.3	Results . . . . .	126
6.1.4	Structural elements resistances . . . . .	127
6.2	Assessment . . . . .	130
6.2.1	Nonlinear model for assessment . . . . .	130
6.2.2	Input ground motions . . . . .	133
6.2.3	Results . . . . .	134

<b>Summary, conclusions &amp; future research</b>	<b>147</b>
<b>A Signal at the bedrock-deposit interface</b>	<b>149</b>
<b>B More refined 3D model elements</b>	<b>153</b>
B.1 Abutments described with shell elements . . . . .	153
B.2 Coupled Bouc-Wen for soil-column elements . . . . .	155
<b>C Static impedances implementation</b>	<b>157</b>
C.1 Springs with a rigid element . . . . .	158
C.2 Euler-Bernoulli beam with a rotational spring . . . . .	159
<b>D Parameters sensitivity</b>	<b>161</b>
D.0.1 Soil-column Bouc-Wen exponent $n$ . . . . .	161
D.0.2 Interface elements passive limit . . . . .	163
D.0.3 Base damper coefficient . . . . .	165
D.0.4 Abutment-deck and piles-deck stiffness ratios . . . . .	166
<b>E Seismic risk results</b>	<b>171</b>
E.1 Results summary . . . . .	171
E.2 Time series . . . . .	172
E.2.1 MI . . . . .	172
E.2.2 NA . . . . .	176
E.2.3 AQ . . . . .	179
<b>Bibliography</b>	<b>183</b>





# Notation

Software names and related commands are written with `typewriter monospaced font`.

## Symbols:

$a_0$	Normalized frequency
$A_{e,i}$	Soil-column element area (embankment)
$A_{s,i}$	Soil-column element area (soil deposit)
$B$	Abutment width (dimension in $y$ direction)
$B_b$	Embankment bottom (base) width (dimension in $y$ direction)
$B_c$	Embankment top (crest) width (dimension in $y$ direction)
$B_s$	Soil deposit width
$c'$	Soil cohesion
$c_b$	Base damper coefficient
$C_f$	Cost of failure
$d$	Pile diameter
$E$	Young modulus (elastic modulus)
$E_d$	Design actions effects
$E_d$	Steel elastic modulus
$F$	force
$F_a$	Active force
$F_p$	Passive force
$F_y$	Soil-column element strength
$g$	gravitational acceleration

---

$G_0$	Soil small-strain shear modulus
$h$	Soil layer thickness
$H$	Embankment height
$i$	Indexing counter
$I$	Second moment of inertia
$k_0$	Bouc-Wen initial stiffness
$k_x$	interface element stiffness
$k_Z$	Interface elements vertical stiffness
$K_0$	At-rest pressure coefficient
$K_a$	Active pressure coefficient
$K_p$	Passive pressure coefficient
$l_a$	Active length
$l_a$	Passive length
$L_d$	Deck length
$L_{e,cr}$	Embankment critical length
$L_p$	Piles length
$m$	Mass
$M$	Bending moment
$n$	Bouc-Wen exponent
$n_p$	Piles number (per abutment)
$N$	Normal stress
$n_p$	Piles number
$P_f$	Probability of failure
$r$	Embankment-soil area ratio
$R$	Risk
$R_d$	Design resistance
$s_1$	BWGG parameter
$s_2$	BWGG parameter
$s_{EDP}$	Response sensitivity parameter (in terms of $EDP$ )

$S$	Embankment slope
$S_a$	Spectral acceleration
$S_\alpha$	Plateau spectral acceleration
$t$	Time
$t$	Thickness
$T$	Vibration period
$T_R$	Return period
$u$	Displacement
$\dot{u}$	Velocity
$\ddot{u}$	Acceleration
$\ddot{u}_g$	Ground acceleration
$u_y$	Yielding displacement
$V$	Shear force
$V_s$	Shear wave velocity
$V_{s,b}$	Bedrock shear wave velocity
$w$	Weight per unit length
$x$	Longitudinal global coordinate
$X_i$	Input parameter
$y$	Transversal global coordinate
$z$	Vertical global coordinate (same as depth)
$z_b$	Bedrock depth ( $z$ axis starting from surface and positive upwards, so this quantity is always negative)
$z_w$	Watertable depth
$\alpha$	Bouc-Wen hardening parameter
$\alpha$	specific soil impedances
$\beta$	Lognormal dispersion
$\gamma$	Soil specific weight
$\gamma$	Bouc-Wen parameter
$\gamma_y$	BWGG parameter

---

$\delta$	Soil-structure friction angle
$\Delta$	Percentage error
$\Delta t$	Time step
$\Delta z_i$	Soil-column element height
$\varepsilon_y$	Yielding strain
$\zeta$	Bouc-Wen internal dimensionless variable
$\eta$	Lognormal median
$\theta$	BWGG function that account for degradation
$\lambda_f$	Failure frequency
$\mu_r$	BWGG parameter
$\ni$	Poisson coefficient
$\rho_b$	Bedrock density
$\rho_d$	Deck density
$\rho_s$	Soil density
$\rho_{XY}$	Correlation coefficient
$\sigma$	Standard deviation
$\sigma'_0$	Soil effective confining pressure
$\sigma'_h$	Soil effective horizontal pressure
$\sigma'_v$	Soil effective vertical pressure
$\phi$	Curvature
$\phi'$	Angle of repose
$\Phi$	Standard Normal CDF

### Acronyms:

<b>3D-NLFEM</b>	3D Non-Linear Finite Element Model
<b>AQ</b>	L'Aquila
<b>BEF</b>	Beam-on-Elastic Foundation
<b>BW</b>	Bouc-Wen constitutive model
<b>BWGG</b>	Bouc-Wen constitutive law (modified by) Gerolymos and Gazetas

---

<b>CDF</b>	Cumulative Density Function
<b>CEN</b>	Comité Européen de Normalisation (European Committee for Standardization)
<b>CL</b>	Center Line
<b>CPU</b>	Central Processing Unit
<b>CS</b>	Conditional Spectrum
<b>DMRB</b>	Design Manual for Roads and Bridges (Highways England)
<b>DoF</b>	Degree of Freedom
<b>DOT</b>	Department Of Transportation (in United States)
<b>DSA</b>	Deterministic Sensitivity Analysis
<b>EDP</b>	Engineering Demand Parameter
<b>ELSA</b>	Elastic Linear Static Analysis
<b>FEM</b>	Finite Element Method
<b>GEO</b>	GEOtechnical
<b>GM</b>	Ground Motion
<b>HPP</b>	Homogeneous Poisson Process
<b>IAB</b>	Integral Abutment Bridge
<b>IDA</b>	Incremental Dynamic Analysis
<b>IM</b>	Intensity Measure (intended as seismic intensity)
<b>IML</b>	Intensity Measure Level
<b>IP</b>	Input Parameter
<b>ITACA</b>	ITalian ACcelerometric Archive
<b>LS</b>	Life Safety limit state
<b>LSM</b>	Linear Static Model
<b>MI</b>	Milano
<b>MSA</b>	Multiple Stripe Analysis
<b>NA</b>	Napoli
<b>NLSA</b>	Non-Linear Static Analysis
<b>NLSM</b>	Non-Linear Static Model

---

<b>NRHP</b>	National Register of Historic Places
<b>NTC</b>	Norme Tecniche per le Costruzioni (Italian code for constructions)
<b>OCR</b>	Over-Consolidation Ratio
<b>OP</b>	Output Parameter
<b>PDF</b>	Probability Density Function
<b>PI</b>	Plasticity Index
<b>RINTC</b>	Rischio Implicito di strutture progettate secondo le Norme Tecniche per le Costruzioni (implicit risk of code-conforming Italian buildings)
<b>RAM</b>	Random Access Memory
<b>ROM</b>	Reduced-Order Model
<b>SD</b>	Severe Damage limit state
<b>SIAB</b>	Semi-Integral Abutment Bridge
<b>SLU</b>	Stato Limite Ultimo (Ultimate Limit State)
<b>SLV</b>	Stato Limite per la salvaguardia della Vita (Life Safety limit state)
<b>SP</b>	Sensitivity Parameter
<b>SPEA</b>	Società Progettazioni Edili Autostradali (Highway constructions design society)
<b>SSA</b>	Stochastic Sensitivity Analysis
<b>SSI</b>	Soil-Structure Interaction
<b>UHS</b>	Uniform Hazard Spectrum
<b>UK</b>	United Kingdom
<b>ULS</b>	Ultimate Limit State (same as SLV)
<b>UPD</b>	Usability Preventing Damage limit state
<b>US</b>	United States

# Chapter 1

## Introduction

In this thesis, the seismic behavior of bridges is investigated using simplified computational models. The bridges considered are those with integral abutments and, in their evaluation, a nonlinear dynamic model, developed by Franchin et al. in 2014 [46] (chapter 2), is extended (chapter 3) and the results are compared with a higher-order model (chapter 4). Further simplified static models are proposed for design (chapter 5). Finally, a seismic risk analysis on the Italian territory has been carried out to assess the reliability of this type of bridges (chapter 6).

### 1.1 Integral abutment bridges: evolution, advantages and current disadvantages

Most of today's bridges have structural joints to handle superstructure deformations. However, there are also some types of bridges without joints. Bridges of the past, like masonry ones, were all joint-less (see figure 1.1).

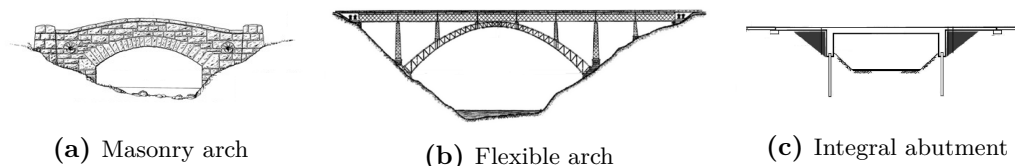


**Figure 1.1.** Example of joint-less bridges.

A special case of joint-less bridges which is gaining popularity in recent years is the one with integral abutments.

An Integral Abutment Bridge (IAB) is a *construction used to overcome an obstacle in which there is no kinematic distinction between superstructure and substructure* (practically there are no joints between deck and abutments<sup>1</sup>). In IABs deck thermal expansion and contraction are absorbed by the movement of the abutments rather than expansion joints [98].

<sup>1</sup>In a more wide sense there are no *thermal joints*. In fact there are so called *Semi-Integral Abutment Bridge* (SIAB) in which deck main girders and abutments are separated, but the slab is continuous.

There are five types of integral bridges<sup>2</sup>, depending on the abutment type, as shown in figure 1.2:

1. *Frame abutments*: abutments act as retaining walls for the embankment backfill soil.
2. *Embedded abutments*: abutments are resting over single piles row that extends to a depth below the retained backfill with restraint provided by the embedded length.
3. *Bank pad abutments*: abutments act like shallow foundations and provide most of the vertical bearing capacity.
4. *Flexible support abutments*: the piles are surrounded by sleeves to increase flexibility and reduce forces on the piles.
5. *End screen abutments*: only the backwall portion of the substructure is connected with continuity joint with the deck. This type of abutments are used in *Semi-Integral Abutment Bridges (SIAB)*.

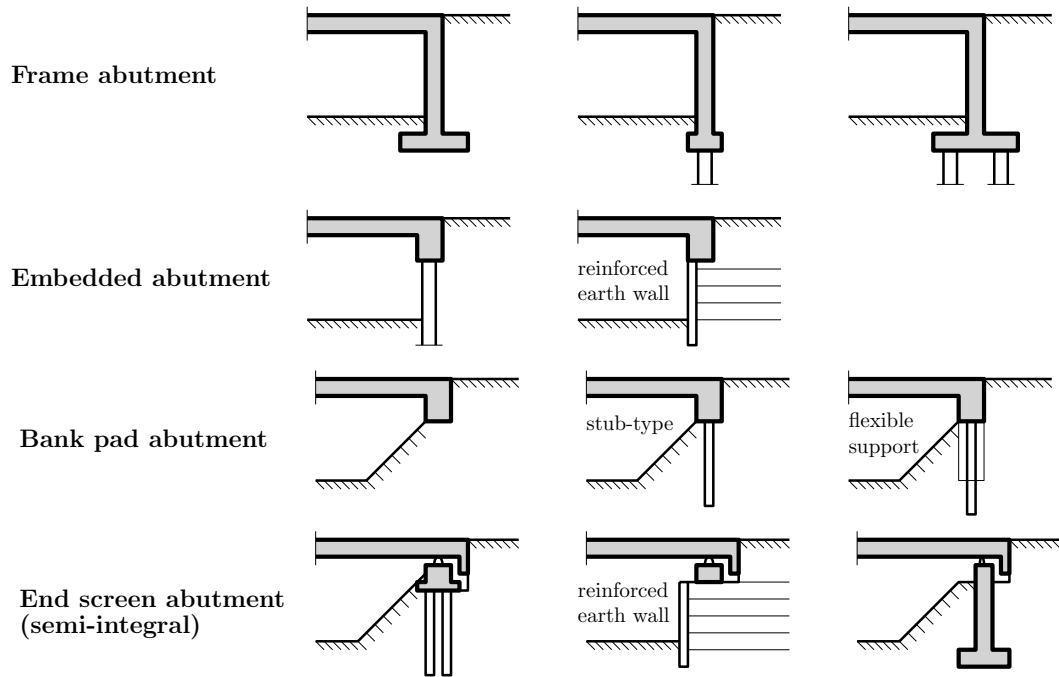


**Figure 1.2.** Abutment types (described in Highways England's *Design Manual for Roads and Bridges (DMRB)*) and respective sub-types (recommended by the North American Study Tour Report (Cooke 2003)) [88].

Integral abutment bridges have been built since the Roman era ( $\sim 150$  BC<sup>3</sup>) where the main structural scheme for bridges and aqueducts was the masonry arch bridge.

<sup>2</sup>Described in Highways England's *Design Manual for Roads and Bridges (DMRB)*.

<sup>3</sup>Built in 142 BC, the *Pons Aemilius* (later named *Ponte Rotto* or "broken bridge" in Italian) is the oldest Roman stone bridge in Rome, Italy, survived nowadays. It has only one surviving arch and pier.



### 1.1 Integral abutment bridges: evolution, advantages and current disadvantages<sup>3</sup>

Integral abutment bridges, in more contemporary sense, have been developed since 1930 in the United States<sup>4</sup> and after the second world war in Europe [10]. Ohio and South Dakota were the first US states to embrace the use of continuous bridges giving, to the respective Highway Department (*ODOT* and *SDDOT*), more than 90 years of experience (Hassiotis and Roman 2005). The states of Kansas, Missouri, and Tennessee are some of the other early adopters of this type of bridges [101]. Initially, in United States, integral bridges were built with pre-stressed reinforced concrete decks with very low abutments resting on steel piles with a "H" section (HP-piles).

These bridges have been built mainly with continuous steel decks since the early 1960s. At that time most had lengths less than 90 m and skew angles less than  $30^\circ$  (limited mainly by the fact that the structural behavior was unknown for this type of structures)<sup>5</sup>.

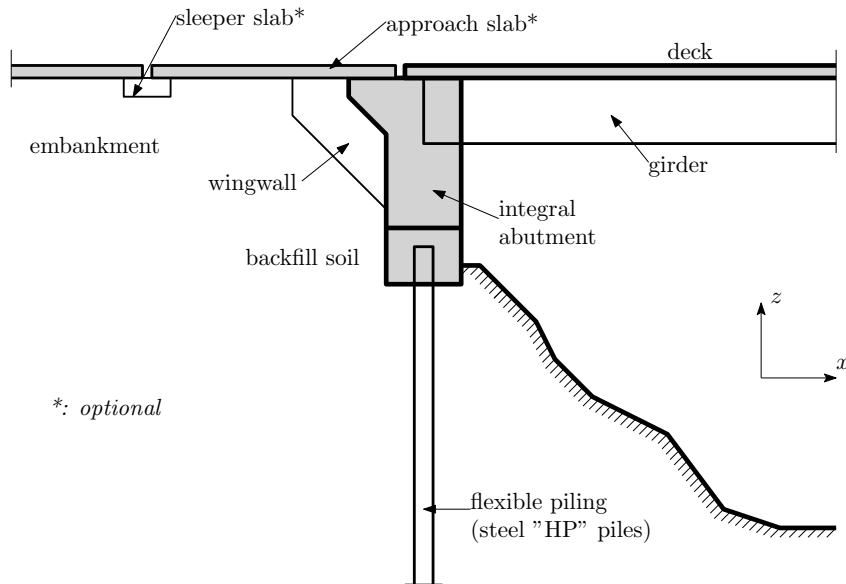


**Figure 1.3.** Integral abutments developed between the 60s and 70s in United States.

Later, other states followed this trend, and by 1987, 87% of the US departments of transportation were using the integral bridge scheme for short- and moderate-length bridges. Gradual design changes allowed for longer IABs based upon the positive maintenance performance (the longest built was a 350 m IAB constructed by the Tennessee DOT in 1980). Main surveys conducted on the use of integral abutment bridges in US national transportation are:

- L. F. Greimann, A. M. Wolde-Tinsae, and P. S. Yang. *Skewed Bridges with Integral Abutments*. In Transportation Research Record 903, TRB, National Research Council, Washington, D.C., 1983, pp. 64- 72.

<sup>4</sup>Some authors [17] claim that this trend toward continuous structural schemes is due to the publication, in 1930 by Prof. Hardy Cross, of a simplified method for analyze structures with many hyperstatic unknowns [25].

<sup>5</sup>Same limitations were taken also in all other countries that introduced this type of bridges in their construction regulations.

- H. W. Lee and M. B. Sarsam. *Analysis of Integral Abutment Bridges*. South Dakota Department of Highways, Pierre, March 1973, 135 pp.
- J. H. Emanuel. *An Investigation of Design Criteria for Stresses Induced by Semi-Integral End Bents*. University of Missouri, Rolla, MO., 1972.
- Integral, *No-Joint Structures and Required Provisions for Movement*. Federal Aid Highway Program Manual, T 5140.13, FHWA, U.S. Department of Transportation, 1980.

Subsequently (since the 2000s), bridges with integral abutments gained widespread use in Europe, particularly in the United Kingdom, where they were introduced for the first time in the construction of the London-Yorkshire motorway M1, inaugurated in 1959. In 1996, the United Kingdom Highways Agency published a document promoting this type of bridges (BA 42/96) due to a survey carried out for the Department of Transport that revealed that expansion joints are a serious source of costly and disruptive maintenance works.

Overall, however, European experience with IABs is significantly less compared with the United States. The few experiences has been positive though. As a result the trend is towards making integral abutment bridges for new bridges across Europe [106].

In 1999, the German Federal Ministry of Transport and Urban Affairs (BMVBS) published a list of recommended archetype types for single-span bridges<sup>6</sup> in which eight of ten were IABs. In 2003, many of the BMVBS recommendations were replaced by the Eurocode-based DIN Fachbericht 101 to 104, which contained no specific rules concerning IABs, so designers still had to rely on their experience. To broaden the knowledge base for IAB design and construction, the *International Workshop on IABs* was held in Stockholm, Sweden in May 2006.

In Europe, within the revision of the Eurocodes<sup>7</sup> started in 2020, simplified methods for the design of integral bridges have been included, establishing the beginning of a shared standard analysis method, at European level, for this type of bridges. The work presented in this thesis partly contributes to this code development.

---

<sup>6</sup>Bundesministerium für Verkehr, Bau- und Wohnungswesen (1999).

<sup>7</sup>Specifically in second generation Eurocode 8 part 2: *Design of structures for earthquake resistance: Bridges* [4].

The main advantages of the Integral Abutment structural scheme are:

- Strong reduction of both construction and maintenance costs, linked to the lack of expansion joints and traditional supports<sup>8</sup>, reduced foundation costs and, in some cases, deck costs [32] [104].
- Better comfort level for users (less vertical "bumps" due to thermal joints).
- Larger reserve of resistance: the continuous structural scheme ensures, in general, a capacity reserve of the bridge structure related to its ductility. Higher than expected seismic actions, or unforeseen actions, draw on this reserve of resistance.

The main problems of IABs are:

- Soil-structure interaction has a strong impact on this type of structures (abutments are active elements of the bridge structure), meaning structural analysis is more difficult [26] [39].
- Difficult structural characterization due to many hyperstatic unknowns. Moreover continuous structure leads to internal forces caused by deformations (thermal, creep, shrinkage, settlements should be evaluated concurrently with all others).
- There are no well-defined and widely accepted design and analysis method, in particular for seismic actions.
- Constant temperature-induced cyclic movements of abutments and traffic load result in settlement of approach fill and wedge near abutments [108] [59] [10] [91] [75] [74].
- Cyclic changes in earth pressures on the abutment tend to influence the rotation of integral bridges with skewed or curved geometry<sup>9</sup> [59] [10].
- The rotation and contraction of the superstructure, differential settlement, creep, shrinkage, thermal stress, and earth pressure can lead to cracks in the bridge's wing walls and other concrete members [91].
- The piles that support the abutments may be subjected to high stresses as a result of cyclic expansion and contraction of the bridge superstructure. These stresses can cause formation of plastic hinges in the piles, and may reduce their axial load capacities [101] [109] [10] [95] [71].

---

<sup>8</sup>One of the most frequent causes of deterioration in traditional bridges is the use of de-icing salts that, transported by water, can cross the joints and attack the main girders and support devices causing them to malfunction. Further joints are usually subjected to continuous wear due to repeated vehicular loads and rheological phenomena that causes deck deformation.

<sup>9</sup>Skewed integral bridges tend to rotate under the influence of cyclic changes in earth pressures on the abutment [59].

- Bridge abutments can be undermined due to water entering into the approach fills at the bridge ends [108] [35] [91] [23]. The foundation should be designed considering this issue.
- The application of integral bridge concept has limitations: they cannot be used with weak embankments or subsoil, and they can only be used for limited lengths, although the maximum length is still somewhat unclear [17] [101] [23].

Some of these have worked well and are widely accepted, and some are debatable, such as the use of approach slabs to reduce the approach fill settlement [10] [33].

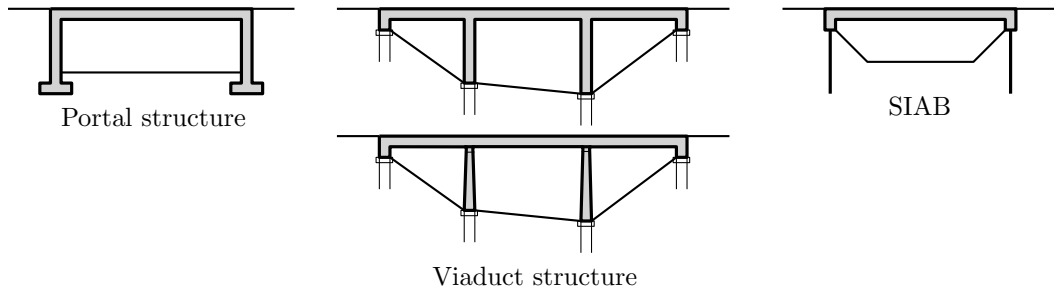


**Figure 1.4.** Integral abutment applications.

Integral abutments are generally used in (figure 1.4):

- *Portal* structures;
- *Viaduct* structures (where the structural scheme is a frame with fixed nodes);
- Existing bridges *made* integral (structural scheme varies greatly from bridge to bridge, but in general can be assimilated to SIAB).

## 1.2 Motivation and objectives

Because of the advantages in terms of costs, comfort and resistance of integral abutment bridges, this structural type has become considerably popular starting from the mid-twentieth century, particularly in the United States and England. It is mainly used in bridges with modest spans (from 10 to 100 meters, in some cases integral bridges of more than 300 meters have also been built with multi-span decks). Because of the rigid connections between the bridge deck and the abutments, integral bridges have improved seismic resistance compared to jointed bridges [59].

There is a lack of sufficiently reliable and easy-to-use calculation tools in the literature that can describe the stresses on the structure due to horizontal loads<sup>10</sup>. This is more evident for seismic analysis, where the action is also dynamic and in

<sup>10</sup>In general earthquakes are one of the major cause of horizontal actions in civil constructions.

the literature few have proposed calculation models for such bridges due to the difficulties introduced by the soil-structure interaction.

In this thesis the objective is reached through simplified Winkler-based dynamic model which is calibrated through the comparison of a higher order model. Then simplified static methods for design are described and compared to the dynamic one.

The main objectives for the present study are therefore:

- Develop a non-linear dynamic modeling strategy for seismic assessment of integral abutment bridges.
- Develop, from it, simplified static methods (non-linear and linear) for design in professional practice.
- Evaluate its robustness in a risk assessment study and in a range of parametric analyses (taking into account parameters variability and different bridges scenarios).
- Gain insight into IABs performance and design issues.

The work presented in this thesis contributed to the draft of the second-generation Eurocode 8 [4] as a design method for Integral Abutment Bridges.

The models presented and, in particular, the seismic risk analysis is part of a broader project within the evaluation of the risk implicit in the code-conforming structures in Italy (ReLUIS:RINTC).



## Chapter 2

# Literature review (state-of-art)

An *integral abutment bridge (IAB)* is a structure designed to overcome an obstacle where there are no thermal joints between a continuous deck and the abutments.

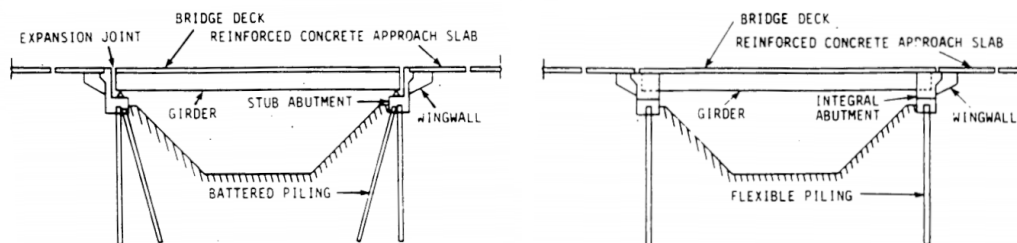


**Figure 2.1.** Comparison between a typical simply-supported bridge (conventionally designed), on the left, and an integral-abutment one, on the right. (Image taken from [101])

In conventionally designed bridges, expansion joints and bearing are required in the bridge deck and at the abutments (figure 2.1). These details have been found to have a tendency to deteriorate leading to large maintenance and/or replacement costs. Failure of these expansion devices can also introduce large stresses that were not considered in the design due to structural scheme modification and can damage the bridge. In many cases [17], "significantly more damage and distress have been caused by the use of movable deck joints at piers and abutments than the secondary stresses that these joints were intended to prevent". The main goal of an integral abutment bridge is to eliminate the expansion joints and bearings completely. Eliminating bearings decreases installation costs<sup>1</sup> and the long-term maintenance costs that have been found to be associated with conventional bridges. The complete removal of these components is accomplished by creating a structural connection between the bridge superstructure and abutments. The connection details between the superstructure and abutments vary depending on the individual countries (Some examples of abutment configuration are shown in Figure 2.2).

<sup>1</sup>Based on an extensive literature review and survey, Wolde-Tinsae and Klinger [108] found that expansion joints have negative economic impact in all phases of highway bridge service life, that is, design, construction, and maintenance. Retrofitting traditional bridges with IAB features has also been shown to be cost effective (Nickerson 1996).

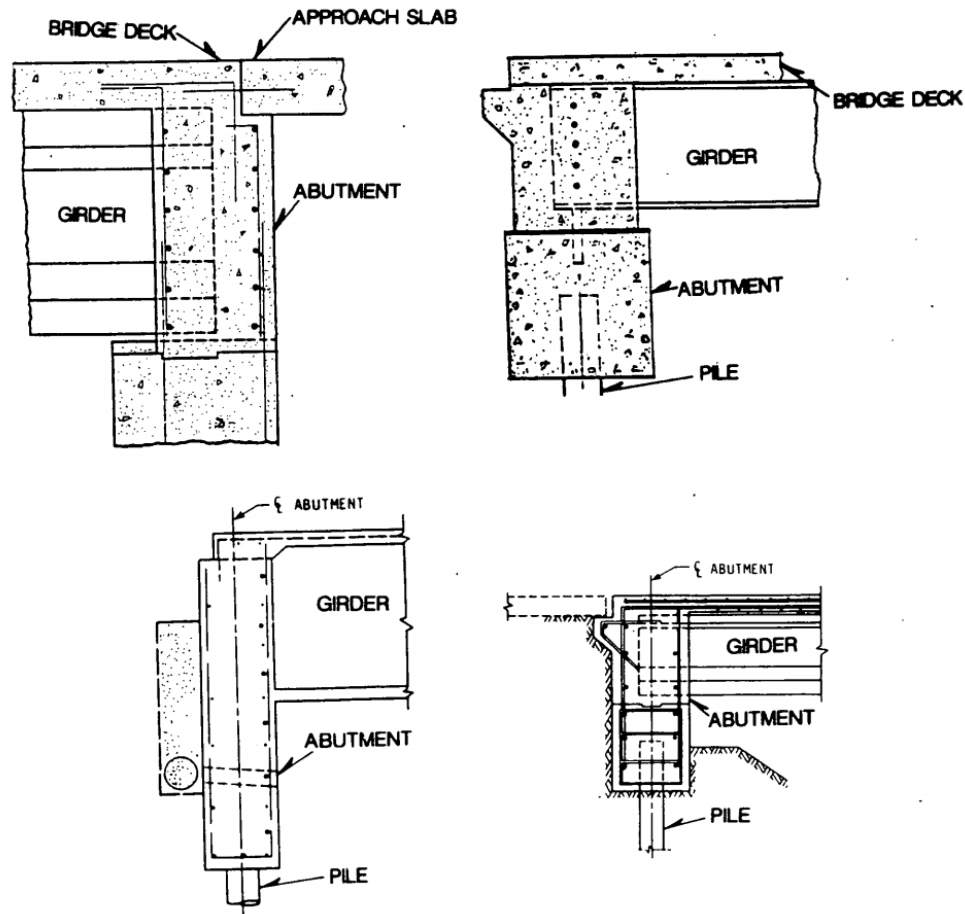


**Figure 2.2.** Integral abutment bridges deck-abutments joints details. (Image taken from [101])

The abutments can be supported on spread footings or on driven piles or drilled shafts (see figure 1.2). It is also common to structurally connect an approach slab to the abutments. This connection allows for a smooth transition between the bridge and approach embankment. For relatively short bridges almost any foundation type is acceptable, but for longer bridges the foundation type selection and design become important. Typical integral abutment bridge details cause the heads of piles to be fixed, but this condition will cause relatively high pile bending stresses in longer bridges. To relieve bending stresses at the pile heads the connection may be detailed as a pinned-head condition or the abutment detailed to create a hinge. (Dunker 2007)

A notable variation of the integral abutment bridge design is a *semi-integral abutment* bridge (SIAB). In this bridge configuration, expansion joints in the deck are still eliminated but girder bearings are placed at the top of the abutments, as can be seen in figure 2.3. The important improvement from a conventional bridge is that the superstructure extends over the top of the abutment, thus protecting the bearing and reducing long-term maintenance costs [60]. Also traditional bridges retrofitted with the elimination of the expansion joints can be considered as a semi-integral



abutment bridges.

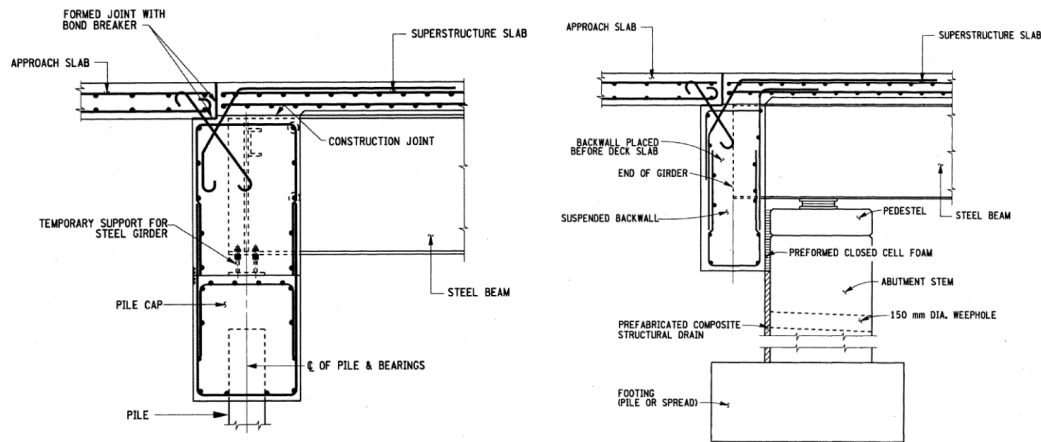


**Figure 2.3.** Deck-embankment connections. On the left there is a detail for an integral abutment while on the right for a semi-integral one. Those details are developed for the New York State, US. (Images taken from [111] and [101])

The semi-integral abutments are designed to minimize the transfer of rotational displacements and bending moments to the abutments and the piles. They do, however, transfer horizontal displacements. Rotation is generally accomplished by using a flexible bearing surface at the top horizontal interface in the abutment. Allowing rotation at the pile top generally reduces the pile load [101]. Field surveys reveal that semi-integral piers experience no distress or noticeable cracking in the deck-piers connections [10].

## 2.1 Main behavior

For an integral abutment bridge, the overall concept is to accommodate the expansion and contraction, due to annual temperature fluctuations, by flexibility in the abutment foundations and pavement expansion joints, rather than by bridge expansion joints. So in integral abutment bridges the piles are usually the most flexible elements and are expected to accommodate the lateral movements due to thermal expansion [109]. The substructure must absorb the induced movements of the superstructure, so it has to be flexible enough to accommodate the movements. This flexibility is provided by the use of a stub abutment supported by a single row of piles [40] [115]. The piles are driven vertically without any batter. This arrangement of piles allow the abutment to move in the longitudinal direction under temperature effects (New Jersey DOT 1987). In the United Kingdom the trend is to have the flexible abutment with a double row of piles [45] [116] [100]. Due to deck-abutment horizontal movements piles in integral abutment bridges are subjected to combined bending and axial loads. In the long term, these bridges can cause a buildup of lateral earth pressures on the abutments due to the soil-mechanics phenomenon known as *ratcheting* [60]. Due to this behavior, that leads to fatigue effects, the maximum length of integral abutment bridges has some limitations [31] [29].

Integral bridges should not be used unless the probability of appreciable abutment settlement is remote [17]. Lateral movement due to thermal expansion and contraction of the superstructure leads to reduction in the vertical load-carrying capacity of the pile. Longitudinal movement of the integral bridges causes passive pressure on the structure, which depends on the area of abutment exposed to pressure, and the magnitude is related to the magnitude of soil compression [17].

Both integral and semi-integral abutment bridges are vulnerable to differential settlements between the approach system and the bridge abutment. This problem is often referred to as the "bump at the end of the bridge." Causes for the bump problem, in order of importance, include:

1. Compression of the fill material
2. Settlement of the natural soil under the embankment
3. Poor construction practices
4. High traffic loads
5. Poor drainage
6. Poor fill material
7. Loss of fill by erosion

*Approach slabs* are usually poured behind integral abutments in order to prevent compaction of backfill soils by traffic loading and offer a smooth transition to the bridge [9]. Studies conducted by the Ohio Department of Highways have shown that the increase in internal stress in the approach slabs and not in the bridge slabs has been the main cause of bridge failures [83]. Such a problem could be resolved easily by providing adequate expansion joints in the approach pavements without any expansion joints on the bridge at all.

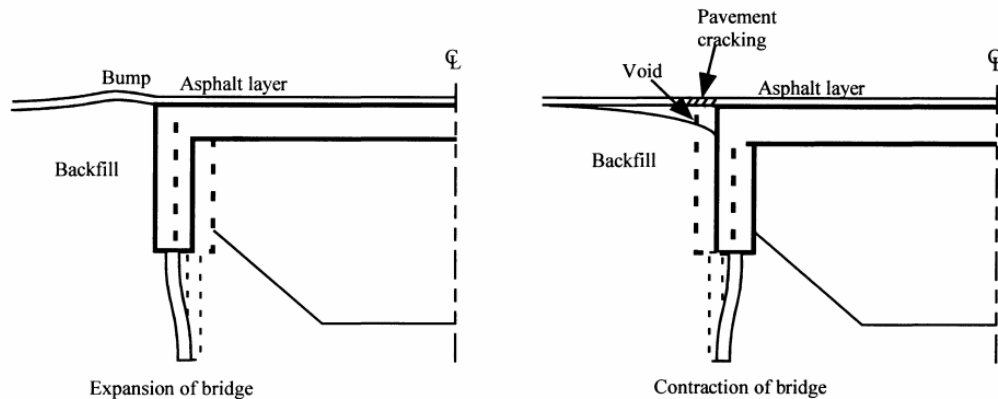


**Figure 2.4.** Interaction mechanism between abutment and approach embankment. (Image taken from [10])

The abutment backfill is a designed material, with properties specified to provide a balance between stiffness and flexibility. In general, granular materials comprising compacted rounded particles of uniform grading can have a peak angle of internal friction,  $\phi$ , as low as  $35^\circ$  and may accommodate thermal expansion without high earth pressures. However, these soils are somewhat vulnerable to settlement. Fill of

compacted, well-graded, hard angular particles can have a peak angle of internal friction as high as  $55^\circ$  with very high resistance to thermal expansion. These soils are less vulnerable to settlement.

## 2.2 Secondary effects

In addition to the primary effects due to dead load, live load, etc., integral bridges are subjected to secondary effects due to:

- creep and shrinkage;
- thermal gradients;
- differential settlement and differential deflections;
- pavement relief pressures when moisture and sustained high temperatures trigger pavement growth;

*Shrinkage* and *creep* effects can be estimated using the Freyermuth (1969) method [49]. The greatest effect of shrinkage is apparent on the positive moment of single spans and on the continuity connection at abutment of continuous spans [22] [17]. Creep effects of continuous single span bridges are greater than shrinkage effects. Both creep and shrinkage are time dependent. Maximum shrinkage moments take place within 30 days of form removal [10], and creep effects continue for a longer period of time.

The bridges appear to be performing well with minimal difficulties, but problems noted by some United States transportation agencies with integral bridge performance included minor cracking, drainage at abutments, and settlement of approach slabs [73]. In Alaska, unexpected adhesion of frozen soil is suspected as the cause of hairline cracking in integral backwalls. Kansas has found shrinkage to be an issue for prestressed bridges and advises engineers to account for this in future construction [73].

There is also a Growth/Pressure (G/P) phenomenon, that the expansion of the road surface is prevented by debris in the pavement joints. This leads to a "blow-up" of the flooring. This is especially noticeable in transition slabs.

Emerson (1977), Hoffman et al. (1983), Imbsen et al. (1985), and Potgieter and Gamble (1989) studied the *temperature distribution* through bridge beams. The most important factors are 1) the maximum temperature differential and 2) the distribution of this differential across the depth of the beams (Oesterle et al., 1998). It appears that in moderate climates, the moments induced by thermal gradients can be ignored (Burke, 1993). Analysis for reduction in vertical load capacity and elastic buckling load under temperature induced displacements can be carried out separately, because they are uncoupled [58]. Main studies on temperature effects on integral abutment bridges are conducted by Dicleli [28] [30] [27] Caristo [19].

The bridge superstructure of the integral bridge may also be subjected to *buoyancy loads* (see figure 2.5), specially in areas where flood hazard is relevant. This bridges are also likely to be subject to *uplift* when fully or partially submerged. This is mainly due to the fact that this bridges are used for small span and small height applications. So integral bridges should be limited to areas where the bridge elevation

is higher than the highest expected flood level [17], or the buoyancy loads should be considered in design [10].

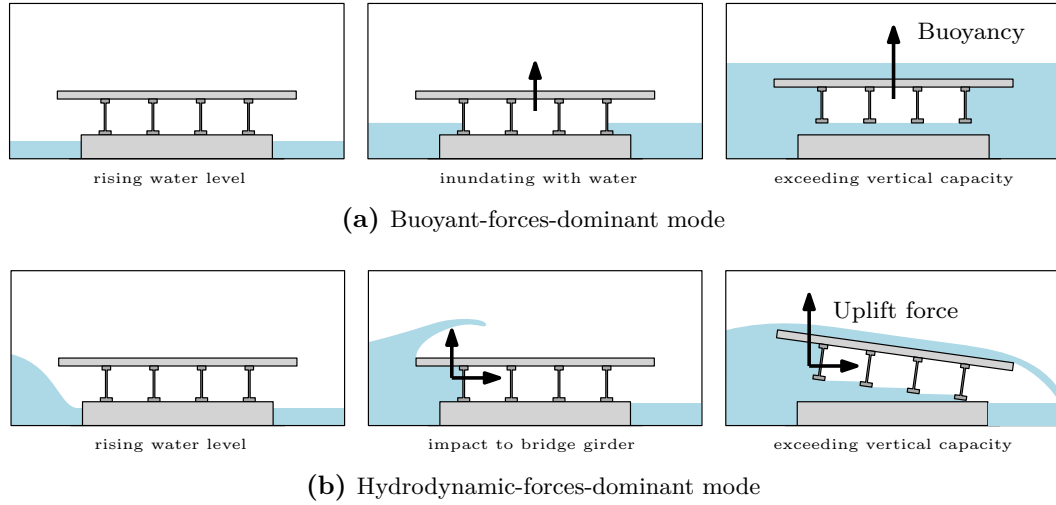


**Figure 2.5.** Water actions on deck, static and dynamic.

The behavior integral bridges with high skew angle is particularly unpredictable and the pressures increase their entity and eccentricity [87]. In fact many countries (mainly USA [10] and UK [107]) prohibit integral abutment bridges with a skew angle greater than a certain value (commonly 30 degrees).

Differential settlements can also result in secondary bending moments. Barker et al. (1991) and AASHTO (1994) provide simple procedures to estimate differential settlements. If differential settlements are less than 38 mm, the induced moments can be ignored [22].

### 2.3 Current practices and applications

Because there isn't a standardized design and construction procedure, this leads to variations in the analysis, design, and construction practices of IABs. This was visible also in surveys over the US Highway agencies [9] and in Europe countries [106].

Steel piles, with a "H" cross-section called *HP-piles*, are frequently used for integral structures (specially in the United States of America in the early days of integral abutment bridges), but other types have also been used, including pipes and cast-in-place concrete piles [73].

Pipe piles, filled with concrete are also used, specially in Europe. They are more ductile than prestressed concrete piles, and have greater resistance to local buckling than steel H-piles. For these reasons concrete filled steel tubular columns are gaining popularity, especially where seismic risk is a concern (Hooper et al., 1999).

Transition slabs are important to overcome the settlement of the embankment at the bridge approach due to the seasonal movement of the abutments and the traffic

loads (approach-slab, run-on slab). This is only the most visible part of a more complex phenomenon that is triggered by the periodic movement of the abutments called *ratcheting* (England, 2001). *Approach fill settlements* should be estimated in the design process. For clay soil consolidation testing and settlement analysis is appropriate while, for sandy backfill and gravelly subsoils, the magnitudes of time dependent settlements can be estimated using the procedures outlined by Duncan and Buchignani (1976) [36]. If the settlements predicted is relatively large the use of an approach slab and a V-shaped abutment is appropriate, while if the settlement is relatively small periodic maintenance consisting of asphalt overlays of the approach fill pavement at the end of the bridge is sufficient and cost effective [10].

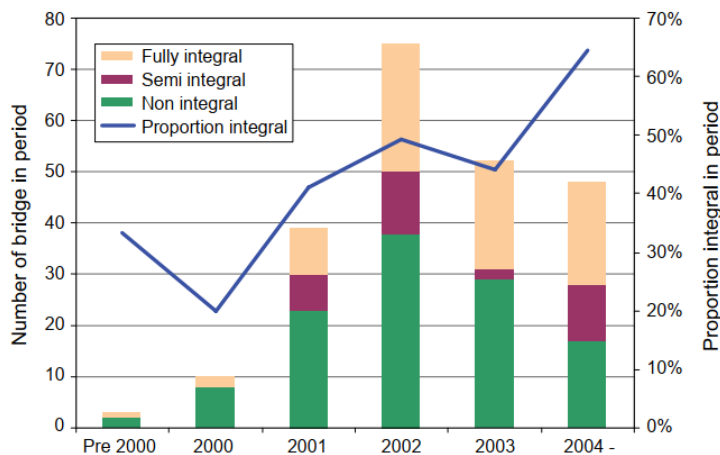


**Figure 2.6.** Summary of bridge types built in United Kingdom (Image taken from Iles, 2006 [65]).

In Europe, compared to the United States, different construction details have been adopted. In particular, IABs have been realized with abutments not resting on piles (spread footing). In addition, circular hollow steel profiles filled with concrete are often used for the piles construction, in contrast to the US where piles with "H" cross-section<sup>2</sup> are used. In Europe, as opposed to the US, is required that backfill operations are conducted evenly on both sides of the structure, to prevent any undue lateral forces on the structure. In addition, not all member states use approach slabs<sup>3</sup>.

The first integral abutment bridge built in the United States was the *Teens Run Bridge* [17] (see figure 2.7). It was built in the 1938 near Eureka, in Gallia County (Ohio). It consists in five continuous reinforced concrete slab spans supported by a capped pile piers and integral abutments. The bridge was determined eligible for inclusion on the National Register of Historic Places (NRHP) in 2012 for his pioneer structural type.

<sup>2</sup>In United States HP-piles are mainly used. Frequently there are also sleeves around the piles to prevent the soil to retain free bending during the structure translation

<sup>3</sup>In some states (like Germany) buried "drag plates" are used to prevent approach embankments deformation due to traffic loads.



**Figure 2.7.** The *Teens Run Bridge* (Gallia County, Ohio). Built in 1938 is the first Integral Abutment Bridge [17].

The longest precast-concrete-girder structure in United States<sup>4</sup> was a 358.4 m bridge built in Tennessee (State Route 50 Bridge over Happy Hollow Creek shown in figure 2.8).



**Figure 2.8.** The State Route 50 Bridge over Happy Hollow Creek (Tennessee) is 358.4 m long and jointless with integral abutments.

The bridge has 9 spans of precast, prestressed concrete bulb-T girders with no expansion joints and bearings. The spans are ranging from 38.8 to 42.2 m. The two-column piers vary in height from 15.5 to 27.7 m. The bridge was built in 1997 and has performed satisfactory during the tests (Bakeer et al., 2005; Wasserman, 2007).

Another important IAB in US is *Maple River Bridge* located in northwest Iowa, which includes some of the most complete and valuable data related to the performance of integral bridges. The Maple River Bridge is 98 m long and 10 m wide with a skew angle of 30 degrees (as it can be seen in figure 2.9). The bridge

<sup>4</sup>The longest steel-girder and cast-in-place concrete bridges in United States were both built in Colorado, measuring 318.4 m and 290.4 m, respectively [73].

has three spans and consists of a composite concrete deck and steel girders [54]. It is important for the relative high skew angle (compared to other integral abutment bridges) and the amount of monitoring data available.

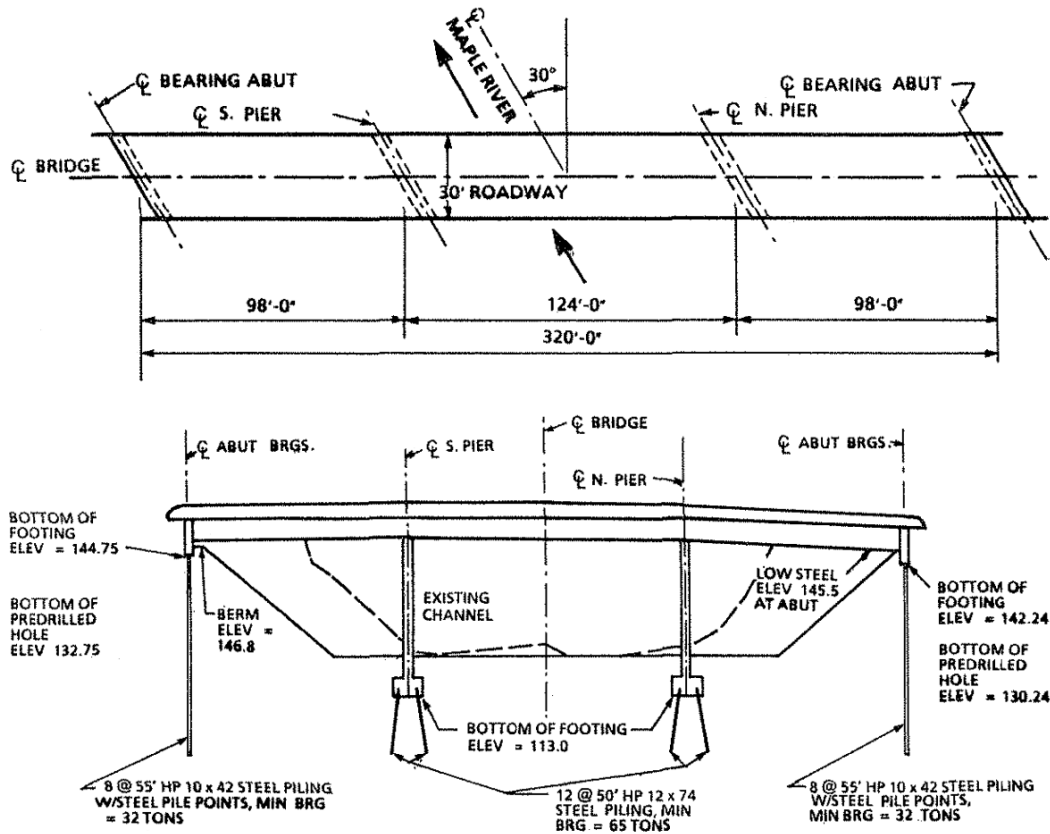


Figure 2.9. Plan and side view of the *Maple River Bridge* (Iowa). (Image taken from [54])

Also in Italy this type of bridges is spreading through engineers [16]. One of the most important in the country is the one located at *Isola della Scala* close to Verona, completed in 2007. The total length of the structure is approximately 400 m, with 13 spans. This makes this bridge the longest with integral abutments up to now (Zordan and Briseghella, 2007).



Figure 2.10. *Isola della scala* bridge, Verona, Italy [117].

A particular example of integral bridge widespread in Italy are the railway manholes, which are mainly masonry arch bridges (60% of the total ).

## 2.4 Analysis models for IABs

Computational modeling strategies for integral bridges can be divided into two macro-categories:

- *"Continuous" models*: Models in which the soil is modeled using two-dimensional (in 2D models) or three-dimensional (in 3D models) elements<sup>5</sup> with constitutive laws suitable for modeling the behavior of the soil in the various degrees of freedom.
- *Discrete models*: Models based on the division of the soil into discrete elements (springs). They may be:
  - *Winkler-Based*: All structural elements are modeled (including foundations) and the soil around the structure is modeled using springs.
  - *Force-Based*: The foundations are discretized by springs applied to the structure representing static impedances and the actions given by the soil are imposed by appropriate pressure distributions.

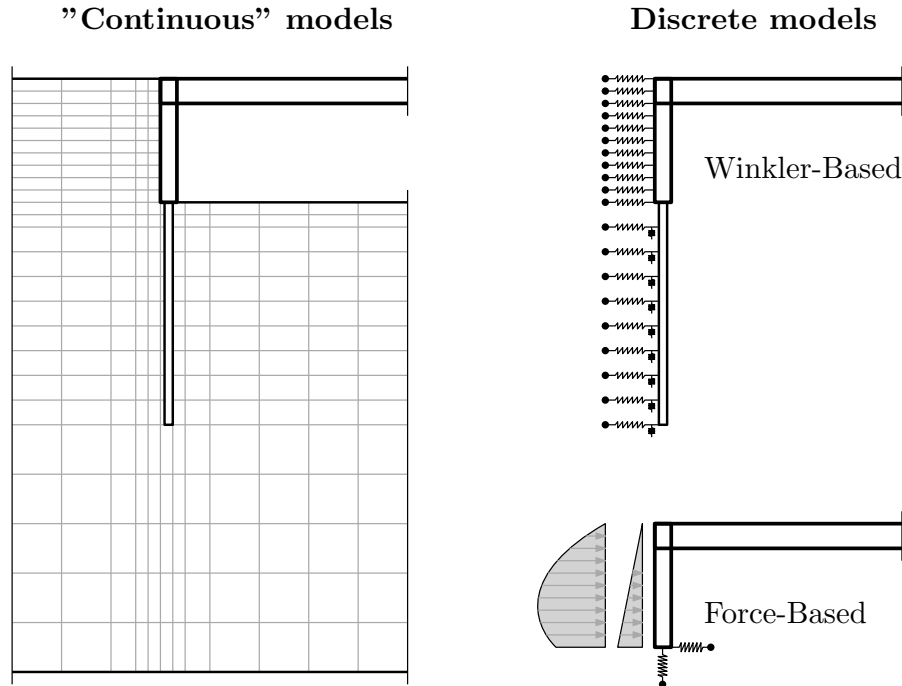


**Figure 2.11.** IAB analysis model types.

Models can be further subdivided through the analysis method used:

<sup>5</sup>They are called "continuous" due to finite elements definition, but they are also discrete.



- *Static models*: those that capture the static behavior of such bridges, also capturing the actions arising from seasonal cycles. Simplified models that attempt to describe dynamic behavior (see chapter 5) are also part of this category.
- *Dynamic models*: Those models used to explicitly describe the dynamic behavior of such bridges. These models are mainly used in the analysis of response to seismic ground motions.

The table 2.1 shows the main computational models developed to study the behavior of integral bridges.

**Table 2.1.** Main model developed for IAB analysis.

Authors	type	analysis
Iowa DOT report (1982)	Winkler-Based	Static
Greimann et al. (1985, 1986, 1987)	Force-Based	Static
Mourad & Tabsh (1998)	Continuous	
Lehenne et al. (1999)	Continuous	Static
Faraji et al. (2001)	Winkler-Based	Static
Duncan & Arsoy (2003)	Continuous	
Franchin & Pinto (2014)	Winkler-Based	Dynamic

Design and analysis of these bridges vary between countries, and considerable research has been done in this field [5] [54] [57] [59] [17].

Often, the soil-pile system is modeled as an equivalent length of horizontally unsupported cantilever beam-column. This latter approach may be accomplished using fairly straightforward analyses (CALTRANS 1981; Greiman et al. 1987; Husain and Bagnariol 1996).

For relatively short bridges, neglecting the effects of the passive pressures may be acceptable. Chen [22] and Burke [17] recommend to use only 2/3 of the full passive pressures for most integral bridges. Bridge designers should adopt a conservative approach regarding earth pressures on abutments. Bending moments induced by passive pressures on abutments counteract the dead and live load bending moments in simple spans. Therefore, overestimating passive pressures is not a conservative approach for such bridges. Neither it is, as shown later, for earthquakes.

#### 2.4.1 "Continuous" models

Lehane et al. [77] used a finite element model with continuum elements to validate a simplified model for integral abutment bridges design. The paper focused on the effects of thermal expansion on frame type bridges supported on shallow foundations (spread footings). The soil was modeled as an elastic continuum of uniform stiffness. This continuum was discretized with eight-node quadrilateral elements. The concrete structure was also modeled using those elements. A simplified plane frame model, was created using data from the finite element model. The equivalent abutment height and stiffnesses of the translational springs were calculated based on the horizontal and rotational restraint provided by the abutment and soil in the continuum model. Moments and axial forces predicted in the bridge deck by the analyses of Lehane et

a1. were compared with that of the simplified model for various load cases. The results of both agree reasonably well. It was determined that the magnitudes of the induced moments and axial stresses in the deck are relatively small. In addition, the predictions were not overly sensitive to the choice of bridge geometry or material properties.

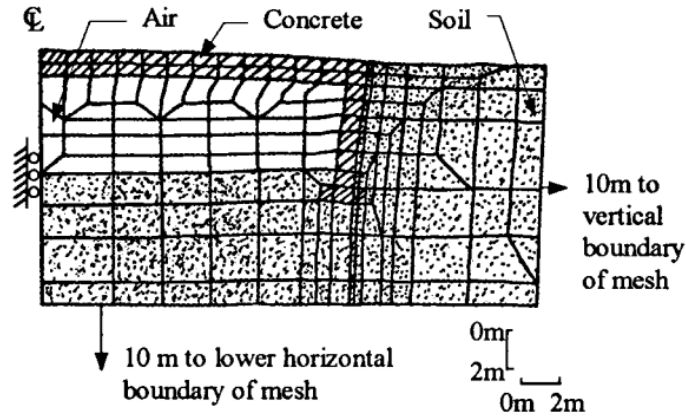


**Figure 2.12.** Deformed finite element model developed by Lehane et al. [77] due to temperature increase in deck. (Image taken from [77])

Duncan and Arsoy [35] used the finite element analysis program *SAGE* (Bentler et al, 1999) to investigate the significance of the interactions among the abutment, the approach fill, the foundation soil and the piles of integral bridges. Specifically, the effects of the stiffness of the embankments and the foundation soil on the stresses in the piles supporting the abutment, as well as the effects of the type of abutment detail were examined. The finite element mesh was symmetric about the centerline of the deck girders. The bridge superstructure and the piles were modeled as beam elements with linear stress-strain properties. The approach fill and the foundation soil were modeled using four-node quadrilateral and three-node triangular elements with hyperbolic stress-strain properties. The finite element mesh is refined near the abutment and coarse near the boundaries of the model as can be seen in figure 2.13.

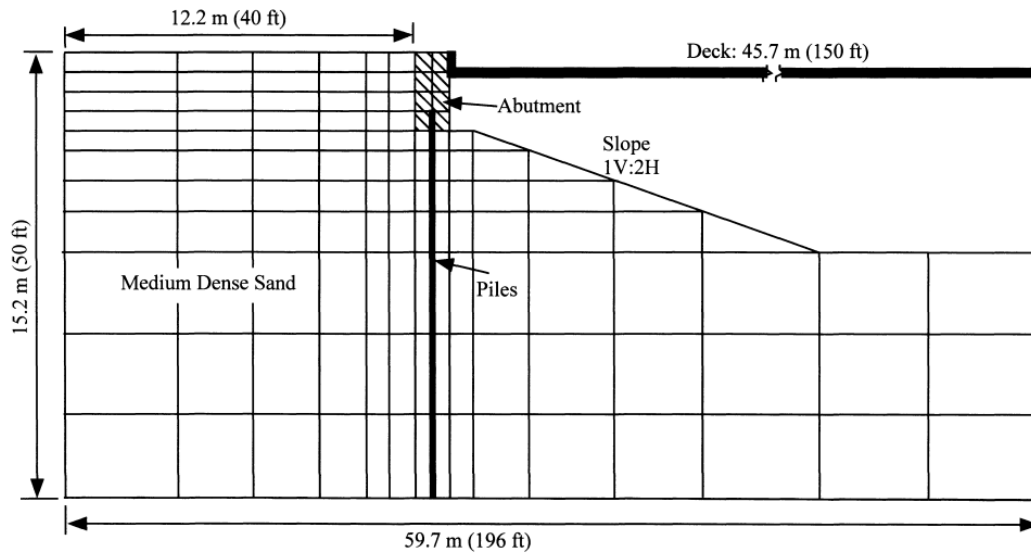


**Figure 2.13.** Finite element model developed by Arsoy et al. 1999. (Image taken from [10])

The results of the finite element analyses show that the soil around the piles moves significantly as the load is applied to the abutments. the moving soil does not produce significant actions in the structure as does the one that does not move, because the stresses provided by soil is governed by the relative movement of the structure with respect to the soil deposit. If the deposit moves by the same amount as the piles, the soil would provide no resistance to pile displacements. The piles would deflect as if they were surrounded by air [10].

#### 2.4.2 "Discrete" models

In the 1960s, in United States, integral abutments were often analyzed by moment distribution using a simple, two-dimensional frame model of the superstructure and piles. That model undoubtedly raised the issue of the condition at the bottom of the piles. In the 1980s, Iowa State University conducted research involving pile behavior with the development of a model that can describe pinned- or fixed-head piles. This model was proposed by Abendroth et al. (1989) [5] and introduced a simplified method for designing IAB piles. It appears to be widely accepted and is based on analytical and finite element studies. They introduces an *equivalent cantilever* column to replace the actual pile (see figure 2.14), so the soil-pile system is reduced down to a simpler one. The piles can be modeled as linear-elastic elements or with an inelastic behavior. Finite element simulations indicated that both alternatives were conservative. This method is used to analyze the system behavior under static loads and mainly describes the vertical load carrying capacity of piles under lateral displacements induced by temperature changes. Girton et al. [54] evaluated this method experimentally and concluded that the equivalent cantilever column model is sufficiently accurate for design purposes.

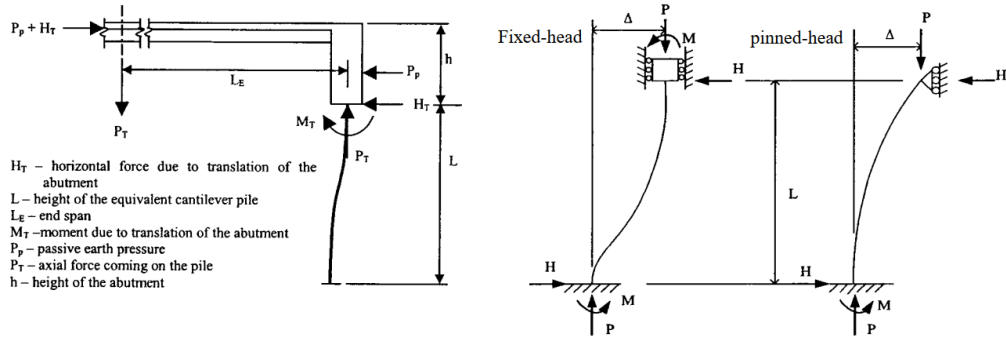


**Figure 2.14.** Equivalent cantilever model developed by Abendroth et al. [5]. (Image taken from [5])

Faraji et al [41] performed finite element studies of IAB with the aim to design and build long-span integral abutment bridges and to evaluate their performance during seismic loads (see figure 2.15).

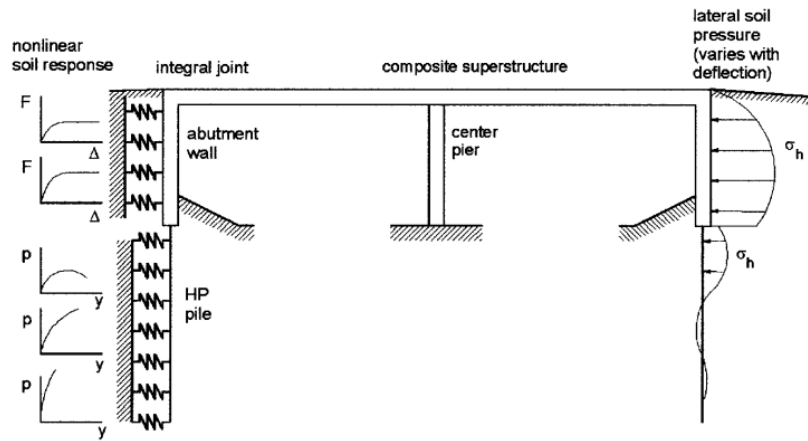


**Figure 2.15.** Typical Soil Response Adjacent to Abutment and Piles. (Image taken from [41])

They developed a full 3D finite-element model (see figure 2.16) which automatically incorporates the nonlinear soil response behind the abutments and adjacent to the supporting piles, and can model both skew and non-skew bridge orientations. The finite-element software *GTSTRU DL* was used to handle the nonlinear soil behavior using nonlinear springs at the abutment wall and pile nodes. The nonlinear force-deflection design curves recommended in National Cooperative Highways Research Program (NCHRP, 1991) design manual were used to represent the soil response behind the abutment wall while the nonlinear  $p$ - $y$  curves recommended by API (1993) were used for the lateral soil response next to the vertical piles.

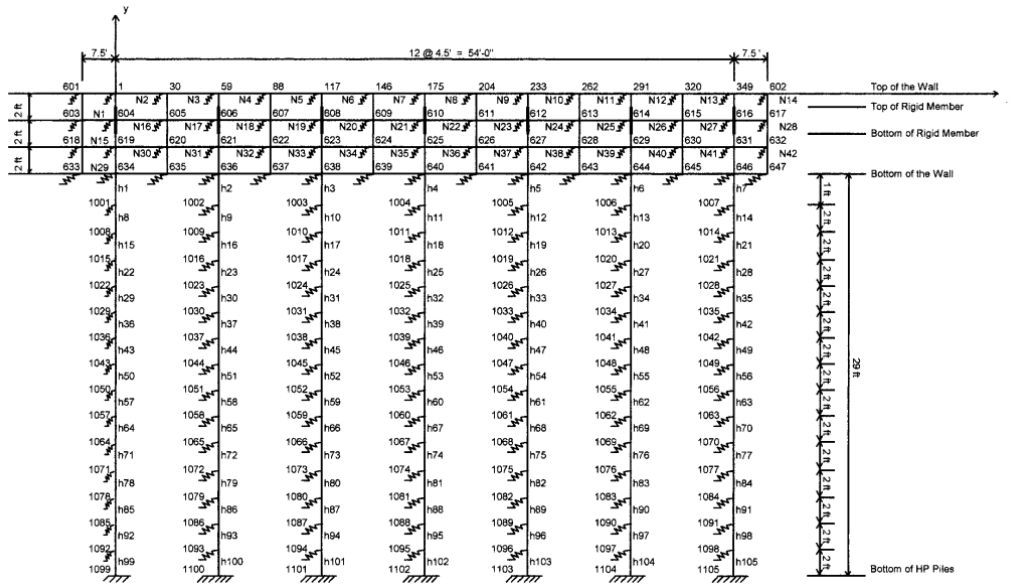


**Figure 2.16.** Elements, nodes, members, and soil springs for north abutment wall and HP piles. (Image taken from [41])

A 3D finite element model of "*Bemis Road Bridge: F-4-20*" in Fitchburg, Massachusetts was analyzed using this approach.

### Franchin-Pinto model

Franchin and Pinto [47] proposed a discrete dynamic non-linear finite element model that uses Winkler beams on non-linear springs for the evaluation of the bridge behavior under seismic actions. Nonlinear Winkler beams are used to discretize the behavior of the bridge sub-structure embedded into soil. This model was initially developed for the study of flexible earth-retaining diaphragms [48] [46] and later extended also for the evaluation of the dynamic behavior of integral bridges due to seismic ground motions [47].

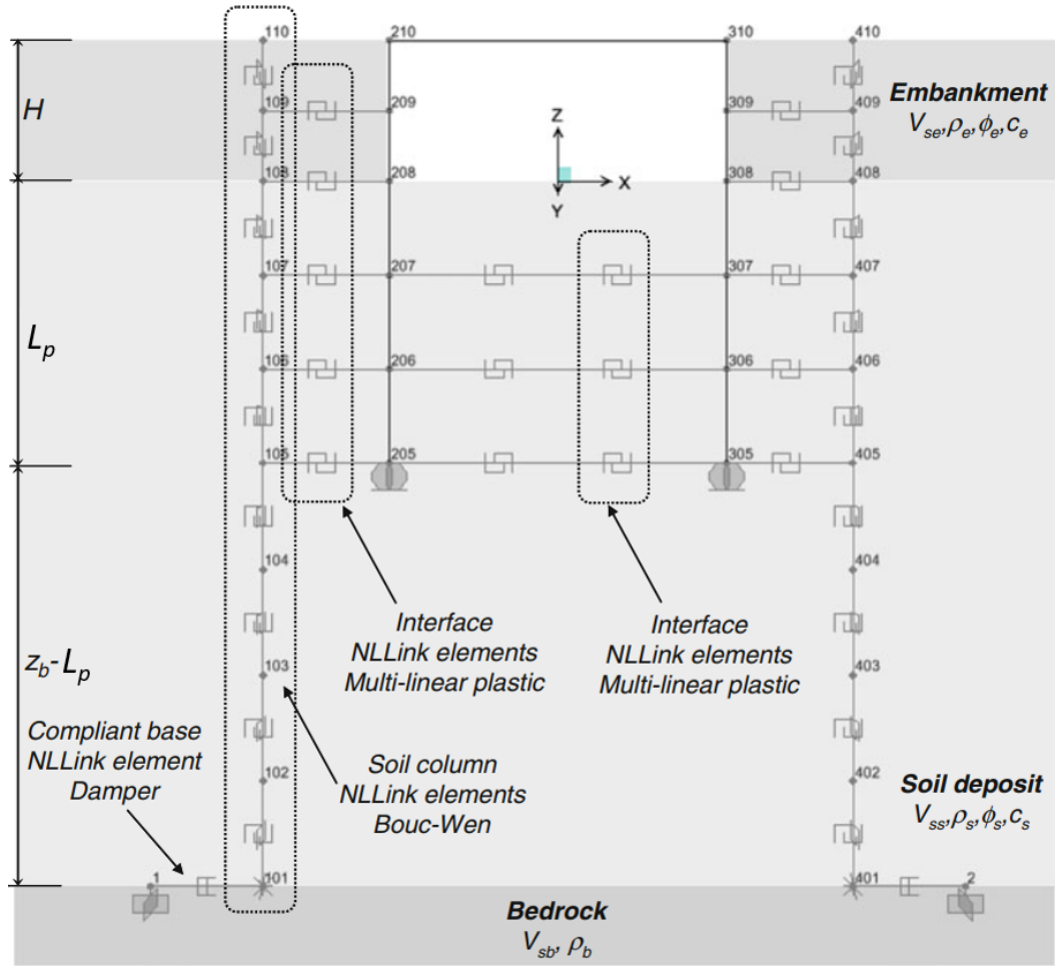


**Figure 2.17.** Franchin-Pinto integral abutment bridges model for seismic assessment. (Image taken from Franchin & Pinto, 2014 [47])

In the original formulation the non-linearity was considered only in the elements that discretize the soil, while the structure is considered linear elastic. The soil elements can be divided into two sets: The elements that describe the shear behavior of the soil deposit (*soil-column* elements) and the elements that discretize the behavior of the soil in contact with the structure (*interface* elements).

The problem of describing the behavior of an integral bridge lies in the fact that the actions in the structure (which are the relevant quantities for design) depend on the displacements of the system and, in particular, of the soil. For this reason, in this model, there are elements that describe the behavior of the soil deposit in which the structure is embedded, called *soil-column elements*. Taking as reference, for transverse displacements (along  $x$ ) of the system, the displacements of the nodes of the soil column, it is ensured that the structure follows the displacements of the soil in which it is placed. The substructure (piles and abutments) interacts with a portion of soil adjacent to the structure and which certainly does not have sufficient mass to modify the behavior of the soil deposit (described by the soil-column elements). To model this behavior, in which the soil deposit at sufficiently great distance from the

bridge behaves as if the structure did not exist<sup>6</sup>, the soil elements were divided into these two categories: *soil-column* and *interface* elements.

The column elements start from the interface between the deposit and the bedrock (at  $z = z_b$ ) and go up to the top of the embankment (at  $z = H$ ), in order to model both the behavior of the deposit and the bridge embankment. These elements can be considered almost as decoupled from the rest of the model, since the area ratios, and therefore the mass and stiffness ratios, are such as to make these elements little affected by the behavior of the rest of the system, both from a static and dynamic point of view.

Interface elements are used to model a very complex phenomenon of soil-structure interaction. The nature of such a model uses the theory of beams on nonlinear subgrade. This theory, in contrast to the theory based on the inelastic continuum, describes the behavior by neglecting the influence that the deformation of the soil in direct contact with a particular point of the structure has on the soil in contact with other points of the structure. The interface elements, in this model, connect both the nodes of the abutment with the soil-column corresponding to the respective embankment (to discretize the behavior of the volume of embankment in contact with the abutment that is modified by the displacements of the latter) and the nodes of the piles with both soil columns (to model the behavior of the *uphill* volume of soil, i.e. on the side of the embankment).

**Soil-Column elements:** Soil-column elements are assigned a Bouc-Wen constitutive law [15] [105] to approximate the horizontal nonlinear shear behavior of the deposit.

The constitutive Bouc-Wen law between  $u(t)$  and  $F(u(t))$  is defined by the following equations:

$$F(u(t)) = \alpha k_0 u(t) + (1 - \alpha) k_0 u_y \zeta(t) \quad (2.1)$$

$$\dot{\zeta} = \frac{\dot{u}}{u_y} [1 + |\zeta|^n (\gamma + \beta \operatorname{sgn}(\dot{u}\zeta))] \quad (2.2)$$

where  $k_0$  is the initial stiffness,  $\alpha$  the hardening ratio,  $u_y$  the yielding displacement and  $\zeta$  is an internal dimensionless variable that describes the hysteresis (whose evolution is governed by the differential equation (2.2)).

The model parameters are expressed as a function of physical system properties as (figure 2.18):

$$F_y = N' \tan(\phi') + A_s c' \quad (2.3)$$

$$k_0 = \frac{G_0 A}{\Delta z} \quad (2.4)$$

where the yielding force  $F_y$  is obtained by the Mohr-Coulomb theory for the soil shear resistance, as a function of the effective axial force  $N'$ , friction angle  $\phi'$  and cohesion  $c'$ . Every parameter, except for  $n$ , is a function of the depth  $z$ .  $N'$  is

<sup>6</sup>The displacements of the structure itself are conditioned by the displacements of the deposit through a volume of soil interacting with the structure

calculated with the effective stress  $N' = \sigma'_v / A_s$  where  $A_s$  is the soil-column cross section area.

Note that to have the force corresponding to the yield displacement be equal to the yield force  $F_y = k_0 u_y$  the following equation must be true [21]:

$$\gamma + \beta = \hat{A} = 1 \quad (2.5)$$

In this case<sup>7</sup>  $\hat{A}$  was placed directly equal to 1 in the internal differential equation (2.2).

The parameters of the internal differential equation (2.2) are:  $\gamma = \beta = 0.5$ ,  $\alpha = 0$  and  $n = 2$ .

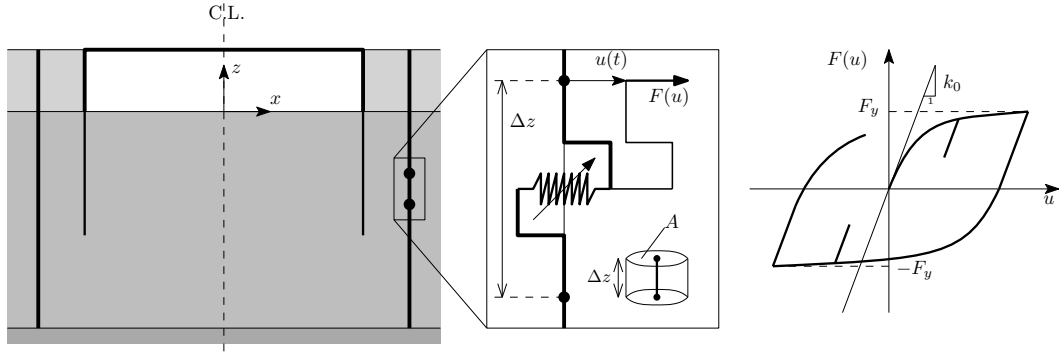


**Figure 2.18.** Soil-column element that describes the soil-deposit shear behavior.

In this model, for the soil-column elements describing the deposit (only for negative  $z$ ), the area  $A_s$  is multiplied by a factor  $r = 100$  to account for the large soil mass surrounding the piles. In fact, in the system first mode of vibration, what matters is essentially the behavior of the deposit, since the mass of the structure is irrelevant with respect to the mass of soil influenced by the structure. It should be noted that, while this factor  $r$  is meant to represent the fact that a relatively large soil mass oscillates with small influence from the embedded structural mass, the exact value of  $r$  assigned by the authors has not been subjected to either calibration or a sensitivity analysis.

The minimum dimension of the embankment length  $L_e$  (defined in figure 3.6) is equal to the critical value  $L_{e,cr}$  given by Zhang and Makris [113] [114]

$$L_e \geq L_{e,cr} = 0.7 \sqrt{S B H} \quad S = \frac{2H}{B_c - B_b} \quad (2.6)$$

where  $B_c$  and  $B_b$  are the embankment width at the top (crest) and the width at the base, respectively,  $H$  is the embankment height (which coincides with the height of the abutment for reasons of vehicular access to the bridge, at least for integral frame-abutments bridges, and  $S$  is the slope of the embankment. The soil mass that vibrates with the structure and, therefore, also the question of the parameter  $r$  will be studied in more detail in section 3.1.2.

<sup>7</sup>Here it is used a slightly different notation from the original model ( $\hat{A}$  instead of  $A$ ) to avoid confusion with the area.



Both soil columns (left and right ones) have a constraint of equal displacements on the only active degree of freedom (displacement along  $x$  axis). This is to account for the continuity of the soil deposit, whose behavior is not decoupled from one side of the bridge to the other. This is a possibly rough approximation, since the soil between the two soil columns is not infinitely rigid, but with its deformability it implies that this constraint of equal displacements is violated in the real system.

Piles bottom nodes have the displacement degree of freedom along  $z$  retained ( $q$ - $z$  spring are rigid).

**Interface elements:** Soil-structure interface elements are assigned an elastic perfectly plastic constitutive law, with non symmetric strength to differentiate for active and passive condition.

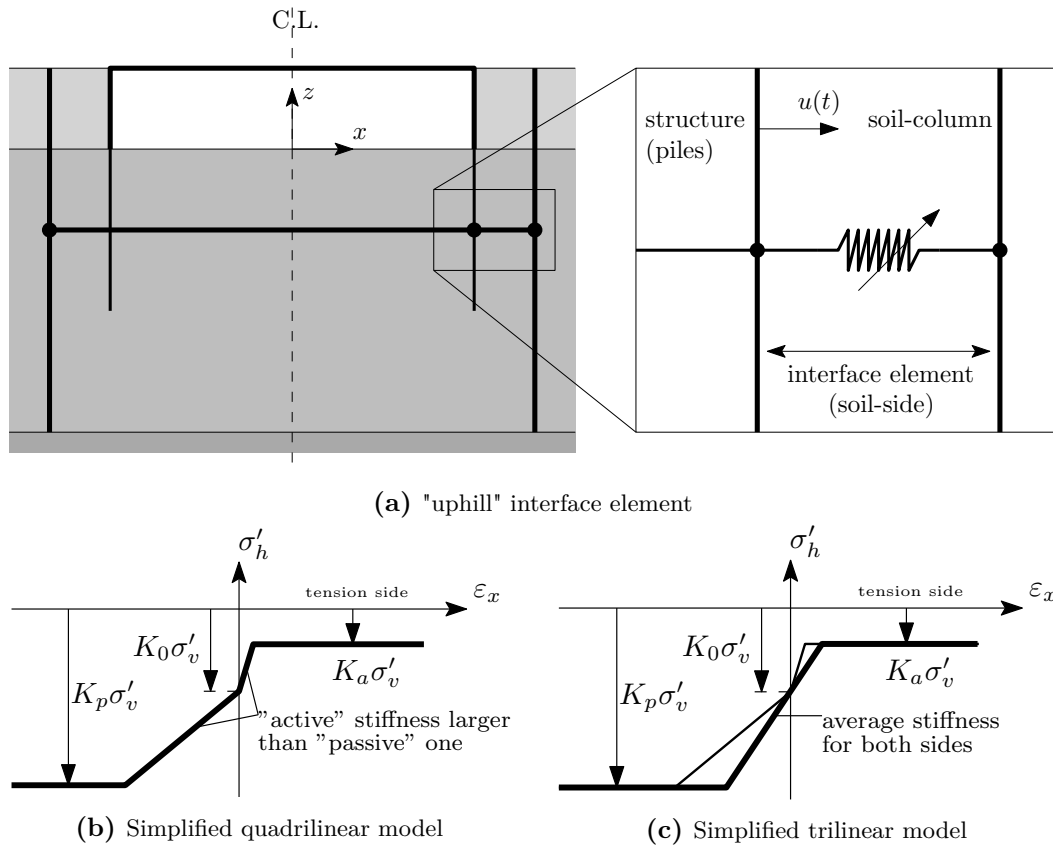


**Figure 2.19.** Interface elements.

The constitutive law is compression-only, since the soil is considered non-reacting to traction (Figure 2.19b and 2.19c). The largest compression corresponds to the passive threshold  $\sigma'_{h,p} = \sigma'_v K_p$ . The maximum value (corresponding to the lowest compression) coincides with the active threshold  $\sigma'_{h,a} = \sigma'_v K_a$ . Franchin & Pinto use the the horizontal, active and passive stress coefficients ( $K_0$ ,  $K_a$  and  $K_p$ , respectively)

from Rankine's [97] theory:

$$K_0 = 1 - \sin(\phi') \quad (2.7)$$

$$K_a = \frac{1 - \sin(\phi')}{1 + \sin(\phi')} \quad (2.8)$$

$$K_p = \frac{1}{K_a} = \frac{1 + \sin(\phi')}{1 - \sin(\phi')} \quad (2.9)$$

Active and passive conditions differ also in terms of stiffness. The actual behavior is continuously non-linear but it can be simplified to a quadrilinear law, as shown in figure 2.19b, with active stiffness being larger than the passive one. From this starting point, Franchin and Pinto in their original implementation in a commercial software (SAP2000) made further simplifications. The first, which is not due to a program limitation, was to adopt a single stiffness value, average between the active and passive ones, as shown in figure 2.19c. The second modification was instead needed since in SAP2000 multilinear constitutive laws that do not pass through zero cannot be defined. The  $\sigma$ - $z$  law is thus "translated" upwards by extrapolating the contribution of the horizontal stress at rest given by the weight of the embankment on the soil column

$\sigma'_{0h} = \sigma'_{0v} K_0$ , as shown in figure 2.20 (note that, for general layered deposit, while  $\sigma'_v$  is continuous,  $\sigma'_{0h}$  is not due to changes in  $K_0$ ).

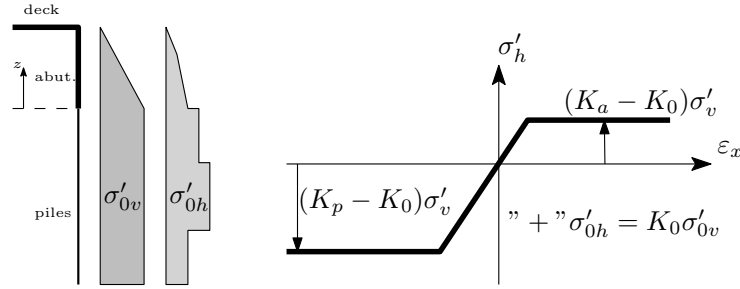


**Figure 2.20.** Interface elements constitutive model as implemented in SAP2000.

The parameters that enter into this law are the stiffness  $k_x$  and the two limits, active and passive, which are  $f_y^+$  and  $f_y^-$ , respectively. The equations that determine the constitutive law parameters from the system properties are:

$$k_x = 1.2 \frac{E A}{l_m} \quad (2.10)$$

$$f_y^+ = -A(K_a - K_0)\sigma_v \quad (2.11)$$

$$f_y^- = -A(K_p - K_0)\sigma_v \quad (2.12)$$

The equation for stiffness  $k_x$  is derived from the theory proposed by Roesset [99] and the length in the denominator is set to the average length between the active

and passive characteristic lengths (Becci and Nova [13]):

$$l_m = \frac{l_a + l_p}{2} \quad (2.13)$$

$$l_a = \frac{2}{3} \min(H + L_p, 2H) \tan\left(\frac{\pi}{4} - \frac{\phi'}{2}\right) \quad (2.14)$$

$$l_p = \frac{2}{3} \min(L_p, H) \tan\left(\frac{\pi}{4} + \frac{\phi'}{2}\right) \quad (2.15)$$

where the dimensions  $H$  and  $L_p$  are the height of the abutments and the length of the piles, respectively (as described in Figure 2.17). The elastic modulus  $E$  is equal to  $E = G_0 2(1 + \nu)$ , where  $G_0$  is the initial shear modulus of the soil. In the previous equations, the parameters  $\phi'(z)$ ,  $G_0(z)$ ,  $A(z)$ , and  $\sigma_v(z)$  depend, of course, on the depth  $z$  (explicit notation has been omitted in the equations for brevity).

Stiffness between the active and passive side are respectively  $k_a = 1.2(E A)/l_a$  and  $k_p = 1.2(E A)/l_p$ . The lengths  $l_a$  and  $l_p$  are the characteristic dimensions of the soil volume on the active and passive sides, respectively. These length are shown in figure 2.21.

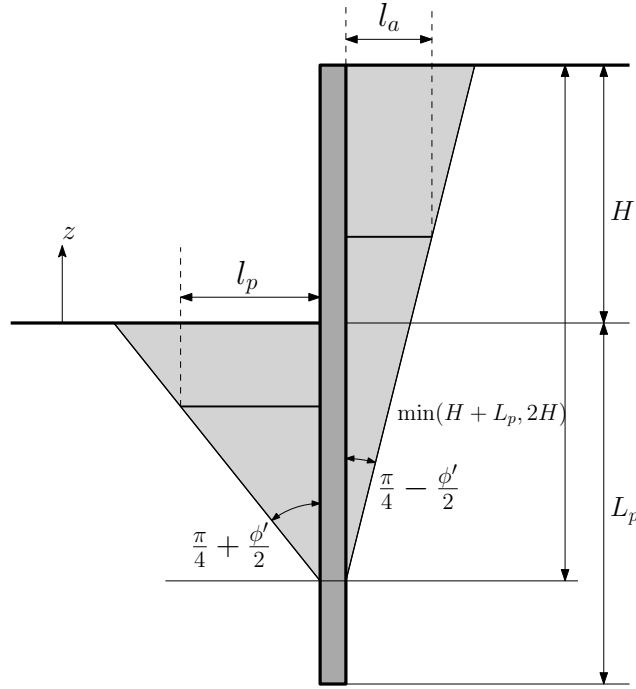


**Figure 2.21.** Interface elements characteristic dimensions of the soil volume interacting with the structure.

**Base damper:** Finally the input motion is applied to the base of the soil columns through velocity time series applied to dampers that describe the absorbing behavior of the bedrock toward incident shear waves (Lysmayer & Kulermayer [82]). The

force applied to the base is equal to:

$$f(t) = c_b \dot{u}(t, z_b) = [\rho_b V_{s,b} A_s(z_b)] \frac{\partial u(t, z_b)}{\partial t} \quad (2.16)$$

where  $\dot{u}(t, z_b) = \frac{\partial u(t, z_b)}{\partial t}$  is the soil horizontal displacement velocity at top surface of the bedrock  $z = z_b$ .  $\rho_b$  and  $V_{s,b}$  are the density and shear wave velocity in the bedrock, respectively, while  $A_s(z_b)$  is the area of the soil-column at its base [72].

**Results:** Figure 2.22 presents some results of the model in terms of bending moment at the deck-abutments connections.

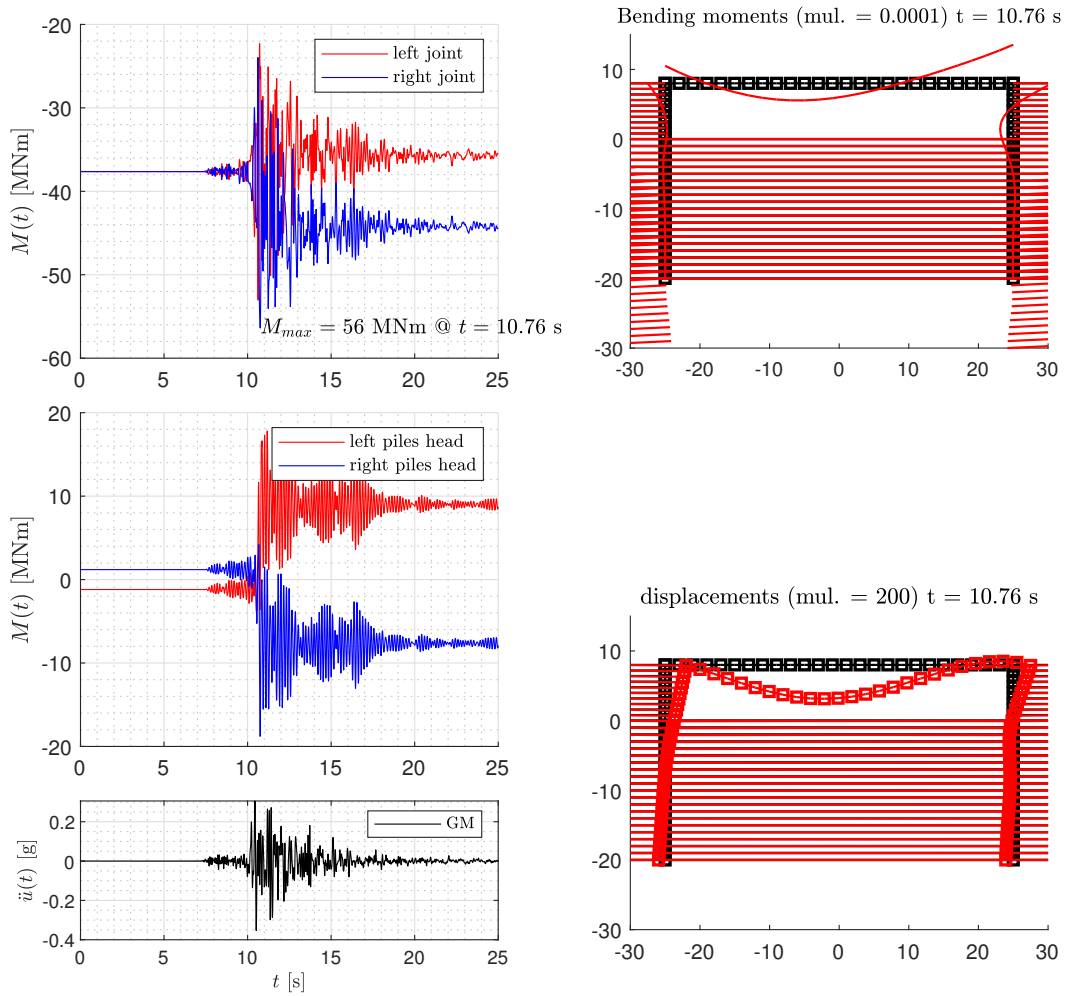


**Figure 2.22.** Results in terms of bending moment at deck-abutments connections.

The model considered is the benchmark system (Gatteo overpass) described in the section 4.2. This model is able to capture the general behavior of the system during the earthquake, at least in terms of bending moments on the substructure elements. In particular, it also manages to capture *ratcheting* behavior due to the

embankments soil, and so post-event stresses (note that the difference between initial and final bending moments in figure 2.22).

Figure 2.23 shows briefly the modal analysis output for this model.

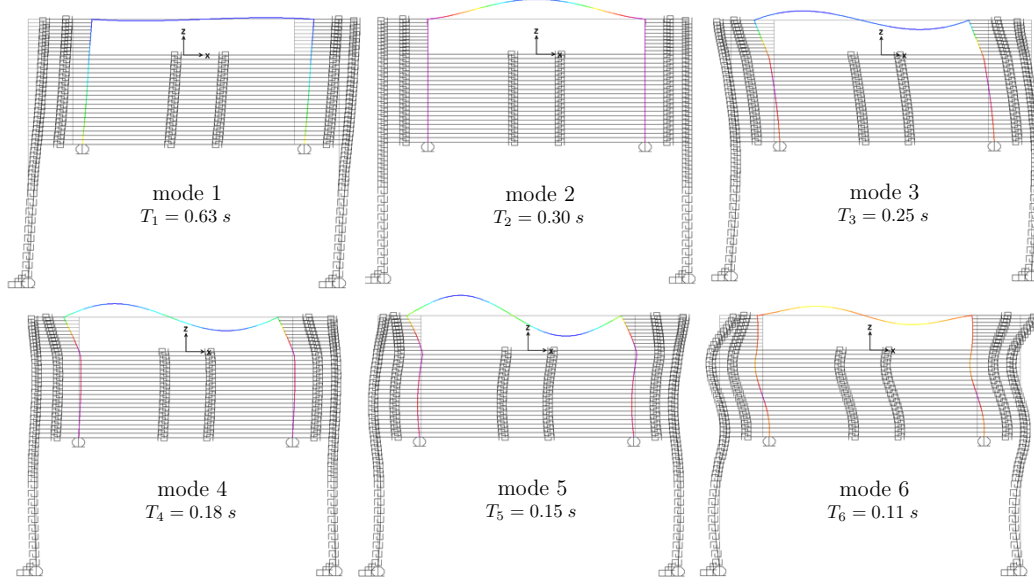


**Figure 2.23.** Modal analysis results: mode shapes and respective periods.

The first two modes are first soil-deposit mode and deck vertical mode, respectively. The structure is sensible mainly to the fourth and higher modes. In fact their modal shapes mainly affect the deformations in the deck-abutments connections, that are the most stressed sections during the seismic event. The first mode<sup>8</sup>, on the contrary, imposes only minimum deformations to the structure that translates following the deposit displacements.

**3D extension:** The authors also extended the 2D model to evaluate the system three-dimensional behavior, as shown in figure 2.24.

<sup>8</sup>For a homogeneous deposit of deformable height  $z_b$  and shear wave velocity  $V_s$  the fundamental period  $T_1$  is equal to

$$T_1 = \frac{4 z_b}{V_s} \quad (2.17)$$

in this equal to 0.61 s using  $z_b = 50m$  and an average value  $V_s = 330m/s$  (for the *Gatteo* benchmark case described in section 4.2).

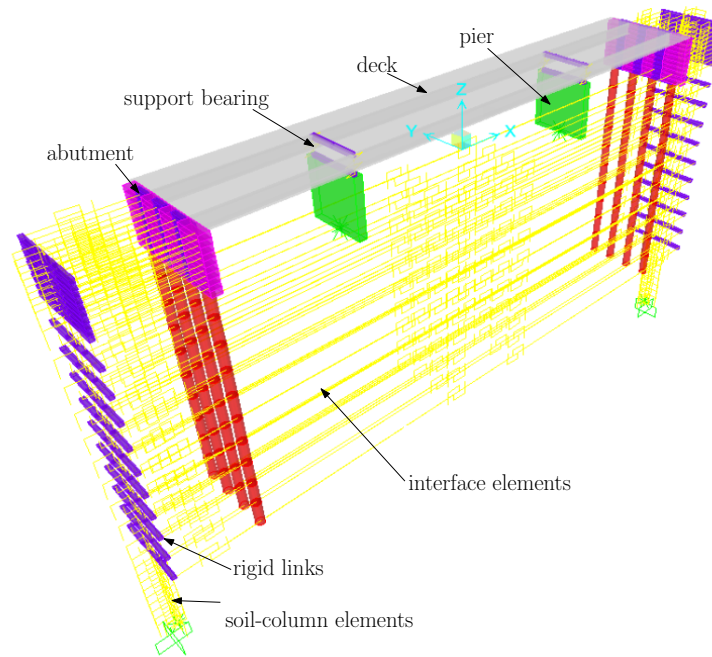


**Figure 2.24.** 3D extension of the original model developed by Franchin & Pinto.

While this model has shown to capture qualitatively the main aspect of the seismic behavior of IABs some important aspects clearly need to be studied further, to make the model predictability fit enough for reliable practical application:

- Actual participating soil mass ( $r$ )
- Soil-column elements constitutive law
- Interface elements constitutive law
- Structural non-linearity
- Damping
- Initial conditions (construction stages and temperatures)
- 3D behavior (only tentatively considered by the authors)

For the above reasons, this model is taken as starting point to develop an improved model in this thesis.

## Chapter 3

# Dynamic model

This chapter introduces a non-linear finite element model fit for response-history analysis and termed in the following dynamic model. The model developed starting from the non-linear Winkler-beam based model by Franchin & Pinto (described in section 2.4.2), aims at improving on all areas identified at the end of the previous chapter. Nonetheless it remains intentionally a practic-oriented model and for this reason is also called a Reduced-Order Model (ROM) as opposed to higher-order 3D nonlinear FE model like that used for validation in the following chapter 4.

This model uses nonlinear springs for the discretization of the soil-structure interaction using the theory of the Winkler beam on non-linear foundation springs bed. Like in the original model those elements are divided into two sets:

- *Soil-column elements*: elements that simulate the shear behavior of the soil deposit.
- *Interface elements*: non-linear springs that describe the behavior of the soil in contact with the structure (piles and abutments).

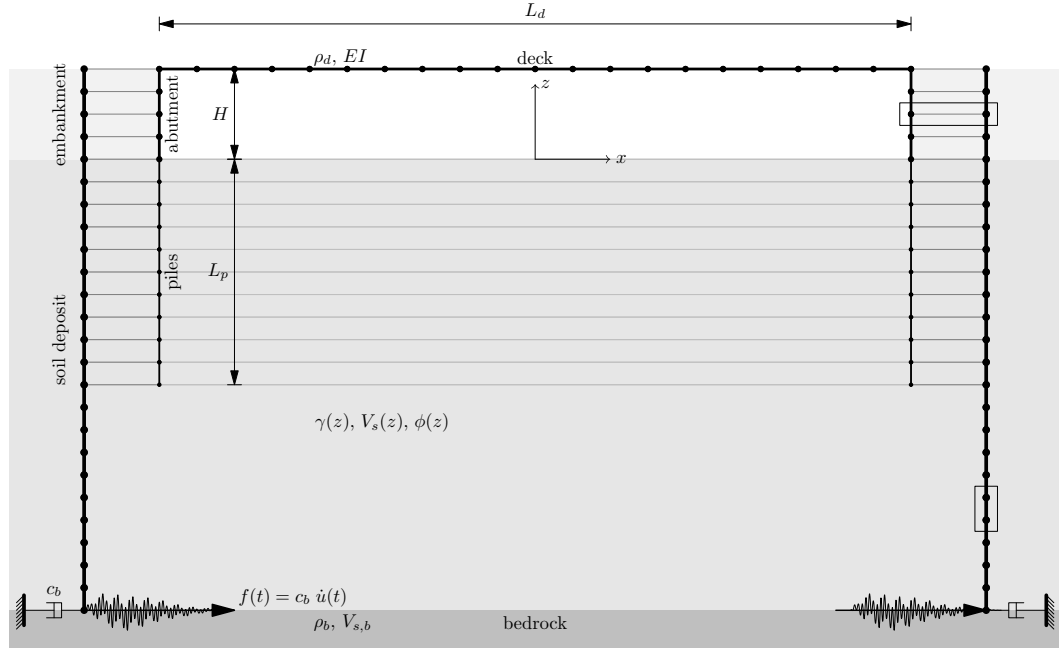


**Figure 3.1.** Dynamic 2D model (ROM).

An integral abutment bridge is a structure embedded in the soil, which contains its deformations due to inertia forces during an earthquake. In fact, at the instant when the bridge is deformed in a certain longitudinal direction due to the inertia actions, the embankment (the one which is going towards the passive condition) reduces the abutment displacements; and since the deck has a relative higher stiffness longitudinally the effect of the embankment backfill is to reduce the entire bridge displacements along  $x$ . This restraining action made by the soil decreases the bending moments in the structure. Finally, during the cyclic action of the earthquake, the soil of the abutments (the one that interact with the structure) presents a ratcheting phenomenon that tends to increase the longitudinal displacements (along  $x$ ) of the pile head towards the inside of the bridge. This main general behavior of integral abutment bridges during earthquakes are described by this dynamic model through the interface elements. The soil-column elements take into account also for site-response analysis and allow to describe more accurately the response of the piles, that are embedded into the soil deposit.

### 3.1 Soil column elements

These elements are used to describe the shear behavior of the deposit and the embankment above it, in fact this computational model is not able to capture the behavior of the system for vertical accelerations. This limitation is legitimate, because the main actions on the structure are given by the horizontal component of the seismic motion, therefore it is sufficient to describe the shear behavior (horizontal) of the soil deposit.



### 3.1.1 Improved constitutive law for fine- and coarse-grained soils

Soil-column elements describe the behavior of the embankment and of the portion of underlying soil between the surface and a stiffer soil stratum (bedrock) or arbitrary deep model base. Explicit definition of these elements allows the model to consider the local seismic response at the price of including the correct motion at the bedrock. More details on the time series applied on the soil-column base are given in section 3.3 and in appendix A.

The column elements are all aligned in a series configuration vertically, and the nodes exhibit displacement only in the  $x$ -direction. The height of the individual element (distance between node  $i$  and node  $i + 1$ ) is equal to  $\Delta z_i$  and has an area denoted by  $A_{s,i}$  for  $z < 0$  (soil-deposit) or  $A_{e,i}$  for  $z > 0$  (embankment). The constitutive law linking this displacement (relative between two nodes element) to the internal shear force is a Bouc-Wen model modified by Gerolymos and Gazetas in 2005 [53] to account for soil degradation. The equations for such a model are:

$$f(u(t)) = \alpha k_0 u(t) + (1 - \alpha) k_0 u_y \zeta(t) \quad (3.1)$$

$$\dot{\zeta} = \theta \frac{\dot{u}}{u_y} [1 + |\zeta|^n (\gamma + \beta \operatorname{sgn}(\dot{u}\zeta))] \quad (3.2)$$

where all symbols have been defined with reference to equation (2.2) and the  $\theta$  is introduced to account for degradation.  $\theta$  decreases the initial tangent with a function of how much the displacement exceeds the yielding one [34].

$$\theta = \begin{cases} \frac{s_1 + \alpha(\mu_r - 1) + s_2}{s_1 + \mu_r} & \mu_r > s_2 \\ 1 & \mu_r < s_2 \end{cases} \quad (3.3)$$

where  $s_1$  is a dimensionless parameter that controls the stiffness degradation upon stress reversal,  $s_2$  is a characteristic value of "strain ductility"  $\mu = \gamma/\gamma_y$  beyond which the effect of  $\theta$  multiplier on stiffness degradation is activated, and  $\mu_r$  is a reference strain ductility defined for every unloading or reloading cycle as the ratio of half the difference in strain  $\gamma$  between two previous reversals over the reference strain  $\gamma_y$ .

The defined law is shown in figure 3.2 in comparison with the classical Bouc-Wen model (equation (2.2) without the  $\theta$  function) with the same parameters.

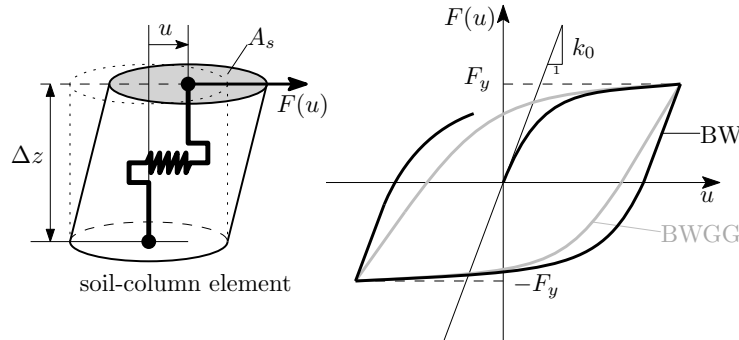


**Figure 3.2.** Bouc-Wen models used in soil-column elements. BW refers to the classic Bouc-Wen model [15] [105], while BWGG refers to the model modified by Gerolymos & Gazetas [53] [34].

Drosos et al. [34] later calibrated the parameters of this simplified BW model to the experimental data from Ishibashi and Zhang [66] (figure 3.3) on fine- and coarse-grained soils as a function of the Plasticity Index (PI) and effective confining pressure

$$\sigma'_0 = \frac{\sigma'_v + 2\sigma'_h}{3} \quad (3.4)$$

Those parameters can be found in table 3.1.

**Table 3.1.** Values of calibrated parameters by Drosos et al [34], according to Ishibashi and Zhang [66] curves, as function of Plasticity Index (PI) and confining pressure  $\sigma'_0$ .

PI	$\sigma'_0$	$\gamma_y^{-1}$	$\beta$	$n$	$s_1$	$s_2$
0	10	3500	0.60	0.40	2.20	0.10
0	50	1400	0.60	0.40	2.20	0.10
0	100	900	0.60	0.40	2.10	0.20
0	200	500	0.60	0.40	2.10	0.20
0	400	300	0.60	0.45	2.10	0.20
0	1000	200	0.60	0.70	2.00	0.20
15	10	1400	0.60	0.50	1.30	0.10
15	50	800	0.60	0.50	1.30	0.10
15	100	600	0.60	0.60	1.30	0.10
15	200	500	0.60	0.60	1.30	0.10
15	400	400	0.60	0.65	1.30	0.10
15	1000	300	0.60	0.75	1.30	0.10
30	10	600	0.60	0.80	1.00	0.00
30	50	500	0.60	0.80	1.00	0.00
30	100	400	0.60	0.80	1.00	0.00
30	200	400	0.60	1.00	1.10	0.00
30	400	400	0.60	1.20	1.20	0.00
30	1000	400	0.60	1.20	1.20	0.00
50	10	400	0.60	1.20	0.90	0.00
50	50	350	0.60	1.20	0.90	0.00
50	100	350	0.60	1.20	0.90	0.00
50	200	320	0.60	1.20	0.90	0.00
50	400	320	0.60	1.20	0.90	0.00
50	1000	280	0.60	1.20	0.90	0.00
100	10	160	0.60	1.20	0.80	0.00
100	50	160	0.60	1.20	0.80	0.00
100	100	150	0.60	1.20	0.80	0.00
100	200	150	0.60	1.20	0.80	0.00
100	400	150	0.60	1.20	0.80	0.00
100	1000	150	0.60	1.20	0.80	0.00
200	10	70	0.60	1.20	0.80	0.00
200	50	70	0.60	1.20	0.80	0.00
200	100	70	0.60	1.20	0.80	0.00
200	200	70	0.60	1.20	0.80	0.00
200	400	70	0.60	1.20	0.80	0.00
200	1000	70	0.60	1.20	0.80	0.00

Intermediate values are calculated through linear interpolation of the table 3.1

data.

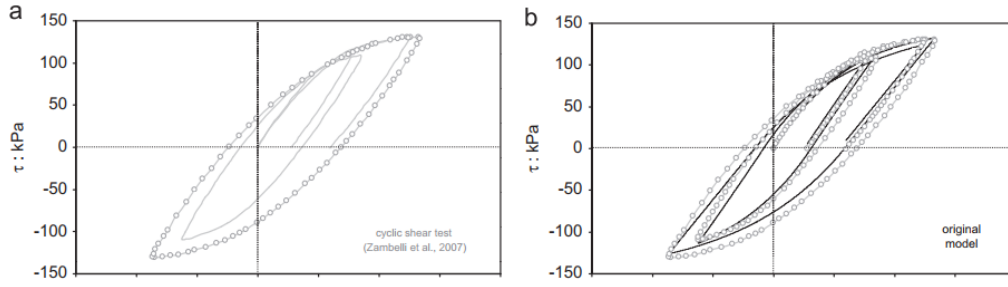


**Figure 3.3.** Stress-strain hysteresis loops of a dense Toyoura sand specimen: (a) experimentally measured (Zambelli et al. [112]); (b) calculated with the BWGG constitutive model. (Image taken from Drosos et al. [34])

Figure 3.4 shows the response of the model as the exponent  $n$  of the equation (2.2) varies.

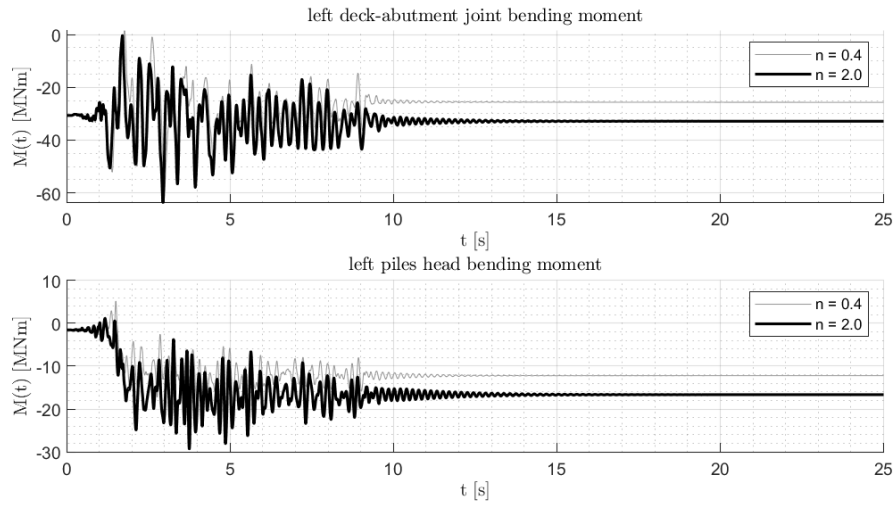


**Figure 3.4.** Global results (in terms of bending moments) of the model with  $n = 2.0$  (original model) and with  $n = 0.4$ .  $n$  is the exponent in the Bouc-Wen constitutive law (equation (2.2)).

The bending moment is higher with  $n = 2.0$  because Bouc-Wen constitutive law exhibit less nonlinear behavior (less hysteresis) and, therefore, the soil columns dissipate less energy.

Instead, the figure 3.5 shows the response of the model with the standard Bouc-Wen constitutive law (BW) [15] [105] and the constitutive law modified by Gerolymos and Gazetas (BWGG) [53]. As shown, the difference between the two bending moment time series is imperceptible.

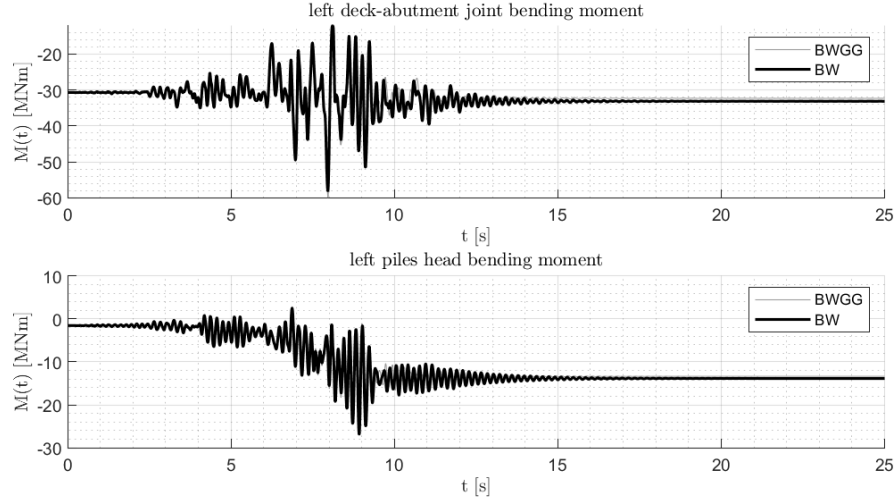


**Figure 3.5.** Global results (in terms of bending moments) of the model with the standard Bouc-Wen constitutive law (BW) [15] [105] and with the Bouc-Wen model modified by Gerolymos and Gazetas (BWGG) [53] for soil-column elements.

Table 3.2 shows the average over 10 seismic ground motions (relative to the sixth stripe of L'Aquila site, as shown in section 6.2.2) of the maximum absolute value of the bending moment at the most stressed cross sections.

**Table 3.2.** Global scalar response parameters as function of soil-column definition.

const. law	$n$	$\text{mean}\left(\max_t  M_{left,joint}  \right)$ [MNm]	$\text{mean}\left(\max_t  M_{left,piles}  \right)$ [MNm]
BWGG	2.0	66.12	31.25
BWGG	0.4	59.54	21.31
BW	0.4	57.24	20.81

As it can be seen, from figures 3.4, 3.5 and table 3.2, the largest difference is given by the modification of the parameter  $n$ , rather than by the introduction of the degradation function  $\theta$  defined via the equation (3.3). While this may be regarded as a favorable fact, since it allows using common implementations of the Bouc-Wen law available in most programs, it must be observed, however, that this law has an inherent instability in the numerical evaluation of the inner function (2.2) when  $n < 1$  (as in this case). The problem is discussed in detail in section 3.5.1. This is particularly evident in the software **OpenSEES** where it prevents convergence and the analysis stops. Therefore, a numerical algorithm has been implemented (also described in section 3.5.1).

### 3.1.2 Calibration of geometric parameter $r$

In order to evaluate, as accurately as possible, the interaction between the structure and the surrounding soil, the stiffness, strength and mass of the latter have to be

evaluated carefully. A smaller area for the soil column would make for a lighter and more flexible soil mass whose motion would be affected to a larger degree by the structure. A larger area, in the limit an infinite one, would be totally unaffected.

The initial stiffness  $k_0$ , yield strength  $F_y$ , and mass  $m$  of the individual soil-column element all depend on its area  $A_s$  (for simplicity the subscripts  $i$  have been dropped). Due to the displacement of the piles within the soil, a portion of the soil adjacent to them is mobilized with its mass and is included in the behavior of the entire system. To account for this additional mass, the area of the soil elements for the subsoil<sup>1</sup> was increased by a factor  $r$  that depends on global geometric factors (such as the bridge length  $L_d$  and the embankment crest and base width  $B_c$  and  $B_b$ ) and global mechanical and geometrical factors (see figure 3.6). The latter are the effective embankment length  $L_e$  and the effective soil width  $B_s$ . The width  $B_s$ , as mentioned earlier, depends on how much soil is mobilized by the foundation through the arch effect between piles and the stress diffusion in the lateral soil beyond abutment footprint. The first phenomenon ensures that  $B_s \geq B_b$ , while the second is more difficult to investigate.

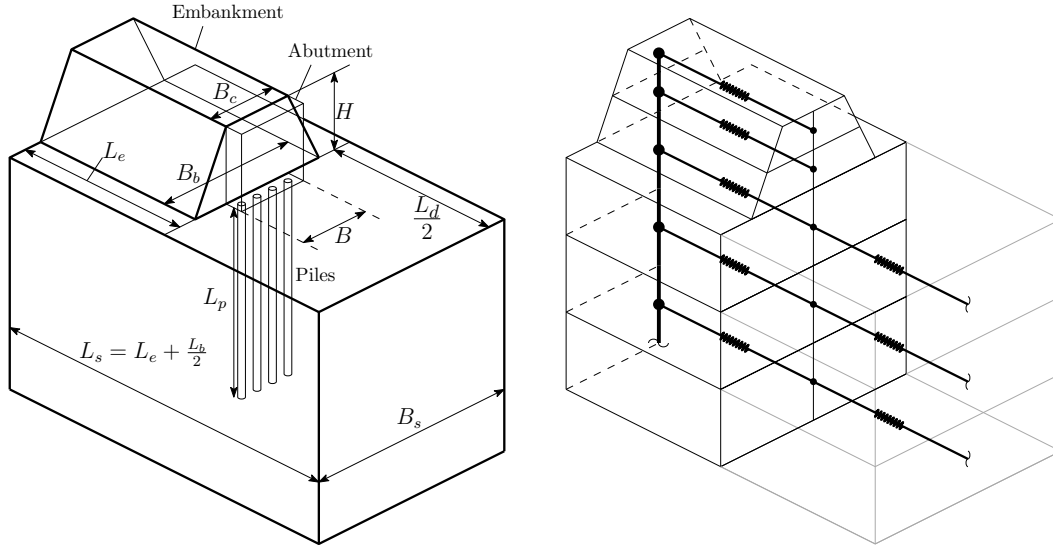


**Figure 3.6.** Half-model scheme for soil-column and interfaces geometry.

From these quantities, a ratio  $r = A_s/A_e$  between the area of the soil-column elements below the base of the embankment and the base area of the embankment can be defined. This ratio is equal to:

$$r = \frac{A_s}{A_e} = \frac{B_s L_s}{B_b L_e} = \frac{B_s \left( L_e + \frac{L_d}{2} \right)}{B_b L_e} \quad (3.5)$$

where  $L_d$  is the bridge deck span.

If the piles are close enough is still not possible to have  $B_s < B_b$  because of the *arch effect*, as shown in figure 3.7.

<sup>1</sup>i.e., at depth  $z$  shallower than the base of the embankment, thus for  $z < 0$  with the global reference system described in this model (defined in figure 3.1).

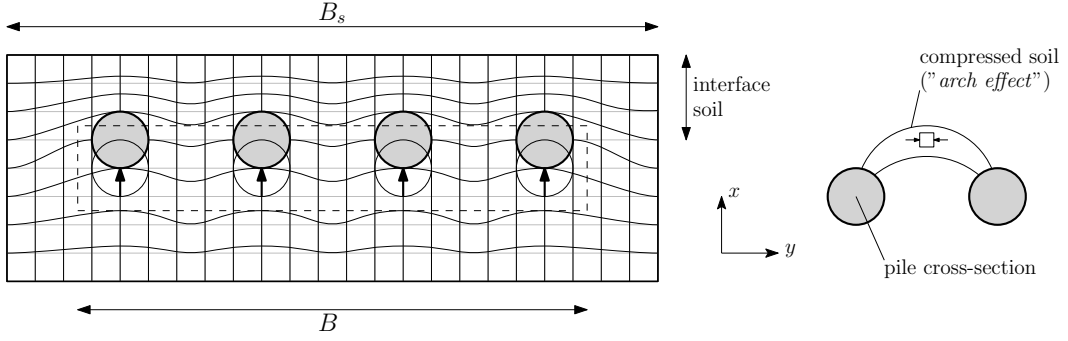


**Figure 3.7.** Soil deformation due to piles horizontal displacements and *arch effect* of the soil between piles.

Note that, even if the soil beyond the foundation footprint is not deformed by the piles displacements and thus  $B_s = B_b$ , still the ratio  $r$  is not equal to one, since the bridge has a span greater than zero ( $L_d > 0$ ).

Another geometric parameter that strongly depends on the soil-structure interaction that affects the definition of the ratio  $r$ , in addition to  $B_s$ , is the embankment length  $L_e$ . In fact the area of the embankment portion of the soil-column  $A_e$  (together with the soil-column elements area  $A_s$  for  $z < 0$ ) determine the soil mass in the coupled system and, obviously, are quite relevant to the overall dynamic response. Area  $A_e$ , the base width  $B_b$  being fixed, is determined by the embankment length  $L_e$ . In the original proposal by Franchin and Pinto [47]  $L_e$  was taken equal to the critical length  $L_{e,cr}$  in Zhang and Makris [113] [114], which, however, increases with the slope  $S = 2H/(B_b - B_c)$  and becomes indefinitely large when the  $B_b$  equals the crest width  $B_c$ , as it happens for the bridge analyzed in the confrontation case described in section 3.6.1. It is therefore set  $L_e = 5.5H = 44m$  equal to the upper bound given in Gorini and Callisto [55] and in Gorini et al. [56], based on the extension of the plastic mechanism of the embankment subjected to a longitudinal crest force.

Finally, it is noted that, for the same value ratio  $r$ , the dynamic behavior of the system changes if  $L_e$  and  $B_s$  are modified accordingly and even modifying  $r$  by changing  $L_e$  or  $B_s$  does not have the same effect on the response (the system is less sensitive to the value of  $L_e$ ).

### 3.2 Interface elements

Interface elements describe the behavior of an effective volume of soil adjacent to the structure to discretize the interaction behavior between soil and structure. By effective volume it is meant the soil that deforms due to the relative displacement between the structure and the soil column: the soil that, deforming, allows to pass from the displacements of the structure to the displacements of the soil deposit at a, theoretically, infinite distance from the bridge (as it can be seen in figure 3.7). Theoretically infinite distance considering always the deposit and the embankment as infinitely extended and always equal (same properties of the soil along the whole axis  $x$ ).

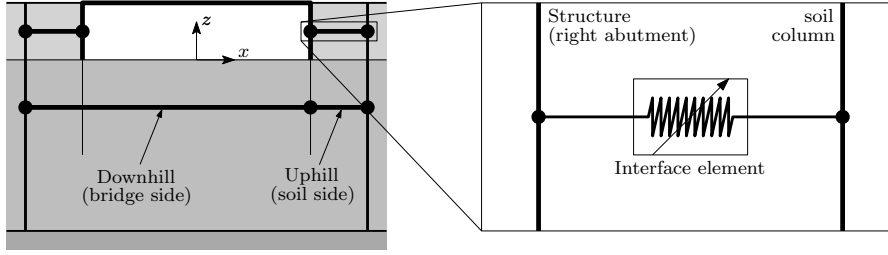


**Figure 3.8.** Interface elements used in the dynamic model and in the static non-linear model described in section 5.1.

### 3.2.1 Stiffness

Initially (in the original Franchin-Pinto model described in section 2.4.2) the stiffness was defined as a mean stiffness between active and passive sides.

Actually, it has been seen that the behavior of interface elements in the active side is not very relevant, being the uphill soil of integral bridge abutments mainly towards the passive state<sup>2</sup>. Also the order of magnitude of the displacement thresholds for the passive and the active resistance are very different. Thus, the soil interacting with an integral abutment bridge is primarily in a state where the stiffness is closer to the stiffness of the passive state, which is lower than the active one. This leads to increased displacements of the structure, which is less constrained by the soil, and thus greater internal actions in the structure. In conclusion, therefore, it was seen that considering, for such elements, a trilinear constitutive law with the stiffness of the elastic section equal to the average between the active and passive stiffness's underestimated the actions on the structure. However, the trilinear model can (to a first approximation) be used as long as the passive stiffness  $k_p$  is used.

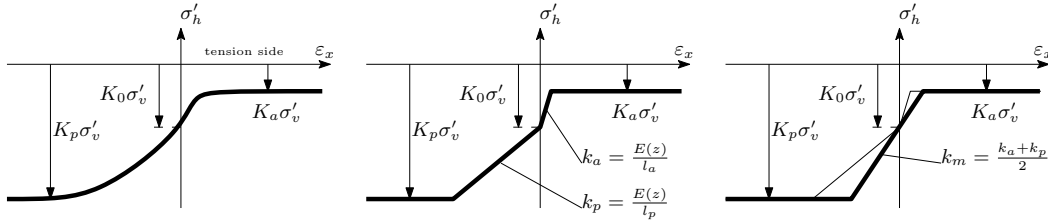


**Figure 3.9.** Constitutive laws evolution for the interface elements (from left to right respectively).

The natural evolution of the trilinear formulation (with only one stiffness) is to use a quadrilinear, i.e. linear function with two constant parts that describe the behavior of the soil passed the active and passive states (perfect elasto-plastic as before) and two linear parts with different stiffnesses for the active side (in case of elongation) and for the passive side (in case of shortening).

As it can be seen from the results of the benchmark model (*Gatteo* overpass, described in chapter 4) displayed in figure 3.10, using the corrected quadrilinear constitutive law the system response (in terms of bending moment at the abutment-pile nodes and at the piles head) changes considerably (see figure 3.10).

<sup>2</sup>compared to the abutments of traditional bridges, i.e. with simply supported decks, where the soil is instead towards the active state [98]

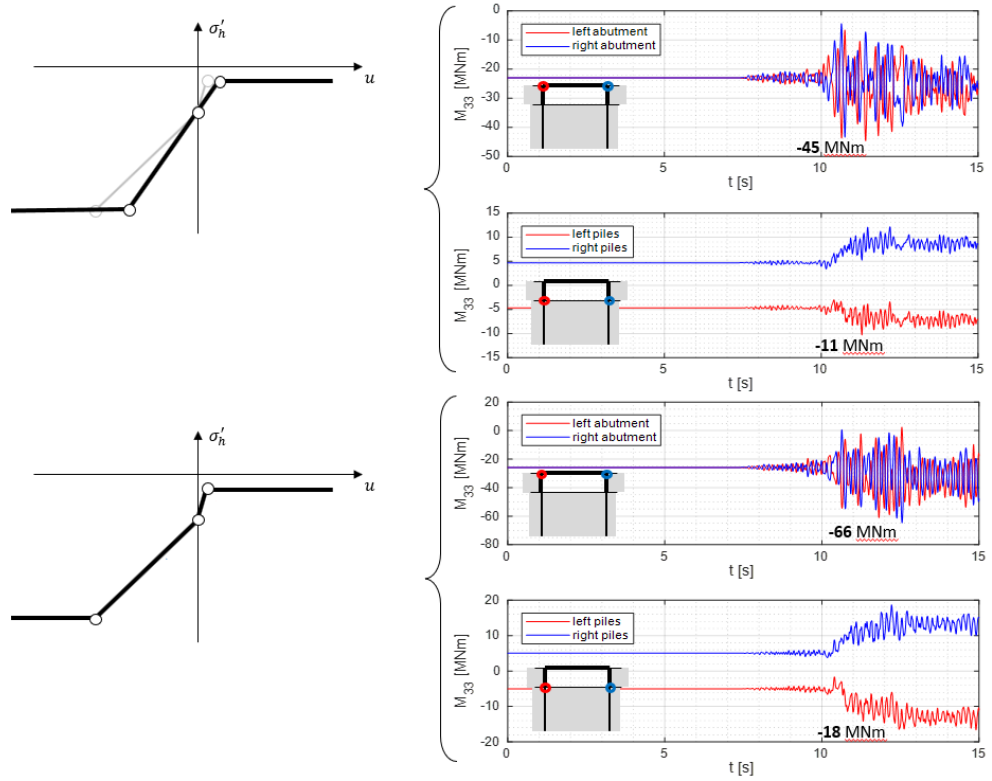


**Figure 3.10.** Analysis results for different interface elements constitutive laws. Trilinear model is used in the original Franchin-Pinto model while the quadrilinear one is the improved one used in the ROM model.

With the average stiffness  $k_m = (k_a + k_p)/2$  results are similar to the quadrilinear case; this is mainly due to the fact that the behavior of the interface springs in the active side does not count much in the global response of the soil-bridge system.

One of the main differences from the original model, in terms of system response, therefore is due to the improved behavior of the interface elements with a quadrilinear constitutive law (different stiffness's for active and passive sides).

This difference is due to the fact that the interface elements are more flexible, as the active threshold has a "yield" displacement that is a few orders of magnitude smaller than that of the passive threshold. So simply averaging results in having stiffer interface elements, which prevented deformation of the structure. By increasing the flexibility of the system the stresses in the structure also increase. Therefore, with the quadrilinear model for interface springs, higher bending moments are obtained than with the trilinear case with average stiffness.

### 3.2.2 Strength

Another important change on the constitutive law of these elements was the revision of the active, but especially passive thresholds. In fact, using Rankine theory to define earth pressure coefficients overestimated the entry in the passive state for the elements. This behavior was mainly evidenced in comparisons with a higher-order model developed by a geotechnical research group in which the elements reached



the passive limit more easily than the results of the higher order comparison model. This behavior is most evident for the passive threshold, the active threshold is the one that matters least, both in terms of forces and, more importantly, in terms of displacements. The physical nature of this behavior can be attributed first of all to the fact that the passive stress coefficient  $K_p$  increases if, with respect to Rankine's theory, the friction between soil and structure is also taken into account (via the soil-structure friction angle  $\delta$ ). This coefficient  $K_p$  changes also when considering the oscillatory nature of the earthquake and how it affects the soil conditions. For these reasons, the active and passive coefficients,  $K_a$  and  $K_p$ , were taken from the theory of Callisto et al. 2011 [96] which modifies the theory of Lancellotta [76] by accounting for seismicity through the seismic coefficients<sup>3</sup>

$$\kappa_h = \frac{\max(\ddot{u}_{g,h}(t))}{g} \quad \kappa_v = \frac{\max(\ddot{u}_{g,v}(t))}{g} \quad (3.7)$$

of the earthquake intensity and how they contribute to changing the soil state and, therefore, also of the stress coefficients  $K_a$  and  $K_p$ . As a function of the seismic coefficient  $\kappa_s$  they are calculated using the following formulas:

$$\theta = \arctan\left(\frac{\kappa_h}{1 - \kappa_v}\right) \quad (3.8)$$

$$\theta_A = \frac{1}{2} \left[ \arcsin\left(\frac{\sin(\delta)}{\sin(\phi')}\right) - \arcsin\left(\frac{\sin(\epsilon + \theta)}{\sin(\phi')}\right) - \delta + \epsilon - \theta \right] \quad (3.9)$$

$$\theta_P = \frac{1}{2} \left[ \arcsin\left(\frac{\sin(\delta)}{\sin(\phi')}\right) + \arcsin\left(\frac{\sin(\epsilon - \theta)}{\sin(\phi')}\right) + \delta + \epsilon + \theta \right] \quad (3.10)$$

$$K_a = \frac{\cos(\delta) \cos(\epsilon) \left( \cos(\delta) - \sqrt{\sin^2(\phi') - \sin^2(\delta)} \right)}{\cos(\theta) \left( \cos(\epsilon + \theta) + \sqrt{\sin^2(\phi') - \sin^2(\epsilon + \theta)} \right)} e^{-2\theta_A \tan(\phi')} \quad (3.11)$$

$$K_p = \frac{\cos(\delta) \cos(\epsilon) \left( \cos(\delta) + \sqrt{\sin^2(\phi') - \sin^2(\delta)} \right)}{\cos(\theta) \left( \cos(\epsilon - \theta) - \sqrt{\sin^2(\phi') - \sin^2(\epsilon - \theta)} \right)} e^{2\theta_P \tan(\phi')} \quad (3.12)$$

where  $\kappa_h$  and  $\kappa_v$  are the horizontal and vertical seismic coefficients, respectively.  $\delta$  is the friction angle between soil and structure that can be set equal to  $\delta = 2/3 \phi'$ .  $\epsilon$  is the angle of inclination of the ground plane (in this case equal to zero since the access embankments are limited to the road reduced regulatory slopes). In the above formulas  $\theta$  represents the inclination of the volume forces, while  $\theta_A$  and  $\theta_P$  represent the rotation of the principal directions in the active and passive sides, respectively. This theory has a limitation; that is, the following condition must be true:

$$\tan(\phi') \geq \frac{\kappa_h}{1 - \kappa_v} \quad (3.13)$$

<sup>3</sup>In Italian code for constructions [3, sec. 7.11] the horizontal and vertical seismic coefficients are taken respectively:

$$\kappa_h = \beta_s \frac{a_{\max}}{g} \quad \kappa_v = \pm 0.5 \kappa_h \quad (3.6)$$

Where the parameter  $\beta_s$  depends on the soil category and the value of maximum acceleration  $a_{\max}$ .

arising from the fact that one must have  $\phi' \geq \theta$ . Otherwise, the radicand is negative and we obtain values with an imaginary component. This implies that there is a limiting value of the horizontal seismic coefficient  $\kappa_{h,lim} = (1 - \kappa_v) \tan(\phi')$  beyond which the equilibrium of the wall-soil system is impossible. For null values of the vertical seismic coefficient  $\kappa_v$  the limiting value becomes  $\kappa_{h,lim} = \tan(\phi')$ . In the case where the value of the seismic coefficient exceeds the limiting value, the Lancellotta theory is used [76]:

$$\theta_P = \arcsin\left(\frac{\sin \delta}{\sin \phi'}\right) + \delta \quad (3.14)$$

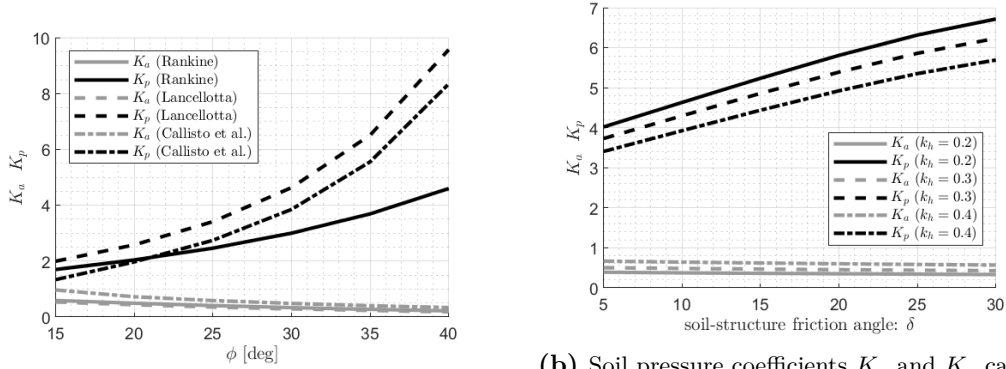
$$\theta_A = \arcsin\left(\frac{\sin \delta}{\sin \phi'}\right) - \delta \quad (3.15)$$

$$K_p = \left(\frac{\cos \delta}{1 - \sin \phi'}\right) \left(\cos \delta + \sqrt{\sin^2 \phi' - \sin^2 \delta}\right) e^{\theta_P \tan \phi'}; \quad (3.16)$$

$$K_a = \left(\frac{\cos \delta}{1 + \sin \phi'}\right) \left(\cos \delta - \sqrt{\sin^2 \phi' - \sin^2 \delta}\right) e^{-\theta_A \tan \phi'}; \quad (3.17)$$

$$(3.18)$$

Where the symbols used are consistent with those in the previous formulas. Figures 3.11a and 3.11b shows the trend of the seismic coefficients as the angle  $\phi'$  and the seismic coefficient change



(a) Soil-foundation friction angle is equal to  $\delta = 2/3 \phi'$ . Seismic coefficients are  $k_h = 0.25g$  and  $k_v = 0$

(b) Soil pressure coefficients  $K_a$  and  $K_p$  calculated with the theory proposed by Callisto et al. [96] for different friction angle  $\delta$  and different seismic coefficient  $k_h$ . Other parameters used are  $k_v = 0$  and  $\phi' = 36^\circ$ .

**Figure 3.11.** Different theories for the soil pressure coefficients.

As it can be seen from figure 3.11a, the theory proposed by Callisto et al. [96] starts from Lancellotta's theory extending it to the seismic case. So the approximation of using Lancellotta's theory, in case one does not have the seismic coefficient available, is quite satisfactory.

The stress coefficient at rest is always equal to:

$$K_0 = 1 - \sin(\phi') \quad (3.19)$$

There are alternative formulations for this coefficient in the literature that also

take into account, for example, the degree of soil overconsolidation via the Over-Consolidation Ratio ( $OCR$ ):

$$K_{0(OC)} = (1 - \sin(\phi'))\sqrt{OCR} \quad \text{Meyerhof 1976} \quad (3.20)$$

$$K_{0(OC)} = (1 - \sin(\phi'))OCR^{\sin(\phi')} \quad \text{Mayne \& Kulhawy 1982} \quad (3.21)$$

Figure 3.12 shows the response in terms of bending moment time series (for left deck-abutment joint and left piles head) as a function of different definition of active and passive pressure coefficients.

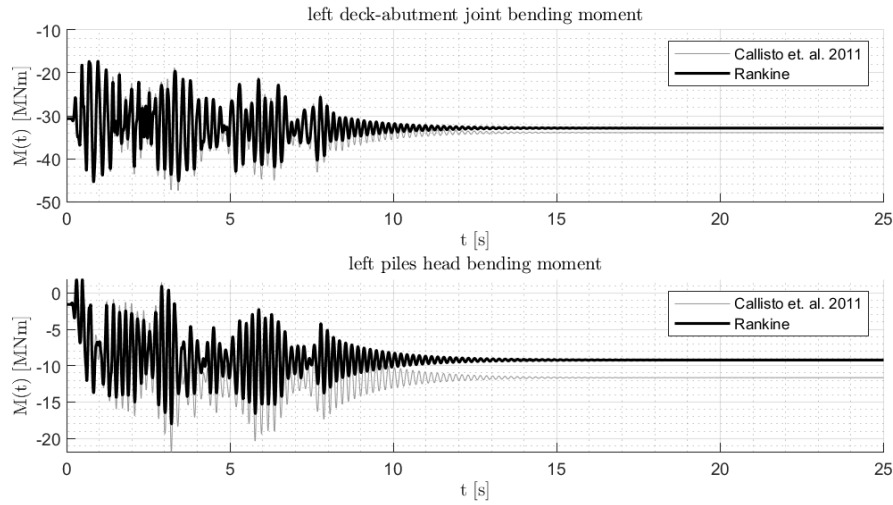


**Figure 3.12.** Model response varying the interface elements definition (Callisto et. al. 2011 [96] vs. Rankine [97] for the definition of the active/passive limits).

Table 3.3 shows the averages over 10 seismic ground motions (relative to the sixth strip of L'Aquila site, as described in section 6.2.2) of the maximum of the absolute value of the bending moment for the most stressed cross sections.

**Table 3.3.** Global scalar response parameters as function of interface elements definition.

theory	$\text{mean}\left(\max_t  M_{left\ joint}  \right)$ [MNm]	$\text{mean}\left(\max_t  M_{left\ piles}  \right)$ [MNm]
Callisto et. al. 2011	59.54	21.31
Rankine	59.44	20.52

As it can be seen, even from the numerical results over 10 ground motions, the difference introduced with the more refined theory of Callisto et al. [96] is moderate (compared to the Rankine theory used in the original model).

### 3.2.3 Vertical (shear) degree of freedom

So far we have analyzed the springs for the so-called  $p$ - $y$  behavior, i.e., the horizontal degree of freedom of the pile in the surrounding soil. In the description of the *vertical*

behavior of the interface we refer to the shear stress along the lateral surface of the pile ( $f$ - $z$  springs) and the normal stresses at the piles head ( $q$ - $z$  spring).

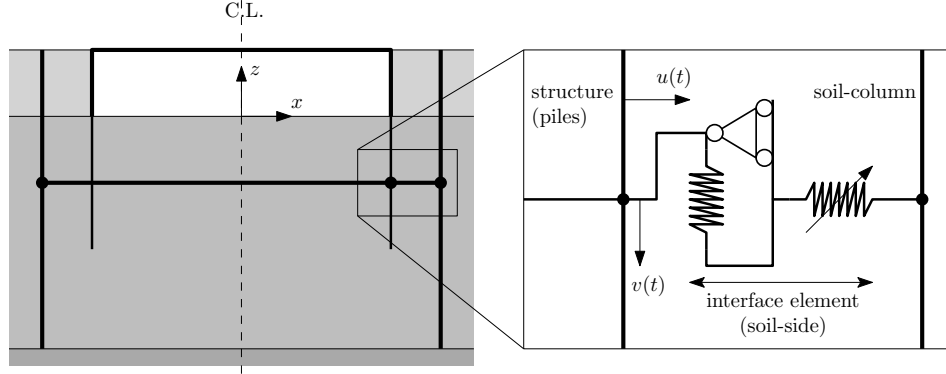


**Figure 3.13.** Vertical interface elements

The justification for considering the vertical behavior (of the friction between the soil and the side surface of the pile and the soil compressed by the pile tip) decoupled from the horizontal behavior lies in which soil volume is activated. In fact, the vertical behavior  $f$ - $z$  is based on the friction and elastic modulus of the soil, which increases as depth  $z$  increases (see also equation (3.23)). The vertical behavior  $q$ - $z$  depends only on the soil volume under the piles tip and thus with the greatest depth. While the lateral behavior of the pile depends on its deformation in the soil. As can be seen from figure 3.14, the deformation is concentrated on the part of the soil at the surface, at least for long piles<sup>4</sup>.

<sup>4</sup>Gazetas, in its work on static impedances [51], proposes for piles an active length equal to (for a non-linear soil stiffness profile shown in figure 5.3c):

$$l_c \approx 2d(E_p/\tilde{E}_s)^{0.22} \quad (3.22)$$

So a "long" piles will have, at least, a length greater than the active one ( $L_p > l_c$ ).

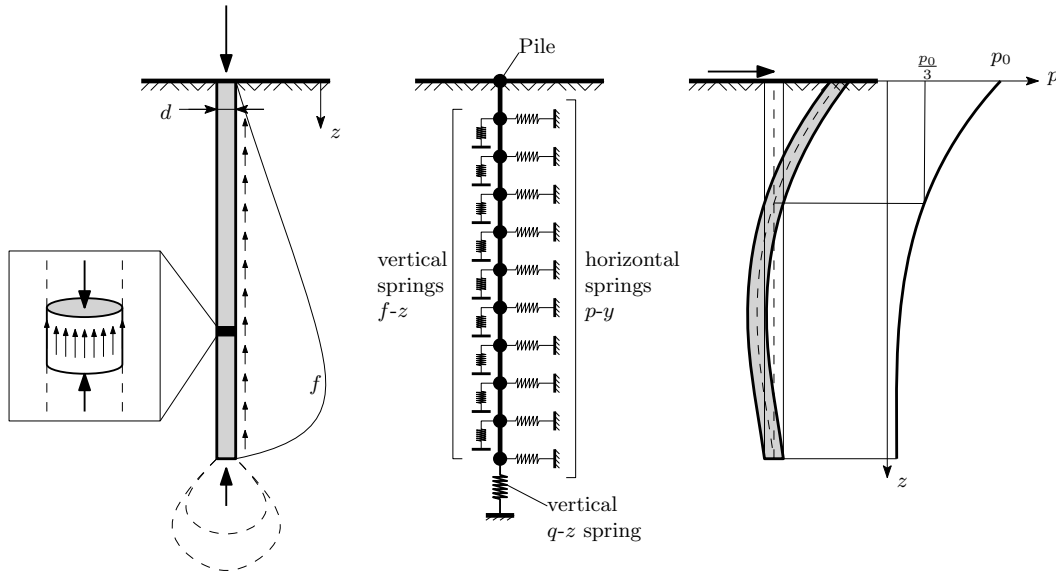


**Figure 3.14.** Soil pressures on pile due to vertical and horizontal pile behavior.

Thus the horizontal behavior is mainly influenced by the soil volume near the surface and the vertical behavior by the volume of soil near the pile head and therefore can be considered decoupled. This consideration is only valid for long piles.

Thus, it is more plausible that there is a coupling between  $f-z$  and  $q-z$  springs, since they depend substantially on adjacent soil volumes.

Specific issues regarding the implementation into structural analysis software are described in section 3.5.2.

### $f-z$ elements

The springs for the vertical behavior, given by soil friction on the lateral surface and along the entire pile length ( $f-z$  springs), can be described, as a very first approximation, by linear elastic springs with stiffness equal to:

$$k_Z(z) = 0.6 E(z) [1 + 0.5\sqrt{a_0}] \quad (3.23)$$

where  $a_0 = \omega d/V_s$  is the frequency normalized with respect to the shear wave velocity (this theory is based on dynamic considerations, this is why is function of the normalized frequency  $a_0$ ),  $E(z) = 2(1 + \nu)G_0(z)$  is the elastic modulus of the soil, and  $d$  is the pile diameter. The frequency dependence of the stiffness is mild over the frequency range of interest and so we use a constant value for the purpose of time domain analysis, placing  $\omega = 2\pi/T_1$ , where  $T_1$  is the fundamental period of the deposit. The theory describes the vertical behavior of the individual pile. In the case there are more the one pile initially the stiffness can be set equal to

$$k_{Z,piles} = n_p k_Z \quad (3.24)$$

where  $n_p$  is the number of piles. In reality the portion of the soil between two pile lateral surfaces sufficiently close will tend to exhibit a shear action on the piles that is proportional to the relative displacement between the two surfaces and not to

the absolute displacement. This fact makes the behavior of the set of piles different from the sum of the behavior of the individual piles.

### 3.2.4 Bilateral interfaces

In evaluating the behavior of the soil interacting with the piles (interface elements for  $z < 0$ ), two elements were considered for each node: one uphill and one downhill (see figure 3.1). This distinction implies a conceptual simplification between elements that are affected by the weight of the embankment (uphill elements) and elements that are not affected by the embankment (downhill elements). This is also inherited from the original model [48] that was developed initially for diaphragm retaining walls. This distinction, however, results in a larger number of elements in the analysis model, and this results also in a greater computational effort (the nonlinear solution algorithm must calculate equilibrium for a larger number of elements). Also in the extrapolation of the actions imposed by the soil to the structure, having to consider two elements instead of just one, this can lead to additional difficulties and errors.

Single interface element, that approximates both the behavior of uphill and downhill soil, is considered. In this case both elements (uphill and downhill) act in parallel on the same node of the structure.

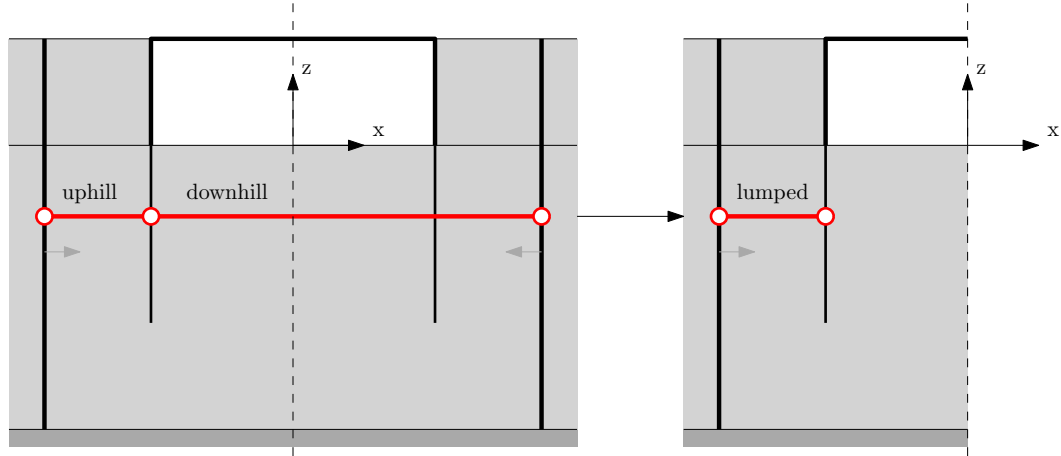


**Figure 3.15.** Lumped interface elements (for  $z < 0$ ).

The uphill and downhill elements are considered in parallel because, even if they start from nodes afferent to different soil-columns, the two columns both have a constraint of equal displacements for each pair of nodes at the same depth  $z$  (Therefore the displacements of the two soil-columns are equal). Since the two elements are in parallel, the resulting constitutive law of the lumped element is the difference of the two original ones.

As can be seen from the figure 3.16, the passive limit ( $F_p = \min(F(u)) \forall u \in \mathbb{R}$ ) becomes:

$$F_p = F_p^{(uphill)} - F_a^{(downhill)} \quad (3.25)$$

where  $F_p^{(uphill)}$  is the passive side force of the uphill spring, and by  $F_a^{(downhill)}$  the active side force of the downhill spring. While the active limit ( $F_a = \max(F(u)) \forall u \in \mathbb{R}$ )

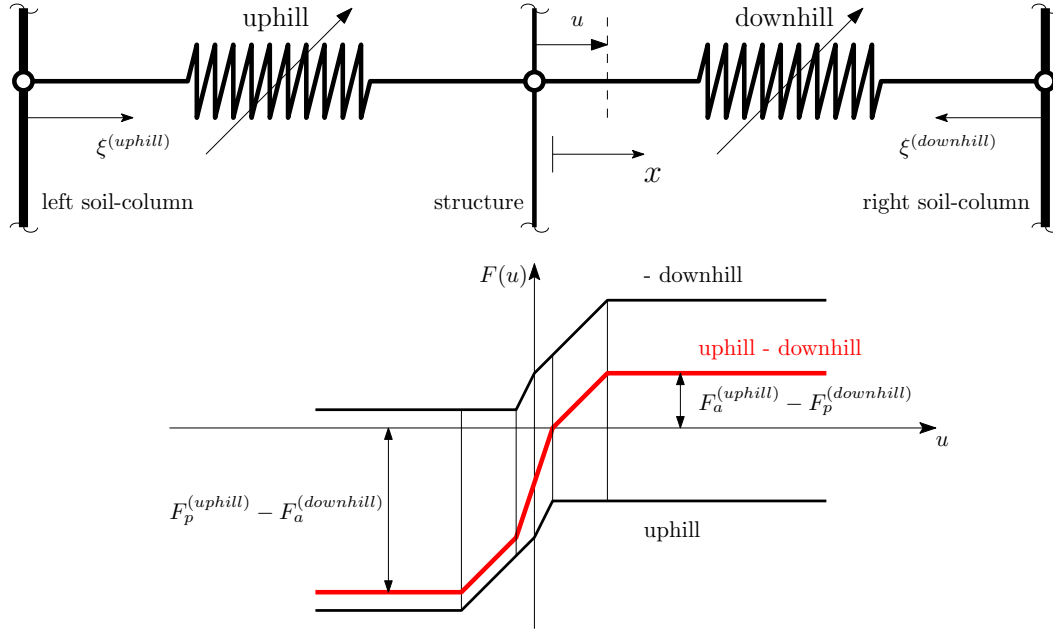


**Figure 3.16.** Constitutive law for lumped elements.

$\mathbb{R}$ ) is equal to:

$$F_a = F_a^{(uphill)} - F_p^{(downhill)} \quad (3.26)$$

The point at which the deformation  $u$  is zero results in:

$$F_0 = F_0^{(uphill)} - F_0^{(downhill)} \quad (3.27)$$

In general, the strain values  $u_{y,a}$  and  $u_{y,p}$  corresponding, respectively, to the onset of active and passive stresses are not the same for uphill and downhill elements since the stresses in the soil are different. This is because the strain values at the end of the linear elastic sections depend on the stiffnesses  $k_a$  and  $k_p$ , which both depend on the soil elastic modulus  $E(z)$  and the characteristic lengths  $l_a$  and  $l_p$ . The characteristic lengths are constant parameters of the model and take the same value for all interface elements. However, the elastic modulus of the soil  $E(z) = 2(1 + \nu)G_0(z)$  in general is different between the uphill and downhill sides, as the stress in the soil changes due to the weight of the embankments backfill. However, as a first approximation, one can consider the two values coincident for the uphill and downhill elements; therefore, the same values  $u_{y,a}$  and  $u_{y,p}$  apply to the condensed element. This approximation is more legitimate if we take a stratified soil where the shear modulus  $G_{0,i}$  is constant on the  $i$ -th layer and does not vary due to the construction of the embankment.

In an analogous way, one could think of condensing the elements of the two soil columns into a single column. In fact every pair of nodes of the two columns, at a given depth  $z$ , have an equal displacement constraint. So the two soil columns have equal displacements along the entire height. However, keeping the two soil columns separate ensures that the masses are considered correctly in case the system studied has embankments with different geometric characteristics (and therefore different masses and ratios  $r$ ).

### 3.2.5 Damping

The model used for the interface elements presents several problems in describing some of the behaviors of the soil interacting with the displacements of the structure<sup>5</sup>.

A first limitation is that hysteresis for small deformations is not described: i.e. those deformations that do not bring the element to the active or passive limit.

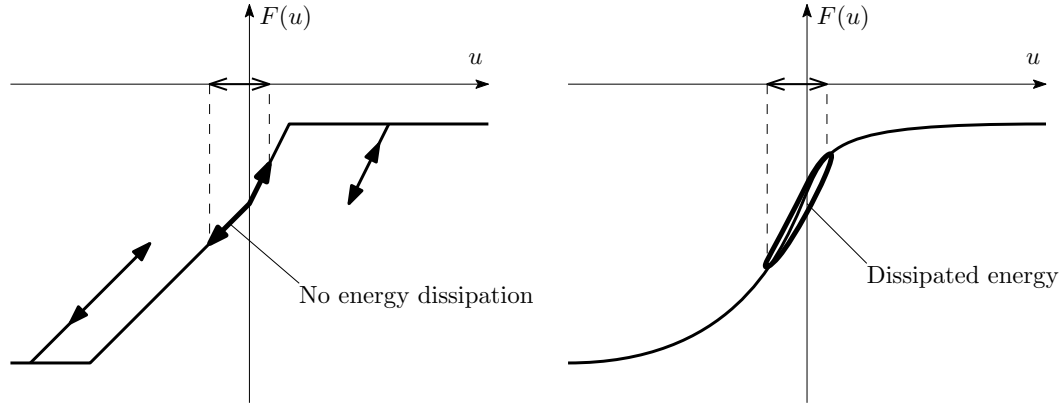


**Figure 3.17.** Small deformation hysteresis over the interface elements.

This behavior could be described by asymmetric Bouc-Wen constitutive law [102] (asymmetric to account for the different thresholds between active and passive limits).

Another problem with these elements is that they do not consider the additional damping given by *radiation damping*. This contribution can be taken into account through the inclusion of additional dampers in the interface elements.

The limitations just described can lead to an under-damped global system response. To overcome this drawback a Rayleigh damping equal to a critical damping ratio of 3% between the periods of modes that deforms the bridge more (described in section 3.6.1) has been introduced in the structural elements only (not in the soil elements). The first mode is not taken into account, since it coincides with the deposit fundamental mode. These considerations, which allow more simplified models to be established, are supported by comparison with the higher-order nonlinear three-dimensional model (see chapter 4).

### Radiation damping

In the description of the horizontal dynamic behavior of a pile *radiation damping* plays an important role. This damping depends on the waves that are laterally diffused by the oscillatory movement of the foundation embedded in the soil as it is highlighted in figure 3.18.

<sup>5</sup>Displacements of the structure with respect to the displacements of the soil deposit at, theoretically, infinite distance from the bridge. Again considering the infinitely extended deposit in the longitudinal direction  $x$



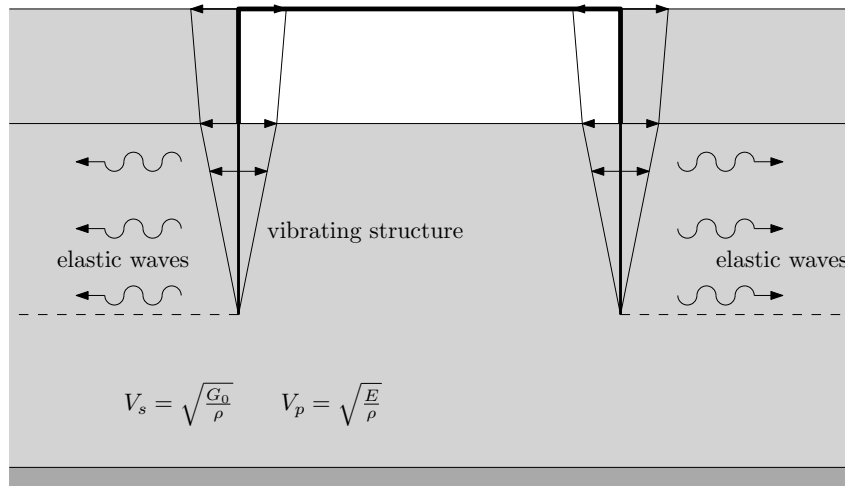


**Figure 3.18.** Radiation damping due to elastic waves irradiating towards the soil deposit.

The radiation damping towards the bedrock is already taken into account by the damper at the base of the soil column (see section 3.3).

This phenomenon (given the discrete nature of the presented model) is described by damper elements inserted within rheological models for the description of the interface elements. The soil column elements remain unchanged together, obviously, with the structural elements.

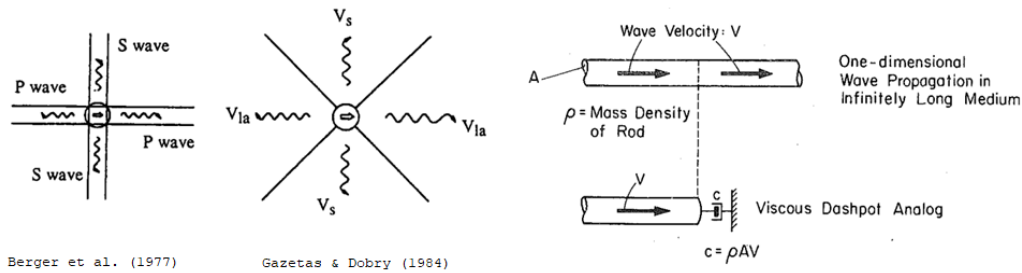


**Figure 3.19.** Radiation damping models for a single pile. (Image taken from Dobry & Gazetas [14] [52])

The simplest model to account for this behavior is to place a damper in parallel with the interface spring, as described by Anoyatis and Lemnitzer [8]. The parallel damper describes the damping according to the theory of Berger et al. [14], later modified in 1984 by Dobry and Gazetas [52]. According to this theory, the damping given by radiation also depends on the frequency of oscillation of the structure, and not only on the characteristics of the soil interacting with the foundation. This parallel damper model was also introduced by Badoni and Makris in 1996 in the study of the lateral behavior of single piles subjected to dynamic seismic actions (figure 3.20).

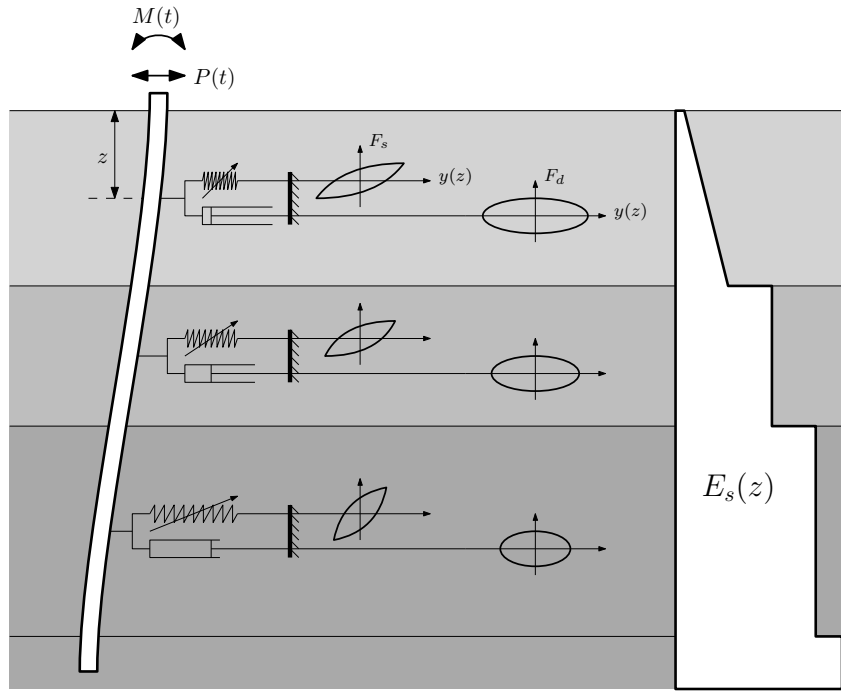


**Figure 3.20.** Badoni & Makris model [11] for lateral behavior excited by an horizontal ground motion.

The problem with this interface elements model is that the damper, being in parallel, for high velocities tends to reduce the force inside the nonlinear spring (because the constitutive law of the damper is proportional to the deformation velocity). This also results in stresses on the interface elements that are greater than the passive one (or even less than the active one), which is not possible according to the soil behavior model. For this reason, the option of inserting an asymmetric friction element in series with the nonlinear spring and damper was considered in order to correctly describe the global behavior of the interface soil.

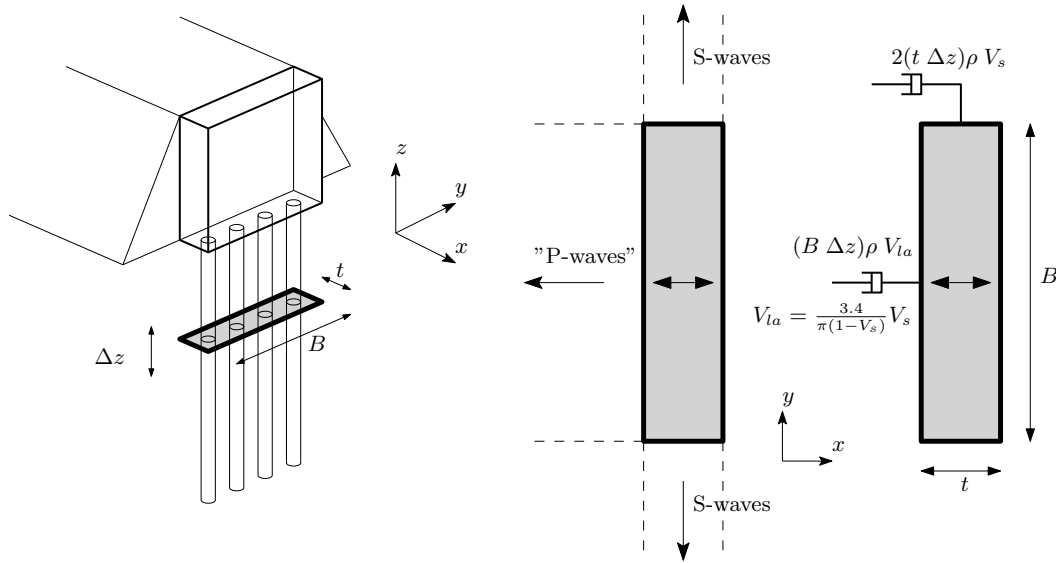


**Figure 3.21.** One-dimensional radiation damping model for a rectangular IAB foundation.

These elements are present only in the portion of soil below the embankment ( $z$  negative) because the waves propagated through the embankment represent the minor contribution, as phenomena of reflection and refraction tend, in this case, to increase the number of waves reflected towards the abutment. In addition, the radiation damping given by the embankment is lower because, even in the theoretical case of perfect and infinite-equal embankment, the surface where the substructure radiates the waves is smaller (compared to the case of piles embedded in the soil). The soil can be divided into lateral radiation surfaces that separates the foundation from the surrounding soil. By radiating surfaces it is meant the four quadrants into which the continuum is divided in the theory of Gazetas and Dobry [52] (figure 3.21). Obviously, the surfaces for driven piles are three instead of four because the waves radiated from one pile, in the direction of the other, being incident on the other pile contribute to the vibration of the system.

The elements with friction model in series present some difficulties in numerical calculation caused by the discontinuous nature of the constitutive law implemented in the friction element itself. This problem leads to calculation times of more than 13 hours<sup>6</sup>. Such numerical problems can be greatly reduced by approximating the friction element constitutive law. A first approximation used was to reduce the stiffness of the elasto-plastic model. This was done taking into account the general behavior of the interface element itself, since the overall stiffness of the element in the elastic phase at that point depend on the stiffness of two springs in series. From numerical and theoretical considerations it was seen that it was enough to consider the friction element stiffness greater than 10 times the spring stiffness in series. With such modifications the computational load is greatly reduced, decreasing the

<sup>6</sup>Time calculated on a model implemented in SAP2000 of the Gatteo benchmark case over 20 seconds of simulation, where the constitutive law implemented in the friction clamp consisted in a elastic perfectly-plastic law with high stiffness (but not too large to avoid numerical problems in inverting the stiffness matrix via pivoting).

calculation time to a few minutes<sup>7</sup>.

If there are rigid elements embedded in the soil near the bridge, they will reflect the waves diffused laterally and the contribution of radiation damping is therefore reduced. Those elements can be foundations of other buildings (in case of integral abutment bridges built in urban areas or near other infrastructures), underground tunnels or other constructions.

### 3.3 Base damper

The vertically propagating shear waves coming from the bedrock reach the surface where, due to boundary conditions (the air doesn't provide shear resistance  $\tau(z = 0, t) = 0$ ) are reflected and return to the deposit-bedrock interface. There, due to differences between specific impedances of the deposit and the bedrock, some of the waves are reflected back towards the surface, while another portion is refracted and propagates back into the bedrock. The percentage of waves reflected and absorbed by the bedrock depends on the ratio between the specific impedances  $\alpha = \frac{\rho_s V_{s,soil}}{\rho_b V_{s,bedrock}}$  of the bedrock and of the deposit in contact with it.

In the literature, dampers placed at the model boundary are commonly used to simulate the behavior of waves that are radiated through the bedrock. The first to implement such a method were Lysmer and Khulemeyer in 1969 [82]. In this case<sup>8</sup>, the seismic action is incorporated into the model by means of a force

$$f(t) = c_b \dot{u}(t, z_b) = (\rho_b V_{sb} A) \dot{u}(t, z_b) \quad (3.28)$$

where  $\rho_b$ ,  $V_{sb}$  and  $A_{s,bot}$  are, respectively, the bedrock density, the shear wave velocity in the bedrock and the area of the soil column in the element at the base. While  $\dot{u}(t, z_b)$  is the velocity of horizontal soil motion at the bedrock-deposit interface.

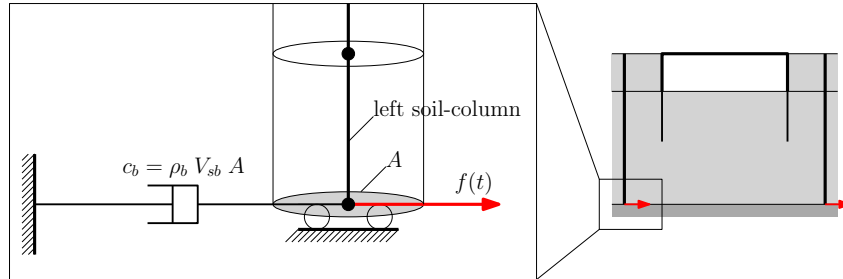


**Figure 3.22.** Base damper for compliant base.

Between the node at the base of the column (on which is also applied the seismic input through the force  $f(t)$ ) and the fixed node (which refers to an inertial reference

<sup>7</sup>Computation time of reduced-stiffness friction element model implemented in **OpenSEES**.

<sup>8</sup>when the boundary is not modeled as a rigid constraint where displacement is imposed (and then the seismic action is applied as a displacement time series  $u_g$  or, alternately, as an acceleration  $\ddot{u}_g$ ) then forces must be imposed. It can be proved that these forces must have the form (3.28) because they are the integral of  $\tau = \rho_b V_{sb} \dot{u}(t, z_b)$ .

system) is inserted the linear viscous damper of constant:

$$c_b = \rho_b V_{s,b} A \quad f_d(t) = f(t) = c_b \dot{u}(t, z_b) \quad (3.29)$$

where  $\rho_b$  is the bedrock density,  $V_{s,b}$  the bedrock shear wave velocity and  $A$  the soil-column bottom element cross-section area.

Figure 3.23 shows the response in terms of bending moment time series (for left deck-abutment joint and left piles head) as the base damper is present or not (compliant vs. non-compliant base). The analyses are carried out imposing the motion through the displacement on the base of the soil-columns.

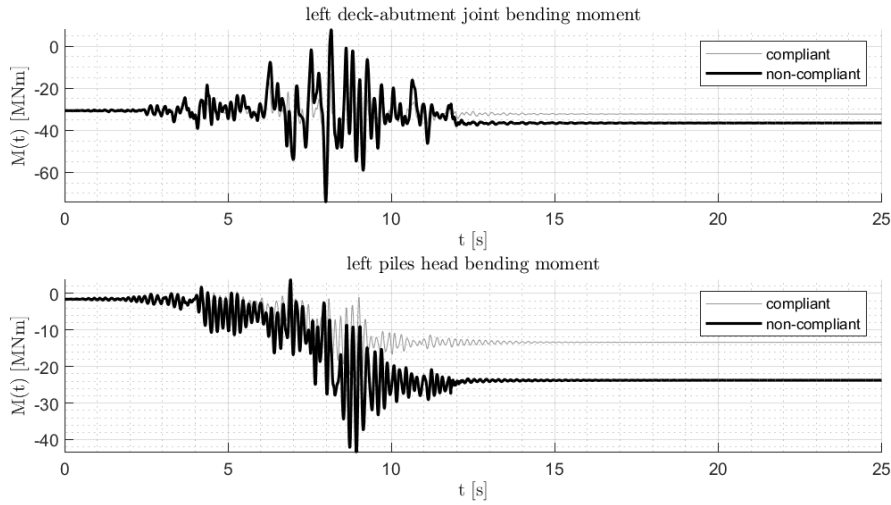


**Figure 3.23.** Model response from compliant (with base damper) and non-compliant bedrock.

Table 3.4 shows the averages over 10 seismic ground motions (relative to the sixth strip of L'Aquila site, as described in section 6.2.2) of the maximum of the absolute value of the bending moment for the most stressed cross sections.

**Table 3.4.** Global scalar response parameters as function of interface elements definition.

base	$\text{mean}\left(\max_t  M_{left,joint} \right)$ [MNm]	$\text{mean}\left(\max_t  M_{left,piles} \right)$ [MNm]
compliant	59.54	21.31
non-compliant	64.33	28.05

The results show, as expected, that the system response increases in case the motion at the base of the soil-columns is imposed as a displacement.

### 3.4 Construction stages

For the seismic response analysis of the soil-structure system, the determination of the initial state (initial instant  $t_0$  for the dynamic analysis, final time of the

construction sequence) is important. In the evaluation of the construction stages, the internal stresses given by temperature and rheological phenomena, needs to be included in the analysis.

The following stages were considered to describe the bridge construction process:

1. Construction of the approach embankments
2. Construction of the foundation piles
3. Construction of the abutments and steel deck
4. Integral connection between the deck and the abutments
5. Construction of the soil backfills
6. Introduction of the deck slab and the non-structural loads (such as pavement and barriers)

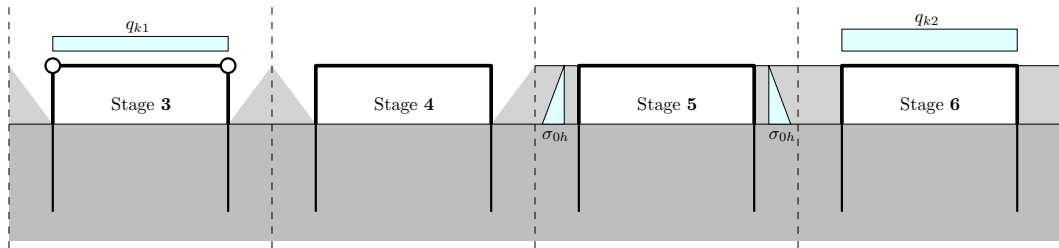


**Figure 3.24.** Bridge structure construction stages.

The stages that, from a structural and model definition point of view, are most relevant are phases 3, 4, 5 and 6 (phases 3, 5 and 6 introduce new loads, while phase 4 modifies the structural scheme). Other stages don't introduce differences in the model definition, at least for this simplified model. In terms of implementation, the main problems associated with these stages are:

- Stage 3: the first where an actual load, that cause bending moment on the structure elements, (the deck main steel girders self weight) is applied to the model.
- Stage 4: the structural scheme is modified and the internal hinges between deck and abutments are fixed, preserving the rotations at the deck ends and the internal actions on the deck itself.
- Stage 5: the backfill soil pressure on the abutments is applied. This stage can be described by "updating"<sup>9</sup> the parameters of the soil springs upstream of the alignments<sup>10</sup>, or by applying an external stress to the alignments (having care to first reduce the contribution of the stresses in the constitutive law of the interface springs, as described in the section 2.4.2). The main difference between the Franchin and Pinto model [47] is that the piles are constructed while part of the embankment is already built, so the soil pressures  $\sigma_0h$  are applied only to the abutments, as shown in figure 3.24.

<sup>9</sup>More details on the deck-abutments joint elements "updating" are given later in section 3.5.5.

<sup>10</sup>For *alignment* it is intended the set of abutment and piles that are on the same global  $x$  coordinate.

- Stage 6: there is a change in the mechanical parameters of the deck due to the slab bond and, therefore, the element cross-section change.

Since these four stages are the only ones where there are changes in the actions or in the structural scheme, these are also the only ones that must be defined in this simplified model. In fact there is no difference between all six stages modeled or only these four, in terms of system configuration at the end of construction sequence.

This model was implemented in both **SAP2000** and **OpenSEES** [85] software. Specific issues in both the implementations are described in section 3.5.5.

## 3.5 Specific issues of platform-dependent implementations

### 3.5.1 Soil-column elements

#### **SAP2000 implementation**

In **SAP2000** the iterative algorithm used in dynamics, as opposed to **OpenSEES**, changes the timestep depending on whether or not the computation converges at each instant. In fact, in terms of computation time, while **SAP2000** takes about 20 minutes to perform a dynamic analysis, **OpenSEES** takes about 20 seconds<sup>11</sup>.

#### **OpenSEES implementation**

Bouc-Wen hysteretic model exhibit numerical problems for exponent parameter  $n < 1$ . This occurs if we apply the Newton-Raphson method for solve the model internal equation (2.2) to find the hysteretic variable  $\zeta(t)$ .

The Bouc-Wen hysteretic model is defined through the equations:

$$f(u(t)) = \alpha k_0 u(t) + (1 - \alpha) k_0 u_y \zeta(t) \quad (3.30)$$

$$\dot{\zeta} = \frac{\dot{u}}{u_y} [A + |\zeta|^n (\gamma + \beta \operatorname{sgn}(\dot{u}\zeta))] \quad (3.31)$$

The value of  $f(u)$  for every  $t > 0$  depends on the value of the internal variable  $\zeta(t)$  that is defined by the first-order differential equation (3.31). So the variable  $\zeta$  have to be determined by a numerical integration method. In this context is used the simplest implicit method that is the *backward Euler* solution scheme:

$$\dot{y} = \tilde{f}(y(t)) \quad \rightarrow \quad y_{i+1} = y_i + \Delta t \tilde{f}(y_{i+1}) \quad (3.32)$$

This is called an *implicit* solution scheme because the discretized equation depends, on both the equal sides, from  $y_{i+1}$ . Solving for  $\zeta$  with this method leads to the equations:

$$\begin{aligned} \zeta_{i+1} &= \zeta_i + \Delta t \tilde{f}(\zeta_{i+1}) = \\ &= \zeta_i + [A + |\zeta_{i+1}|^n (\gamma + \beta \operatorname{sgn}((u_{i+1} - u_i)\zeta_{i+1}))] \frac{(u_{i+1} - u_i)}{u_y} \end{aligned}$$

<sup>11</sup>The computation times are relative to a computer with an Intel® Core™ i7-8550U CPU @ 1.80 GHz, 16 GB RAM and an integrated video card.

To solve this equation and find the value for  $\zeta_{i+1}$  we need a nonlinear solution scheme. Newton-Raphson method is applied to find the solution to the equation  $f(\zeta_{i+1}) = 0$ , where  $f(\zeta_{i+1})$  is equal to:

$$\begin{aligned} f(\zeta_{i+1}) &= \zeta_{i+1} - \zeta_i - \Delta t \tilde{f}(\zeta_{i+1}) = \\ &= \zeta_{i+1} - \zeta_i - [A + |\zeta_{i+1}|^n (\gamma + \beta \operatorname{sgn}((u_{i+1} - u_i)\zeta_{i+1}))] \frac{(u_{i+1} - u_i)}{u_y} \end{aligned}$$

The Newton-Raphson solution scheme is an iterative method that iterates in the index  $k$  (different from the index  $i$  used for the iterations of the backward Euler solution scheme)

$$\zeta_{k+1} = \zeta_k - \left( \frac{\partial f(\zeta_k)}{\partial \zeta_k} \right)^{-1} f(\zeta_k) \quad (3.33)$$

So we have to find the derivative of  $f(\zeta_{i+1})$  in the variable  $\zeta_{i+1}$  that is:

$$\frac{\partial f(\zeta_{i+1})}{\partial \zeta_{i+1}} = 1 + n|\zeta_{i+1}|^{n-1} \operatorname{sgn}(\zeta_{i+1}) (\gamma + \beta \operatorname{sgn}((u_{i+1} - u_i)\zeta_{i+1})) \frac{(u_{i+1} - u_i)}{u_y} \quad (3.34)$$

that is valid  $\forall (u_{i+1} - u_i)\zeta_{i+1} \neq 0$ . This derivative depends on the term  $|\zeta_{i+1}|^{n-1}$  and so has an asymptote when  $n < 1$  and  $\zeta_{i+1} = 0$ . This discontinuity on the derivative leads to numerical instability of the Newton-Raphson method. For this reason another methods is implemented into **OpenSEES** to solve the equation  $f(\zeta_{i+1}) = 0$  when the Newton-Raphson solution scheme fails.

In particular, when the Newton method doesn't converge after few steps, a combination of *bisection* and *false position* methods are applied for narrowing the search interval and, eventually, find the proper solution.

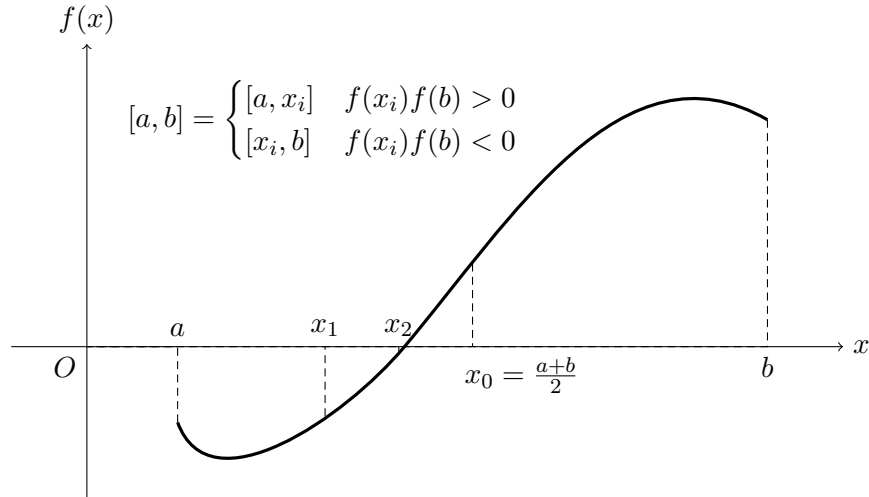


**Figure 3.25.** Bisection method for solving non-linear function root finding ( $x$  such that  $f(x) = 0$ ).

The range of values that the variable  $\zeta$  can take is limited by the value of [21]:

$$\zeta_{max} = \left( \frac{A}{\gamma + \beta} \right)^{\frac{1}{n}} \quad (3.35)$$



so we always have  $-\zeta_{max} \geq \zeta(t) \geq \zeta_{max}$ . Having set<sup>12</sup>  $\gamma + \beta = A$  and  $A = 1$  for the constitutive law used in the soil-columns elements, then we always have

$$\zeta(t) \in [-1, 1] \quad (3.37)$$

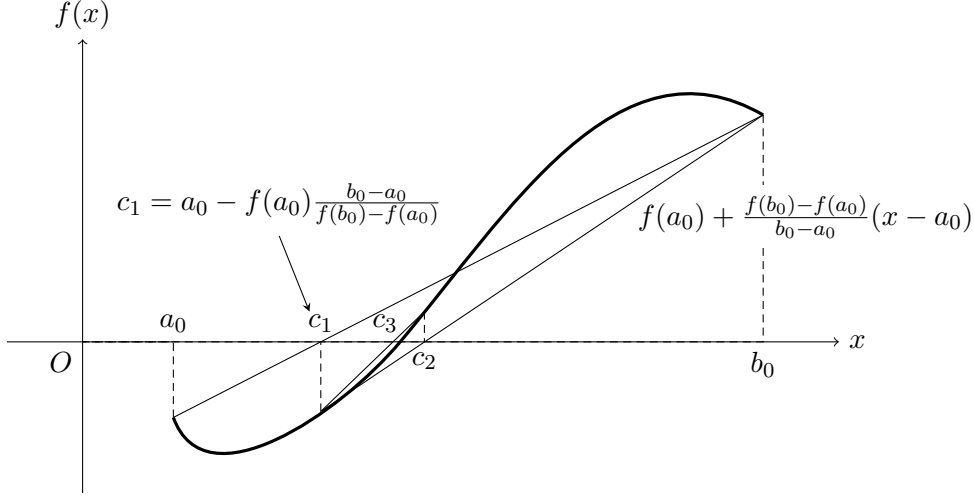


**Figure 3.26.** False position method for solving non-linear function root finding ( $x$  such that  $f(x) = 0$ ).

*False position* method is a modified version of the bisection method: given an interval (that contains only one solution) the procedure narrows this interval towards the solution. the convergence speed is greater than the bisection method. This method is based on the idea of function approximation using the linear interpolation of the function between the interval end points for narrowing the interval itself. Given the interval  $[a_i, b_i]$ , instead of the interval midpoint (like the bisection method) the control point  $c_{i+1}$  is where the interpolation function intersect with the  $x$  axis

$$c_{i+1} = a_i - f(a_i) \frac{b_i - a_i}{f(b_i) - f(a_i)} \quad (3.38)$$

where  $f(x)$  is the nonlinear function of which we want to know the solution. The new interval, used for the new step, is equal to

$$[a_{i+1}, b_{i+1}] = \begin{cases} a_{i+1} = a_i, & b_{i+1} = c_{i+1} & f(a_i)f(c_{i+1}) < 0 \\ a_{i+1} = c_{i+1}, & b_{i+1} = b_i & f(a_i)f(c_{i+1}) > 0 \end{cases} \quad (3.39)$$

<sup>12</sup>Early studies by Constantinou and Adnane [24] suggested imposing the constraint

$$\frac{A}{(\beta + \gamma)} = 1 \quad (3.36)$$

to reduce the model to a strain-softening formulation with well-defined properties.

The convergence on the value of the internal parameter  $\zeta(t)$  is achieved when the absolute error is less than a specified tolerance

$$|\zeta_i - \zeta_{i+1}| < \text{tolerance} \quad \zeta(t) = \zeta_{i+1} \quad (3.40)$$

This tolerance, in the analysis made in this thesis, is always less than  $10^{-8}$ .

The algorithm implemented initially try to find the solution with the Newton-Raphson method. If the convergence test is not passed after 50 steps, it narrows the search interval using the bisection method and then try again with Newton method. If it fails again after 50 steps it finds the solution with the false position method. To summarize, the algorithm implemented to speed up the calculation of column elements consists of the following steps:

1. Make 50 steps with Newton-Raphson method
2. If the convergence test is not passed narrows the search interval with the bisection method. It stops the bisection when the interval is equal to 10 times the tolerance on the Newton-Raphson method
3. Make another 50 steps with Newton method
4. If the convergence test is not passed it finds the solution with the false position method

If the bisection, or the false position, steps are more than 100 the algorithm exit showing a fail message.

### 3.5.2 Interface elements

#### SAP2000 implementation:

SAP2000 does not allow non-centred constitutive laws (null displacement may not correspond to a non-zero force), therefore the springs needs to be pre-loaded to reproduce the earth pressure at rest, as described previously in section 2.4.2. For this reason the at-rest contact forces were applied as external forces to the abutment, while the yield forces of the springs were taken are proportional to reduced earth pressure coefficients  $\bar{K}_a = K_a - K_0$  and  $\bar{K}_p = K_p - K_0$ , where  $K_0$  is the earth pressure coefficient at rest defined in equation 3.19.

The approach is described in section 2.4.2 (see figure 2.20) and is implemented in SAP2000 through modified constitutive laws (without the preloading, i.e. the at-rest pressure) and the at-rest pressure is applied to the structure through equivalent horizontal forces to the abutment and piles nodes along  $z$ .

#### OpenSEES implementation:

Interface elements (with vertical DoF described in section 3.2.3) are implemented in OpenSEES via `twoNodeLink` elements. Interface elements present an axial constitutive law to describe the horizontal behavior of the interface soil with the structure (this is because such elements are placed horizontally). When including also the vertical behavior, by means of shear constitutive law in the element, due to the

implementation of such elements, an internal bending moment is created which also depends on the length of the element. For this reason, this behavior was assigned to independent springs applied to the same nodes as the horizontal springs and to an inertial reference system.

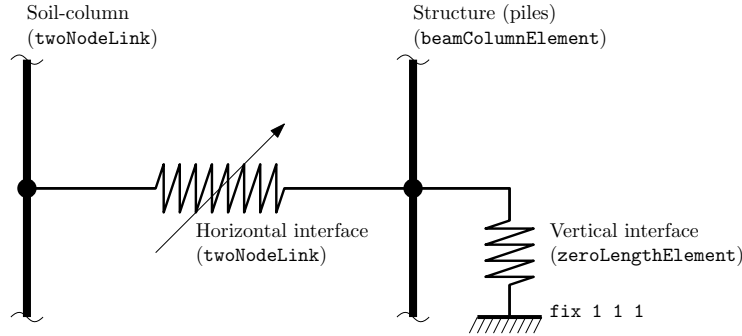


**Figure 3.27.** Vertical interface elements in the OpenSEES implementation.

### 3.5.3 Base damper

In the implementation of the damper the calculation codes used (SAP2000 and OpenSEES) present a spring in series. The stiffness of this spring, in the proposed model, is infinite. Computationally speaking this element parameter cannot be set to an infinite value, as excessively high numbers would make it impossible for the calculation code to find the solution. From various tests on the performance of this model it was found that a stiffness of 10 times the maximum stiffness of the column elements is sufficient.

$$K_{\text{damper}} = 10 \max_z(k_0) \quad (3.41)$$

### 3.5.4 Structural elements

Being a model primarily meant for design the structural elements are modeled with linear elastic elements. In fact for the design of overpasses a damage of the structural elements is not accepted, being the repair operations laborious and complicated. However, structural elements can also be defined by elements that describe their nonlinear behavior, such as fiber elements. When using elements with fiber sections, a strong coupled behavior between bending moment and normal stress was shown in the abutments and piles elements, especially using a mass matrix that automatically assigns translational and rotational masses to the elements. Therefore, in order to avoid the presence of these spurious inertia actions, it is possible to proceed either by manually assigning masses to the nodes (translational only, setting rotational inertias equal to zero), or by explicitly describing the elements sectional constitutive law. This second approach has been used in the context of this thesis for the calculation of seismic risk, because it offers greater computational performance.

### 3.5.5 Stages

#### SAP2000 implementation

In SAP2000 the stages were modeled via a "*Nonlinear Staged Construction*" loading scheme, in which all load cases and modifiers were included, summarized in figure 3.28.

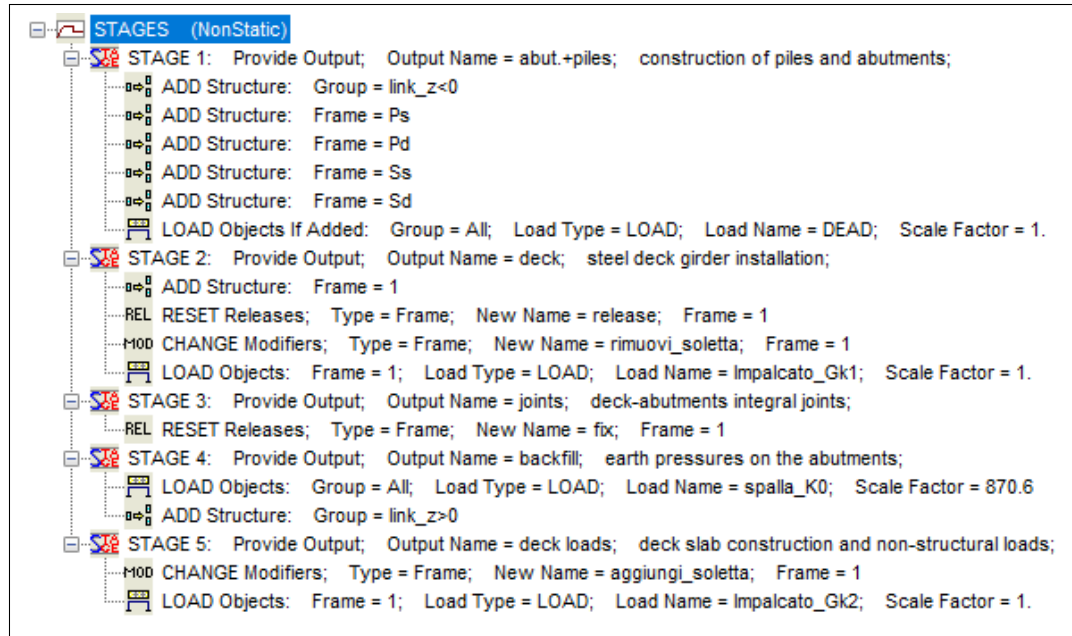


**Figure 3.28.** Construction stages implemented in SAP2000 via *Nonlinear Staged Construction* load case (link\_z<0 is the group of `LLink` describing interface elements for  $z < 0$ ; `Ps` the group describing the left piles and `Pd` the right piles; `Ss` the group describing the left abutment and `Sd` the right abutment). Note that the stage numbering is off-by-one with respect of the actual stage numbering described in section 3.4.

In `OpenSEES` instead, since there is no specific tool to perform analysis of nonlinear construction stages, some tricks and techniques have been used to describe them correctly.

#### OpenSEES implementation

The computational code `OpenSEES` version 3.2.0 was used for the analyses. Due to some peculiarities of the software, modeling strategies were implemented for the construction phases which are exposed herein.

The most critical stages, from the implementation point of view, are stage 3 (where the deck-abutments joint is fixed) and stage 5 (where the embankment is completed with the backfill and loads the abutments, modifying also the stress state of the underlying soil).

For stage 3, since when `OpenSEES` adds an element, its geometry is determined by the end nodes displacements at the time of insertion resulting in a deformed element configuration and associated internal forces<sup>13</sup>, a small artifice is required:

<sup>13</sup>This means that, in this case, the deck result always fixed with the abutments, increasing the

the use of fixing elements that have only the rotational degree of freedom defined. The constitutive law used is a elastic perfectly plastic one that, initially, has a very small yielding moment and rotation (with a high stiffness to avoid force pulses during the calculation phase). Later, when flexural continuity between the deck and abutments has to be introduced, an update is made on this law by including a high stiffness and yielding moment (not excessively high to avoid numerical problems, a value of  $10^{14}$  for both is sufficient).

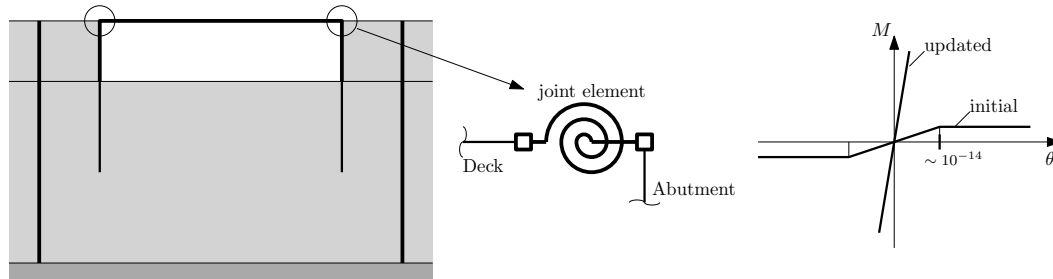


**Figure 3.29.** Joint elements to model the deck-abutment connections inside the staged construction.

Two techniques have been implemented to describe stage 5, both of which lead to similar results. The first method is to modify the interface elements constitutive law by passing it through the  $(0,0)$  point and adding corresponding horizontal forces  $\sigma_{0h}$  to the respective nodes on the structure. This technique is analogous to what was presented in the original Franchin-Pinto model and implemented in SAP2000 (since the program does not allow to define a constitutive law that not passes the point  $(0,0)$ ). The alternative method (and also the more rational in terms of interface element outputs) is to introduce the actual spring constitutive law for the elements, without inserting horizontal forces. To do this, it is necessary to update the parameters of the backfill elements to model the change in soil characteristics caused by the backfill weight on the underlying soil.

To make parameter updates in elements constitutive laws (for either technique) the **OpenSEES** commands `parameter` and `updateParameter` are used [85].

The static phases were calculated with both a static and a dynamic analysis. This was done to verify that the result of the analysis for the construction stages is correct and does not falsify the dynamic seismic analysis. This analysis was important to make adjustments in the implementation since the code **OpenSEES** has some pitfalls in the calculation of the phases for these models<sup>14</sup>. The figure 3.30 shows the trend of the bending moment in deck-abutments joints for the three phases (up to second 1 there is the deck installation, then up to second 2 there is the interlocking of joints and backfill over the abutments and finally, from second 2 to second 3, the deck is loaded).

bending moment at the deck joints according to the girder load. This is wrong because, in the first stages, the deck is simply supported and no loads are transferred to the end nodes.

<sup>14</sup>For example if the static sages are calculated with "**Linear**" patterns instead of "**Constant**" ones, the calculation results are incorrect. This problem was in fact discovered using both dynamic and static analysis for construction stages analysis.

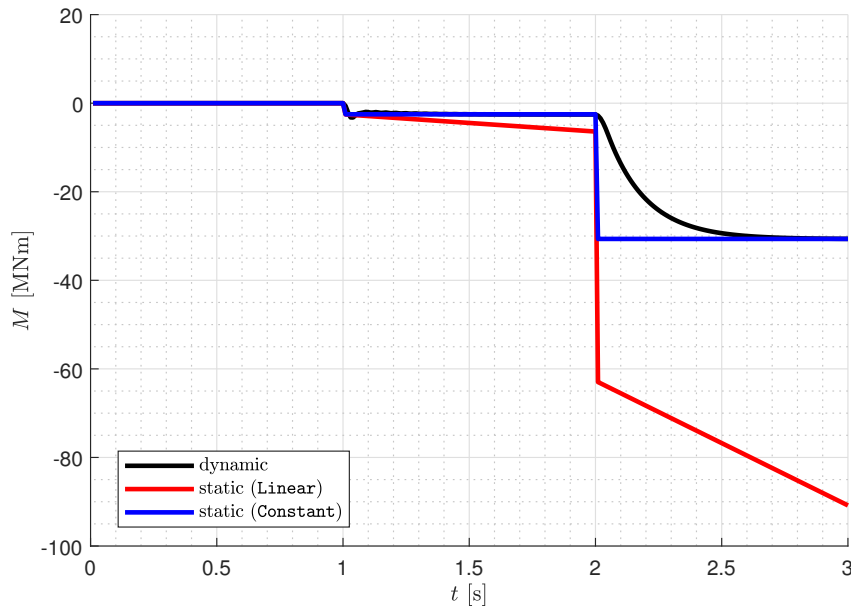


**Figure 3.30.** Bending moment of the deck-abutments joints during the construction stages (up to time  $t = 1$  s there is the deck installation, then up to  $t = 2$  s there is the joints fixing and the embankments construction and finally, from  $t = 2$  s to  $t = 3$  s, the deck is loaded).

Figure 3.30 shows the value of the bending moment at the deck-abutment joints (the quantity most sensitive to construction sequence modeling) is the same for both the dynamic calculation and the static one implemented in `OpenSEES` with load Pattern of type "Constant".

### 3.6 Sample model results

In this section, the main results of the ROM model (described previously) are reported and commented. The sample case study is the *Gatteo* overpass described in section 4.2, subjected to the ground motion of *Parkfield* (2004) described in the same section.

#### 3.6.1 Results for the construction stages and modal analysis

Figure 3.31 shows the bending moments on the bridge structure (deck and abutments) at the most relevant bridge construction stages.

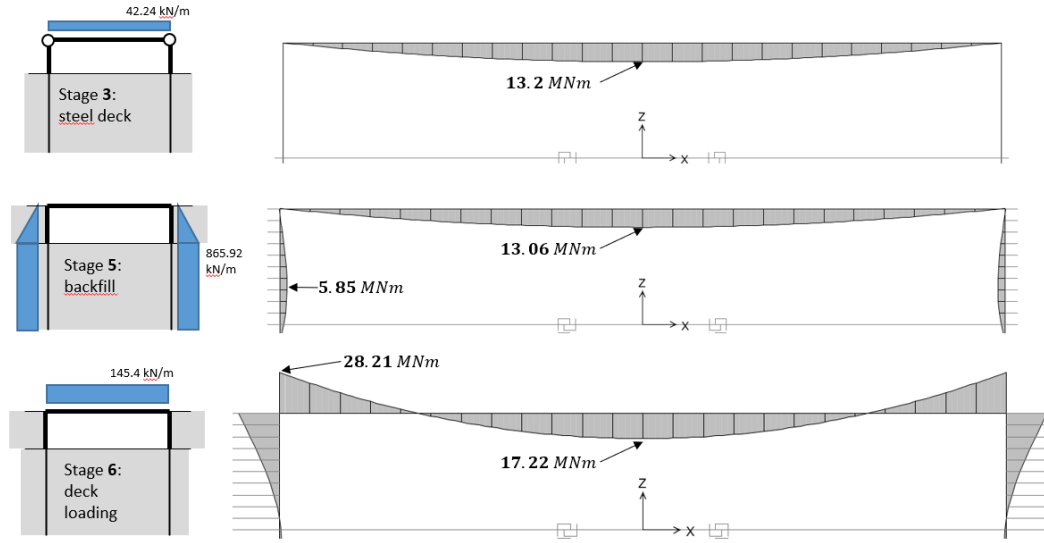


**Figure 3.31.** Construction stages bending moments on the bridge structure. Values are for the *Gatteo* flyover described in section 4.2.

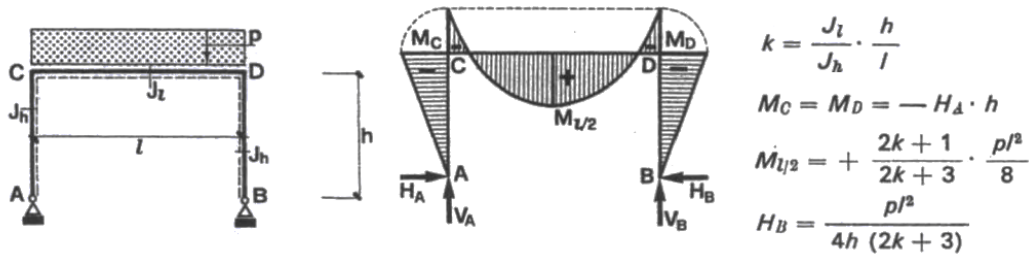
Considering the structure, in a very first approximation, as a portal structure<sup>15</sup> we have a very low stiffness ratio

$$\kappa = \frac{I_{deck}}{I_{abut.}} \frac{H}{L_b} \approx 0.009 \quad (3.42)$$

This parameter  $\kappa$  indicates how much the beam (in this case the deck) behaves as a simply supported beam (in the case of infinitely flexible abutments  $\kappa \rightarrow \infty$ ) or as a fixed end beam (in the case of infinitely stiff abutments  $\kappa \rightarrow 0$ ). For this reason, the bending moment diagram (especially after interlocking) is very similar to that of a fixed end beam.

Figure 3.32 shows the first 5 vibration modes for the *Gatteo* overpass sample case.

<sup>15</sup>The effect of the uniform gravitational load on a simple portal structure are listed in the figure below:



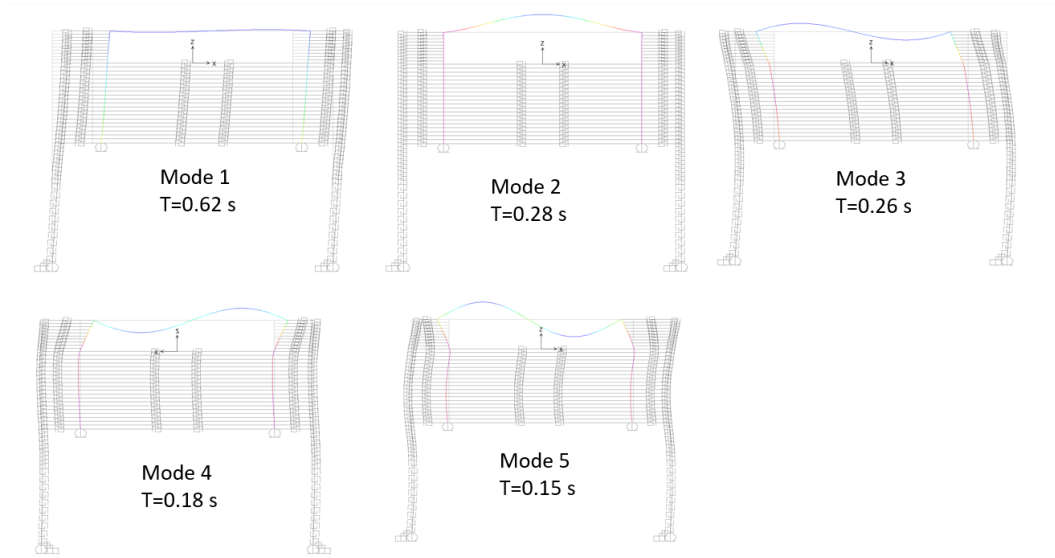


**Figure 3.32.** First 5 vibration modes of the *Gatteo* flyover described in section 4.2.

Some general characteristics of the vibration modes can be identified for this type of bridges. First of all, the first mode always coincides with the first mode of the soil-deposit (*soil-deposit mode*). This first mode is also the one that has the largest participating mass, since the mass of the soil columns is necessarily greater than the mass of the bridge. This first mode of vibration, however, does not greatly affect the bending moment response of the bridge, since, as can also be seen from the mode shape, this mode is not the one imposing the largest curvature to structural members.

A deck *vertical mode* follows in this case (the second one in the figure 3.32). The vibration period and modal shape are similar to those obtained for a fixed end beam. In fact, in terms of the first mode of vibration a fixed end beam has a period equal to

$$T_1 \approx 0.2808 \sqrt{\frac{m}{EI}} \quad (3.43)$$

which, for the data of this particular bridge, is about 0.261 s.

The higher modes (in this case from the third one onwards and in particular the first of them) can be called *structural modes* (to distinguish them from the "soil" modes of which the first one is part). These vibration modes are the ones that most affect the structural response (in terms of bending moment) of the bridge structure. Analyzing the response of the bridge to the *Parkfield* and *Yamakoshi* ground motions time series (shown in figure 4.4) one can see that the frequency content, amplified by the system, is close to the vibration period of these "structural" modes.



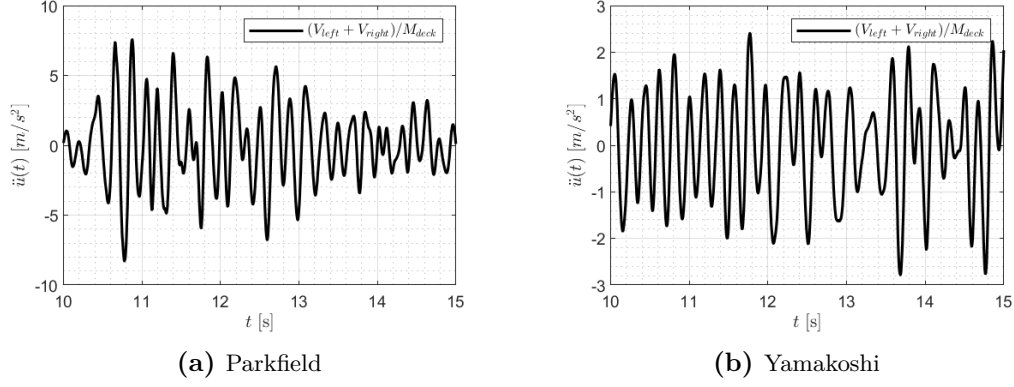


**Figure 3.33.** Deck absolute acceleration.

Figure 3.33 shows the sum of shear internal resultants on top of the abutments, divided by the deck mass.

$$\ddot{u}_{deck}(t) = \frac{V_{left} + V_{right}}{M_{deck}} \quad (3.44)$$

This is equivalent to the absolute acceleration of the deck during the earthquake. Even by simply counting the peaks of the response (29 peaks for Parkfield and 26 for Yamakoshi in 5 s), that the response (in terms of deck absolute acceleration) presents a dominant period close to that of the forth vibration mode (first "structural" mode described previously,  $T_4 = 0.18s$ ).

More details on the frequency content of the system response are discussed in section 3.6.2.

For the 3D extension of the ROM model there are additional vibration modes in  $y$  direction. This is further discussed in section 6.2.3.

### 3.6.2 Results for a sample motion

The main results of the model, in terms of global response of the structure, are mainly the bending moments in the most stressed sections of the deck (at deck-abutments joints) and of the piles (at the piles head), together with the displacements and pressures on the soil-side of the abutments.

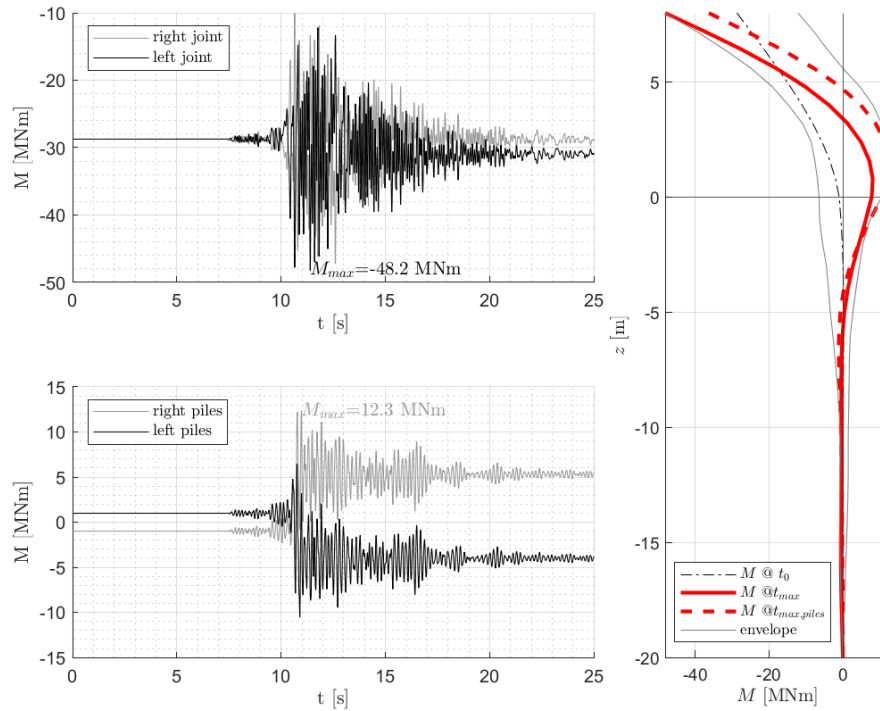


**Figure 3.34.** Benchmark bridge response to the *Parkfield* (2004) signal. The bridge response is lumped in its main internal forces, i.e. the bending moments at deck-abutment joints and at piles heads.

Figure 3.34 shows the bending moments at the left and right deck-abutment joints. As can be seen from the response, the two bending moments, obviously negative, present a difference at the end of the earthquake given by the plastic deformations accumulated during the event. The *Parkfield* ground motion<sup>16</sup> is in fact particularly demanding, in terms of intensity and frequency content, for this bridge. As far as the piles are concerned, this behavior is even more evident, since the contribution of the horizontal soil pressure of the embankments is added, which tend to impress forces directed towards the inside of the bridge. This increases the difference, in terms of bending moment at the piles head, between the left and right piles. This phenomenon can be compared to the phenomenon of *ratcheting*, usually associated with seasonal thermal deformations.

By exporting the actions within the interface elements it is possible to extrapolate the pressure of the soil on the structure. Figure 3.35 shows the pressures on the left abutment-piles alignment.

<sup>16</sup>Parkfield 2004 ground motion has a magnitude of 6.0 and this signal is recorded with a distance of 4.25 km. The Peak Ground Acceleration (*PGA*) is equal to 0.35 g and the Arias intensity is 0.787 m/s.

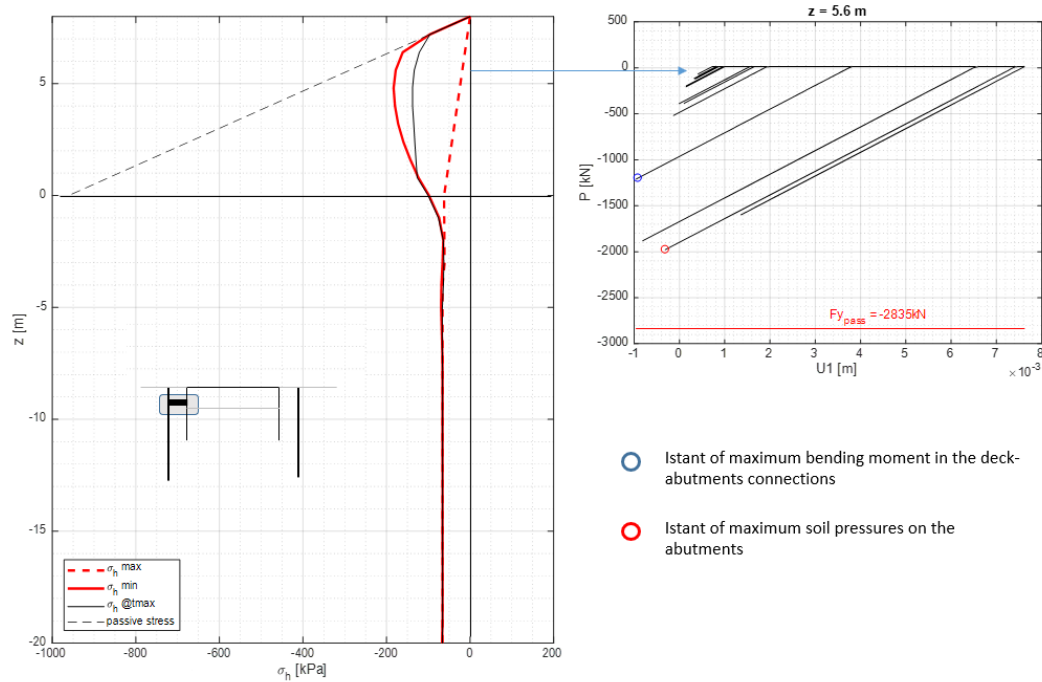


**Figure 3.35.** Soil pressure on the left alignment (left abutment and corresponding piles) on the benchmark bridge *Gatteo* for the *Parkfield* (2004) ground motion.

The instant in which there is maximum bending moment on the abutment (in the top section) does not concur with the instant in which there is maximum soil pressure on the abutment and piles. This behavior is not limited to the response of this particular benchmark bridge subject to this particular ground motion, but has also been found in other analyses with different systems and GM time series. Thus, in general, it can be said that maximum moments and maximum soil pressures are not necessarily simultaneous. This aspect complicates the treatment of simplified force-based static models, thus in particular for the linear-elastic one: in fact the linear-elastic model (LSM) is conceived with the idea that the bridge is subjected to the soil pressures that cause the maximum bending moment in the structural elements, but maximum bending moments and maximum earth pressures are not contemporary.

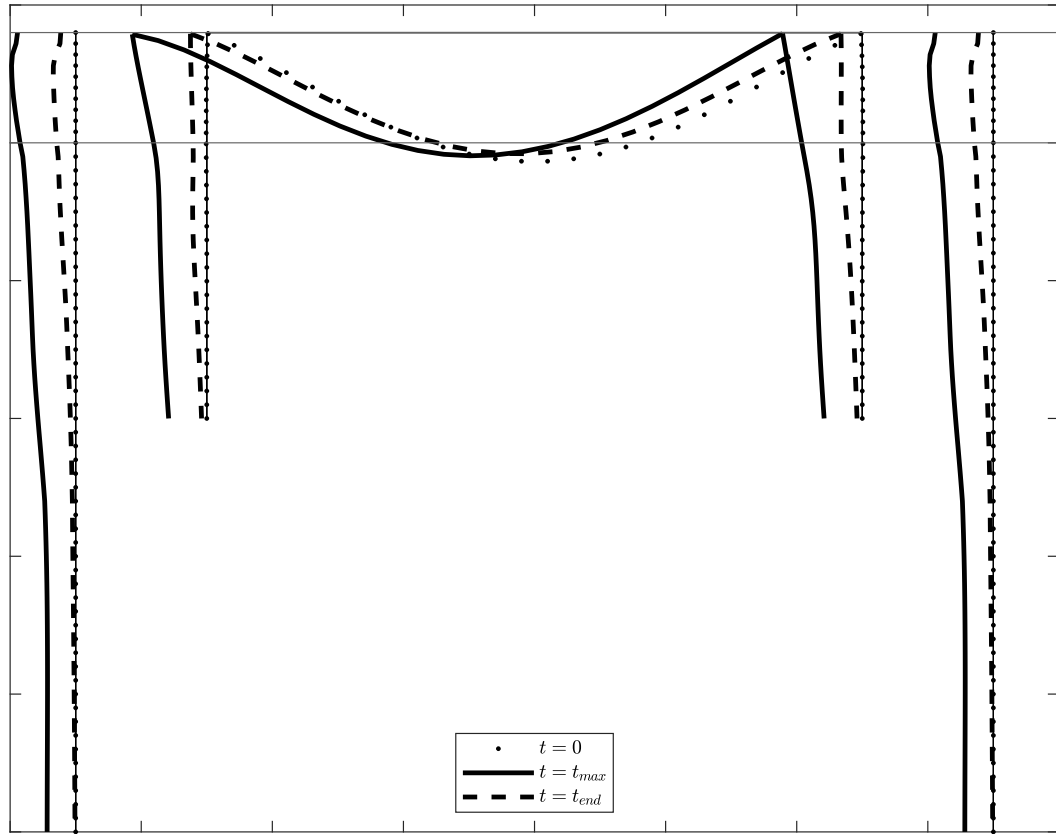
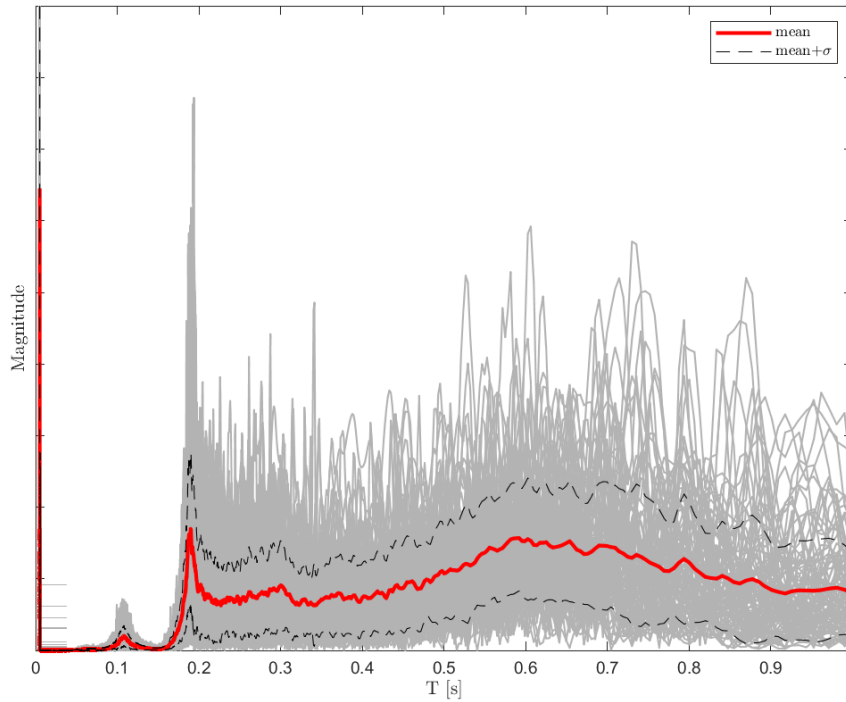


**Figure 3.36.** Bridge displacements (multiplied by 200) for the initial state  $t_0$ , the instant in which the abutments are subjected to the maximum bending moment  $t_{max}$  and the final deformation  $t_{end}$  on the benchmark bridge *Gatteo* for the *Parkfield* (2004) ground motion.

Figure 3.36 shows the displacements of the model during *Parkfield* Ground Motion. As it can be seen, the deformation at the instant of maximum moment at the joints  $t_{max}$  is qualitatively similar to the modal shape of the fourth vibration mode. It can also be seen that the system exhibits residual deformation at the end of the seismic event  $t_{end}$ . It can also be noticed that the displacement along  $z$  of the bridge midspan shifts upward at the end of the earthquake due to the deformation of the piles head toward the inside of the bridge. This behavior increase the rotation of the deck end sections and, thus, the displacement of the center point in  $z$  direction.

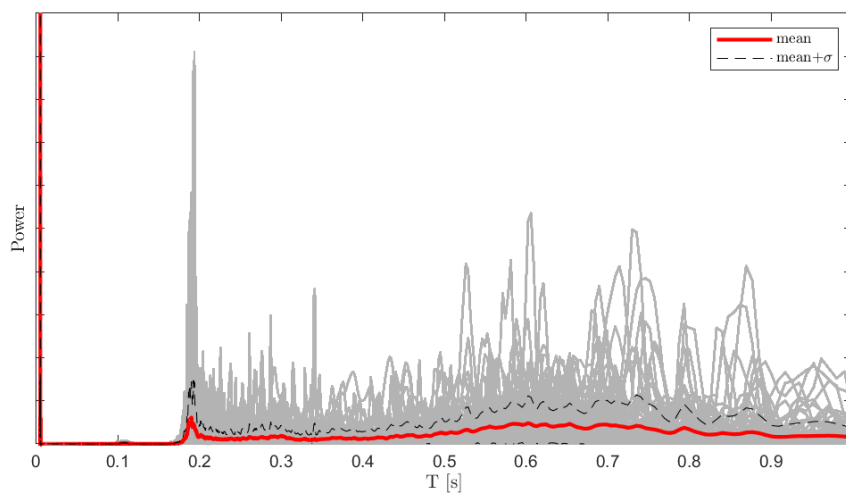
### Frequency domain

Figure 3.37 shows the frequency content of the system response in terms of bending moment at left deck-abutment joint. The input signals are the same as those used for the correlation analysis between the seismic intensity measure and the system response, described in section 3.7.



**Figure 3.37.** Fourier spectrum for the bending moment at left deck-abutment joint.

The results of the Fourier analysis show a peak at the period of the second structural mode (fourth mode described in section 3.6.1), i.e. for about 0.18 s. A second peak is also seen, at a higher structural mode (for a period of about 0.12 s). The peak in correspondence of the first structural mode is more visible considering the power spectrum, shown in figure 3.38.



**Figure 3.38.** Power spectrum for the bending moment at left deck-abutment joint.

In the power spectrum the second peak at  $T = 0.12s$  is smaller.

Considering the moment at the piles head as the system response, this behavior is even more evident, as seen in the figure 3.39.

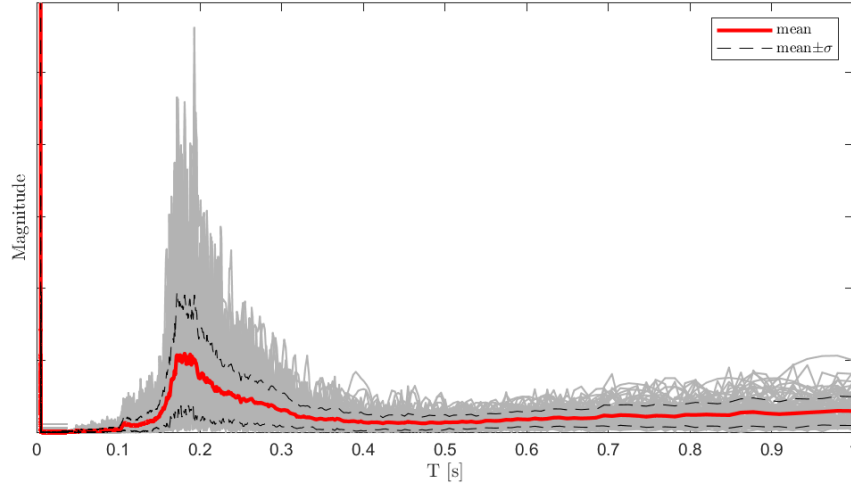


**Figure 3.39.** Fourier spectrum for the bending moment time series at left piles head.

### 3.7 Intensity measure and structural response correlation

In this section, the attention is focused on the seismic *Intensity Measure* (IM) best correlated to structural response. This study was conducted primarily to justify the use of spectral acceleration as IM in risk analysis. Given the presence of *ratcheting* in this type of bridges and given that this phenomenon appears to be duration-dependent by analyzing if these intensity measures were, in any way, correlated with the model response.

An IM was chosen as reference for all others, i.e. is used the spectral acceleration (at surface, as modified by the deposit) relative to the mode that most deforms the bridge structure (vibration period of the first structural mode, described in section 3.6.1). In order to evaluate if this local seismic intensity measure is sufficient to characterize the behavior of the system, an analysis was performed to see the correlation between this and others intensity measures and the system response.

#### 3.7.1 Ground motion selection

Initially, a selection of 100 ground motions was carried out for the L'Aquila site in central Italy. The return period  $T_r$  chosen is 1000 years and the attenuation law is that of Ambraseys 1996 [6].

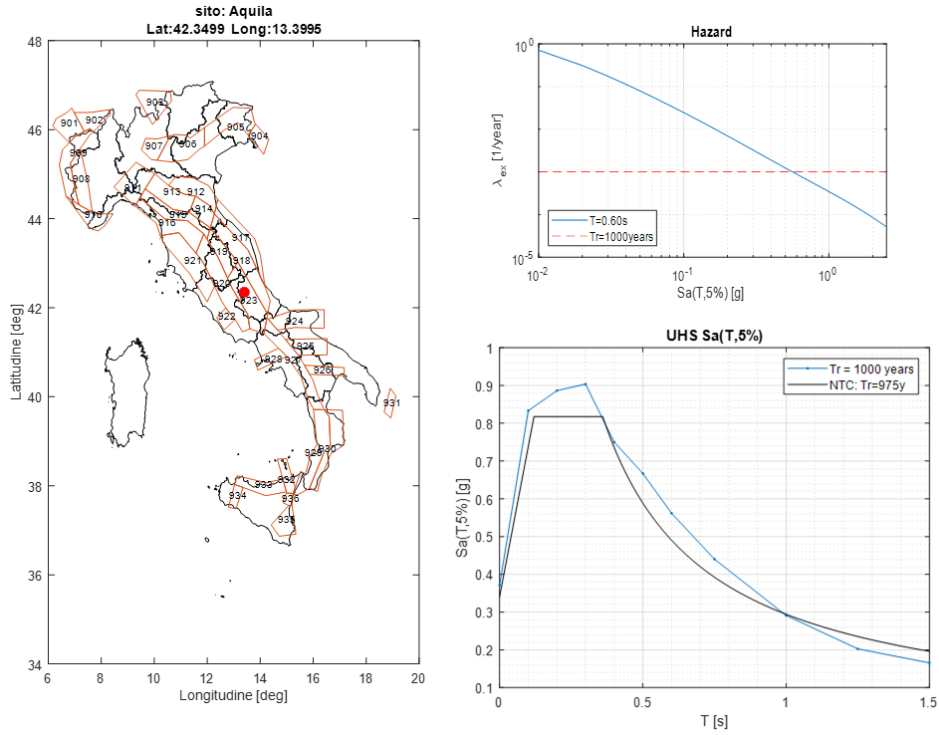


**Figure 3.40.** Hazard definition for the signals selection.

Ground motions were selected based on the Conditional Spectrum (CS) [80] [79] (with a conditioned period of 0.6 s) by sampling the CS and matching natural signals by acceleration response spectrum. The time series are taken from the ITACA [81] and NGA-West2 [7] catalogs.

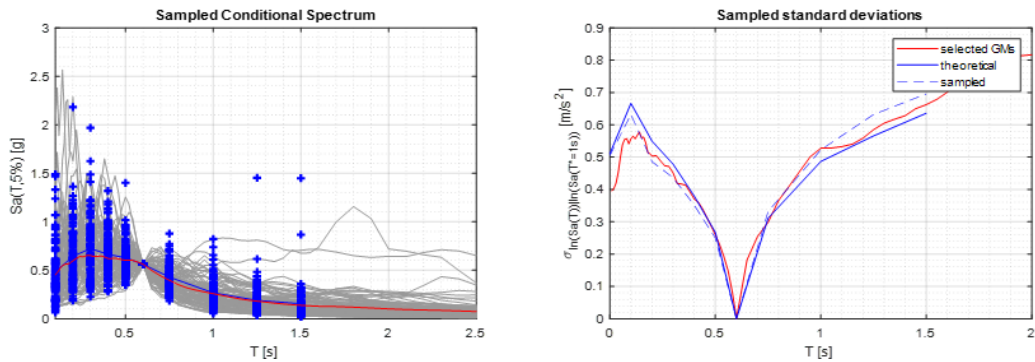


**Figure 3.41.** Conditional Spectrum and selected motions response spectra.

In the selection of natural recorded motions, scale factors not smaller than 1/6 and not larger than 6 have been applied to preserve, as much as possible, the correlation between magnitude, distance and frequency content of the original recordings. The figure 3.41 shows the spectra for the selected motions with the CS.

The global and local intensity measures (IM) considered herein are:

- Moment magnitude  $M_w$
- Epicentral distance  $R$
- 5~95% signal duration  $D_{5\sim 95}$
- Arias intensity  $I_a$
- Peak Ground Acceleration ( $PGA$ )
- Spectral acceleration at first structural mode period  $S_a(T = 0.18s, 5\%)$

### 3.7.2 Response parameters ( $EDP$ ) considered

For the system global response scalar measure (called herein *Engineering Demand Parameter* ( $EDP$ )), the following quantities are considered. The scalar parameter that describe the *maximum* bending moment reached during the earthquake is defined as:

$$EDP_m = \max \left[ \max_t |M_{left}(t)|, \max_t |M_{right}(t)| \right] \quad (3.45)$$

While the response measure to account for the *residual* actions at the end of the earthquake is equal to:

$$EDP_r = \max [|M_{left}(t=0) - M_{left}(t=\infty)|, |M_{right}(t=0) - M_{right}(t=\infty)|] \quad (3.46)$$

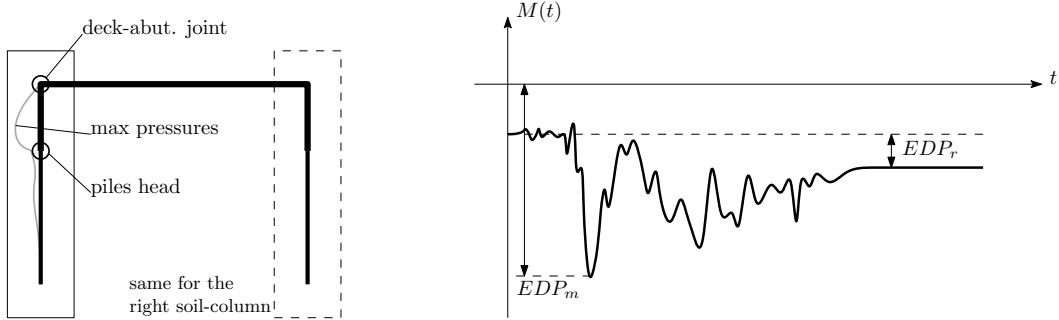


**Figure 3.42.** Global response scalar measures ( $EDP$ ) as function of system response.

These response measures were evaluated by considering the bending moment  $M(t)$  (along  $y$ ) for both the abutments top cross sections and the sections at the top of the piles (for the left and right alignment).

### 3.7.3 Results in terms of correlation

Table 3.5 presents the results in terms of correlation<sup>17</sup> between input intensity (IM) and the response measure ( $EDP$ ).

<sup>17</sup>The correlation between the two random variables  $X$  and  $Y$  is calculated in terms of *Pearson linear correlation coefficient*  $\rho_{XY}$ :

$$\rho_{XY} = \frac{COV(X, Y)}{\sigma_X \sigma_Y} \quad (3.47)$$

where  $COV(X, Y)$  is the covariance between  $X$  and  $Y$  and  $\sigma_X, \sigma_Y$  are the two standard deviations.



**Table 3.5.** Correlation coefficients between IM and  $EDP$  in term of bending moments.

IM	IM name	deck-abut. joints		piles head	
		$EDP_m$	$EDP_r$	$EDP_m$	$EDP_r$
$M_w$	Magnitude	-0.092	-0.035	-0.035	-0.060
$R$	Distance	-0.424	-0.309	-0.309	-0.317
$I_a$	Arias intensity	0.543	0.684	0.684	0.684
$D_{5\sim 95}$	5~95% signal duration	-0.219	-0.181	-0.181	-0.180
$PGA$	Peak Ground Acceleration	0.773	0.650	0.650	0.645
$S_a$	Spectral acceleration	0.760	0.846	0.846	0.808

The highest correlation is on the  $PGA$  and spectral acceleration at the main vibration period for the bridge (the one whose modal shape most deforms the structure, i.e. the first "structural" mode). Again table 3.5 shows that the correlation with the epicentral distance  $R$  is negative. This was expected, since, as the distance increases, the demand on the structure is expected to decrease. Another aspect to note is that the correlation with Arias intensity  $I_a$  is relatively high. This can be explained by the progressive degradation of the interface soil leading to ratcheting phenomena.

Results in terms of bending moments at the piles head are similar to those obtained by considering the bending moments at the sections between the deck and abutments. In this case the correlation with spectral acceleration is even more evident (see table 3.5). The correlation with Arias intensity is greater than in the case of bending moment at the joints because, for elements embedded in the soil like the piles, the ratcheting phenomenon has a greater impact.

### 3.7.4 Analytical fit

For each  $EDP$  and  $IM$  considered, the analysis results are fitted with the analytical function:

$$\mu_{EDP} = a (IM)^b \quad (3.48)$$

This function describe the mean of the output parameter  $EDP$ , which is a random variable.

Figure 3.43 shows the results (for the 100 signals), on the  $EDP_m - S_a(T = 0.18, 5\%)$  and  $EDP_m - PGA$  planes, together with the exponential function fit (3.48).

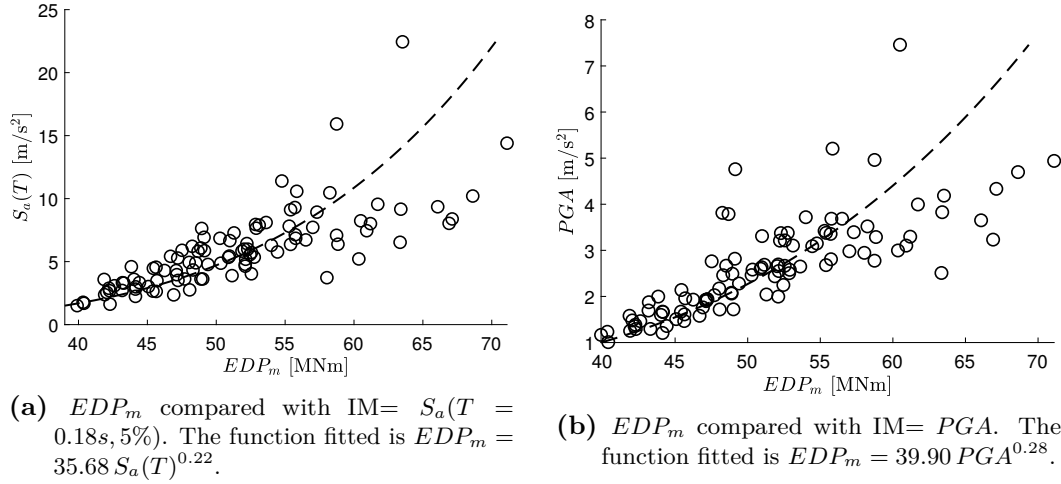


**Figure 3.43.** Response parameter  $EDP_m$  for bending moment at deck-abutments joints compared with IM, with the exponential function fitted.

The parameters  $a$  and  $b$  used in the equation (3.48), for each combination of  $EDP$ , are listed in the table 3.6.

**Table 3.6.** Parameters  $a$  and  $b$  used in the equation (3.48), for each  $EDP$  (bending moment in MNm) and  $IM$ .

IM	param.	deck-abut. joints		piles head	
		$EDP_m$	$EDP_r$	$EDP_m$	$EDP_r$
$PGA$	$a$	39.90			
	$b$	0.28			
$S_a$	$a$	35.68	1.26	5.20	
	$b$	0.22	0.64	0.58	

In order to assess whether the system output ( $EDP$ ) depends on other intensity measure (IM), the correlation between the IM and  $\varepsilon$  is calculated; where  $\varepsilon$  is the random variable that describe by how much the EDP deviates from its mean value  $\mu_{EDP}$  given by the expression (3.48).

$$\begin{aligned}
 \varepsilon &= \frac{\ln(EDP_i) - \ln(\mu_{EDP_i})}{\sigma_{\ln \varepsilon}} = \frac{\ln(EDP_i) - \ln(\mu_{EDP_i})}{\sigma_{\ln(EDP_i) - \ln(\mu_{EDP_i})}} = \\
 &= \frac{\ln(EDP_i) - \ln(a S_a(T)^b)}{\sigma_{\ln(EDP_i) - \ln(\mu_{EDP_i})}} = \frac{\ln(EDP_i) - \ln(a) + b \ln(S_a(T))}{\sigma_{\ln(EDP_i) - \ln(\mu_{EDP_i})}} \quad (3.49)
 \end{aligned}$$

The values of  $a$  and  $b$  are fitted to the analysis results as shown in figure 3.43 and Table 3.6 shows their values.

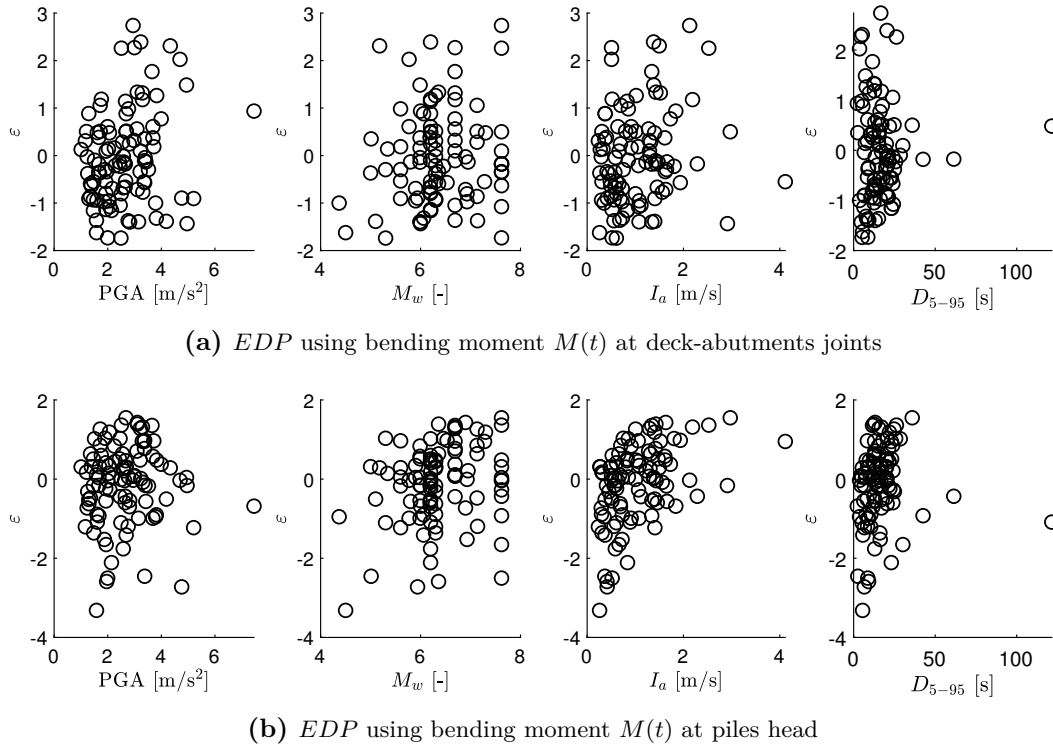


**Figure 3.44.**  $\varepsilon$  compared with various seismic measures.

As can be seen from Figure 3.44 and Table 3.7, the highest correlation is with PGA regarding the bending moment at the top of the abutments and with Arias intensity regarding the bending moment at the piles head.

**Table 3.7.** Correlations between  $\varepsilon$  and IM. Response parameter considered is  $EDP_m$  defined in terms of analytical expression (3.48) using parameters listed in table 3.6.

IM	$M(t)$ at deck-abut. joints	$M(t)$ at piles head
$M_w$	0.112	0.245
PGA	0.229	0.025
$D_{5\sim 95}$	0.032	0.087
$I_a$	0.178	0.443

However, this correlation is relatively low (0.44). The reason why the correlation between *varepsilon* and  $I_a$  came high can be explained by the fact that the Arias intensity is related to cumulative stress phenomena and that the bending moment at the piles head is particularly sensitive to the increase of the bending moment during ground motion (similar to earth-retaining walls). The results show that, in general, there are no particular trends with other intensity measures.

### 3.8 Parameters sensitivity

In reliability theory there are two approaches [90] for the sensitivity analysis [20] of the models on certain input parameters:

- *Deterministic Sensitivity Analysis (DSA)* where a series of analyses are performed gradually changing certain model input parameters. Model output response  $EDP$  is studied to recognize the influence of the input parameter  $X_i$  change. Often this type of analysis is also called *parametric study*.
- *Stochastic Sensitivity Analysis (SSA)* consider realistic statistical models for model input parameters. This approach is based on sampling for numerical evaluation of the system using Monte-Carlo simulations. This allows a better description of the real system behavior gaining a broader knowledge on the output, but it is computationally more intensive.

In this chapter the Deterministic Sensitivity Analysis is used.

For validity range, the various parameters were considered as independent random variables. Therefore no analysis on the eventual correlation between the input parameters is done.

For each step of parameter variation the system is calculated with a set of ground motions, in order to evaluate the response of the system regardless of the particular characteristics that the single accelerogram may have. This set is characterized by containing all ground motions selected from the same conditional spectrum. In particular, for the following analysis, a 1000 year return period spectrum conditioned to a period of 0.5 s was used for the L'Aquila site (located in central Italy). These signals are the same as those that were used for the risk analyses (see section 6.2.2) for the 6<sup>th</sup> stripe.

### 3.8.1 Input and output parameters

The Input Parameters (IP) that are considered for sensitivity analyses are:

- exponent  $n$  of Bouc-Wen constitutive law for soil-column elements
- passive limit  $K_p$  for interface elements ( $\hat{K}_p = \hat{r}_{K_p} K_p$  where  $K_p$  is defined in equation (3.12))
- base damper coefficient  $c_b$
- stiffness ratio  $\hat{r}_{EI}$  between abutments, piles and deck ( $EI = \hat{r}_{EI} \S EI_{deck}$ )

The analysis are done keeping all parameters to values of the single span benchmark case (*Gatteo* overpass described in section 4.2) and varying only the parameter of interest between the specified limits.

The output parameters (OP)<sup>18</sup> considered in the sensitivity analysis are the same as those used in section 3.7 on correlation with IM. In addition to the OP defined in the equations 3.45 and 3.46, a scalar parameter, that depends on the resultant of the earth pressures  $EDP_p$  on the structure, is also defined.

$$EDP_p = \max_t \int |\sigma_{\text{soil-structure}}(t, z)| dz \quad (3.50)$$

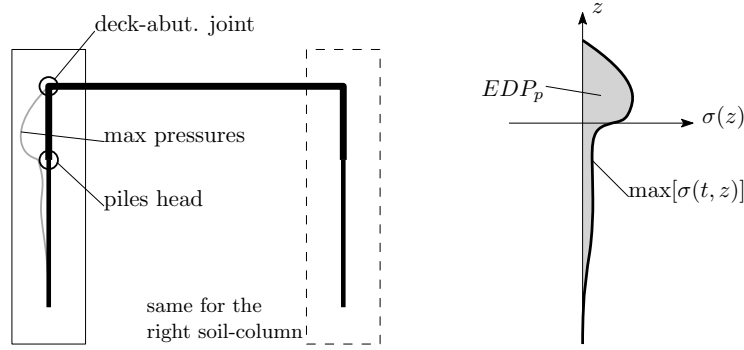


**Figure 3.45.** Global response scalar measures as function of system response in terms of earth pressure ( $EDP_p$  defined in equation 3.50).

### 3.8.2 Results summary

The input parameters and their ranges of variation are given in the table 3.8, along with the Sensitivity Parameter (SP)  $s_{EDP}$ .

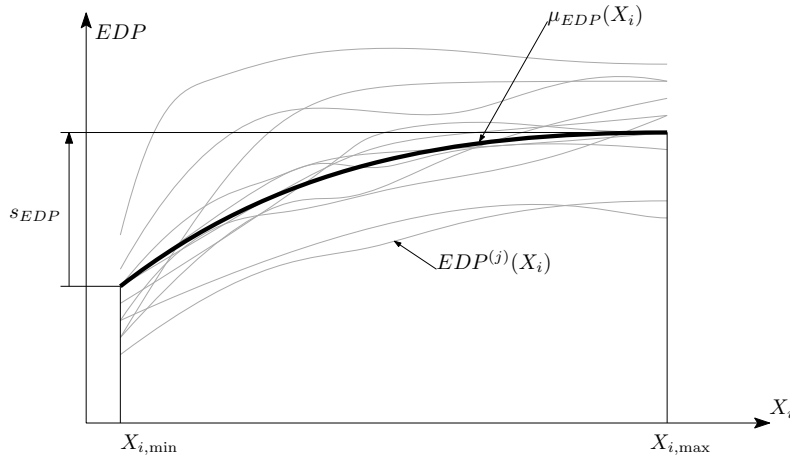


**Figure 3.46.** Sensitivity Parameters (SP) as function of  $\mu_{EDP}(X_i)$ , which is the mean of the response  $EDP^{(j)}(X_i)$  over all the  $(j)$  ground motions considered.

Since locally the function  $\mu_{EDP}(X_i)$  (which is the mean of the response  $EDP^{(j)}(X_i)$  over all the  $(j)$  ground motions considered) presents some discontinuities, caused mainly by the lack of convergence of some signals at the variation of the parameters, as scalar value indicative of the sensitivity  $s_{EDP}$  of the parameter is taken the

<sup>18</sup>Global response scalar measure. The expressions of the output parameters considered (as a function of the bending moment  $M(t)$  along  $y$  for the most stressed cross sections and the earth pressure  $\sigma(t, z)$ ) are summarized below:

$$\begin{aligned}
 EDP_m &= \max_t |M(t)| \\
 EDP_r &= |M(t=0) - M(t=\infty)| \\
 EDP_p &= \max_t \int |\sigma(t, z)| dz
 \end{aligned}$$

difference between the values of  $\mu_{EDP}(X_i)$  at the extremes of the interval.

$$s_{EDP} = \mu_{EDP}(X_{i,\max}) - \mu_{EDP}(X_{i,\min}) \quad (3.51)$$

where  $X_i$  is the  $i$ -th parameter (which varies between  $X_{i,\min}$  and  $X_{i,\max}$ ) and  $\mu_{EDP}$  the average response  $EDP$  of the system (the maximum stress  $EDP_m$ , the residual stress  $EDP_r$  or the resultant of the soil pressures  $EDP_p$ ; as defined in the equations (3.45), (3.46) and (3.50)). Because of its definition  $s_{EDP}$  depends on the magnitude of the corresponding  $EDP$ . Figure 3.46 shows the SP on the  $X_i - EDP$  plane.

As it can be seen from table 3.8 the parameters that most influence the response of the system in terms of  $EDP_m$  for the bending moment at deck-abutment joints are the Bouc-Wen exponent  $n$  and the coefficient of the base damper  $c_b$ . As  $n$  increases the response quantities also increase, this is due to the higher hysteretic damping as  $n$  decreases [21]. The coefficient of the damper  $c_b$  at the base of the soil-columns also affects this response, however this can be explained by the fact that as  $c_b$  increases, the seismic action imposed at the base of the model also increases (and consequently the response also increases).

**Table 3.8.** Sensitivity and range for each input parameter.

Input parameter $X_i$			deck-abut. joints		piles head		
	$X_{i,\min}$	$X_{i,\max}$	$s_{EDP_m}$	$s_{EDP_r}$	$s_{EDP_m}$	$s_{EDP_r}$	$s_{EDP_p}$
$n$	0.1	2.0	12.5	-0.80	15.9	9.08	981
$\hat{r}_{K_p}$	4/6	8/6	0.73	1.07	1.26	0.58	239
$c_b$	$10^6$	$10^8$	10.4	0.08	6.86	5.86	492
$\hat{r}_{EI}$ abut./deck	0.5	2.0	1.38	1.53	-0.34	0.42	-64
$\hat{r}_{EI}$ piles/deck	0.5	2.0	1.80	0.54	9.22	3.56	45
$\hat{r}_{EI}$ (abut.+piles)/deck	0.5	2.0	0.20	0.66	10.6	5.24	79

Compared to the other parameters, the parameter  $n$  also has a greater influence on the response in terms of  $EDP_m$  for the bending moment at the piles head and in terms of the resultant of the soil pressures  $EDP_p$ . The flexural stiffness ratio  $\hat{r}_{EI}$  between the piles and the deck (changing only the stiffness of the piles or also that of the abutments) has a greater influence on the response quantities  $EDP$  for the bending moment on the piles, showing that stiffer piles are subject to greater bending moments.  $\hat{r}_{EI}$  between the abutment and deck seems to matter slightly more than the others with respect to the residual moments at the end of the earthquake for the deck-abutments joints.

More details about the individual parameters  $X_i$  and the results of the various analyses are described in appendix D.

### 3.9 3D model

In order to better describe the behavior of integral abutment bridges, a three-dimensional model was also established (figure 3.47). To extend the 2D model presented thus far, the transverse behavior (i.e. parallel to the  $y$  direction) of the soil

and the structure is added. The extension of the model to describe the 3D behavior was also tentatively undertaken as proof of concept by Franchin et al. . Here it is studied further.

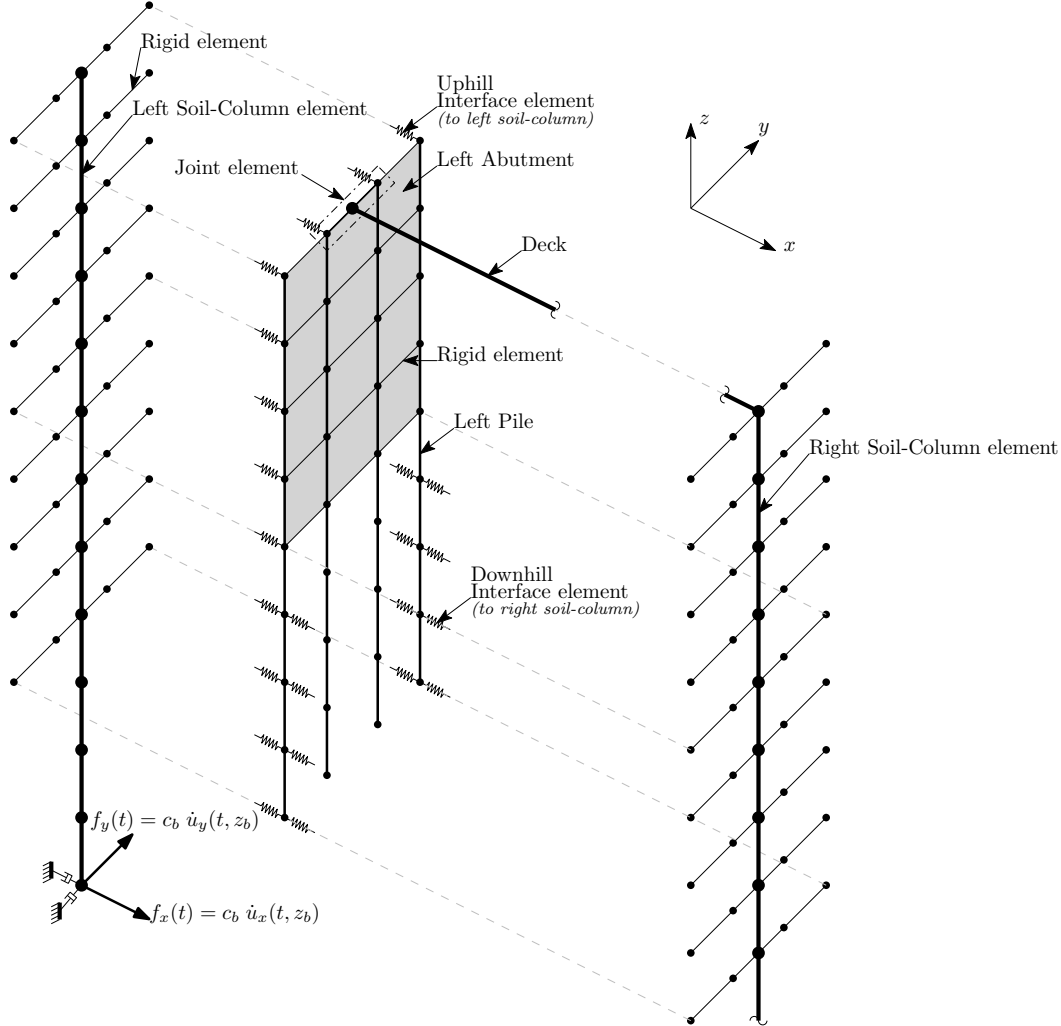


**Figure 3.47.** Exploded view of the 3D model for the integral abutment bridges seismic assessment.

Adding the degree of freedom along  $y$  axis also made it necessary to modify the soil-column and interface elements.

However, it must be considered that this model was conceived to describe mainly the response of the bridge to a longitudinal ground motion (along  $x$ ). In fact in the  $y$  direction the stresses in the bridge are less influenced by soil-structure interaction.

### 3.9.1 Structure elements

The model is subdivided into as many layers as the number of piles in the  $y$  direction. Such discretization facilitates the results reading and the comprehension of the model because there is a distinct finite element for every pile. Therefore also the abutments are consistently subdivided into the same amount of "stripes". Since

the abutment is a unique element, the elements in  $y$  direction are connected by transverse elements that restore the continuity in a classical "*grillage*" model. As a very first approximation these elements were taken as rigid elements, but also analysis using flexible elements was carried out. Abutments modeled with *shell* elements was also considered to see how much the increased flexibility of the element affects the overall response of the system. However the response of the system does not change in global terms. More details are given in appendix B.1.

### 3.9.2 Interface elements

The abutments nodes are connected through the corresponding soil-column nodes by interface elements.

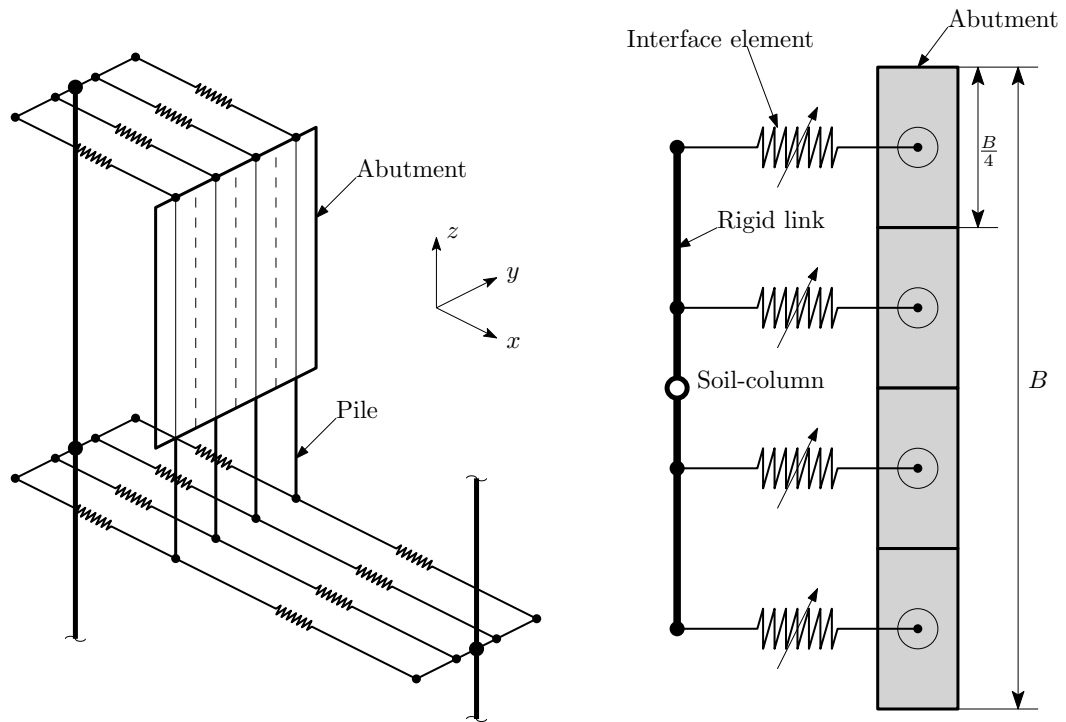


Figure 3.48. 3D interface elements.

So the interface elements are defined on the areas of influence that, with respect to the two-dimensional case, are divided by the number of elements in the  $y$  direction (being careful in case the extreme elements, or those with the minimum and maximum  $y$ , refer to smaller areas).

The displacements of the structure along  $y$  are initially considered equal to the displacements of the soil column, without considering the  $\tau$ -sliding behavior of the interface between abutment and embankment backfill in the  $y$  direction. In reality, the interface soil will exhibit non-zero deformation for transverse actions on the bridge, so this initial approach will need to be improved. Considering the interface soil non-deformable for the bridge transverse behavior, equal displacement constraints along the  $y$  axis are inserted between the nodes of the structure and the nodes of the soil-columns.



A spring is inserted on each node of the piles, with another node fixed on an inertial reference, to account for the vertical behavior of the pile (thus inserting  $f$ - $z$  and  $q$ - $z$  elements described in section 3.2.3). More details on the implementation are given in section 3.5.2.

### 3.9.3 Soil-column elements

Extension to 3D for the soil-column elements is relatively straightforward, since the force-displacement behavior in the  $y$  direction can be modeled with the same constitutive law used for the  $x$  direction (assumption of homogeneous deposit and with the same stratigraphy along  $x$  and  $y$  directions). The only degrees of freedom allowed are the displacements in the  $x$  and  $y$  directions, and the constitutive law is the same as discussed above (see section 3.1 and its implementation in section 3.5.1).

In the appendix B.2 the use of a coupled constitutive law in the two directions  $x$  and  $y$  is evaluated.

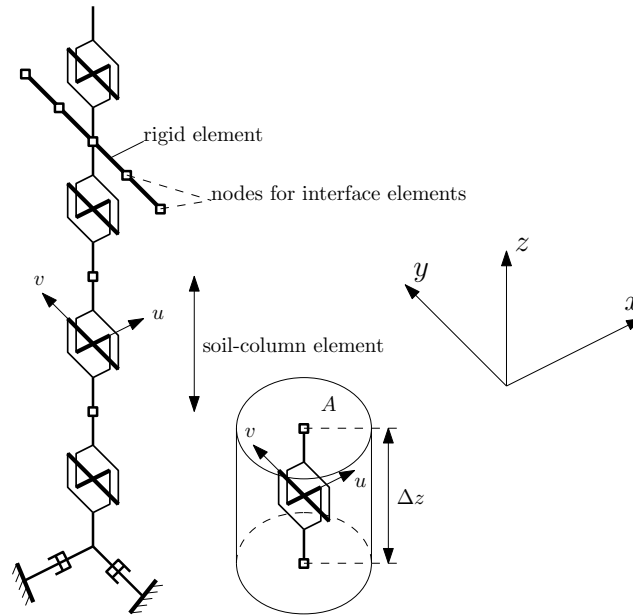


Figure 3.49. 3D soil-column elements.

Dampers for the compliant base in the  $x$  and  $y$  directions are present at the soil columns base (lowest nodes). Obviously distinct ground motion time series are applied in the two directions, consistent with the seismic event studied.

To connect the soil-column to the multiple structural members in which the abutments are discretized, multiple interface elements are required at each stripe and depth  $z$ , therefore rigid links (or other form of kinematic constraints) are introduced between the soil-column and the soil-side ends of the interface elements. Since the soil-column nodes can only translate in the  $x$ - $y$  plane then it is sufficient to insert the added nodes, for the interface springs, in an equal displacements constraint with the soil-column nodes at a given depth  $z$ . In fact, given a depth  $z$ , all left and right soil-columns nodes at that depth are constrained to have the same displacements in  $x$  and  $y$  directions. Thus, in terms of implementation, for each set of nodes in the

soil-columns at a given depth there is only one master node and all others are slaves to that node.

### 3.10 Limit skew angle for the applicability of the model

The three-dimensional model is used for assess the effect of skew angle on integral abutment bridges. The analysis was performed varying the  $y$  coordinates of the right alignment; and thus considering a skew angle  $\Theta$  greater than zero.

For these analyses, the 20 ground motions of the third stripe ( $T_R = 100$  years) and the sixth stripe ( $T_R = 1000$  years) for the L'Aquila site described in section 6.2.2 were used. In addition, the deck was described with a grillage model. Finally, the behavior along  $y$  of the embankment, as a function of relative displacements with the abutment, was modeled with linear springs with the stiffness corresponding to a simple shear model for the embankment wedge  $K_{y,emb.} = \frac{G_0 B_c L_e}{H}$ .

The results in terms of maximum moments ( $EDP_m$ ) normalized with respect to the maximum moment value for a zero angle  $\Theta$  are shown in Figures 3.50 and 3.51.

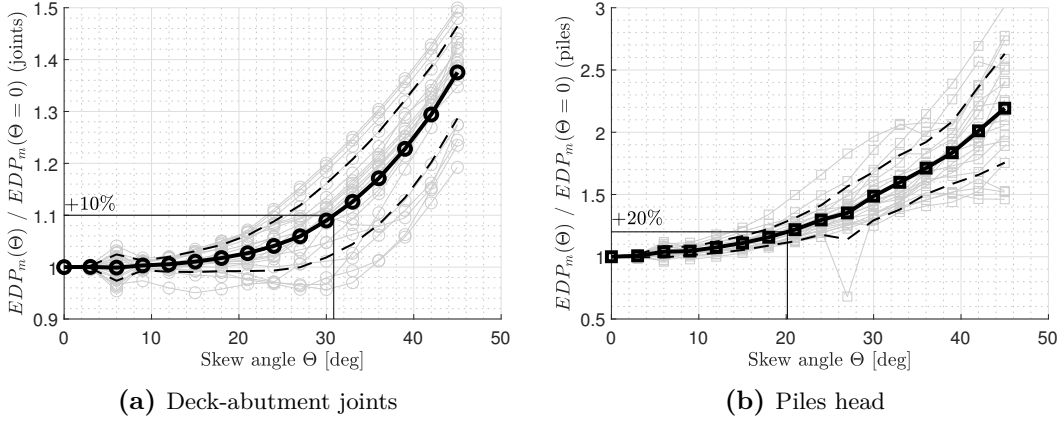


**Figure 3.50.** Maximum bending moment in  $y$  direction as function of the skew angle  $\Theta$  for the third stripe ( $T_R = 100$  years).

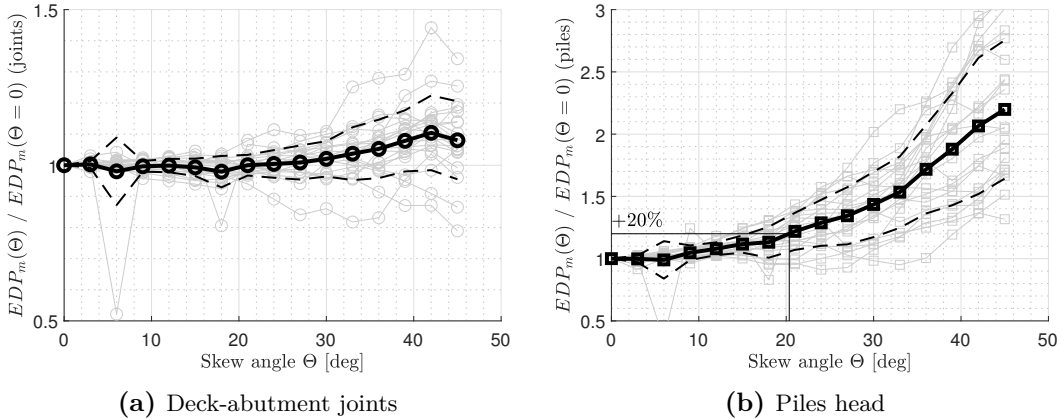


**Figure 3.51.** Maximum bending moment in  $y$  direction as function of the skew angle  $\Theta$  for the sixth stripe ( $T_R = 1000$  years).

The results show that, the bending moment at the piles head is the most sensitive response quantity. It increases, on average about 20% with respect to the case  $\Theta = 0$  for a skew angle of about 20 degrees. The deck-abutment moment, on the contrary, increases for the same skew angle only about 10% (figure 3.50a), at the lower service-level intensity. For the stronger, dimensioning intensity, this moment is ,on average, almost independent of the skew angle (figure 3.51a). Therefore it can be stated, from the result of these preliminary analyses, that the model presented in this thesis can still be applied to bridges with skew angles  $\Theta$  less than 20 degrees.

Figure 3.52 shows the values, in terms of  $EDP_m$ , the flexural bending moment at the deck-abutment joints along  $z$  as the angle  $\Theta$  increase.

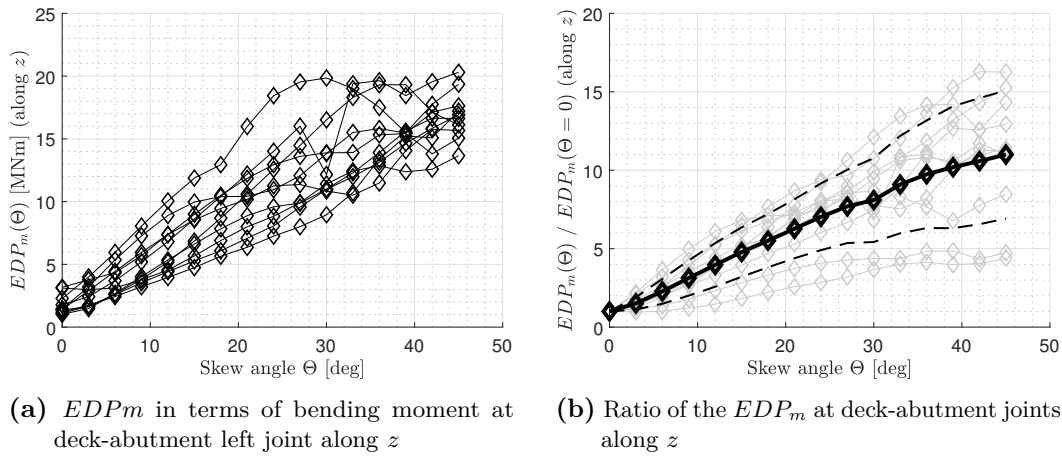


**Figure 3.52.** Maximum bending moment in  $z$  direction as function of the skew angle  $\Theta$  for the third stripe ( $T_R = 100$  years).

The bending moment along  $z$  increases considerably as the angle  $\Theta$  increases. As it can be seen from the figure 3.52a, however, the values of the maximum moment  $EDP_m$  are smaller than the bending moment along  $y$  (38 MNm for the third stripe and 50 for the sixth). In fact, low values for a null angle lead to high ratios. Moreover it was expected that increasing the skew angle of the bridge would increase the joints moment along  $z$ . The increase of the moment along  $z$  at the joints also explains, in part, why the bending moment along  $y$  most influenced by the skew angle is the one at the piles head. In fact, they are the structural elements that resist this increase in torsion at the bridge abutments. Note that the maximum moment reached along  $z$  is about 20 MNm. Considering a cylindrical failure surface around the piles of diameter  $B$  and length  $L_p$ , together with the Mohr-Coulomb failure criterion, leads to a soil capacity of about 22 MNm. Considering that this resistance is very similar to the maximum value obtained (20 MNm) and that this result was obtained for the third stripe ( $T_R = 100$  years), one wonders about the need to explicitly consider the nonlinear behavior of the soil subjected to the torsion (moment along  $z$ ) of the abutment. Such considerations are left for an eventual development of such model that considers also integral bridges with skew angle different from zero.

The figure 3.53 shows the ratio of the maximum bending moment at the head of the outer piles (in the acute and obtuse corners) to the inner piles.

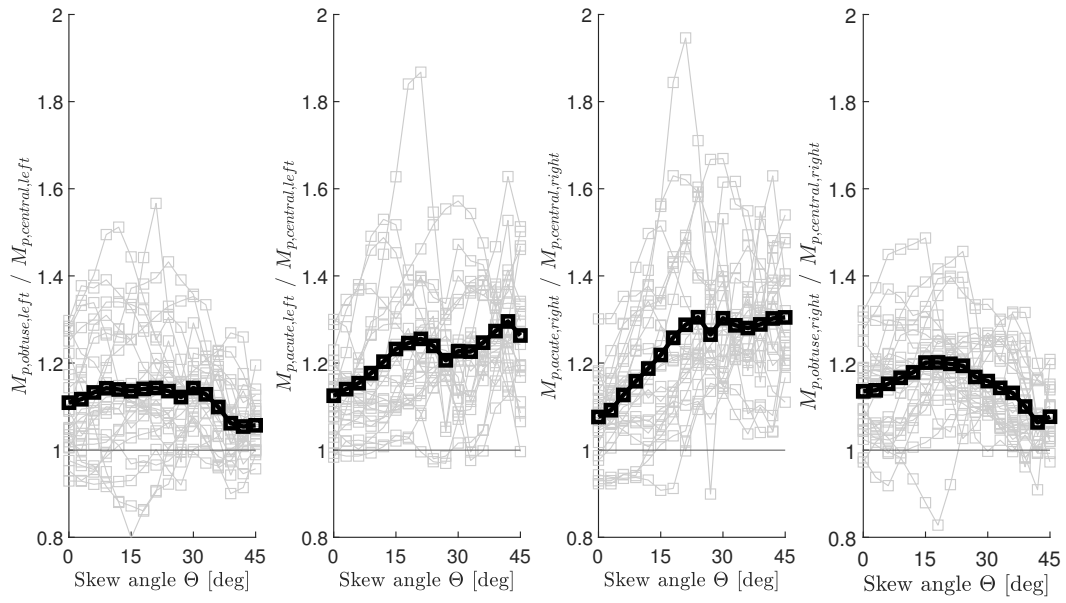


**Figure 3.53.** Maximum bending moment ratio between external piles and internal ones (for the third stripe).

Results show that, as expected, the outer piles exhibit, on average, higher bending moments than the inner piles, with the moment increment becoming larger with  $\Theta$  for the piles at the acute angles.

## Chapter 4

# Comparison with a higher-order model

In this chapter the previous results are compared with a higher order non-linear 3D FEM model. The latter was developed as part of a PhD thesis in geotechnical engineering by candidate Domenico Gallese, under the supervision of Professor Luigi Callisto and Dr. Davide Gorini .

Results are presented in terms of time series of selected internal stress resultant, particularly the bending moment at the deck-abutments joints, as well as vibration modes, seismic site-response analysis of the soil deposit, and soil pressures on the structure.

In the following sections both models are referenced as:

- *Reduced Order Model (ROM)*: the model described in chapter 3 developed in this thesis. For comparisons is used the 2D model.
- *3D NonLinear Finite Element Model (3D-NLFEM)*: the higher-order model developed by Domenico Gallese.

### 4.1 Higher-order 3D FEM model

In this model [50] the soil is represented by three-dimensional solid elements, and in particular by eight-node hexahedra with a single integration point. In the software **OpenSEES** such elements are implemented in computationally efficient finite elements (called **SSPbrick**). The model presented in this thesis (see chapter 3) and the higher-order one have the same global coordinates ( $z$  upwards,  $x$  on the bridge longitudinal direction and  $y$  follows the right-hand rule). The three-dimensional model has been simplified by exploiting symmetry with respect to a system vertical plane and is loaded with only the longitudinal component of seismic actions (along  $x$ ) as it can be seen in figure 4.1. For simplicity, the embankment has a rectangular section: this configuration is made possible by periodic constraints that connect the nodes positioned on the opposite vertical faces, reproducing a condition similar to that of an embankment made with reinforced soil.

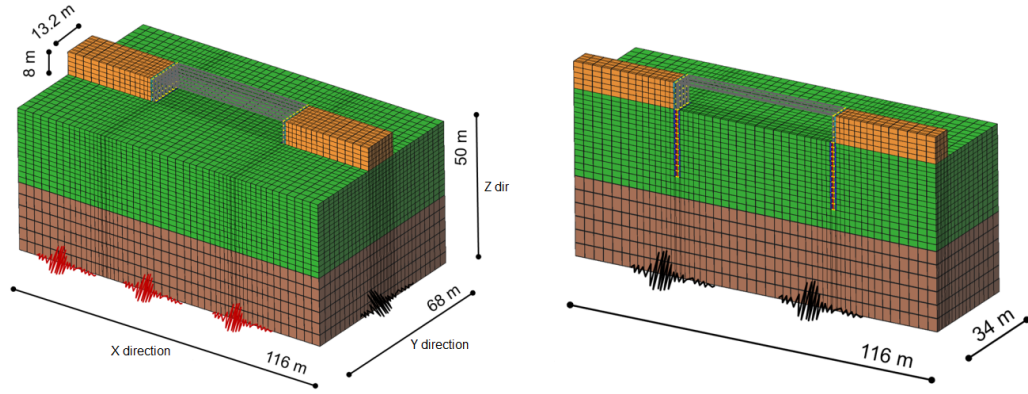


**Figure 4.1.** Higher order 3D-NLFEM confrontation model [50].

The soil mechanical behavior is described by the elasto-plastic constitutive model with hardening of Yang et al. (2003) [110] (called PDMY in *OpenSEES*). The model includes a Drucker-Prager critical state condition with a non-associative flow rule and a kinematic hardening rule (pressure dependent multi-yield in *OpenSEES*). In this constitutive model, plasticity is formulated based on the multisurface-plasticity framework of Prévost (1978) [94]. The PDMY model is able to reproduce the dependence of the energy dissipation on the strain amplitude. The foundation piles are simulated with elastic beam elements, connected through rigid link elements to finite elements with degraded mechanical properties, which act as interface elements, in turn connected to the undisturbed soil. Two-dimensional structural elements are represented through grids of beam elements connected in a similar manner to the soils, where necessary. An additional small damping ratio equal to 1-2% was introduced in the soil domain using the Rayleigh formulation, in order to attenuate the effects of spurious high frequencies.

At the end of the simulation of the construction stages, the ground motion, expressed in terms of velocity, is applied to the basis of the models, simulating bedrock deformabilities by interposing appropriate viscous dampers (Joyner and Chen 1975 [69]). At this stage, conditions on the lateral contours (excluding the symmetry planes) limit the reflection of seismic waves through additional viscous dampers, or through periodic constraints. All analyses required a significant computational effort and were made possible by the use of parallel computing (*OpenSeesSP*, McKenna and Fenves 2007 [85] [84]) and the computational resources of the *Texas Advanced Computing Center* (Rathje et. al 2017).

## 4.2 Benchmark case

For the purpose of comparison, a case study (inspired by the integral abutment flyover actually realized in Italy [43]) was analyzed.

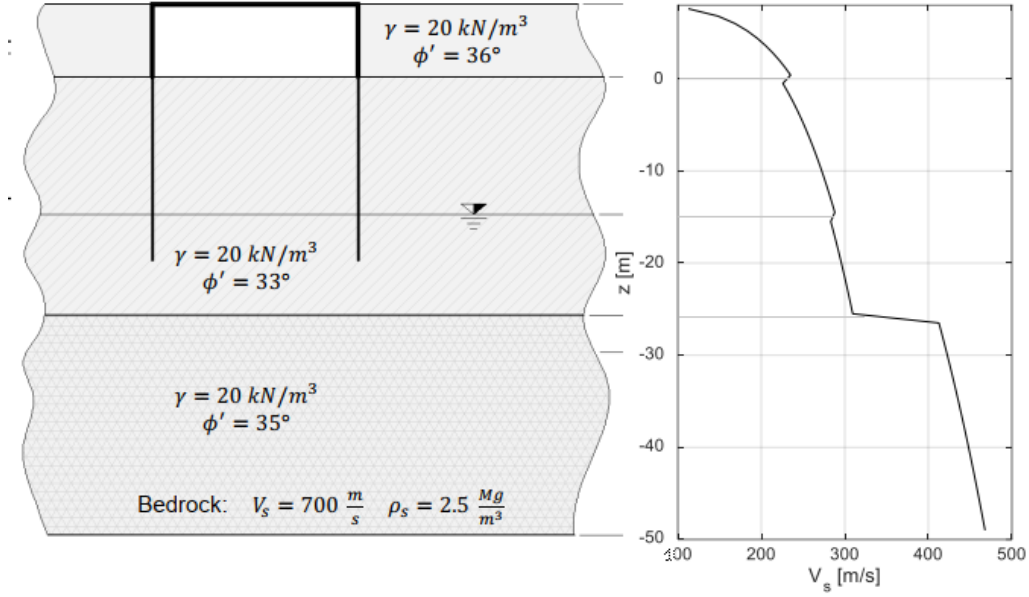


**Figure 4.2.** Benchmark case study soil stratigraphic profile.

The changes made to the actual bridge (overpass *Gatteo Rubicone* built by ANAS on the Italian A14 highway [European route E55]) are:

- Different soil stratigraphic profile.
- Reduction of the foundation piles length from 40 m to 20 m.
- Minor changes of section properties (an increase of 25% in the section inertia).

The soil stratigraphy is shown in the figure 4.2. The following analytical function is fit to the soil deposit initial shear modulus:

$$G_0(p') = G_r \sqrt{\frac{p'}{p'_r}} \quad (4.1)$$

where the parameters  $G_r$  and  $p'_r$  are listed in table 4.1 for each soil layer;  $p'$  is the spheric part of the effective stress  $\sigma'$ , and (if the horizontal component  $\sigma'_h = K_0 \sigma'_v$  is proportional to the vertical component  $\sigma'_v$  through the at-rest coefficient  $K_0$  defined in equation (3.19)) is equal to  $p' = \sigma'_v(1 + 2K_0)/3$ . Table 4.1 lists thickness, mechanical properties and parameters of the function (4.1) for all the layers of the soil deposit.

**Table 4.1.** Soil deposit stratigraphic parameters for the benchmark case (*Gatteo overpass*). ( $h$  is the layer height,  $V_{s0,m}$  the mean initial shear wave velocity and  $G_{0,m}$  the mean initial shear modulus).

soil type	$h$ m	$\gamma$ kN/m <sup>3</sup>	$K_0$ -	$c'$ kPa	$\phi'$ deg	$V_{s0,m}$ m/s	$G_{0,m}$ kPa	$G_r$ kPa	$p'_r$ kPa
embankment	8	20	0.41	0	36			115 000	100
gravelly sand	15	20	0.46	0	33	252	$1.30 \times 10^5$	98 000	100
gravelly sand	11	20	0.46	0	33	252	$1.30 \times 10^5$	95 000	105
gravelly sand	24	20	0.43	0	35	400	$3.26 \times 10^5$	165 000	100

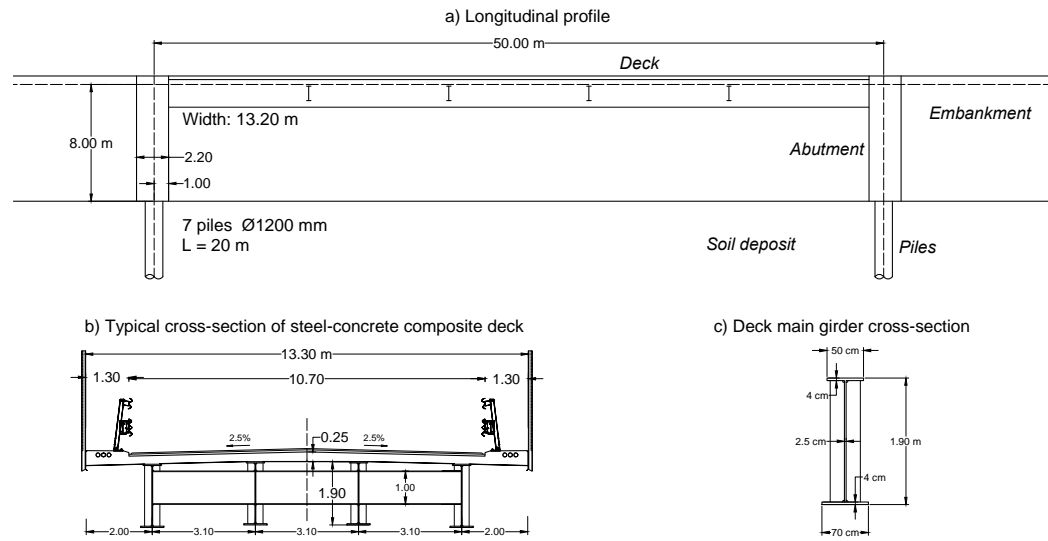


**Figure 4.3.** Benchmark case study (inspired from *Gatteo overpass* in use on the Italian highway A14 [43]).

The geometrical and mechanical parameters of the bridge are described in the table 4.2.

**Table 4.2.** Gatteo flyover geometrical and mechanical properties of the structure and sub-structure elements.

Material	steel-concrete
$E_s$	210 GPa
$L_d$	50.0 m
$B$	13.3 m
$A$	1.2036 m <sup>2</sup>
$I_y$	0.6784 m <sup>4</sup>
weight	9382.1 kN

(a) Deck

Material	C32/40
$B$	13.2 m
$H$	8.0 m
$t$	2.2 m

(b) Abutments

Material	C32/40
$d$	1.2 m
$L_p$	20.0 m
piles n.	7
span	1.8 m

(c) Piles



### 4.2.1 Ground motions

Two ground motion time series were selected: *Parkfield* (2004) and *Yamakoshi* (Chūetsu earthquakes, 2004). The general data of the two signals are shown in table 4.3.

**Table 4.3.** Macroseismic parameters and intensity of ground motions used.

Ground motion	M	R	PGA	$I_a$
	[-]	[km]	[g]	[m/s]
Parkfield	6.0	4.25	0.35	0.787
Yamakoshi	6.2	9.10	0.41	4.117

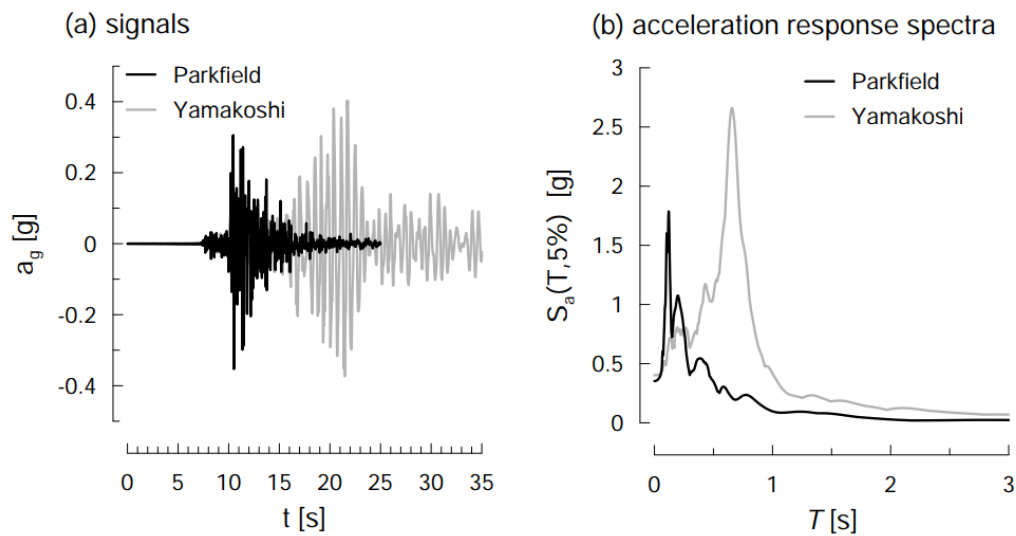


**Figure 4.4.** Parkfield and Yamakoshi acceleration time series and response spectra.

In both models the ground motions were applied at the soil deposit-bedrock interface without performing the time history correction to account for the difference in specific impedances between bedrock and deposit (see appendix A). This means that the bedrock input time series, in terms of velocity, is the same as the outcrop one.

The maximum amplification for the more severe Yamakoshi record occurs in the period range of 0.5-0.8 s, exciting the fundamental global mode of the soil-bridge system. Instead, for the Parkfield ground motion, the maximum spectral amplification occurs at periods lower than about 0.4 s, that are closer to the higher vibration modes of the system.

## 4.3 Analysis of construction stages

The results of the construction stages are in excellent agreement for the two models (at least for the bending moments on the abutment-piles alignment), as it can be seen from the figure 4.5.

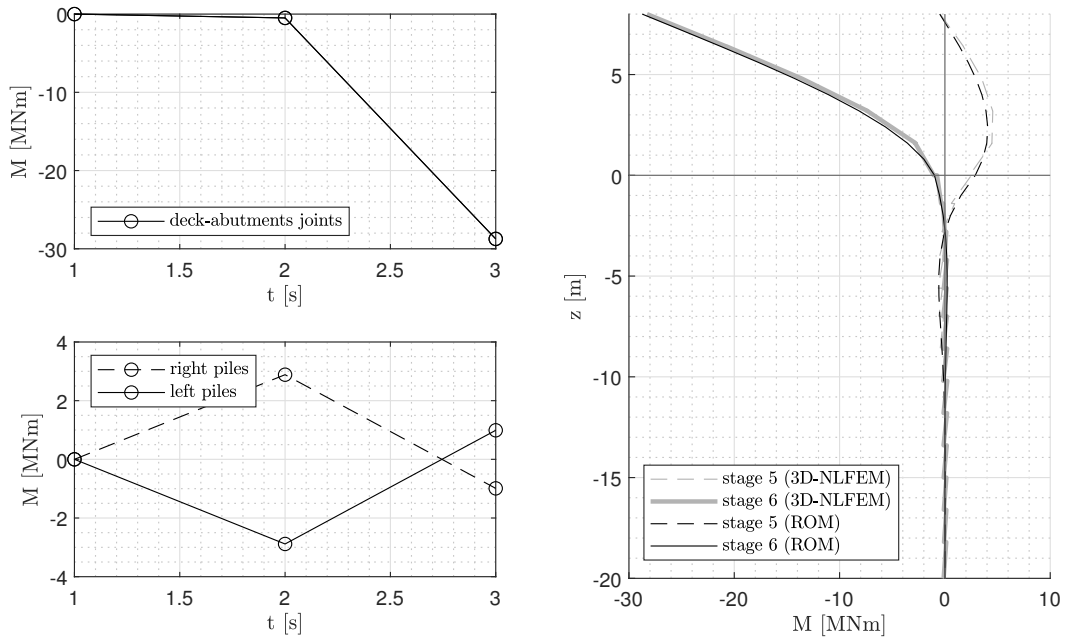


**Figure 4.5.** Bending moment on the left abutment-piles alignment for the construction stages (stage 5 and 6).

Results are provided only for stages 5 and 6, that are the most relevant in terms of bending moments.

#### 4.4 Free-field site-response analysis

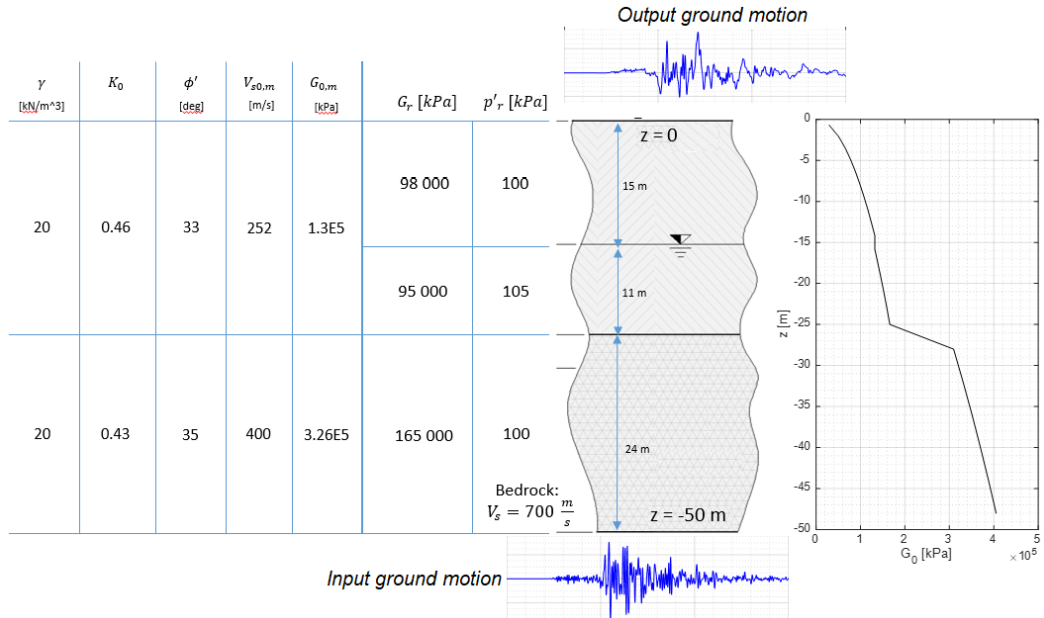


**Figure 4.6.** Soil deposit parameters used for the site-response analysis without the embankments and the bridge (*free-field*).

To evaluate the approximation introduced modeling the soil deposit with soil-column elements, a nonlinear seismic site-response analysis was performed on the deposit alone. In both models (3D-NLFEM and ROM) the motion at surface  $z = 0$  was evaluated applying the ground motion to the bedrock, without considering the bridge structure and embankments. The results were further verified with the code for nonlinear seismic site-response analyses **MARTA** (Callisto, 2015 [18]). Figure 4.7 shows good agreement with all three methods (ROM, 3D-NLFEM and **MARTA**) in terms of the response spectra of the surface ground motion (applied at the soil deposit base denoted as *Bedrock* and the signal at the surface representing the result of the analysis).

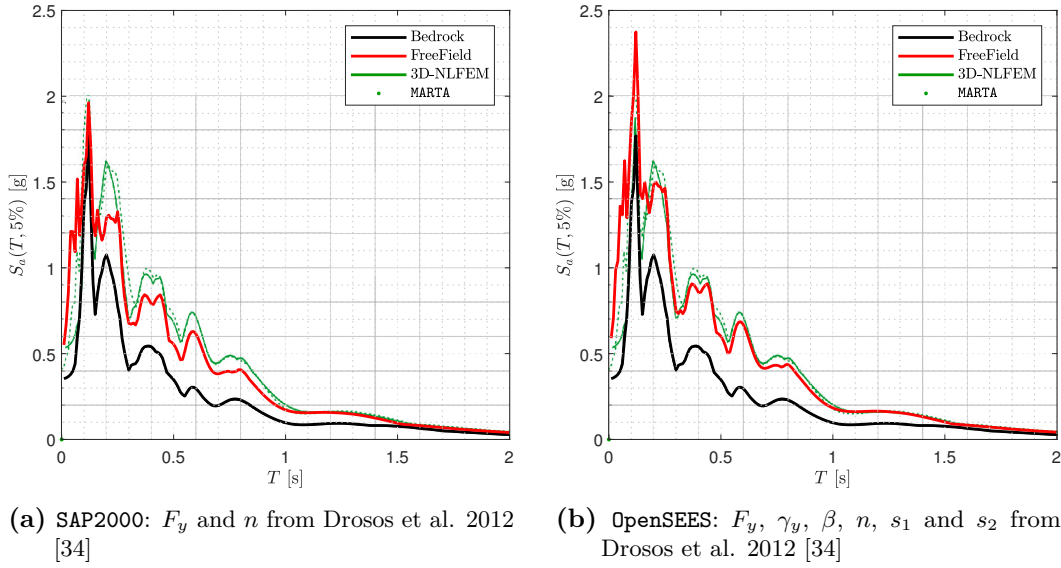


**Figure 4.7.** Results of the free-field analysis in terms of response spectra of the surface ground motion.

The two panels in the figure 4.7 refer to two different implementations of the Bouc-Wen model. In **SAP2000**, due to the limitation in defining constitutive laws, a standard Bouc-Wen constitutive law was defined [21] with parameters  $\gamma = \beta = 0.5$ . While in **OpenSEES** the Bouc-Wen constitutive law modified by Gerolymos and Gazetas [53] could be implemented. As can be seen from figure 4.7 the difference in considering the more advanced law implemented in **OpenSEES** is not excessive compared to the simplified model<sup>1</sup>. In both cases the constitutive law parameters were taken from Drosos et al. 2012 [34]. Force-displacement hysteresis cycles for soil elements at a depth of  $z = -25$  m for both ROM and 3D-NLFEM models are shown in figure 4.8.

<sup>1</sup>This is due, in part, to the fact that soil-column elements do not have deformations much greater than the yielding one.

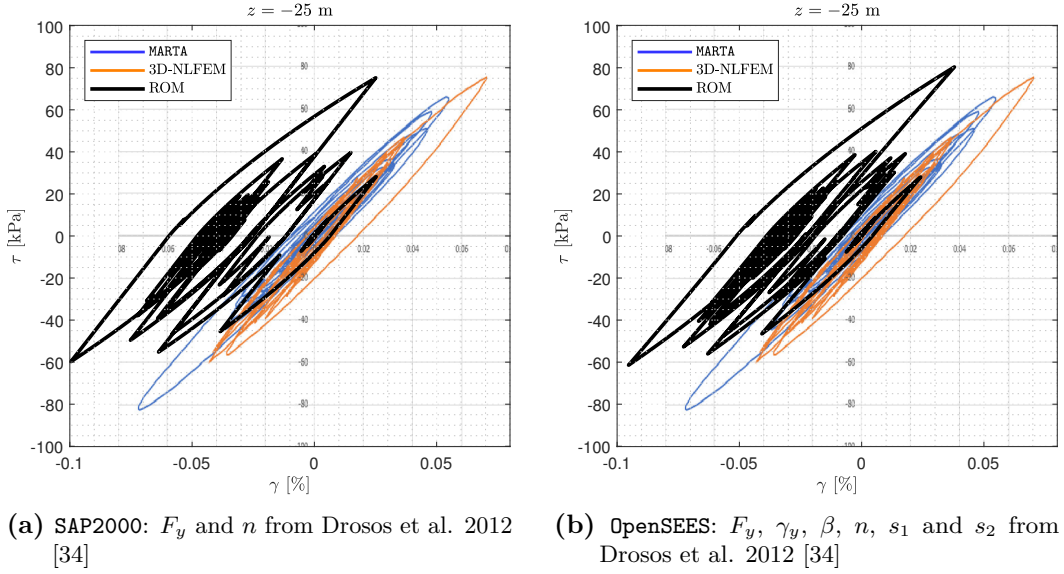


**Figure 4.8.** Results of the free-field analysis in terms of soil force-displacements. Shear resistance is equal to  $\tau = 337$  kPa.

As can be seen from the results, in terms of shear stresses within the soil, there is good agreement between the two models. There is slightly less correspondence in terms of shear strains, however still acceptable.

The comparison, in terms of acceleration response spectra, of surface motion for the Bouc-Wen model with  $n = 0.2$  and with  $n = 2$  (as per the original model of Franchin-Pinto, 2007) is shown in figure 4.9.

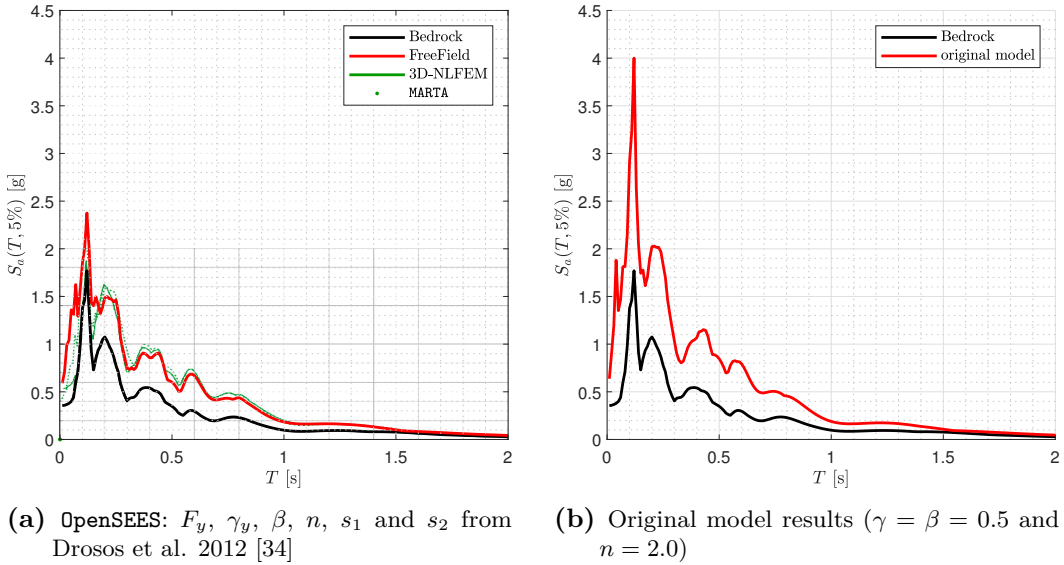


**Figure 4.9.** Results of the free-field analysis in terms of response spectra of the surface signal. Comparison between the Bouc-Wen model with  $n = 0.4$  and  $n = 2$ .

As it can be seen, the response of the model with  $n = 2$  is less damped and

exhibits an amplification of almost twice as much as the case with  $n = 0.2$ . This is due to the fact that, by increasing the exponent  $n$ , the Bouc-Wen model becomes closer and closer to an elasto-plastic one [21]. Conversely, decreasing the value of  $n$ , results in a more "curvilinear" response and this has the effect of increasing the dissipation of the model via hysteresis loops for small deformations. Increasing the dissipation, for the case of  $n = 0.4$ , also reduces the response of the soil column. This is discussed previously in section 3.1.1.

## 4.5 Modal analysis

Given the importance of modal output in the dynamic characterization of the system, a careful comparison was made between the two models, also in terms of modal analysis. The comparison was made both on the periods of the first modes and on the modal shapes of the structure.

The first mode of the system has been called *deposit mode*, because it basically coincides with the first mode of the soil deposit, without considering the structure (see section 3.6.1). In fact, the soil mass in which the structure is immersed is so large, relative to the mass of the structure, that only the soil deposit matters for the first mode as it can be seen in figure 4.10.

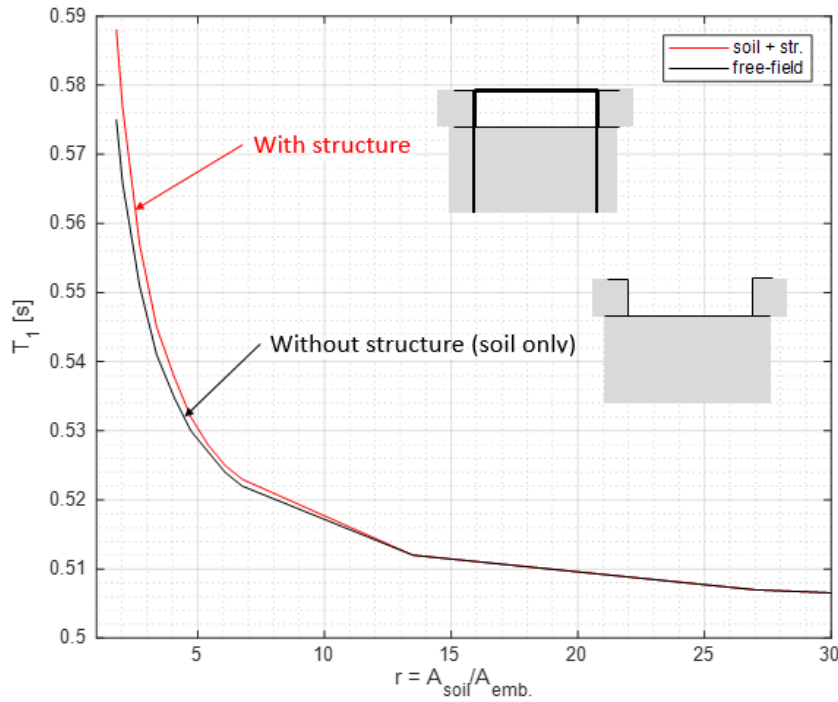
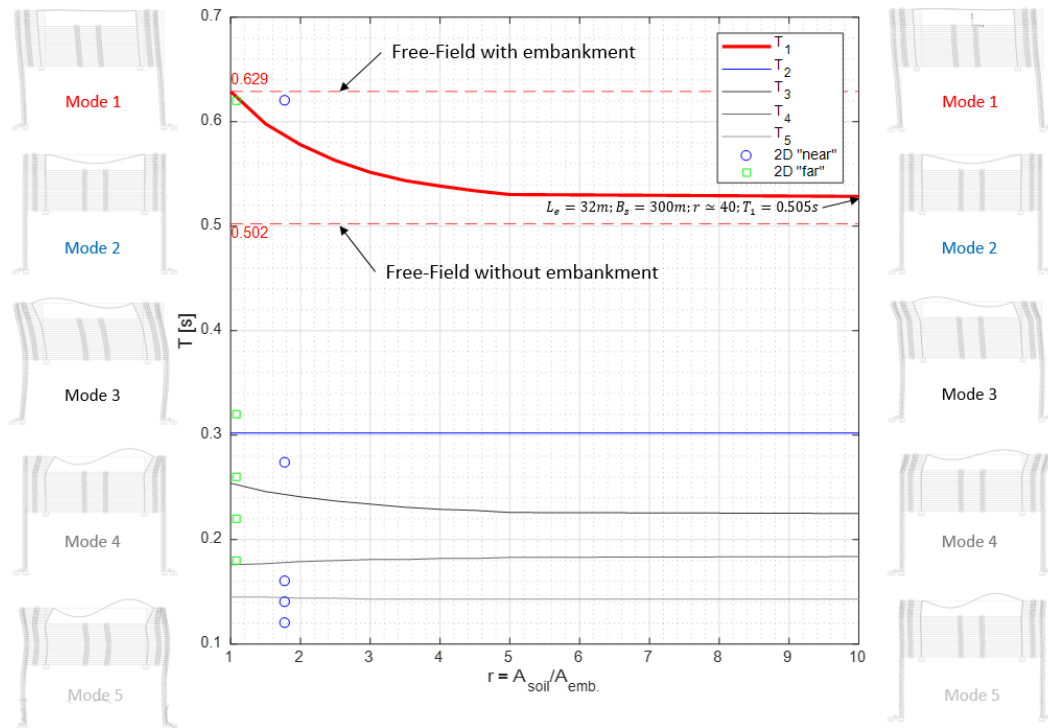


**Figure 4.10.** First mode period compared with the soil area ratio  $r = A_s/A_e$ .

Regarding the vibration period of the first mode of the system we have a slight dependence on the soil area ratio  $r = A_s/A_e$ . In fact, theoretically, when  $r \rightarrow \infty$  the system tends to the column without embankment while when  $r \rightarrow 1$  the solution tends to that for a soil column that also includes the embankment (as if it were

an additional layer of deposit). The figure 4.10 was obtained by parametrically generating the models by varying the effective width of the soil  $B_s$ . As can be seen from the figure, the first mode is essentially insensitive to the dynamic characteristics of the structure. In fact, the difference, in terms of the first mode vibration period, between the solution with and without structure, is 2.3% for  $r = 1.78$ .

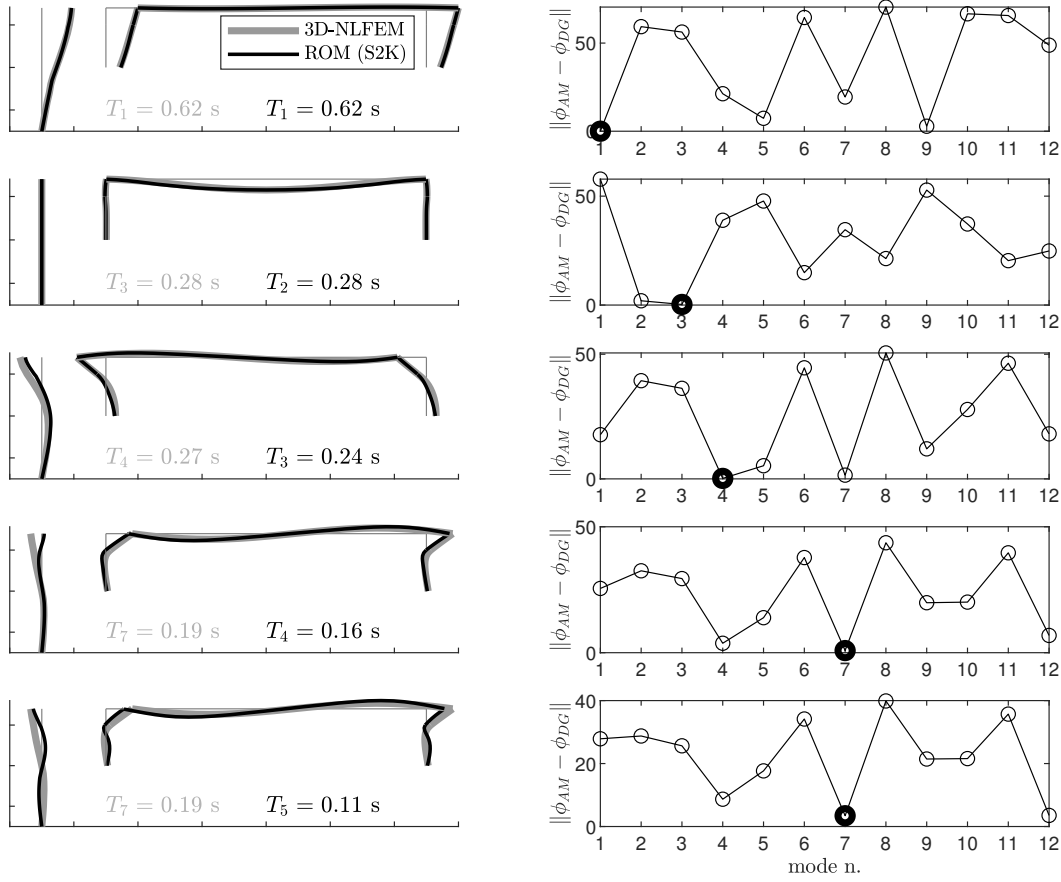
The mode most sensitive to the variation of the ratio  $r$  turns out to be mainly the first one. This can be deduced from the figure 4.11, where are indicated the periods of vibration (on the ordinate) of the first 5 modes as the ratio  $r$  varies.



**Figure 4.11.** First five mode periods compared with the soil area ratio  $r = A_{soil}/A_{embankment}$ .

Figure 4.11 shows also the values of the vibration periods of the soil column alone (with and without embankment) derived from the free-field analysis. In the same figure, moreover, on the left are shown the vibration mode shapes of the system for  $r = 1$ , while on the right the mode shapes for  $r = 10$ . As it can be clearly seen, there is no appreciable difference in terms of modal shapes. Higher modes one are less affected by the ratio  $r$ .

Even comparing the difference between the two models (ROM and 3D-NLFEM) in terms of modal shapes the results seems to be positive, as shown in the figure 4.12.



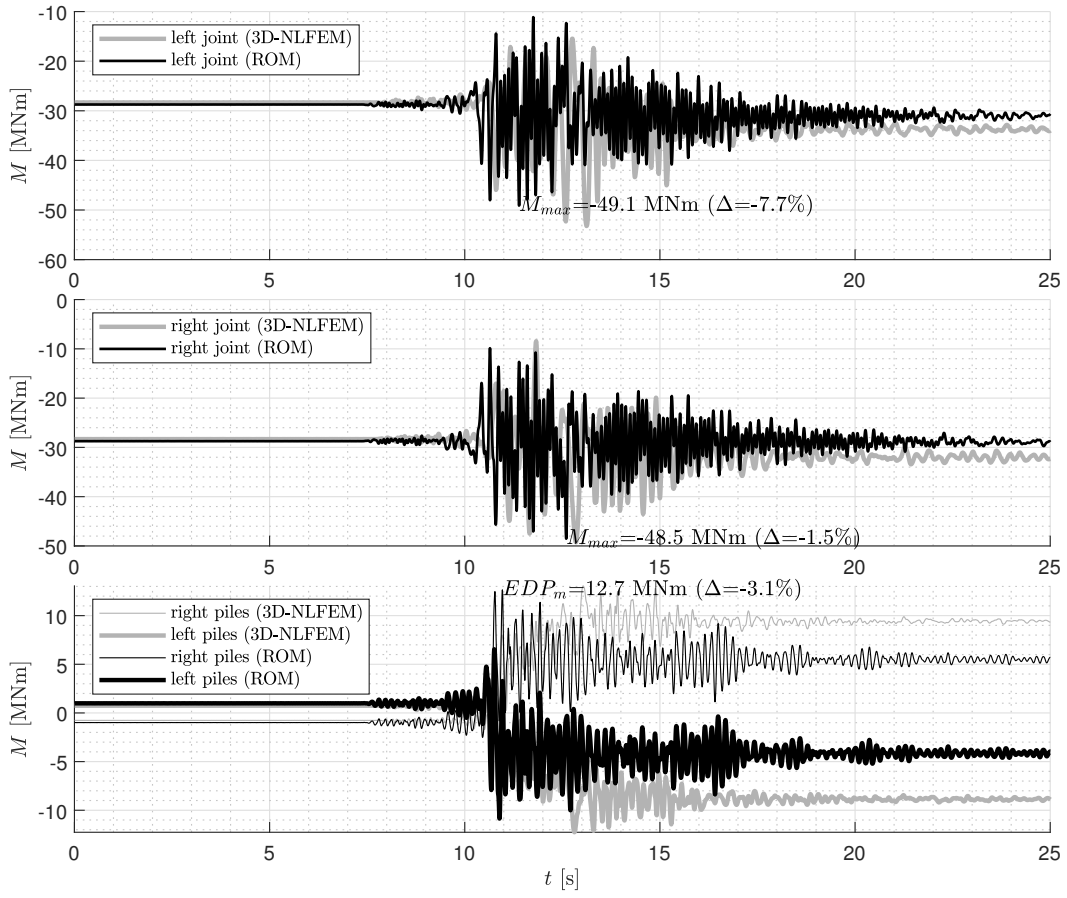
**Figure 4.12.** Modal-shapes confrontation between ROM (implemented in SAP2000) and 3D-NLFEM.

Figure 4.12 shows the comparison for the first five modal shapes of the ROM model compared to the corresponding modal shapes of the 3D-NLFEM model. In fact, due to the differences between the two models, the numbering of corresponding modes is not consistent. To highlight the corresponding mode in the 3D-NLFEM model, the norm of the difference vector of the two mode-shape vectors was used. Thus, in figure 4.12, the modal shapes are shown in the left column for comparison. While in the right column the norm of the difference of the two modal shapes is displayed. The corresponding mode, in the 3D-NLFEM model, is the one for which the difference is the lowest. The modal shapes compared were both normalized to the same criterion, so that there is a consistent representation for all modal shapes.

## 4.6 Time series of the selected quantities

Also in terms of time-histories the comparison between the two models response seems to be good. In the figures 4.13 and 4.14 the responses, in terms of bending moments on the structure in the most stressed sections<sup>2</sup>, have been compared.

<sup>2</sup>The most stressed sections under seismic actions, for this particular type of structures, are the abutments top section (deck-abutments joints) and the section at the top of the piles (piles head).



**Figure 4.13.** Bending moments time histories confrontation for *Parkfield* ground motion.



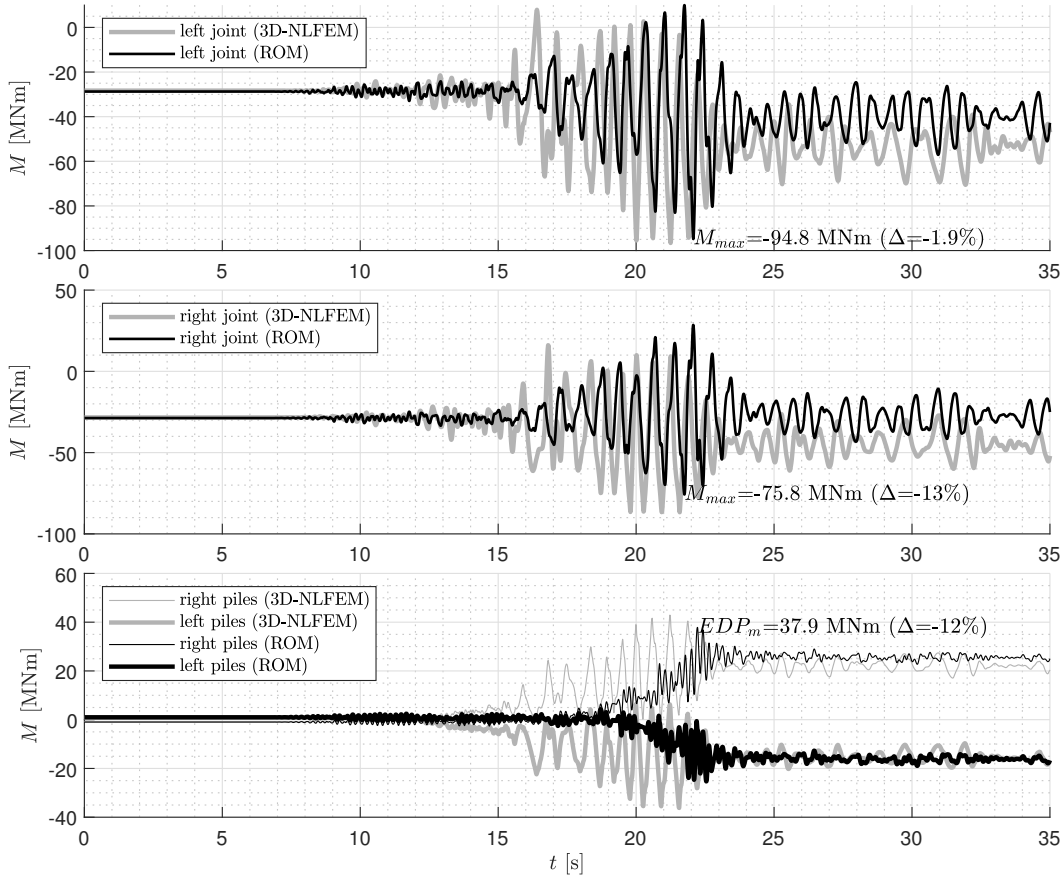


**Figure 4.14.** Bending moments time histories confrontation for *Yamakoshi* ground motion.

Despite the fundamental differences between the ROM model and the 3D-NLFEM model<sup>3</sup> both exhibit a substantially similar response. At least with respect to these global system quantities.

<sup>3</sup>The two models compared are quite different in terms of their approach to soil-structure interaction analysis:

- ROM: two-dimensional discrete soil-structure interaction with nonlinear Winkler springs.
- 3D-NLFEM: three-dimensional continuous with elasto-plastic constitutive law with hardening designed specifically to describe nonlinear soil behavior.

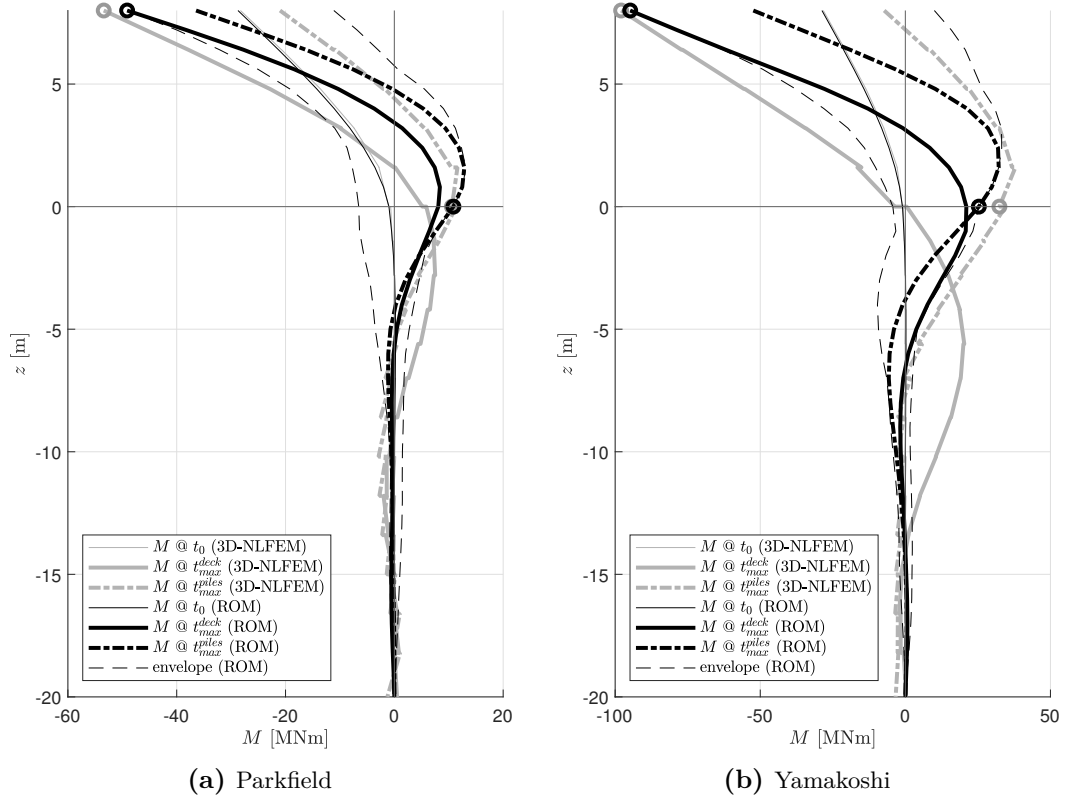


**Figure 4.15.** Bending moments diagrams confrontation at left piles-abutment alignment.

Also in terms the bending moments diagrams on the left alignment<sup>4</sup>, as it can be seen in figure 4.15, the distribution of the bending moments is similar for both models. Bending moment diagrams are extrapolated for the end of the static stages ( $t = t_0$ ), for the instant in which the bending moment at deck-abutment joint is maximum ( $t = t_{\max}^{\text{deck}}$ ) and when the bending moment at piles head is maximum ( $t = t_{\max}^{\text{piles}}$ ).

## 4.7 Conclusions

The simplified model described in chapter 3 has been validated through a systematic comparison with the higher-order method, through the development of a large three-dimensional continuous domain including both the soil and the structure. Despite the large differences in complexity, the seismic responses provided by the two models were seen to be in a good agreement. The two models showed a comparable modal response, and a similar temporal variation in the internal forces when subjected to two very different seismic motions. Minor discrepancies, related to the instantaneous distribution of the internal forces the pile-abutment system, appeared to be related to the discontinuous representation of the soil in the simplified model. In fact the

<sup>4</sup>*Alignment* is the set of the abutment and the corresponding row of piles. Necessarily each model have at least two alignments, the left one (characterized by the negative  $x$ , always if the origin of the axes is located in correspondence of the centerline of the deck) and the right one (for the positive  $x$ ).

---

major difference between the two discretization methods lie in the interface elements used in the simplified model.



## Chapter 5

# Static models for design purposes

The development of simplified models for the design of integral bridges has been carried out within the larger scope of the structural Eurocodes<sup>1</sup> revision, and in particular of Eurocode 8 Part 2 (CEN, 2022 [4]).

The design of integral bridges is challenging due to soil-structure interaction. Simplified models which can nonetheless capture the fundamental aspects of the behavior of such structures subjected to a seismic action, play a fundamental role. Therefore, in this thesis, further simplified models have been developed, in particular static models.

The confidence in the discrete dynamic model proposed in this thesis comes from the positive results (albeit limited to the single case of the *Gatteo* overpass) of the comparison with the continuous three-dimensional nonlinear finite element model (see chapter 4). For this reason two static models are derived and calibrated by taking the dynamic model from chapter 3 as a reference (figure 5.1):

- *Non-Linear Static Model (NLSM)*: uses the same inelastic soil-structure interface elements discussed earlier (see section 3.2) to account for soil behavior in the active, but more importantly, passive state. In the language of Eurocode 8, this model is appropriate for use in a displacement-based approach, i.e., used for Non-Linear Static Analysis (NLSA).
- *Linear Static Model (LSM)*: this model is further simplified, with respect to the previous one, and soil pressure on the structure (in particular on the abutments) is not exerted by nonlinear interface elements but, rather, applied as a deformation-dependent load (which makes the linear analysis iterative). Again, according to Eurocode 8, this model is intended for use in a more

---

<sup>1</sup>*Eurocodes* are constructions structural codes in Europe. Eurocode 8 (EN 1998) is relative to seismic-resistant constructions. The first generation Eurocodes have been drafted starting in the 1990s and have been published in the early 2000s (for instance, EN1998-2, Part 2 of Eurocode 8, devoted to seismic design of bridges, has been released in 2005 [2]). The European Commission has asked the European Standardization Committee (CEN) to revise the structural Eurocodes with mandate M515. The multi-year project started in 2015 and is about to end at the time of writing this thesis.

traditional force-based approach, i.e., used in Elastic Linear Static Analysis (ELSA).

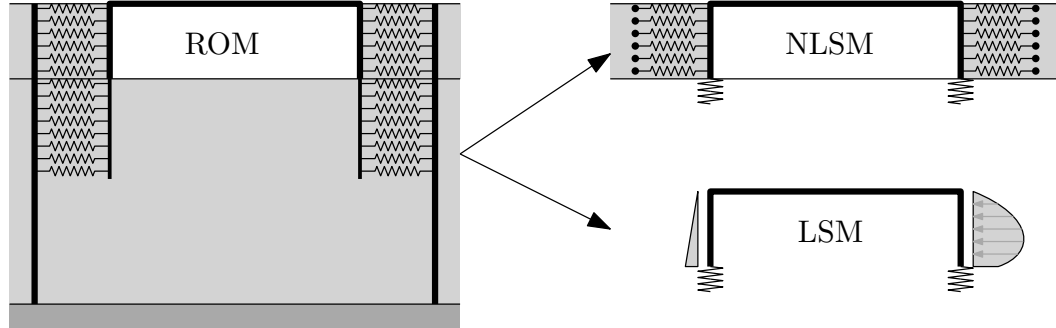


**Figure 5.1.** Static models derived from the nonlinear dynamic one. Non-Linear Static Model (NLSM) and Linear Static Model (LSM).

The static models described in the following sections (sections 5.1 and 5.2) approximate the behavior of integral bridges with frame and embedded abutments (see figure 1.2) in the longitudinal direction (along  $x$ ). These models are also, consistently, not capable of capturing the behavior of bridges with a skew angle such that it can only be described by three-dimensional models<sup>2</sup>.

Finally, as a further simplification, both models focus on the response of the structure alone, modeling the foundations with equivalent impedances. The forces in the latter can then be used to design the foundation (they provide the inertial SSI effects, to be superimposed with the kinematic ones, if relevant)

## 5.1 Non-linear static model

In this model the non-linearity is concentrated in the interface elements between soil and structure (column elements are not present and structure elements are modeled as linear since, as a design goal, structural elements should remain essentially elastic for the design seismic action).

The concept behind this model is that the bridge, due to the inertia forces, displaces leaning against the embankment. Owing to the relative smaller displacements of the embankments when compared to those of the structure, the soil-end of the interface elements can be fixed resulting in a model without the soil columns<sup>3</sup>. Stress resultants on the structure are calculated as a result of the deformations of the bridge and the interface soil elements.

<sup>2</sup>These models are applicable for Integral Abutment Bridges with skew angles lower than about 20°, based on the results from the 3D model shown in section 3.10.

<sup>3</sup>In reality the soil column nodes, which represents the embankment, have displacements given by the deformation of the soil column in the "structural" mode. However, it has been seen that, in the case study considered, this displacement is negligible compared to the displacement of the structure when they are taken as relative to the  $z = 0$  reference (the model is truncated with foundations modeled through static impedances). In the benchmark case considered, for the forth mode (i.e. the first "structural" mode), the embankment drift is an order of magnitude less than the abutment one (see forth mode shape in figure 3.32).

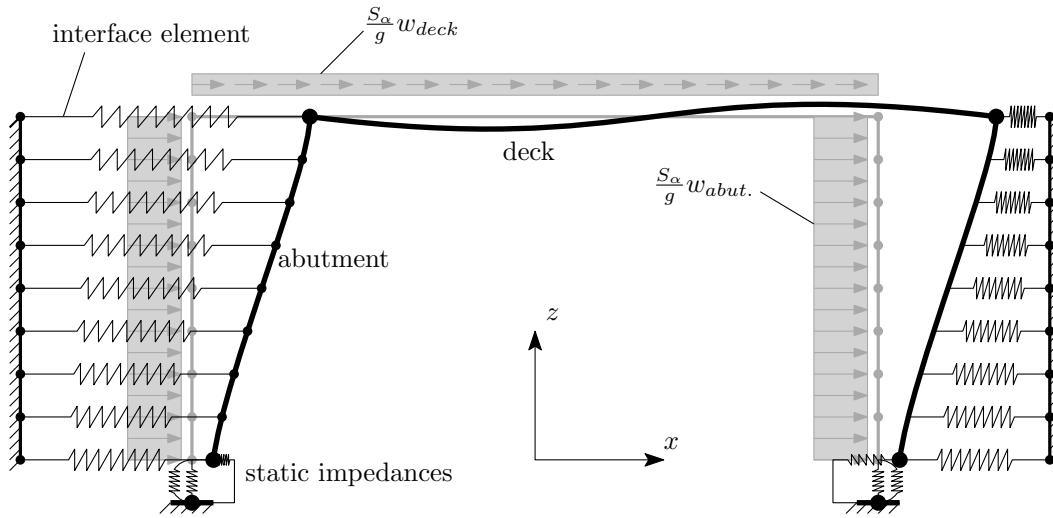


**Figure 5.2.** Non-Linear Static model.

The non-linear static model is closer to the nature of the system under consideration, in fact the soil-structure interaction, in this type of structures, is essentially a problem of displacements imposed on the foundation by the surrounding soil and by the deformation of the abutments against the embankments.

### 5.1.1 Static impedances

Given the displacement-dependence of the earth pressure on the abutments, the foundation flexibility needs to be accounted for to derive an accurate distribution, among backfill and foundations, of reactions to the inertia forces on the structure. Foundations are therefore modeled by means of equivalent static impedances. The evaluation of these impedances through the reactions caused by unit displacements imposed at the pile head calculated using only the pile portion of the full model (negative  $z$ ) would give the closest approximation of the dynamic model. This approach, however, involves the setup of the full model (even for just one pile) and this would imply an effort that contradicts the very idea of a simplified model. For this reason, impedances were instead taken from the literature, and in particular, from the current draft of second generation Eurocode 8 Part 5 [4], as it is expected that a designer would do in practical application. Static impedances of a single foundation pile (figure 5.3a), are given for a constant stiffness ( $E_s = \text{const}$ ) profile as (figure 5.3b):

$$K_{HH} \simeq E_s d \left( \frac{E_p}{E_s} \right)^{0.20} \quad (5.1)$$

$$K_{MM} \simeq 0.15 E_s d^3 \left( \frac{E_p}{E_s} \right)^{0.75} \quad (5.2)$$

$$K_{MH} = K_{HM} \simeq -0.22 E_s d^2 \left( \frac{E_p}{E_s} \right)^{0.50} \quad (5.3)$$

where  $K_{HH}$  is the pile horizontal stiffness,  $K_{MM}$  the flexural stiffness, and  $K_{MH} = K_{HM}$  the stiffness of the two coupled degrees of freedom (rocking).  $E_s$  is the Young's

modulus of the soil,  $E_p$  that of the pile, and  $d$  the diameter of the pile. In a first approximation the vertical static impedance can be taken as the piles axial stiffness

$$K_{VV} = n_p \frac{E_p A_p}{L_p} \quad (5.4)$$

where  $n_p$  is the number of piles under the abutment. This approximation is not suited for friction piles.

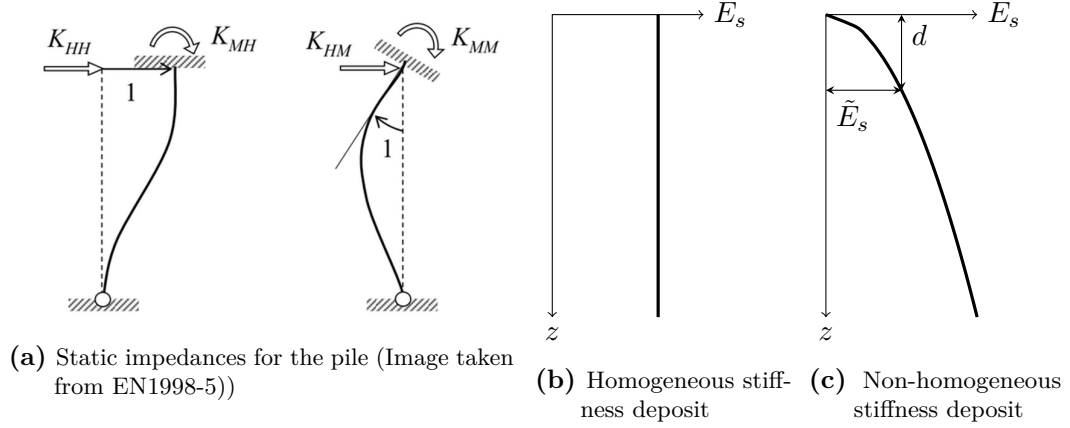


**Figure 5.3.** Single pile static impedances definition and soil stiffness analytical descriptions.

For non-constant stiffness profiles, stiffness values can be found in the work of Gazetas [51] and are equal to (for a nonlinear increase of soil modulus according to  $E_s = \tilde{E}_s \sqrt{\frac{z}{d}}$  where  $z$  is the depth as illustrated in figure 5.3c):

$$K_{HH} \simeq 0.8 \tilde{E}_s d \left( \frac{E_p}{\tilde{E}_s} \right)^{0.28} \quad (5.5)$$

$$K_{MM} \simeq 0.15 \tilde{E}_s d^3 \left( \frac{E_p}{\tilde{E}_s} \right)^{0.77} \quad (5.6)$$

$$K_{MH} = K_{HM} \simeq -0.24 \tilde{E}_s d^2 \left( \frac{E_p}{\tilde{E}_s} \right)^{0.53} \quad (5.7)$$

The limitations of considering these approximate impedances' expressions lie both in the fact that: a) in general they only approximately correspond to the actual stiffness variation of the real stratigraphic profile of the deposit, through simplified analytical variations; b) they do not depend on frequency.

Finally another important limitation is that group effects are not considered. In fact, static impedances are simply multiplied by the piles number  $n_p$  to obtain group impedances.

Obviously, having reduced a dynamic problem to a static one, the inertia forces on the bridge must be explicitly included<sup>4</sup>. The acceleration acting on the bridge, for design purposes, is taken to be equal to the plateau value of the spectral acceleration.

<sup>4</sup>This approach has been known since 1743 (*Traité de dynamique* by Jean Baptiste Le Rond d'Alembert) and is often referred to as *D'Alembert's principle*.



This assumption is further justified in the following section 5.1.2. The use of spectral ordinates to characterize the seismic action appears adequate based on the earlier verification of its correlation with response quantities of interest in section 3.7.

More details on the static impedances evaluation and the comparison with the ROM model response, are discussed in section 5.3.1 with reference to a validation example.

### 5.1.2 Acceleration of the structural masses

As previously shown in section 3.6.1, the structure is mostly deformed by the first "structural" mode of the complete soil-bridge system. More details on the frequency content of the system response are discussed in section 3.6.2. Based only on the definition of simplified static models it is not possible to obtain the correct value of the vibration period of the structural mode (which is the period for which  $S_a(T)$  is to be evaluated by the response spectrum of the signal amplified by the deposit). In the sample cases considered for the model validation (the *Gatteo* overpass described in section 4.2) and for seismic risk assessment (the three span overpasses described in section 6.2.1) the period of the first "structural" mode, turns out to be always low (between 0.15 and 0.2 seconds), systematically larger than  $T_B$ . The plateau acceleration  $S_\alpha$  is thus conservatively proposed as an approximation in a codified design procedure, as shown in figure 5.4.

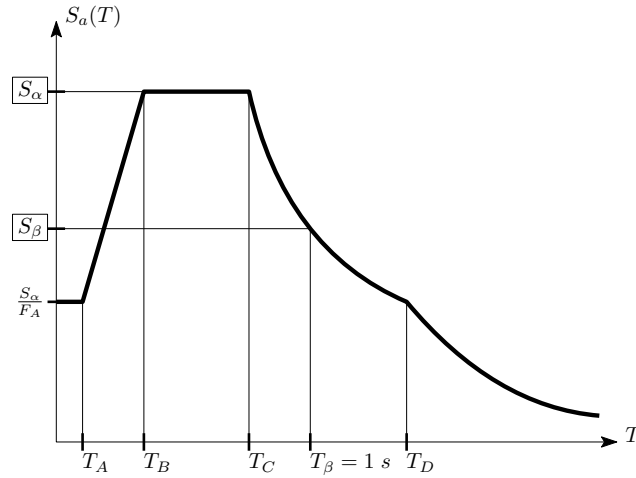


**Figure 5.4.** Spectral acceleration spectrum, as parametrized in the second generation Eurocode 8 [4].

The parameters of the response spectrum are  $S_\alpha$  and  $S_\beta$ ; more details on the values of  $F_A$ ,  $T_A$ ,  $T_B$ ,  $T_C$  and  $T_D$  are given in the Eurocode 8 Part 1 [4, par. 5.2.2.2].

## 5.2 Linear static model

The linear static model includes only the structural elements and the foundation static impedances described in section 5.1.1. Soil-structure interaction at the abutment walls is taken into account through appropriate pressure distributions on the

abutments. Inertia forces on the structure are modeled as in the non-linear static model.

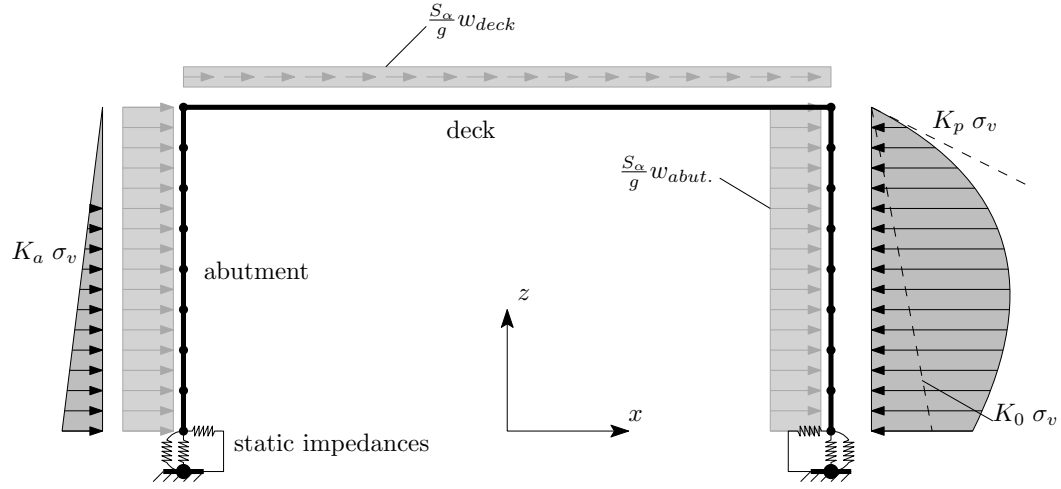


**Figure 5.5.** Linear Static Model (LSM).

Due to the generally modest spans these bridges have, the motion of the soil-column masses can be considered the same on both sides. Therefore, while the structure deforms in one direction, on one side the soil pressure attains the active limit (where the abutment moves "away" from the deposit) and on the other side it tends to the passive limit (where the abutment goes "towards" the deposit). The displacement threshold for which the passive limit is reached is greater<sup>5</sup> than the threshold for active one. The longitudinal deformation (along  $x$ ) of the bridge with respect to the embankment, is thus generally not large enough to mobilize the full passive pressure over the entire abutment height.

Therefore, in the instant of maximum displacement (relative to the embankment), one abutment will be subject to the soil active pressure (the left abutment in figure 5.5) while the other will be subject to a pressure distribution that depends on the characteristics of the backfill embankment soil and on the displacement<sup>6</sup> of the abutment (the right one in figure 5.5).

The pressure distribution will be intermediate between the at-rest and the passive conditions, and can be expressed, e.g., as:

$$\sigma_{p,mob}(z) = \left[ K_0 + (K_P - K_0) \frac{u(z)}{a z + u(z)} \right] \gamma z \quad (5.8)$$

where  $K_0$  is the at-rest pressure coefficient,  $K_P$  the passive pressure coefficient,  $u(z)$  is the abutment displacement in  $x$  direction at depth  $z$  from the deck level (note

<sup>5</sup>The deformation threshold for which the passive condition is activated is about 100 times the corresponding one for the active state. Using the Callisto et al. [96] theory, instead of Rankine's one, the passive deformations threshold is greater than the active one (always with the same order of magnitude).

<sup>6</sup>Displacement always intended as relative between the abutment and the soil column. Since, in this model, the soil column is not explicitly considered, in this case it is simply the displacement of the model

this is a different convention from that adopted so for the dynamic model) and  $a$  is a non-dimensional soil-dependent parameter<sup>7</sup> that account for adhesion between soil and wall, which is described in [42].

Due to the fact that the displacement profile of the abutment  $u(z)$  is not known in advance, an iterative method is necessary. As a first approximation a linear trend can be used for the evaluation of the abutment displacements  $u(z)$ . This approximation is more legitimate the stiffer the abutment is compared to the embankment.

### 5.3 Comparison with the non-linear dynamic model on the *Gatteo* case

This section compares the results of the static models with the reference ones from the non-linear dynamic model described in chapter 3. All results refer to the *Gatteo* overpass already used in chapter 4.

#### 5.3.1 Evaluation of static impedances

Table 5.1 reports static impedances calculated: a) using the truncated finite element model (using only piles elements and soil elements with  $z \leq 0$ ); b) Eurocode 8 part 5 formulas; c) Gazetas formulas for nonlinear soil stiffness profile described previously. The FEM model and the parameters are the ones from the *Gatteo* sample model (see section 4.2).

**Table 5.1.** Comparison between FEM-, Gazetas- and Eurocode-calculated static impedances for *Gatteo* overpass described in section 4.2. Nonlinear function for soil elastic modulus is fitted on the benchmark case soil profile. Units are expressed in kN, m and radians ( $E_p = 30GPa$ ,  $d = 1.2m$ ,  $n_p = 7$ ,  $E_s = 0.34GPa$ ,  $E_s^* = 0.0215GPa$ ).

Model	$K_{HH}$	$K_{MM}$	$K_{HM}$
Constant (prEN1998-5:2022)	$7.00 \times 10^6$	$1.78 \times 10^7$	$-7.08 \times 10^6$
Linear (prEN1998-5:2022)	$1.37 \times 10^6$	$1.28 \times 10^7$	$-5.42 \times 10^6$
Gazetas ( $\tilde{E}_s = 1.2 \times 10^5 kPa$ )	$3.79 \times 10^6$	$1.53 \times 10^7$	$-5.42 \times 10^6$
FEM	$1.81 \times 10^6$	$1.27 \times 10^7$	$-3.43 \times 10^6$

Table 5.1 shows that the static impedances obtained from Gazetas are closer to the result obtained with the finite element model. The stiffness profile of the soil has been fitted with that of the case study of the *Gatteo* overpass, as shown in the figure 5.6.

<sup>7</sup>In first approximation equal to 0.1 for loose soil and 0.01 for firm soil.

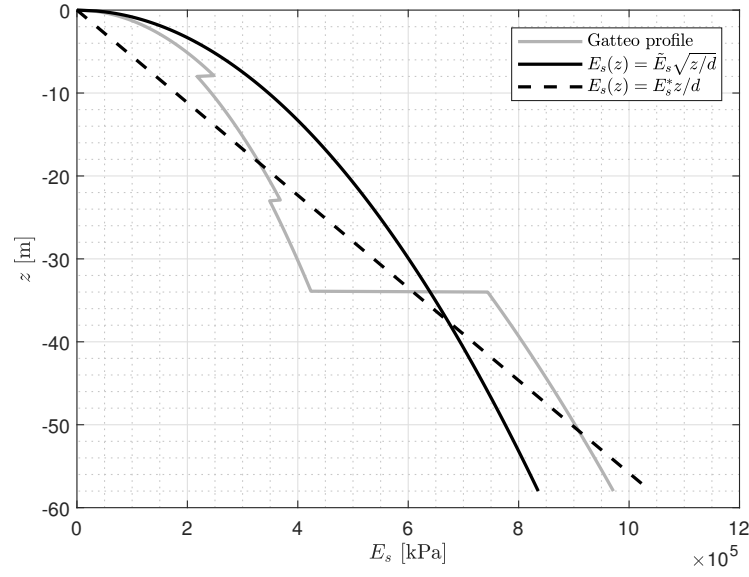


**Figure 5.6.** Soil stiffness profiles, for linear and Gazetas [51], fitted to the *Gatteo* benchmark case ( $E_s^* = 2.15 \times 10^4 \text{ kPa}$  and  $\tilde{E}_s = 1.2 \times 10^5 \text{ kPa}$ ). Soil Poisson constant is taken equal to 0.1.

### 5.3.2 Seismic actions (equivalent lateral forces)

The ground motion used is the one represented in the figure 5.7 and is a natural signal (recording of the *Colfiorito* earthquake) scaled to have a PGA equal to 0.25 g. Figure 5.7 shows the response spectra for bedrock (equal to the outcrop) and the surface ground motion.

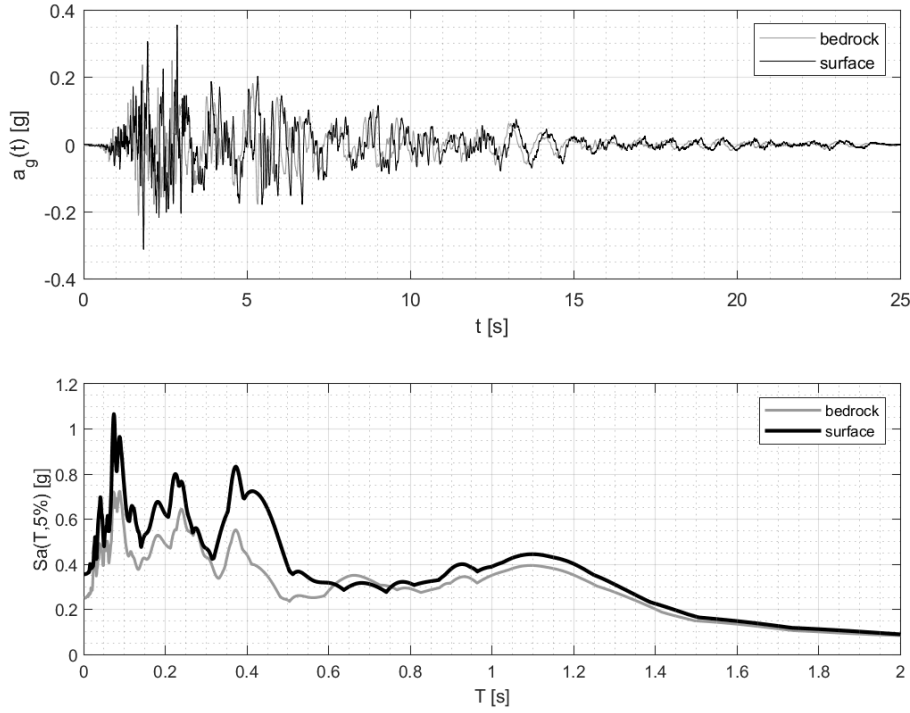


**Figure 5.7.** Time series and spectra of the bedrock and the surface ground motion.

The period of the first "structural" mode is about 0.18 s and the corresponding spectral acceleration is equal to  $S_a(0.18s, 5\%) = 0.63$  g. With the data from the *Gatteo* overpass (see section 4.2) the resultant of the inertia forces during the earthquake is equal to  $m \cdot S_a = 13\,229$  kN. These forces are applied as if the acceleration is uniform, so the structural elements have distributed load proportional to their weight per unit length. More details on the frequency content of the system response are discussed in section 3.6.2.

The loads considered during the static stages are the same as defined in section 3.4 for the dynamic model, on the structural elements only (deck and abutments). Figure 5.8 shows the deck loads used for construction stages and the uniform distributed inertia loads due to seismic actions.

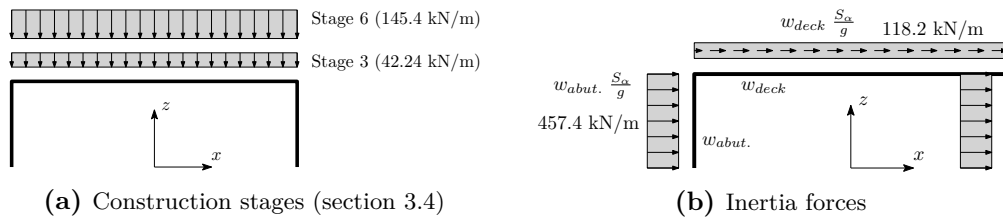


**Figure 5.8.** Loads for both static models (non-linear and linear) for the ground motion displayed in Figure 5.7.

### 5.3.3 Results

Figure 5.9 shows the results, in terms of bending moments, of the non-linear and the linear static models.

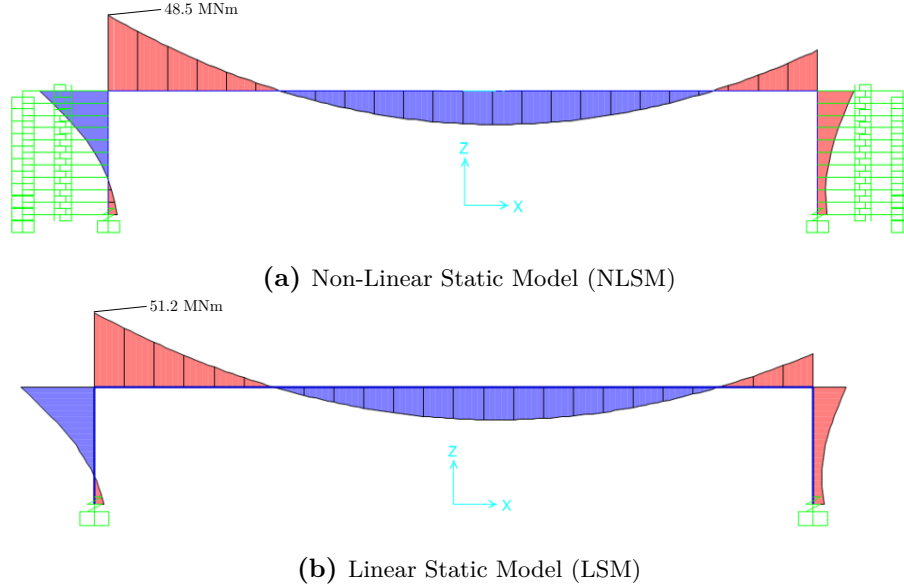


**Figure 5.9.** Results in terms of bending moments of the static models. Analysis are done with the commercial software SAP2000.

Considering that, for the signal considered, the dynamic model presents a maximum bending moment in the left deck-abutment node equal to 45 MNm, the result of the non-linear static analysis is in good agreement.

In this particular case the bending moment at the left deck-abutment joint is higher in the static analysis than in the dynamic one, and this is in favor of safety. Elastic linear model presents also a higher bending moment (in favor of safety). It should also be noted that, again in this case, the bending moment in the most stressed section is also higher than in the static non-linear case (48.5 MNm). This is consistent with the fact that a coarser modeling, in general, should return a higher value of the actions in favor of safety.

Figure 5.10 shows the results, in terms of earth pressures, of the non-linear and the linear static models.

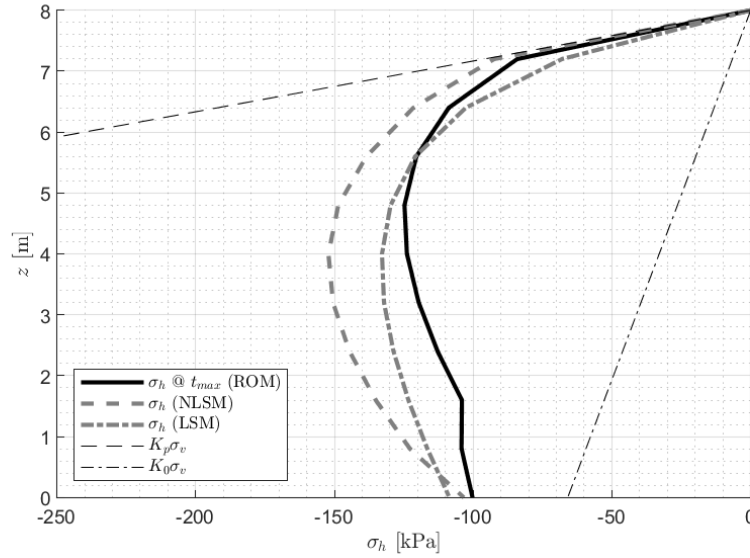


**Figure 5.10.** Soil pressures on the "passive side" abutment (the one on the right in figure 5.5) compared to the ROM soil pressure results (for the instant  $t_{\max}$  where the bending moment on the top abutment cross section at its maximum).

The trend of the contact pressures between the soil and the structure confirms how the passive stress is not mobilized along the whole height of the abutment (in this case the passive limit is high due to the passive coefficient defined by the theory of Callisto et. al [96]). As highlighted also in the literature, considering the soil pressure at its maximum value (passive stress mobilized along the whole abutment height) in general does not coincide with the condition of maximum bending moment on the structure.

## 5.4 Parametric study

After a first comparison of predictions of the static methods with those of the dynamic model for the single case-study of the Gatteo overpass.

In order to further support the validity of the proposed models, a parametric analysis was performed to cover a representative range of applications. The parameters varied are the number of spans, the soil profile, the main span<sup>8</sup> length  $L$  and the abutment height  $H$ . All cases considered are shown in table 5.2 .

Figure 5.11 show the 24 cases in table 5.2 .

Soil profiles are the same used for seismic risk analysis for the sites of Milano, Napoli and L'Aquila described in chapter 6, taken as representative of low, moderate, and high seismicity, respectively.

The seismic ground motions used in the analyses were selected based on their compatibility with the Italian code spectra at each of the three sites. The acceleration

<sup>8</sup>For two- and three-span bridges, all spans are determined one the main span is assigned under the assumptions that spans are equal on the two-span case and side spans have length  $0.5 L$  for the three-span case.

**Table 5.2.** Cases considered for the parametric study. Soil deposit profile for Milano is indicated with number 1, Napoli with number 2 and L'Aquila with number 3.

case	span n.	soil	$L$ [m]	$H$ [m]
01	1	1	50	8
02	1	1	50	5
03	1	1	38	8
04	1	1	38	5
05	1	2	50	8
06	1	2	50	5
07	1	2	38	8
08	1	2	38	5
09	1	3	50	8
10	1	3	50	5
11	1	3	38	8
12	1	3	38	5
13	3	1	50	8
14	3	1	50	5
15	3	1	38	8
16	3	1	38	5
17	3	2	50	8
18	3	2	50	5
19	3	2	38	8
20	3	2	38	5
21	3	3	50	8
22	3	3	50	5
23	3	3	38	8
24	3	3	38	5

spectra<sup>9</sup> of the selected GMs, together with their average spectrum, are compared to the code target spectrum in figure 5.12. The code spectra refer to a return period  $T_R$  of 975 years, appropriate for highway overpasses, on rock (soil A according to Eurocodes classification).

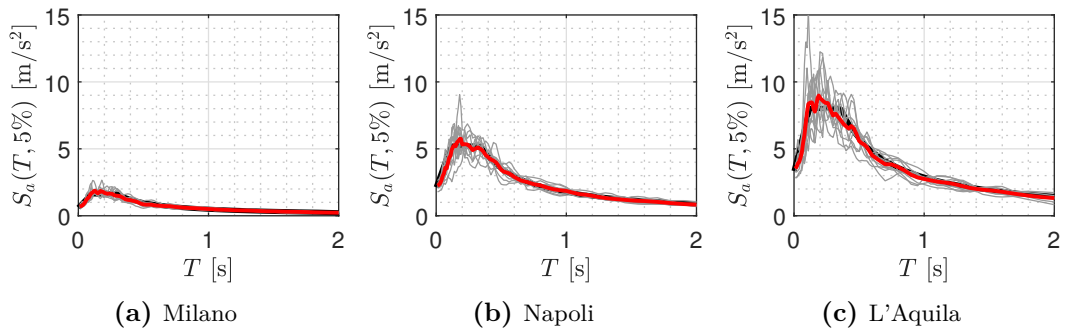


**Figure 5.12.** Selected signals spectra for the three sites (three seismic intensities considered).

<sup>9</sup>Acceleration spectra calculated for a critical damping ratio  $\zeta = 5\%$ .



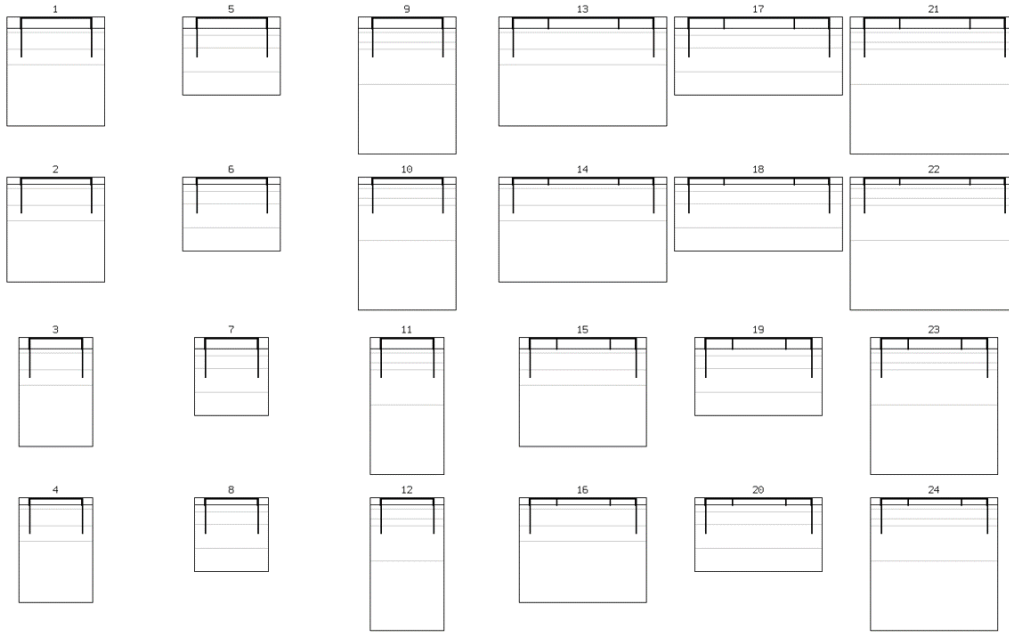


**Figure 5.11.** Cases considered for the parametric study

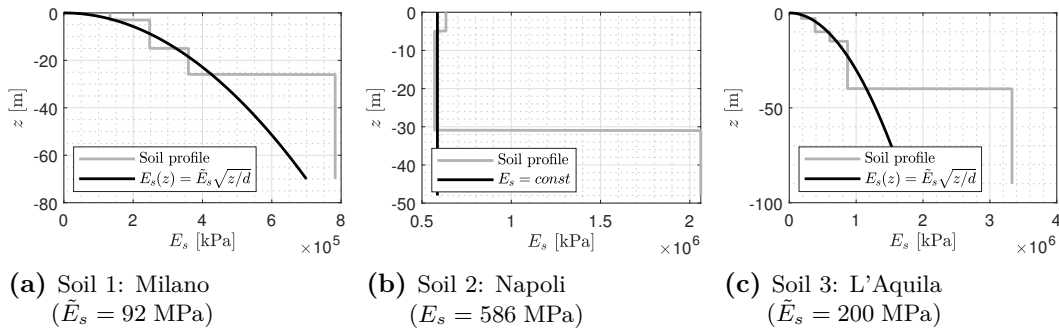


**Figure 5.13.** Soil profiles and fitted impedances profiles (black) for the three soil profiles (gray).

For the definition of the static impedances for the static models (NLSM and LSM), the parabolic profiles for soils 1 and 3 and the constant profile for soil 2 were taken; as shown in Figure 5.13. Note that the impedance profiles (in black) are fitted only in the shallow part of the profile; for a depth equal to the piles length  $L_p$ .

Table 5.3 lists the values of the plateau acceleration  $S_\alpha$ . The first row reports  $S_{\alpha, \text{bedrock}}$ , which is the value on rock/stiff soil, i.e., the value from the target spectra used in GM selection. The remaining three rows report the average of the spectral acceleration values obtained after site response analysis for each of the selected GM. The average is performed over the range of periods  $[T_B, T_C]$  of the target code spectrum, and it is thus the best estimate of  $S_\alpha$  at the surface, i.e., the value to be used for static analysis (both linear and non-linear). Each entry in Table 5.3 correspond to a combination of soil profile and site seismicity. Bold values on the main diagonal represent cases where seismicity and profile are from the same site (Milano, Napoli, L'Aquila). Off-diagonal cases are added to increase the number of explored combinations. Overall, a total of 3 seismicity for 24 bridges (for 1 static

**Table 5.3.** Plateau acceleration for the three sites considered and after the site-response analysis.

site:	MI	NA	AQ
$S_{\alpha, \text{bedrock}}$	0.17 g	0.53 g	0.82 g
soil 1 (MI)	<b>0.31</b> g	0.99 g	1.49 g
soil 2 (NA)	0.21 g	<b>0.71</b> g	1.17 g
soil 3 (AQ)	0.29 g	0.99 g	<b>1.56</b> g

linear, 1 static non-linear, 7 nonlinear dynamic and 1 modal analyses) lead to a total of 720 analyses.

Figure 5.14 shows the vibration periods of the first 10 modes for the one- and three-span cases. As it can be seen, apart from the period of the first mode, all others fall within the  $[T_B, T_C]$  range of periods at which plateau acceleration occurs for the target spectra used in input ground motions selection (i.e.  $T_i \in [0.1s, 0.35s]$   $i = 2, 3, 4, 5$ ). This corroborates the proposal of using  $S_{\alpha}$  in the static methods.

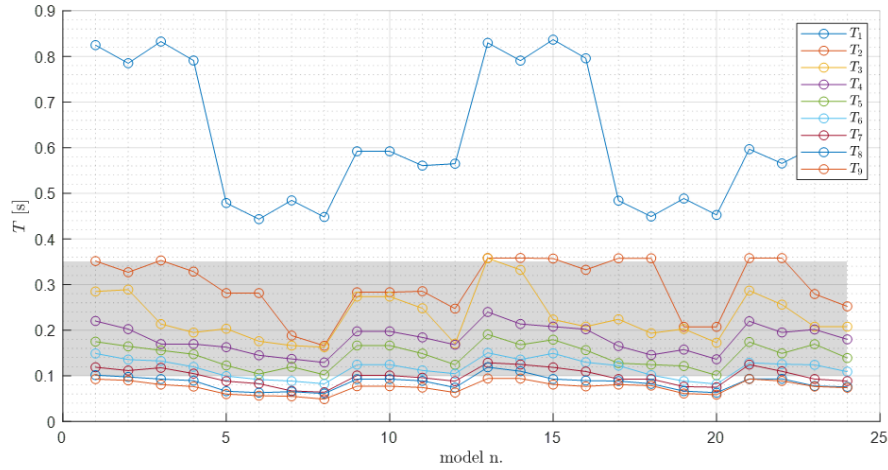
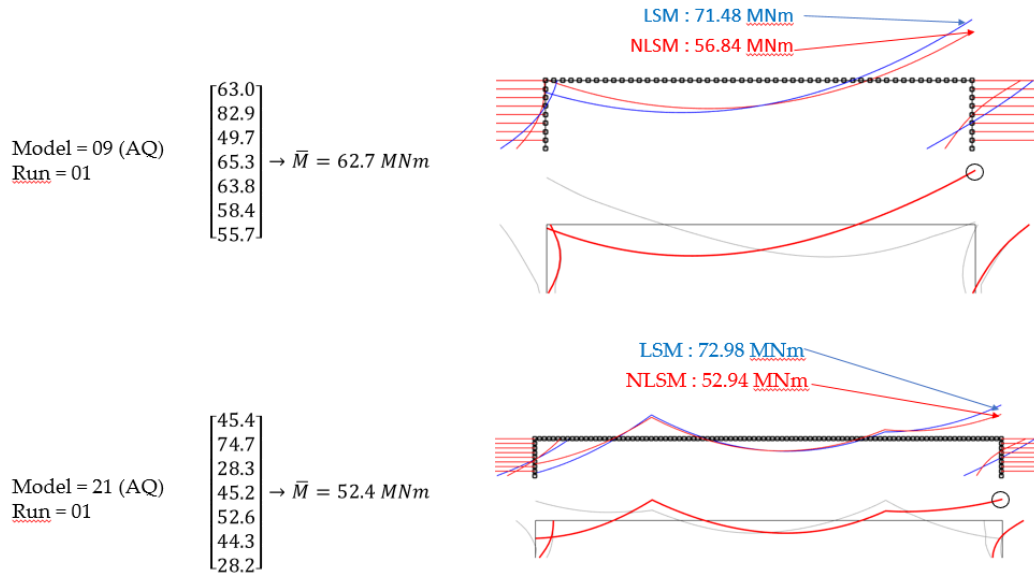
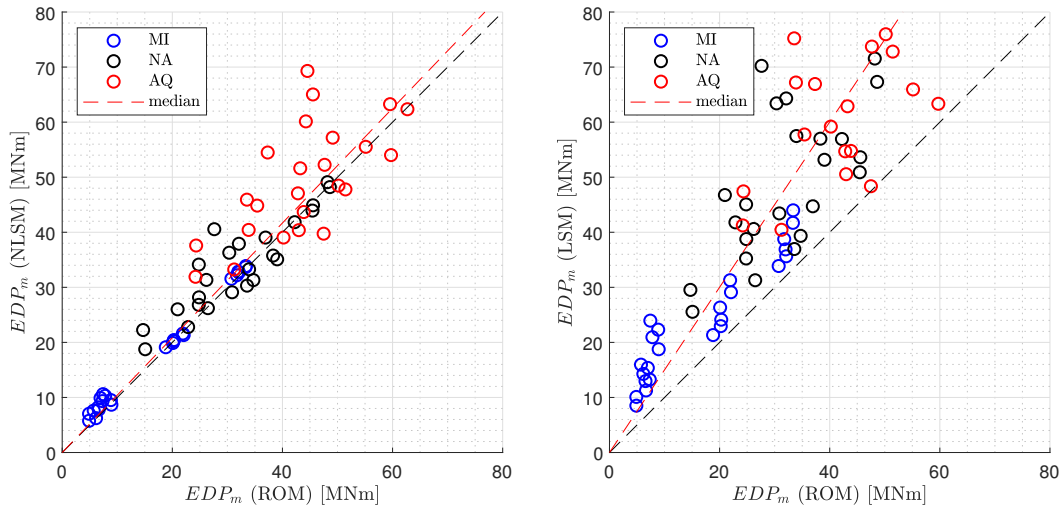
**Figure 5.14.** Vibration periods for the cases listed in table 5.2. Plateau range of periods is indicated with shaded area.

Figure 5.15 shows the average over the 7 GMs of the results in terms of maximum bending moment  $EDP_m$  for the ROM model and the corresponding results for the NLSM and LSM; for both the single- and three-span overpasses.



**Figure 5.15.** Maximum bending moments and diagrams for the ROM and static models (NLSM and LSM).

Figure 5.16 shows the relationships between the maximum bending moment at deck-abutment joint (denoted  $EDP_m$ ) obtained using the dynamic model (ROM) and static models (NLSM for the nonlinear static model and LSM for the linear model) over all cases. The figure shows on the abscissae the ROM results and, on the ordinates, those computed via static models. The 1:1 line indicates a perfect agreement.



**Figure 5.16.**  $EDP_m$  comparison in terms of bending moment at deck-abutments joints between non-linear dynamic model (ROM) and static models (NLSM and LSM).

As it can be seen from the figure 5.16 there is a good match between NLSM and ROM. The match is slightly worse for the LSM, however the median is on the safe

side of the figure<sup>10</sup>.

As for the bending moment at the piles head (at the lower abutment cross-section), the match is slightly worse, as shown in figure 5.17. The bending moments at the piles head are higher compared to those calculated with ROM. This higher degree of conservatism can be attributed to the approximate nature of the foundation impedances. In fact, if the whole system were modeled, nonlinear static analysis would yield to the impedance values obtained by the ROM model.

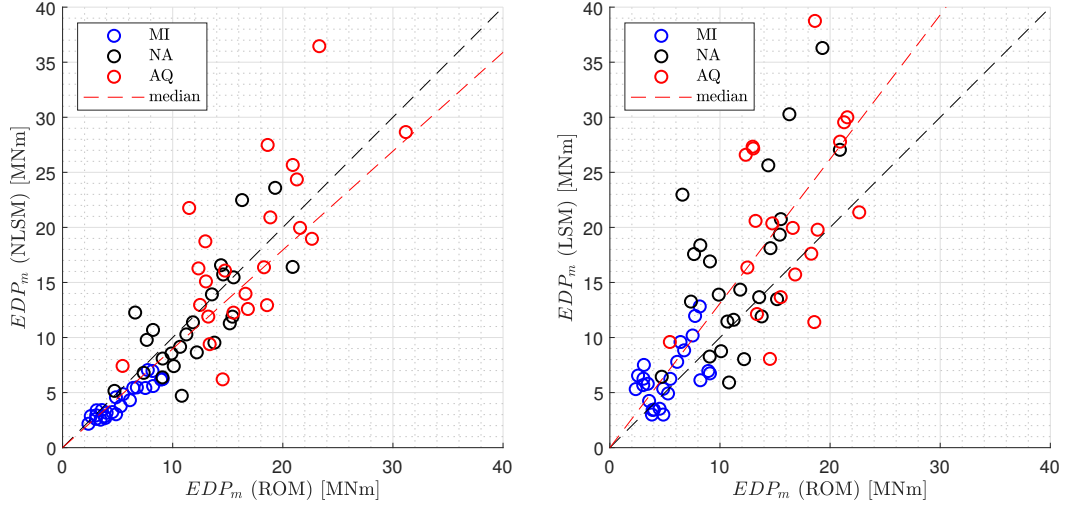


**Figure 5.17.**  $EDP_m$  comparison in terms of bending moment at piles head between non-linear dynamic model (ROM) and static models (NLSM and LSM).

Table 5.4 shows the statistical parameters of the ratio  $\frac{EDP_m^{\text{static model}}}{EDP_m^{\text{dynamic model}}}$ . In this table  $CV$  is the coefficient of variation  $CV_X = \frac{\sqrt{Var[X]}}{E[X]}$ , where  $X$  is a random variable,  $E[X]$  its expected value (first moment) and  $Var[X]$  its variance (second moment); the correlation is calculated by the Pearson correlation coefficient described in section 3.7.3.

**Table 5.4.** Statistics of the parametric analysis results in terms of  $\frac{EDP_m^{\text{static model}}}{EDP_m^{\text{dynamic model}}}$  ratio and correlation coefficient.

model	section	median	$CV$	correlation
NLSM	joints	0.97	0.13	0.96
NLSM	piles	1.29	0.43	0.88
LSM	joints	1.17	0.22	0.91
LSM	piles	1.90	0.47	0.83

<sup>10</sup>The linear static model (LSM) gives results, in terms of maximum moment at the joints, which are, on average, higher than ROM ones and this is in favor of safety

## Chapter 6

# Probabilistic seismic risk assessment

Risk  $R$  is most commonly defined as the product of the *probability of failure*<sup>1</sup>  $P_f$  and the *cost*<sup>2</sup>  $C_f$  of such failure [86].

$$R = P_f C_f \quad (6.1)$$

*Seismic risk*, however, is somewhat inconsistently defined, in the earthquake engineering literature, as the probability of failure  $P_f$ , not considering the cost. This latter definition is adopted in the following.

The risk analyses were carried out within the RINTC-p project<sup>3</sup> [63].

A three-span integral abutment overpass was designed at three Italian sites considered in the project (Milano, Napoli and L'Aquila, ordered by increasing seismic hazard as can be seen in figure 6.1 and in table 6.1), using the code-like force-based approach presented in chapter 5, and then analyzed with the three-dimensional dynamic model described in chapter 3.

---

<sup>1</sup>*Failure* is intended as exceeding a certain limit state. In this case, therefore, the failure may not coincide with the collapse (partial or total) of the structure.

<sup>2</sup>*Cost* often indicated simply in economic terms, or in terms of human lives.

<sup>3</sup>This study has been carried out within the ReLUIS-DPC 2019-2021 research program, funded by the Italian Department of Civil Protection.

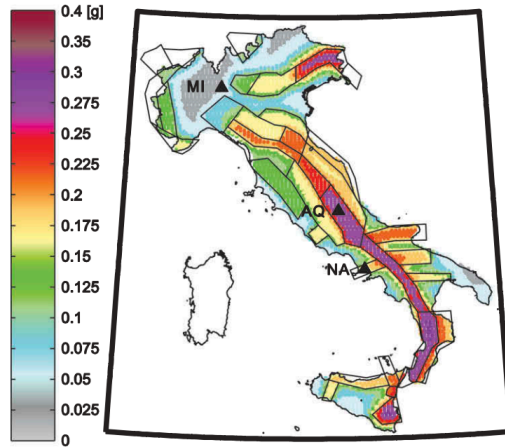


**Figure 6.1.** Italian seismic source zones and official hazard map in terms of PGA with 475-year return period of exceedance on rock. Sites taken for the risk analysis are shown (Milano (MI), Napoli (NA) and L'Aquila (AQ)) are highlighted. (Image taken from *Iervolino, Spillatura, Bazurro (2018)* [64])

**Table 6.1.** General data for the three sites in the Italian territory. These sites are representative, respectively, of low, medium and high seismic intensity. PGA is evaluated for A-type soil and a return period of 475 years.

Site	Lat.	Lon.	PGA
Milano (MI)	45.47	9.19	0.05 g
Napoli (NA)	40.85	14.17	0.17 g
L'Aquila (AQ)	42.35	13.40	0.26 g

The IAB considered has three-span with steel-concrete deck with a total 76 m span (19+38+19 m) and simply supported intermediate piers (as can be seen in figure 6.2). The deck is simply supported by the two intermediate piers and the abutments have a height of 7 meters. The archetype for this structure has been taken from the case study in Torricelli et al. (2012) [44] who carried out a research work within a wider project concerning the design of overpasses on the Italian territory commissioned by SPEA<sup>4</sup>. The overall geometrical properties and the deck cross-section was taken as reference for members sections design. Design in three Italian sites was carried out for the life-safe limit state considering seismic actions with a return period of 950 years (i.e. with an exceeding probability of 10% in 100 years).

<sup>4</sup>SPEA *Ingegneria Europea*, then partner of the major National highway concessionaire, *Autostrade per l'Italia*, dedicated a special attention to research and implementation of innovative structural solutions for short and medium span flyovers, aimed at minimizing both initial and maintenance costs.



Tables 6.2, 6.3 and 6.4 show the geometric and mechanical properties of the soil deposits for the three sites. Where  $h$  is the layer thickness,  $\gamma$  is the specific weight,  $\phi'$  the friction angle,  $c'$  the cohesion,  $V_{s0,m}$  the average initial shear wave velocity, and  $G_{0,m}$  the average initial shear modulus.

**Table 6.2.** Soil deposit model for L'Aquila (AQ).

layer	description	$h$ $m$	$\gamma$ $kN/m^3$	$\phi'$ deg	$c'$ kPa	$V_{s0,m}$ $m/s$	$G_{0,m}$ kPa
A1	silt	3	20	26	10	192	7.52e+04
A2	silt	7	20	24	10	281	1.61e+05
A3	clay	5	20	24	10	352	2.53e+05
A3	clay	25	20	24	10	422	3.63e+05
A4	clay	55	20	24	10	825	1.39e+06
bedrock	-	-	22	-	-	1000	2.24e+06

**Table 6.3.** Soil deposit model for Napoli (NA).

layer	description	$h$ $m$	$\gamma$ $kN/m^3$	$\phi'$ deg	$c'$ kPa	$V_{s0,m}$ $m/s$	$G_{0,m}$ kPa
N1	sand and debris	5	20	36	0	360	2.64e+05
N2	silty sand	9	18.5	36	0	360	2.44e+05
N2	silty sand	16.4	18.5	36	0	360	2.44e+05
N3	yellow tuff	17	17	0	1750	704	8.60e+05
becrock	green tuff	-	19	-	-	790	1.21e+06

**Table 6.4.** Soil deposit model for Milano (MI).

layer	description	$h$ $m$	$\gamma$ $kN/m^3$	$\phi'$ deg	$c'$ kPa	$V_{s0,m}$ $m/s$	$G_{0,m}$ kPa
M1	gravelly sand	3	20	0	33	165	5.55e+04
M1	gravelly sand	12	20	0	33	225	1.03e+05
M1	gravelly sand	11	20	0	33	271	1.50e+05
M2	gravelly sand	44	20	0	35	400	3.26e+05
bedrock	-	-	22	-	-	1000	2.24e+06

Bedrock depth  $z_b$  and watertable depth  $z_w$  for the three sites are listed in table 6.5.

**Table 6.5.** Bedrock depth  $z_b$  and watertable depth  $z_w$  for the three sites considered.

site	$z_b$ [m]	$z_w$ [m]
L'Aquila (AQ)	95	15
Napoli (NA)	47.4	5
Milano (MI)	70	15



Subsequently, the *Multiple Stripe Analysis* (MSA) [67] [68] was used through three-dimensional nonlinear dynamic analysis (using the 3D model described in section 3.9). Using this technique, the structure is analyzed at various seismic intensity levels, where signals are selected for each level using the Conditional Spectrum (CS) [80] [79]. This approach provides a probabilistic characterization of the seismic response for a range of ground-motion intensities at the site of interest.

## 6.1 Code conforming archetype bridge design

The design followed the methods presented in chapter 5 and proposed in the draft second generation Eurocode 8 part 2, which will be released for public enquiry in 2022 [4].

### 6.1.1 Model for design

Simplified static models described in chapter 5 were used for the seismic design of these bridges. Both linear and nonlinear static models were used in order to compare the results; however only the values obtained with the Linear Static Model (LSM, described in section 5.2) are used for bridges design.

The models were implemented in the commercial software SAP2000 (figure 6.4) to find the internal structure stress resultants corresponding to the life-safety limit state.

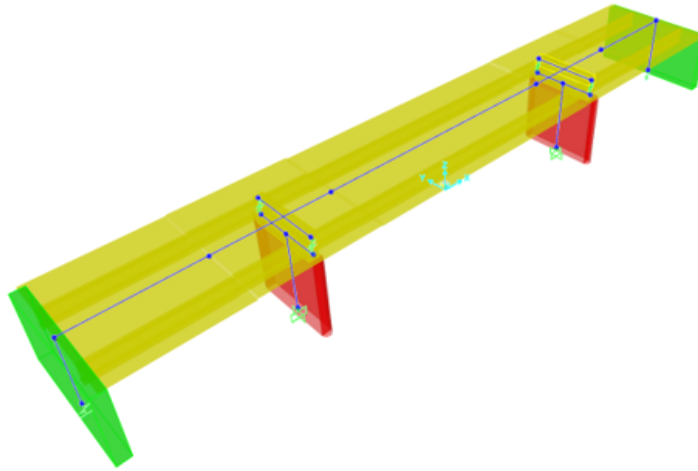


**Figure 6.4.** 3D extruded view of the static model used for design, implemented in SAP2000.

The properties of the static impedances applied to the base nodes depend on the stratigraphic characteristics of the three sites considered.

Three-dimensional models were set up for the design, however it is the analyses in the  $x$ - $z$  plane that were decisive in the sizing of the structural elements.

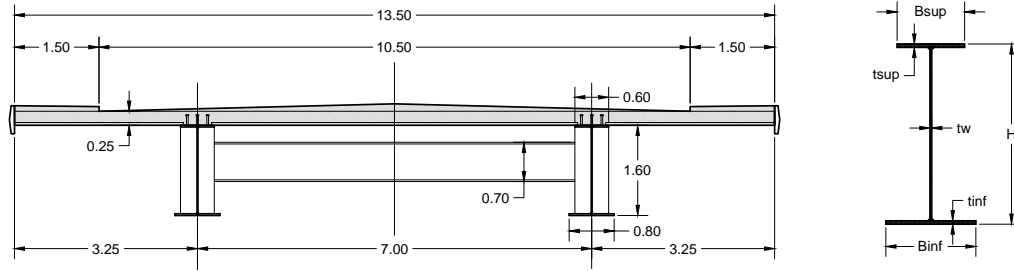


**Figure 6.5.** Deck cross-section. The archetype is taken from Ferretti Torricelli et al. [44] Dimensions are expressed in meters.

The weights due to the various elements are dependent to the deck cross-sections geometric characteristics reported in figure 6.5 and in the tables 6.6 and 6.7.

**Table 6.6.** Sections geometric parameters (measure are expressed in meters). For the notation used see figure 6.5

section	$H$	$B_{sup}$	$t_{sup}$	$t_w$	$B_{inf}$	$t_{inf}$	$A$	$y_g$	$I_x$	$W_{el,x}$
A	1.60	0.6	0.03	0.015	0.8	0.03	0.065	0.728	0.0317	0.0363
B	1.60	0.6	0.06	0.02	0.8	0.06	0.114	0.719	0.0598	0.0678

**Table 6.7.** Sections used along the bridge length.

span	section			$L_i$ [m]
	AQ	MI	NA	
1	B	A	A	12
1	B	B	B	7
2	B	B	B	5
2	A	A	A	28
2	B	B	B	5
3	B	B	B	7
3	B	A	A	12

The average deck cross-sectional area along the whole bridge is  $0.0804 \text{ m}^2$  for Napoli and Milano, and  $0.0957 \text{ m}^2$  for L'Aquila. Due to the higher seismic intensity the deck sections at the abutments have a "stronger" section for the bridge located at L'Aquila.

### 6.1.2 Actions

The structural self-weight is equal to  $103.31 \text{ kN/m}$  for Milano and Napoli, while it is equal to  $106.92 \text{ kN/m}$  for L'Aquila. The load due to non-structural elements is  $51.40 \text{ kN/m}$ . The total gravitational distributed load on the deck (due to gravity loads) is  $154.7 \text{ kN/m}$ .

For traffic actions, three standard lanes (width  $B_{\text{lanes}} = 3\text{m}$ ) were considered according to the Italian regulations (*Norme Tecniche per le Costruzioni* NTC 2018

[3] which in this respect coincides with EN1991 [1]). These correspond to a total distributed load of  $27 + 7.5 + 7.5 + 2.75 = 45.75 \text{ kN/m}$  and appropriately concentrated vertical loads whose resultant is  $600 + 400 + 200 = 1200 \text{ kN}$ . This load coincides with load Model 1 from EN1991.

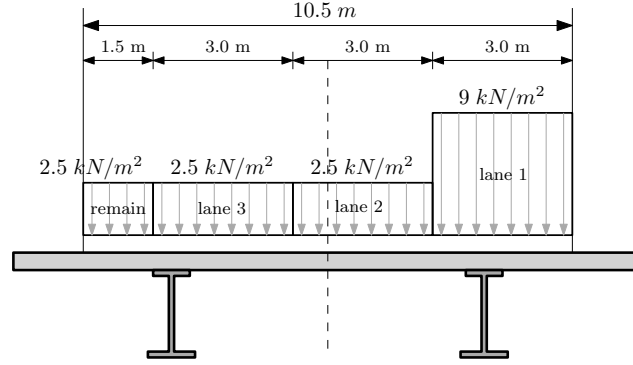


**Figure 6.6.** Standard lanes loads defined for *model 1* from EN1991 [1].

Since the arrangement of the lanes has an eccentricity along  $y$  the load on the two main girders is different. In fact the beam closest to the resultant of the traffic loads presents an increase of actions (compared to the other beam) of 150%. This aspect has been considered with the Courbon method. The effect of varying load position in  $x$  direction is accounted in the setup of the model in **SAP2000** through *moving loads* option for the traffic load pattern. The braking action (equal to  $7.44 \text{ kN/m}$ ) is distributed over the slab surface in the longitudinal direction (along  $x$ ). Since the section of the deck has an eccentricity equal to  $0.31 \text{ m}$  between the cross-section centroid and the surface of the slab, this distributed action also causes distributed moments on the element axis line equal to  $2.32 \text{ kNm/m}$ .

The wind exerts on the lateral surface of the deck a pressure equal to  $2.5 \text{ kN/m}^2$  (value taken from the Italian code for L'Aquila site). Since the height of the bridge section is  $1.85 \text{ m}$  plus  $3.0 \text{ m}$  high noise barriers; the horizontal distributed wind action is  $12.13 \text{ kN/m}$  and the distributed moment on the element axis (due to eccentricity) is  $15.28 \text{ kNm/m}$ .

In the various actions combination, reference was made to the Ultimate Limit State (SLU), for which the load combination is equal to:

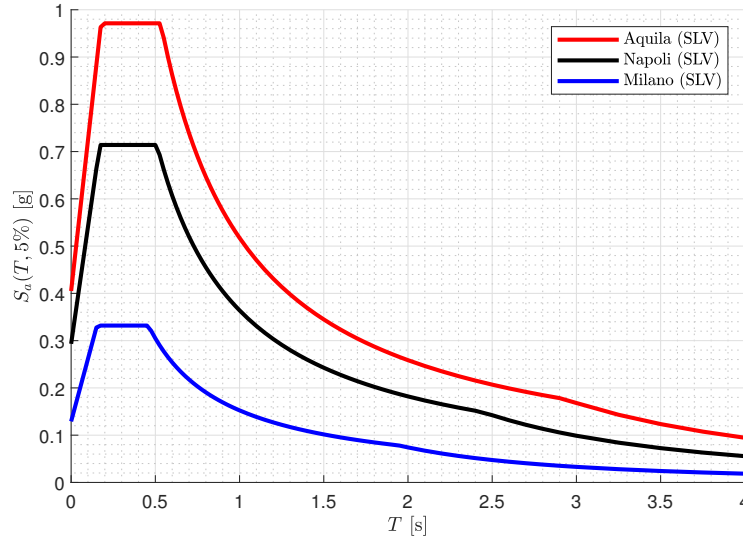
$$E_d = \gamma_{G1} G_{k1} + \gamma_{G2} G_{k2} + \gamma_{Q1} Q_k + \Psi_{02} \gamma_{Q2} W_k \quad (6.2)$$

where  $G_{k1}$  and  $G_{k2}$  are the characteristic values of gravitational actions due to structural and non-structural elements respectively,  $Q_k$  is the traffic load,  $W_k$  the wind load. The partial factors are equal to:  $\gamma_{G1} = 1.35$ ,  $\gamma_{G2} = 1.50$ ,  $\gamma_{Q1} = 1.35$  and  $\gamma_{Q2} = 1.5$  ( $\Psi_{02} = 0.60$ ).

For the seismic action, the code spectrum was taken [3] for a return period of 950 years for the L'Aquila site. The return period is calculated as a function of the nominal life and use class of the construction. With a nominal life  $V_N = 50$  years and a use class IV appropriate for strategic structures such as highway overpasses (which provides  $C_U = 2.0$ ) one has  $V_R = V_N C_U = 100$  years and:

$$T_R = -\frac{(V_R)}{\ln(1 - P_{V_R})} \approx 950 \text{ years} \quad (6.3)$$

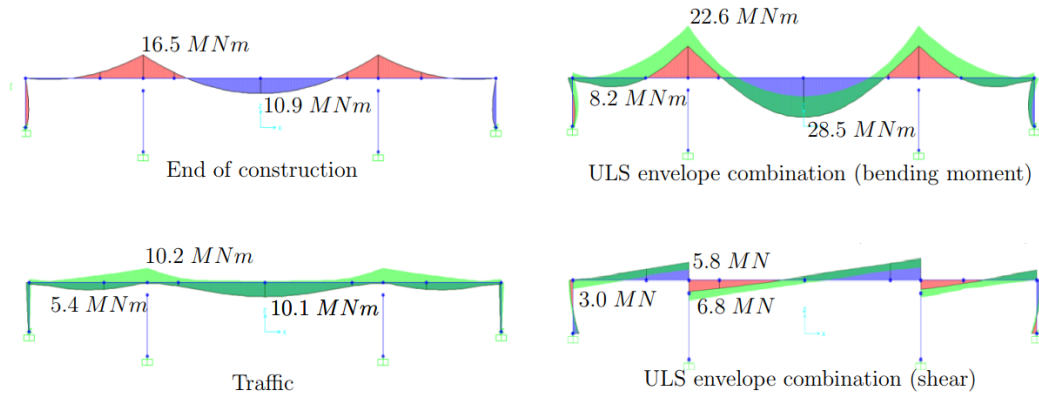
where  $P_{V_R}$  is the probability of exceedance in the reference period  $V_R$  taken equal to 10% (life safety limit state). Note that the adopted combination  $V_R = V_N C_U$  leads to a reference period for the evaluation of the seismic action that is equal to the usual design life  $t_L = 100$  years adopted for bridges in EN1990. The design spectra for the three sites are shown in figure 6.7.



**Figure 6.7.** Elastic acceleration spectra for the three sites considered for a 950 years return period and a 5% viscous damping ratio. Maximum values are 0.971 g, 0.714 g and 0.332 g for L'Aquila, Napoli and Milano respectively.

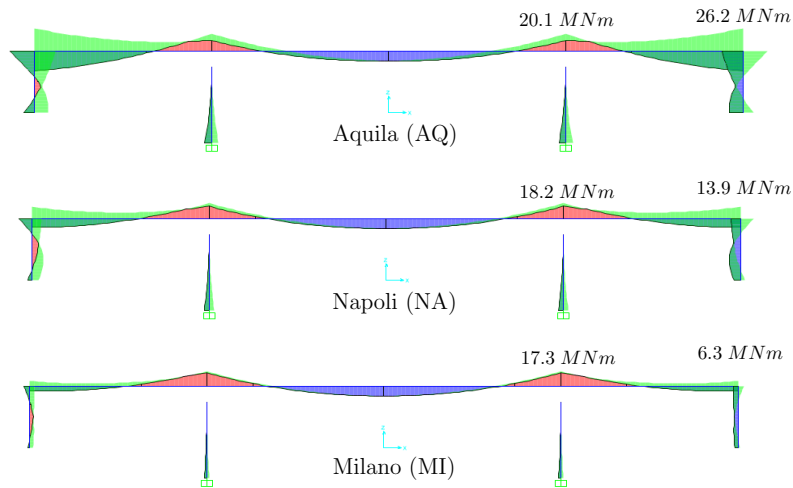
### 6.1.3 Results

Figure 6.8 shows the design bending moments from linear static analysis under non-seismic actions.



**Figure 6.8.** Bending moments and shear due to "static" actions.

Figure 6.9 shows maximum bending moments diagrams for seismic action (for life-safety limit state (SLV)).



**Figure 6.9.** Bending moments due to seismic actions (life safety limit state).

**Table 6.8.** Bending moments (at life safety limit state) and spectral plateau accelerations for each site.

	Aquila	Napoli	Milano
$M_{\max}$	26.2 MNm	13.9 MNm	6.3 MNm
$S_{\alpha}$	0.971 g	0.714 g	0.332 g

Due to the fact that the span ratio is 1:2:1 the bending moments at the deck-abutments joints are very small for static loads (also for traffic ones). This moment at the joints, however, increases as the horizontal actions caused by the earthquake increase (this can be seen clearly in figures 6.8 and 6.9).

#### 6.1.4 Structural elements resistances

The abutments elements have a reinforced concrete rectangular cross section with a base of 13.5 m and a height that depends on the site (1.6 m for Milano and Napoli and 2.0 m for L'Aquila). They are reinforced with 24 mm diameter bars with a 200 mm spacing. They have stirrups of 16 mm diameter with spacing 250 mm for Napoli and Milano and 200 mm for L'Aquila. Moreover, together with the stirrups, there are hooks that connect the two layers of reinforcement (along the shorter side) with 16 mm diameter rebars and with 500 mm spacing.

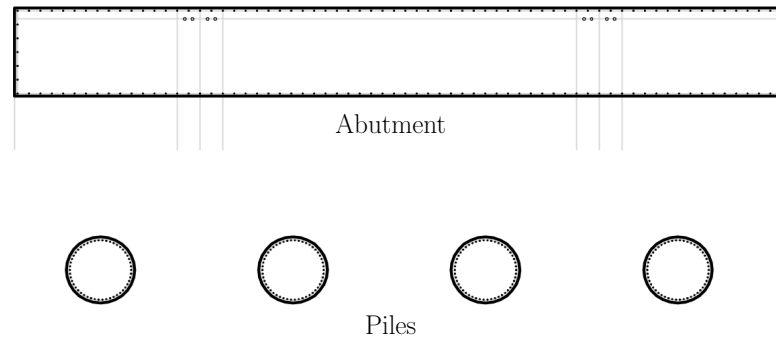


**Figure 6.10.** Abutment and piles cross sections (for Napoli and Milano).

The piles have a reinforced concrete circular cross section with a diameter of 1.2 m and a longitudinal reinforcement consisting of 28 bars of 26 mm diameter for Milano and Napoli and 28 mm diameter for L'Aquila. As transversal reinforcement they have a double stiffening cage with 250 mm spacing for Milano and Napoli and 200 mm for L'Aquila.

Structural materials used are:

- *Concrete*: C32/40. With compression strength equal to 40 MPa and Young modulus equal to 33.35 GPa. It is modeled inside **OpenSEES** through **Concrete04** with yielding strain equal to -0.002 and ultimate strain equal to -0.005.
- *Steel*: B450C. With a yielding stress equal to 537.9 MPa, a Young modulus equal to 206 GPa and an hardening ratio equal to 0.0044.<sup>5</sup>

Figure 6.11 shows the moment-curvature diagrams for the deck, abutment, and piles cross-sections calculated by fiber section analysis in **OpenSEES**.

<sup>5</sup>Values are taken from the OPUS report on the seismic performance of steel and steel-concrete structures by standardising material quality control [70].

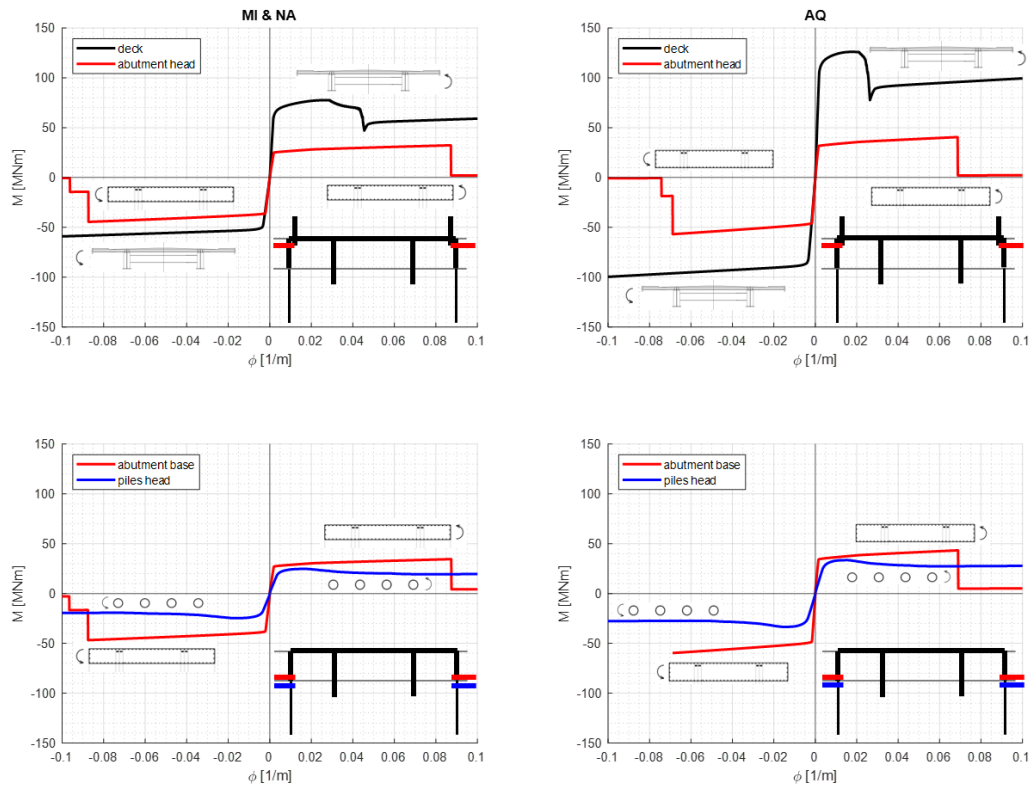


**Figure 6.11.** Elements cross-section moment-curvature curves obtained numerically through fiber-section analysis.

In the table 6.9 are listed the ratios  $R_d/E_d$  between the resistances ( $R_d$ ) and the actions ( $E_d$ ) for the structural elements, for each site. Bending moments on the piles head are equal to the bending moments at the bottom cross-section of the respective abutments.

**Table 6.9.** Design actions effects ( $E_d$ ) and resistances ( $R_d$ ) ratios for the bridge structural elements, for each site.

element	scenario	check	AQ	NA	MI
Deck	construction	bending $M$	3.2	3.2	3.2
		shear $V$	6.5	6.5	6.5
	SLU	bending $M$	1.1	1.1	1.1
		shear $V$	1.8	1.8	1.8
		bearing $\delta$	2.3	2.3	2.3
	EQ (LS)	bending $M_z$	2.1	2.8	6.0
		bending $M_y$	1.5	2.1	5.2
Abutments	SLU	bending with axial force	4.2	4.2	4.2
	EQ (LS)	bending with axial force	1.3	2.1	6.2
Piles	SLU	axial force $N$	9.8	9.8	9.8
		bending with axial force	5.7	5.7	5.7
Foundations	SLU (GEO)	axial force $N$	1.5	1.1	1.2

The deck was designed for ultimate limit state (SLU) actions and the piles for geotechnical combination (GEO). The dimensions of the abutment for Napoli, but especially for Milano, was strongly influenced by the deck-abutment node detailing (a deck with 1.6 m high girders cannot be embedded into a too thin abutment).

## 6.2 Assessment

As previously introduced, a multiple stripe analysis was performed taking, for each of the 3 sites, 10 intensity levels characterized by different return periods. For each of these intensity levels, 20 multi-component ground motions were selected by means of conditional spectrum method [79] with  $S_a$  at the period of 0.50 s as the conditioning IM. A total of  $3 \times 10 \times 20 = 600$  motions (in both  $x$  and  $y$  directions) are used. In the table 6.10 are listed the return periods  $T_r$  and the intensity level  $S_a$  for each stripe.

**Table 6.10.** Intensity level ( $S_a(T^* = 0.5s, 5\%)$  in  $g$ ) as function of return period ( $T_r$  in years) at Intensity Measure Level (IML) for each stripe and each site. Values are from the ReLuis-RINTC project [64].

IML:	1	2	3	4	5	6	7	8	9	10
$T_r$	10	50	100	250	500	1 000	2 500	5 000	10 000	100 000
$S_a(T^*)$ (AQ)	0.054	0.140	0.204	0.329	0.469	0.667	1.053	1.465	1.992	5.306
$S_a(T^*)$ (NA)	0.029	0.087	0.129	0.204	0.277	0.365	0.508	0.640	0.795	1.499
$S_a(T^*)$ (MI)	0.017	0.035	0.046	0.064	0.081	0.101	0.133	0.162	0.195	0.341

Two performance levels were considered for the definition of failures, intentionally different from the conventional code-based limit states:

- *Usability Preventing Damage* (UPD): A state of limited damage such that the bridge requires intervention, to restore operations, which takes a short time (less than a week).
- *Severe Damage* (SD): Damage such that the bridge requires structural repairs, to restore operation, which takes a longer time (in order of months, accounting for all phases of the process, including tender, worksite setup, etc.).

Bridges (and in particular integral bridges) do not exhibit failures in terms of mechanisms, leading to partial or total collapse of the load-bearing structure. For this reason, these limit states have been introduced as a function of the *resilience* (time taken to bring the bridge back into service).

### 6.2.1 Nonlinear model for assessment

For the evaluation of the seismic performance of these structures, the three-dimensional dynamic model described in section 3.9 was used. In order to evaluate the performance of the bridge considering the failure of the structural elements, structural nonlinearity was also introduced.

Initially, non-linearity of structural elements was introduced via fiber section elements with a formulation based on flexibility [103] [89] and a mass matrix consistent



with the elements distributed mass [61]. However, this model had additional fictitious inertia forces on the elements due to the interaction between the bending moment and the normal force. This problem was solved in two ways:

- By defining the masses only at the nodes (and not distributed over the elements) and setting the rotational inertias, due to the mass of the elements, equal to zero.
- Defining a uncoupled section law between stress resultants and generalized deformations, for bending moment and normal force.

Since the results did not change depending on which of the two methods was used and the use of the uncoupled approximate section model was computationally faster, the latter was employed.

Nonlinear section behavior was considered only for the bending degree of freedom, while axial response was left linear elastic:

$$\begin{bmatrix} N \\ M \end{bmatrix} = \begin{bmatrix} EA & 0 \\ 0 & f(\phi, N^*) \end{bmatrix} \begin{bmatrix} \varepsilon_0 \\ 1 \end{bmatrix} \quad (6.4)$$

where  $\varepsilon_0$  is the element axial deformation,  $\phi$  its curvature, and  $f(\phi, N^*)$  a nonlinear function that depends on the fixed value of axial load  $N^*$  and the curvature. Actually the normal force  $N$  varies during the system motion, changing also the elements flexural resistance. However this variation is modest and therefore, it has been neglected by taking  $N$  constant and equal to the normal stress  $N^*$  at the end of the static stages. A perfect elasto-plastic law has been taken as a nonlinear function where the resistant moment is calculated by fiber-section analysis and the yield curvature  $\phi_y$  is taken from Priestly [92] [93] and equal to:

$$\begin{aligned} \text{Rectangular section (abutments):} \quad \phi_y &= 2.10 \frac{\varepsilon_y}{h} \\ \text{Circular section (piles):} \quad \phi_y &= 2.25 \frac{\varepsilon_y}{d} \end{aligned}$$

where  $h$  is the height of the rectangular section,  $d$  the diameter of the circular section,  $\varepsilon_y$  the steel yield strain. In the figure 6.12 a moment-curvature diagram, derived from a fiber section numerical analysis, and the equivalent decoupled model is shown.

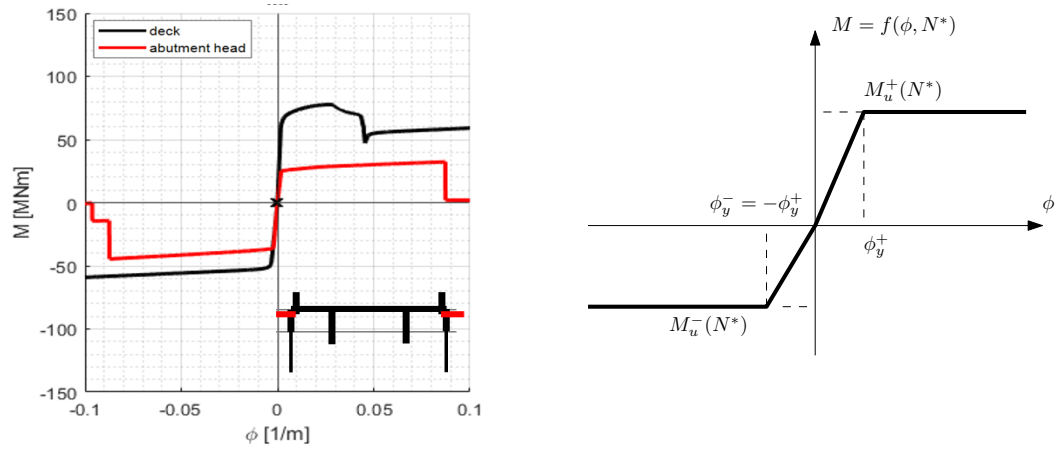


**Figure 6.12.** Non-linear uncoupled constitutive law used for structural elements formulation (see figure 6.10).

Post-yielding hardening, of less than 0.01% of the initial stiffness, was added to reduce numerical instabilities.

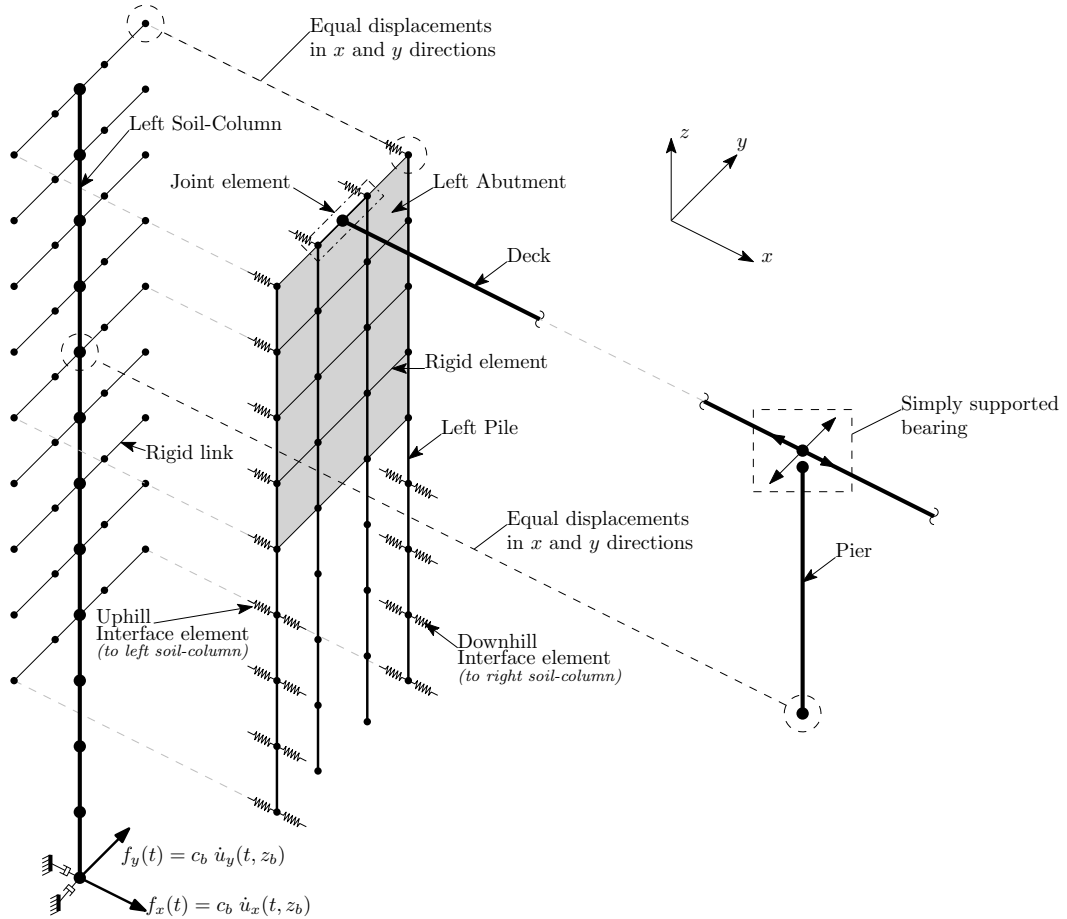


**Figure 6.13.** Exploded view of the non-linear dynamic 3D finite element model used for seismic risk assessment.

The main difference with the model described in section 3.9 is that, in this case, there are intermediate piers on which the deck is simply supported with multidirectional bearings as it can be seen in figure 6.13. The piers are therefore modeled by means of single linear beam finite elements (given the flat sliding bearing on top, the limited height and the wall-type section, they are expected to perform elastically at all intensities). They are fixed at the base and the base node has equal displacements constraints in  $x$  and  $y$  with the corresponding nodes of the soil columns at the same height of the piers base. This modeling strategy is an approximation. In fact, the real behavior of the piers is different, as the motion of the portion of the soil on which they rest (the soil between the abutments) may exhibit a differences with that of the soil deposit. The approximation is judged reasonable since the difference in motion would not be such as to cause exceedance of the flat bearing displacement capacity.

The main failure mechanisms considered for the UPD performance level are the exceedance of the bending moment and the yielding curvature for the most stressed sections (joint sections between deck and abutments and at the piles head). While for the SD the ultimate moment and the ultimate curvature have been taken as thresholds. Since the elements have elastic- perfectly plastic constitutive laws, considering the yielding curvature or the yielding moment is the same thing. In addition, the exceeding of the shear resistance of the abutments and piles and the relative displacements of the supporting bearings have been taken as failure mechanisms for the SD.

The table 6.11 shows the quantities used in defining the exceedance of performance levels.

**Table 6.11.** Response quantities used for limit-states evaluation.

structural component	UPD			SD		
	description	EDP	lim.	description	EDP	lim.
deck	elastic limit	moment	$M_y$	exceeding resistance	moment	$M_u$
abutments	deck-abut. sections	curvature	$\phi_y$	deck-abut. sections	curvature	$\phi_u$
	plasticization			resistance		
piles	abut.-piles sections	curvature	$\phi_y$	abut.-piles sections	curvature	$\phi_u$
	plasticization			resistance		
bearings	-	-	-	incipient exit of the plate from its housing	displacement $d_1^*$	

### 6.2.2 Input ground motions

Each of the 600 ground motions (20 for ten strips at three sites) has three components: along  $x$ ,  $y$  and  $z$ . However, for these analyses the vertical component is disregarded.

Figure 6.14 shows the characteristics (in terms of PGA, PGV, Arias intensity  $I_a$  and effective duration  $D_{5\sim 95\%}$ ) of the selected signals.

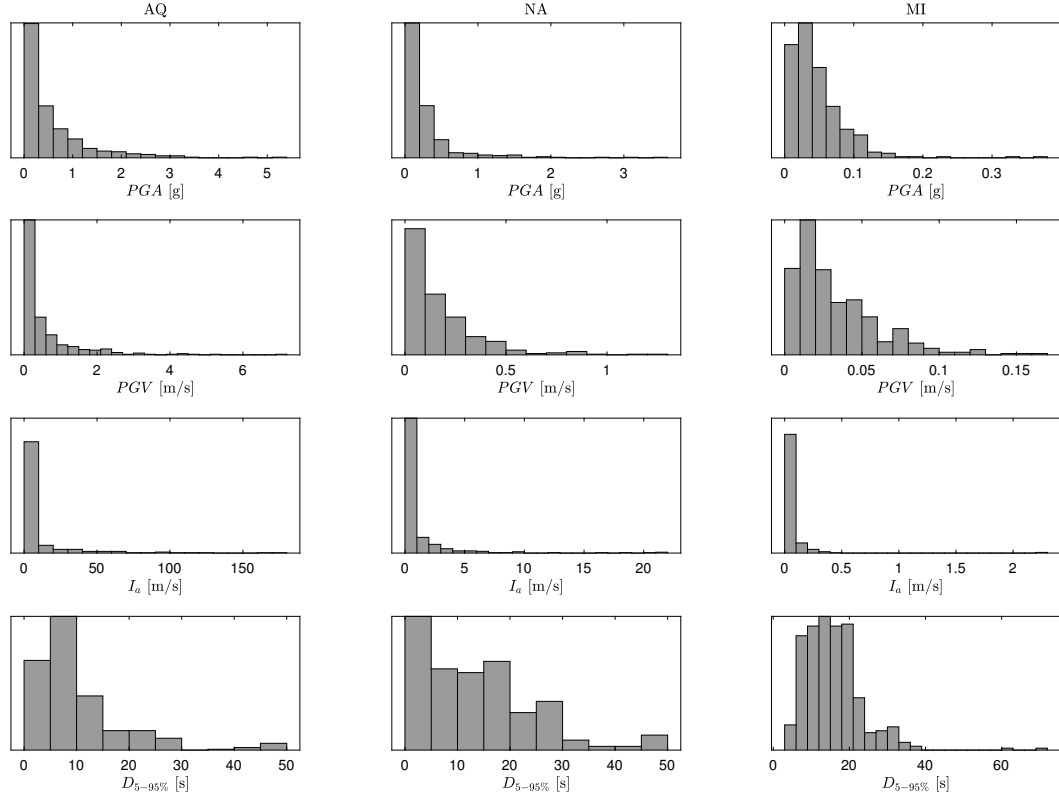


**Figure 6.14.** From left to right are presented selected signals information for L'Aquila (AQ), Napoli (NA) and Milano (MI) respectively.

PGAs up to 5 g for L'Aquila (and 3 g for Napoli) depends on having considered, especially for the 10<sup>th</sup> strip, large return periods. In particular, a return period of 100 000 years corresponds, roughly, to events that have a high magnitude and a small epicentral distance [63]. For such events the  $\epsilon$  however does not exceed 3 [64]. .

The selected ground motions are related to rigid soil (category A soil for Italian code). The acceleration were converted into velocity to be used in the model (see section 3.3). This was done by numerical integration of the signals via the *trapezoids method*:

$$\dot{u}(t) = \int_0^t \ddot{u}(\tau) d\tau \quad \rightarrow \quad \dot{u}(i \Delta t) = \dot{u}_i \approx \sum_{k=1}^i \frac{\ddot{u}((k-1)\Delta t) - \ddot{u}(k \Delta t)}{2} \Delta t \quad (6.5)$$

In order not to have constant speed at the end of the signal the "tails" have been truncated to have zero velocity at the end of the ground motion. Other modifications (namely *baseline correction*) have been avoided.

Velocity proportional forces were applied to the model directly at the interface between bedrock and deposition via base-dampers elements (see section 3.3 and 3.9).

### 6.2.3 Results

In this section, results are presented in terms of the system's vibration modes, response time series for sample ground motions, maxima of all relevant response

parameters at all sites and, finally, fragility curves.

### Modal analysis

The first two vibration modes of the system are the fundamental vibration modes of the soil deposit (first mode) in the  $x$  and  $y$  directions, as it can be seen in figure 6.15. The soil-deposit model has the same properties in both  $x$  and  $y$  directions so the first two modes are equal.

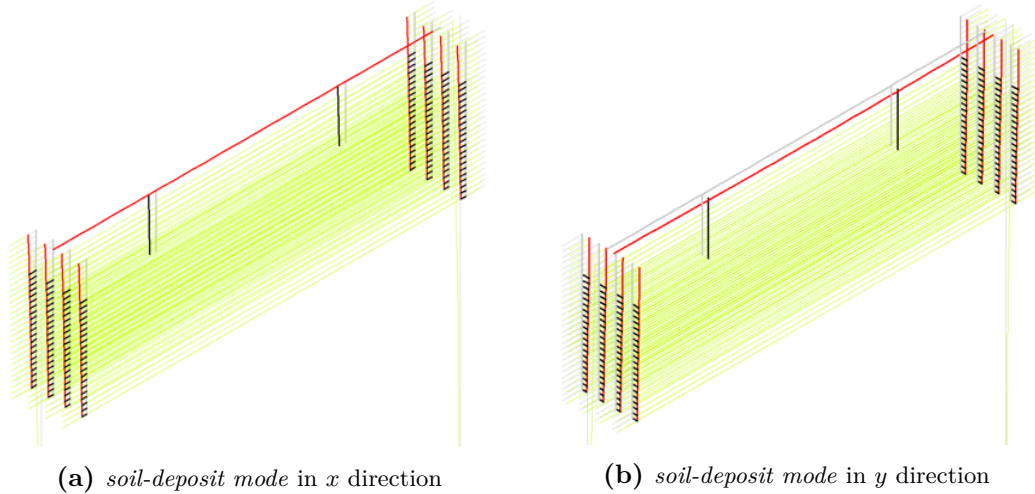


**Figure 6.15.** First two modes of vibration.

As with the 2D and 3D models (without intermediate piers) for these initial vibration modes, the structure undergoes little deformations, as the bridge essentially translates along with the more superficial layers of the deposit. These two modes (which have almost the same vibration period, with only a small difference due to the bridge presence) are referred to as *soil-deposit modes*. The soil-deposit modes are those that have the greatest participating mass (more than the 70% of the total model mass), since they involve the soil domain that possess most of the mass of the system.

The next is a mode that only affects the deck bending (and thus also the section at the top of the abutments) in the  $z$  direction, as it can be seen in figure 6.16.

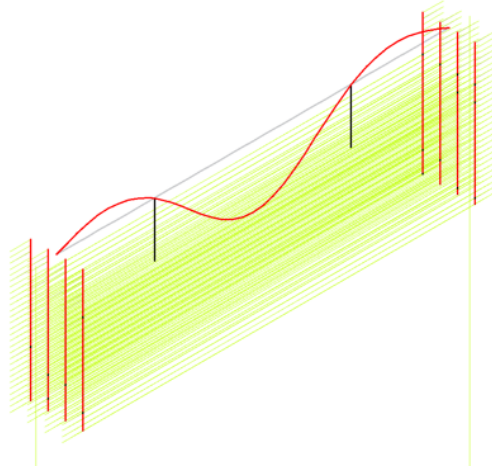


**Figure 6.16.** *Vertical mode*: first vertical mode (deck in direction  $z$ ).

This vibration mode is the main *vertical mode* for the model and has the largest differences between the model described in section 3.9 due to the presence of the intermediate piers.

Unlike the two-dimensional model, the 3D model (and thus this one as well) also has a deck *horizontal mode* (as it can be seen in figure 6.17).

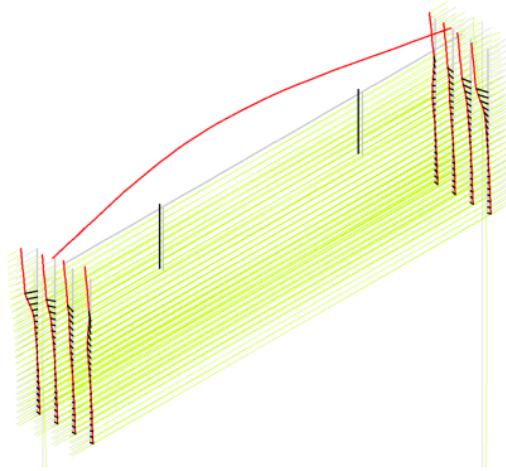


**Figure 6.17.** *Horizontal mode*: first horizontal mode (deck in direction  $y$ ).

This transverse mode leads to a torsion on the abutments and an additional bending moment on the foundation piles of the abutments. In this case, the presence of the intermediate support piles does not bring changes in the modal shape since the supports are multidirectional in  $x$ , but especially in  $y$ .

*Pier modes* are, for both sides, piers bending in  $x$  direction (only piers because the deck is simply supported with multidirectional bearings on piles head).

Finally the "structural" modes are also present, for which the modal deformation mainly affects the elements of piles, abutments and deck ,as it can be seen in figure 6.18.

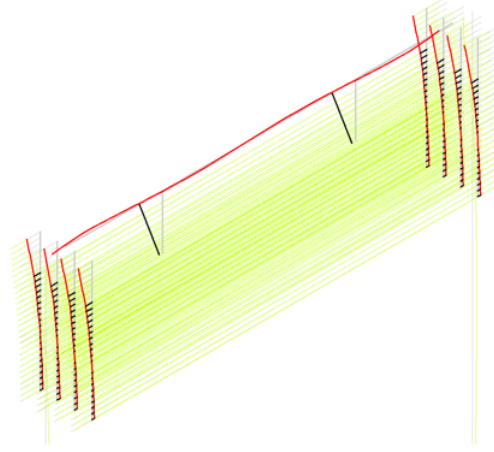


**Figure 6.18.** *Structural modes:* higher modes whose deformation mostly affects the structure (the deformation involves heavily the deck-abutments joints).

The vibration modes types described previously and periods for the three bridges at the three sites of L'Aquila, Napoli and Milano are shown in table 6.12.

**Table 6.12.** Modes type and period for the three bridges located in L'Aquila (AQ), Napoli (NA) and Milano (MI). Mode types are described in the figures 6.15, 6.16, 6.17 and 6.18.

mode	AQ		NA		MI	
	mode type	$T_i$ [s]	mode type	$T_i$ [s]	mode type	$T_i$ [s]
1	Soil-deposit $x$	0.61	Soil-deposit $x$	0.46	Soil-deposit $x$	0.84
2	Soil-deposit $y$	0.61	Soil-deposit $y$	0.46	Soil-deposit $y$	0.84
3	Vertical	0.34	Vertical	0.35	Structural	0.35
4	Horizontal	0.28	Piers	0.25	Soil-deposit $y$	0.35
5	Structural	0.28	Piers	0.25	Vertical	0.35
6	Piers	0.25	Horizontal	0.25	Horizontal	0.27
7	Piers	0.25	Structural	0.20	Piers	0.25
8	Horizontal	0.25	Soil-deposit $y$	0.17	Piers	0.25
9	Structural	0.19	Structural	0.17	Structural	0.21
10	Soil-deposit $y$	0.18	Structural	0.13	Soil-deposit $y$	0.21

### Sample results from inelastic response history analysis

The following figures show the results, in terms of bending moments in the most stressed sections (abutments and piles top-sections), for three signals at the L'Aquila site representative of three seismic intensities. The three intensities were chosen equal to the third, sixth, and ninth strip.

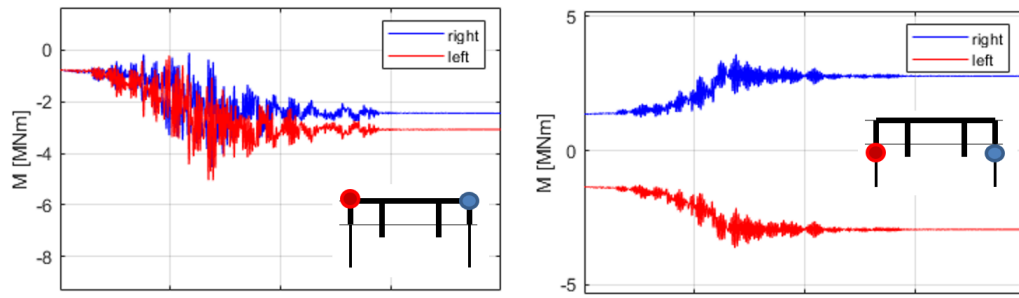


**Figure 6.19.** Time history bending moments results for L'Aquila: 3<sup>rd</sup> stripe (1<sup>st</sup> signal).

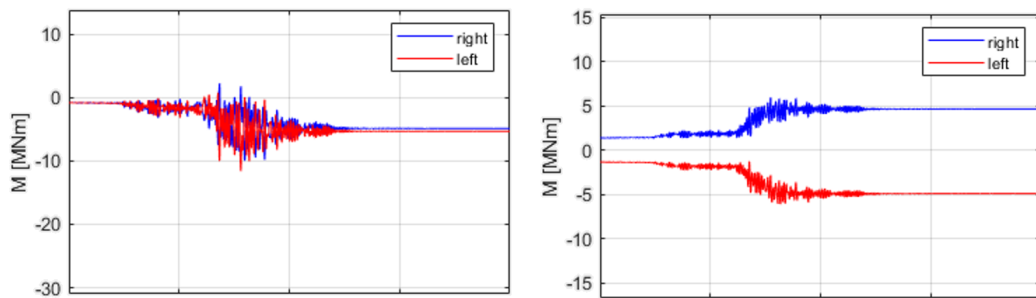


**Figure 6.20.** Time history bending moments results for L'Aquila: 6<sup>th</sup> stripe (1<sup>st</sup> signal).

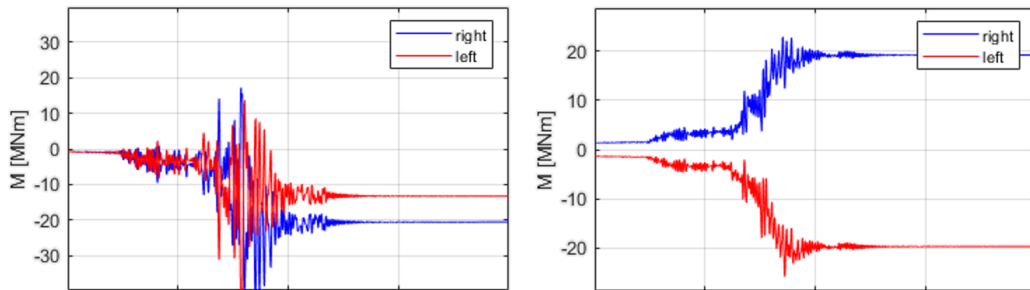


**Figure 6.21.** Time history bending moments results for L'Aquila: 9<sup>th</sup> stripe (1<sup>st</sup> signal).

in figure 6.22 are the earth pressures on the left alignment for the 20 signals of the sixth strip at l'Aquila.



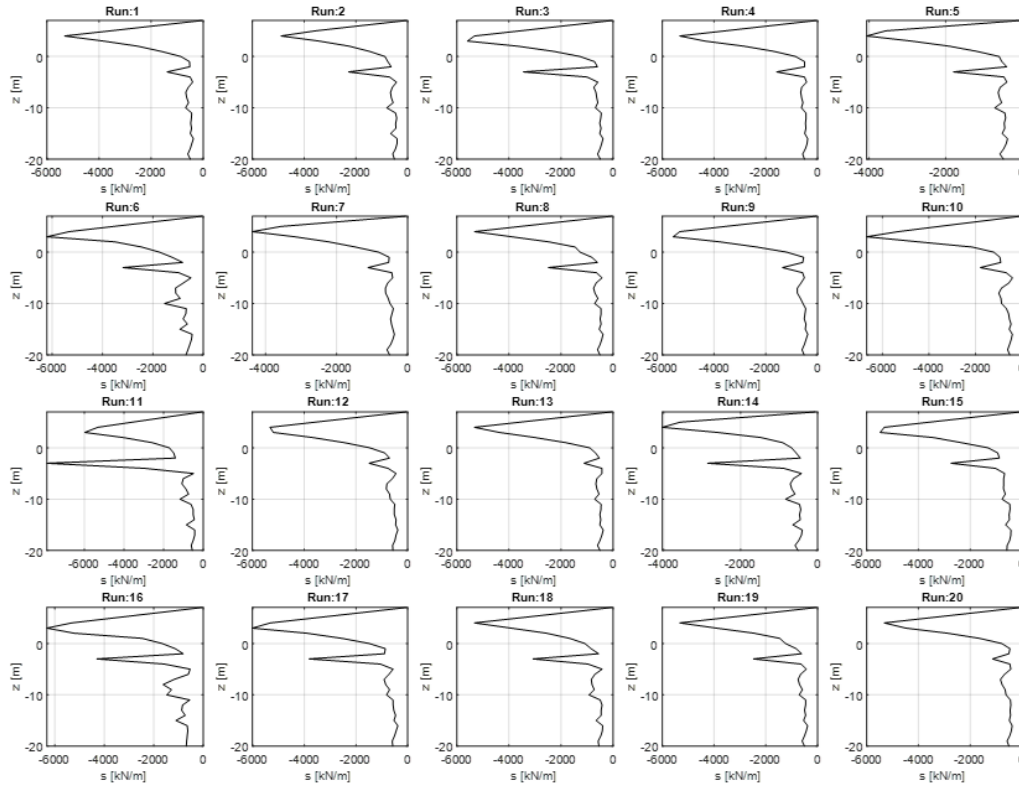


**Figure 6.22.** Soil stresses over the left abutment-piles alignment for L'Aquila: 6<sup>th</sup> stripe.

The discontinuities on the trend of the stresses are due to the different characteristics of the soil deposit layers.

In appendix E more results are listed for each site and each stripe considered.

### Global multiple-stripe analysis results

This section presents results in terms of global response maxima for all intensities considered in the multiple stripe analysis.  $EDP_m$  is taken (as global response parameter the maximum in absolute value of the bending moment as stated in equation (3.45).

Figures 6.23, 6.24 and 6.25 show individual  $EDP_m$  values from each motion, for all intensity levels together with lognormal probability density functions fitted, for the site of Milano, Napoli and L'Aquila respectively. The dashed line marks the flexural resistance for the Severe Damage limit state (see section 6.1.4).

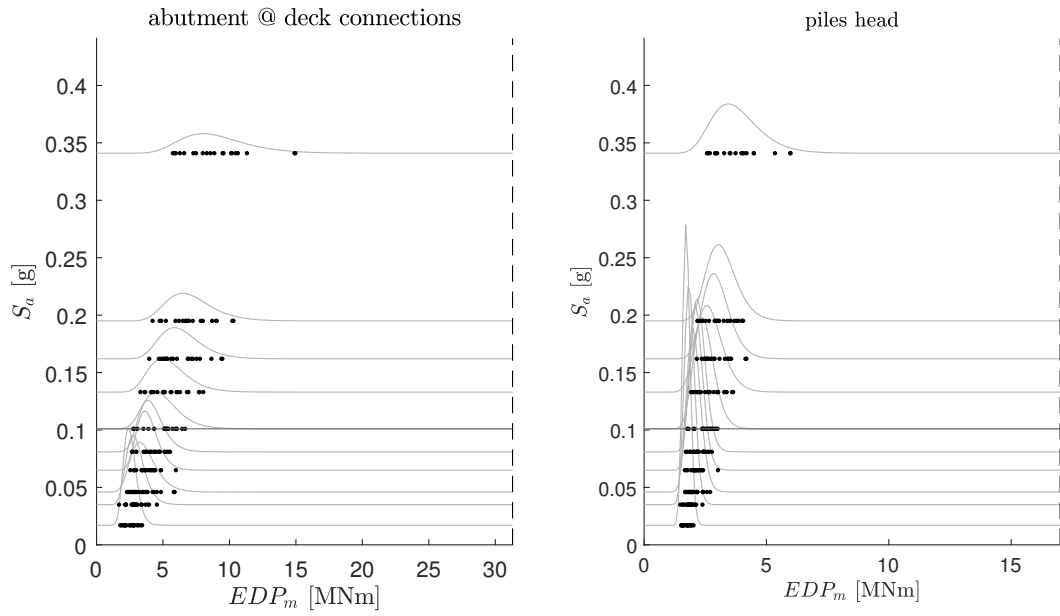


Figure 6.23. Global results for Milano.

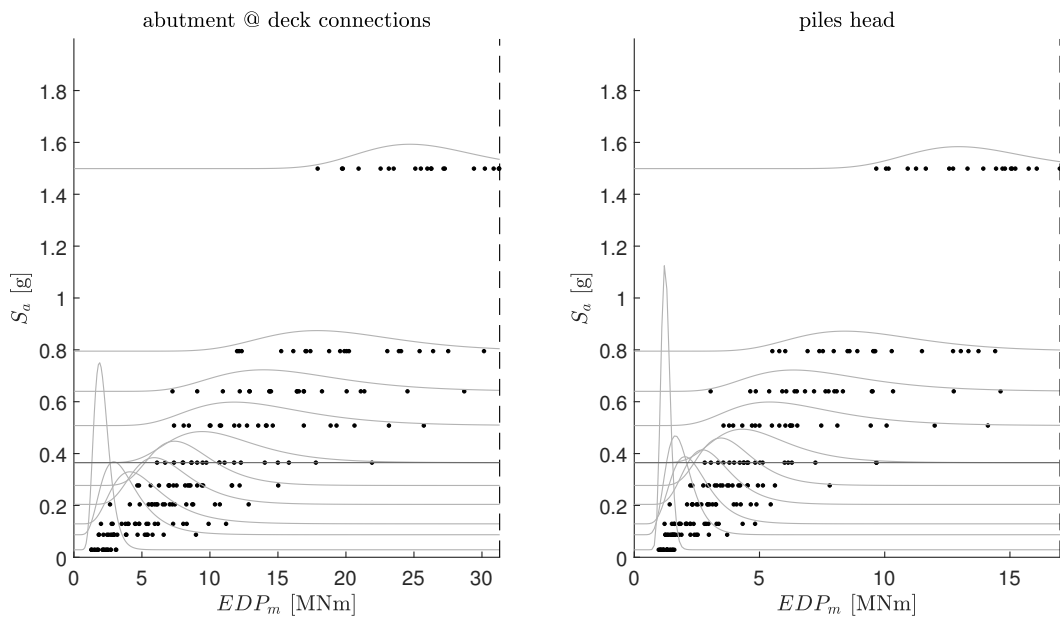
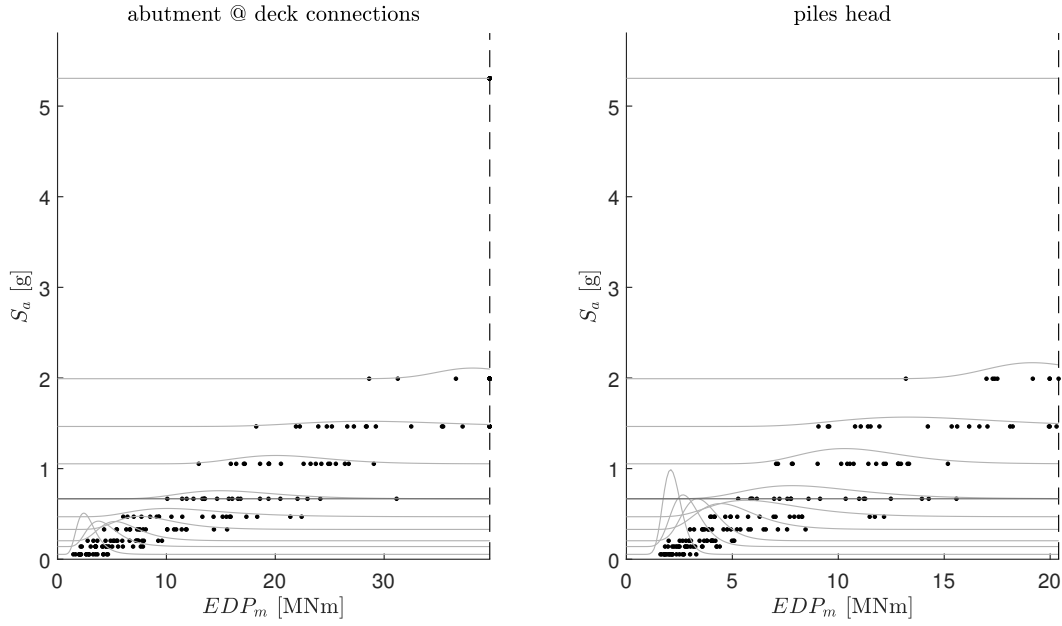


Figure 6.24. Global results for Napoli.



**Figure 6.25.** Global results for L'Aquila.

Milano does not present any failure (i.e. the points on the graphs never reach the dashed lines, while failures are visible for Napoli, but especially L'Aquila. Exceedance are localized in the stripes above the sixth one, which corresponds to a return period of 1000 years (table 6.10). This return period almost coincide with that one used for the design ( $T_R = 950$  years, see equation (6.3)) and, therefore, the results essentially confirm the effectiveness of the proposed simplified design models (a more in depth analysis is described in section 5.4). The site of Milano shows a different trend compared to the other two sites (see figures 6.23 6.24 and 6.25) because, due to the low seismicity, the design of the deck, the abutments and the piles is limited to the gravitational loads. Therefore the overpass designed in the site of Milano shows lower failure rates due to the structural elements oversizing against the seismic actions.

As it can be seen from figure 6.26, the bending moment on the deck (in the sections over the piers and in the middle of the central span) is less influenced by the earthquake than the deck-abutments sections and the sections at the piles head. The same behavior is noted in the results for Milano and Napoli, not shown here for brevity. This result was anticipated earlier and is confirmed now in these analyses for all three sites.

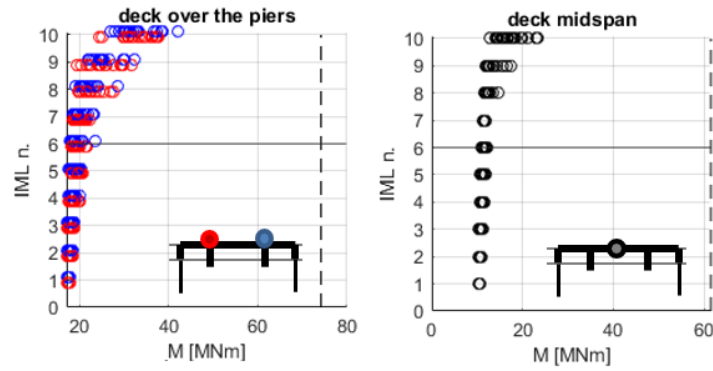


**Figure 6.26.** Global results for L'Aquila.

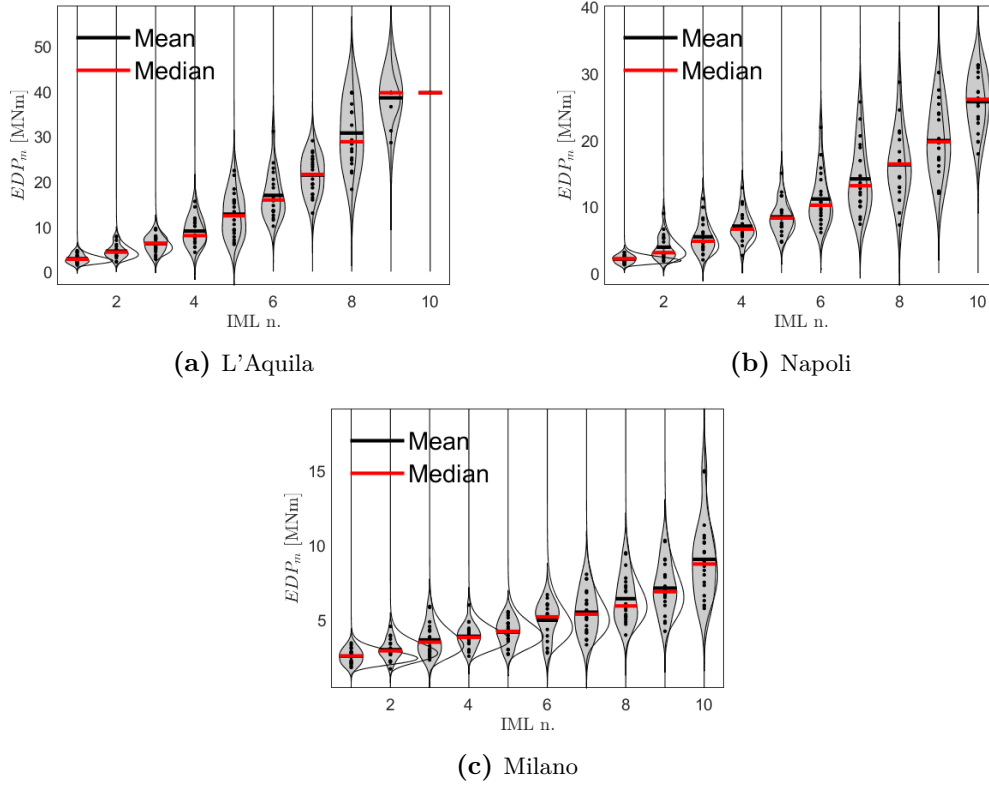
For L'Aquila, in the tenth strip, the distribution is not present since all analyses lead to failure and, since the elements section constitutive law is the elasto-perfectly plastic, the points are all concentrated on the value of  $EDP_m$  corresponding to the collapse.

Table 6.13 summarizes the number of failures per strip for all sites considered.

**Table 6.13.** Number of failures  $k_i$  for each stripe  $i$  and each site considered.

Site	Limit State	IML1	IML2	IML3	IML4	IML5	IML6	IML7	IML8	IML9	IML10
AQ	UPD	0	0	0	0	0	1	0	11	19	20
AQ	SD	0	0	0	0	0	0	0	3	11	20
NA	UPD	0	0	0	0	0	0	1	2	7	14
NA	SD	0	0	0	0	0	0	0	0	0	0
MI	UPD	0	0	0	0	0	0	0	0	0	0
MI	SD	0	0	0	0	0	0	0	0	0	0

Figure 6.27 shows the distribution of  $EDP_m$  conditional on no collapse for each strip, along with the lognormal fit. As it can be seen qualitatively from the figure the assumption of lognormal distribution of  $EDP_m|NC$  for each intensity (defined in equation 3.45) is generally a good approximation.



**Figure 6.27.**  $EDP_m$  distributions for each stripe (Bending moment  $M(t)$  at deck-abutments joints).

### Fragility curves

If the damage in the system does not accumulate over multiple seismic events, then we can describe the structural failure due to the earthquake as a Homogeneous Poisson Process (HPP). This is particularly convenient because HPP is one-parameter model and the probability of failure depends only on the failure frequency:

$$\lambda_f = \int_{im} P[f|im] |d\lambda_{im}| \quad (6.6)$$

where  $d\lambda_{im} = d(im) \frac{d\lambda_{im}}{d(im)}$  depends on the derivative of the *hazard curve* and  $P[f|im]$  is the probability of failure given an intensity measure.  $P[f|im]$  is the fragility curve of the soil-structure system. Often [62], fragility is expressed analytically via a lognormal CDF:

$$P[f|im] = \Phi \left[ \frac{\ln(im) - \eta}{\beta} \right] \quad (6.7)$$

where  $\Phi$  is the standard normal CDF and  $\{\eta, \beta\}$  its parameters. An EDP-based method<sup>6</sup> with the *binomial likelihood* was used to find the parameters estimate

<sup>6</sup>An EDP-based method for the fragility assessment is intended as the evaluation of the structural failures (through non-linear dynamic analyses), intended as  $EDP > edp$ , at given  $IM = im_i$ .

$\{\hat{\eta}, \hat{\beta}\}$ :

$$\{\hat{\eta}, \hat{\beta}\} = \arg \max_{\eta, \beta} \left[ \sum_{i=1}^m \left( \ln \binom{n}{k_i} + k_i \ln \left\{ \Phi \left[ \frac{\ln(im_i) - \eta}{\beta} \right] \right\} + (n - k_i) \ln \left\{ 1 - \Phi \left[ \frac{\ln(im_i) - \eta}{\beta} \right] \right\} \right) \right] \quad (6.8)$$

where  $m$  is the stripes number (in this case 10),  $n$  the total number of analysis per stripe (in this case 20),  $k_i$  the number of failures for  $IM = im_i$  (i.e. for the stripe  $i$ ) and  $(n - k_i)$  the number of non-failures for the stripe  $i$ .

In figure 6.28 fragility curves, together with empirical percentiles  $k_i/n$ , are shown for UPD and SD limit states considered.

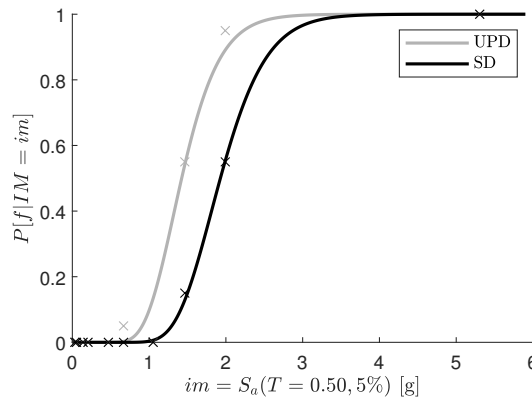
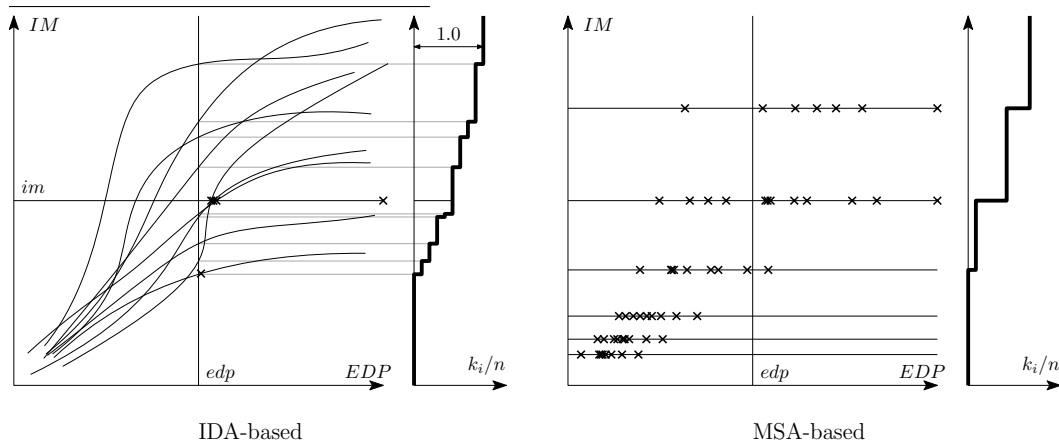


**Figure 6.28.** Fragility curves for L'Aquila for the UPD and SD limit states.

In the site of Napoli there are no failures for the SD limit state and for Milano there are no failures even in the UPD limit state. This leads to a difficulty in calculating fragility curves, particularly at the curve "tail".



The analysis can be carried out using *Incremental Dynamic Analysis* (IDA) or using *Multiple Stripe Analysis* (MSA) [12]. In this case the MSA is used.

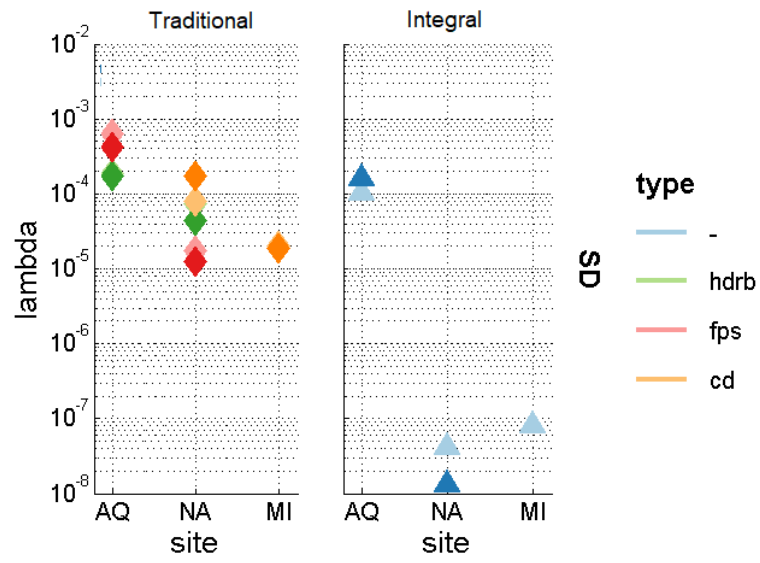


**Figure 6.29.** Failure frequency  $\lambda_f$  (defined in equation (6.6)).





# Summary, conclusions & future research

This thesis dealt with practice- and design-oriented analysis models of integral abutment bridges.

It started by extending an existing non-linear dynamic model of the behavior of integral abutment bridges during seismic events developed by Franchin et al. [48] [47] [46]. This approximate model is based on describing the soil-structure interaction by nonlinear Winkler springs, and it allows to dynamically evaluate the complete bridge-soil system in terms of design-relevant quantities such as the internal stress resultants at all critical structural sections (deck, abutments, piles, etc.).

This thesis turned this model, which was more a proof of concept, to a practically applicable one by studying in depth the effect of its parameters (appendix D) and improving selected model components, such as the force-deformation laws of the interface springs<sup>7</sup> and the soil column<sup>8</sup>, or the evaluation of the participating soil mass<sup>9</sup> (chapter 3).

A fundamental step in this developments was a comparison made between the proposed model and a continuous three-dimensional model, developed in parallel as part of a PhD thesis in geotechnical engineering (Gallese 2022), which allowed evaluating the critical aspects of such approximate modeling. The step-wise comparison of the responses of the two models (deposit amplification, the mode shapes and periods, pressure and internal forces distribution during construction, the dynamic response to two largely different ground motions) provided the precious means to calibrate otherwise judgmental parameters. A more correct definition of the construction stages has also allowed a more precise evaluation of the bending moments acting on such bridges.

From the complete dynamic model, two partial static models have been developed for the design of such bridges. These models, like the dynamic one, have been implemented both in **OpenSEES** and in the commercial software **SAP2000** in order to evaluate the models' predictive ability even in computational codes, like the latter, that do not allow a totally faithful implementation of the constitutive laws in the model formulation.

Finally, a probabilistic seismic risk analysis has been also carried out on archetypical three-span integral abutment overpasses designed with the proposed static

---

<sup>7</sup>In particular, a constitutive law with distinct stiffness between the active and passive sides.

<sup>8</sup>In particular the definition of the parameter  $n$ .

<sup>9</sup>The value of  $r$ .

methods at three sites of the Italian territory<sup>10</sup>, assessing their response by means of the dynamic model.

The model presented in this thesis (thanks also to the improved algorithm for the evaluation of the Bouc-Wen constitutive law with  $n < 1$ ) is computational efficient and extremely fast<sup>11</sup>. This has allowed it to be used for probabilistic analyses, which require a large number of analyses to be performed. The results show the validity of the design method with the static models and a good performance, in terms of failure frequency, of the integral abutment overpasses compared to traditional ones.

The work carried out in this thesis has been included in the draft for the new version of Eurocode 8 as a fulfillment of the request for a European-wide calculation method for integral abutment bridges under seismic action. This represents a significant step forward in the definition of a unified and shared calculation method for this type of structures in the professional practice.

The objective initially defined has been achieved: i.e. the improvement of the Franchin-Pinto model and its extension to 3D, the definition and validation of static methods for design, the calculation of seismic risk to verify the performance in the seismic field. The proposed model still has many aspects to be improved, and in particular:

1. Better definition of the interface springs like radiation damping (as stated in section 3.2).
2. Improved definition of the initial state of the system by modeling rheological phenomena and cyclic effects due to seasonal thermal loads between the end of construction process and the seismic event arrival.
3. Extensive comparison between the bi-dimensional and three-dimensional models.
4. Comparison against large scale experimental campaigns outcomes [78] [38] [45].

The main limitation of the dynamic model is that it is validated only in one higher-order numerical case (*Gatteo* overpass described in section 4.2). Moreover the presented framework is limited to skew-less (skew angle lower than  $20^\circ$  as further described in section 3.10) frame-abutment bridges (the model doesn't take into account for other substructure types like the ones listed in figure 1.2). The main approximation in the dynamic model is concentrated in the soil-structure interface elements, that have a roughly approximated phenomenological constitutive law that can be further improved (the very idea of describe the soil-structure interaction with non-linear Winkler springs is a rough approximation). Also the static models can be further improved (for example the linear static one can be modified to eliminate the need for an iterative solution).

---

<sup>10</sup>L'Aquila, Napoli and Milano, indicative respectively of high, medium and low seismicity.

<sup>11</sup>For 2D models it allows to obtain results in real time (the calculation time is smaller than the duration of the simulation).

## Appendix A

# Signal at the bedrock-deposit interface

The Joyner and Chen [69] procedure allows to consider the deformability of the bedrock and, therefore, the dissipation of energy due to the propagation of seismic waves from the rigid outcrop to the contact surface between the bedrock and the superficial loose-soil deposits. The method is based on the assumptions of vertical propagation of a shear wave harmonic, bedrock with elastic-linear mechanical behavior and deposit consisting of a set of horizontal stratifications. The objective is to determine the tangential tension that is transmitted at the interface between the bedrock and the overlying deposit. In the discussion, the reference system is vertical uniaxial, called  $z$ -axis, with origin at the ground plane and positive downward direction. An illustrative diagram of the method under consideration is presented in Figure below.

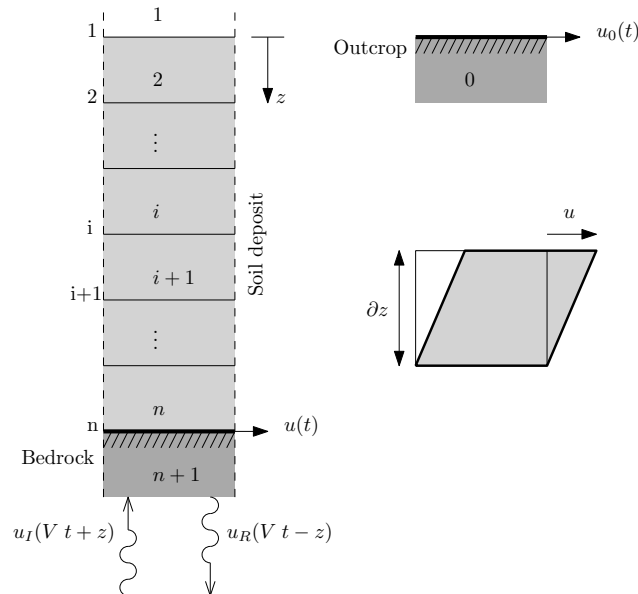


**Figure A.1.** Illustrative scheme to describe the input motion at the bedrock-deposit interface.

That said, the incident wave at the bedrock roof will be partly reflected and partly refracted due to the strong contrast of specific impedances between the bedrock cluster and the overlying loose soil. For the incident wave and the reflected wave, the histories of displacements of the generic soil particle,  $u_I$  and  $u_R$  respectively, are functions that satisfy the equations of motion and thus are presented in this form:

$$u_I = u_I(V_R t + z) \quad u_R = u_R(V_R t - z) \quad (\text{A.1})$$

where in equation (A.1) the minus sign appears because the reflected wave propagates downwards in the positive direction of the  $z$  axis and vice versa for the incident wave. From the theory of elasticity we derive the tangential stresses transmitted at the interface:

$$\tau_b(t) = G_b \gamma_b(t) = G_b \frac{\partial u_b}{\partial z} \quad (\text{A.2})$$

developing we get:

$$\tau_b(t) = \rho_b V_b \left( \frac{\partial u_I}{\partial t} - \frac{\partial u_R}{\partial t} \right) \quad (\text{A.3})$$

so if the motion of the incident wave and the reflected wave in the bedrock is known, the tangential stresses acting on the interface can be defined. The position obtained, however, is not usable in the present case because the seismic input refers to the rigid outcrop and therefore the seismic motion along the separation surface between the bedrock and the loose deposits is not known. Therefore, a link must be found between the motion at the outcrop and the tangential stresses produced at the base of the deformable deposit. The resultant wave crossing the interface is given by the composition of the incident wave with the reflected wave:

$$\frac{\partial u_n}{\partial t} = \frac{\partial u_{I,n}}{\partial t} + \frac{\partial u_{R,n}}{\partial t} \quad (\text{A.4})$$

from which we derive the expression of the motion of the reflected wave at the interface.

$$\frac{\partial u_{R,n}}{\partial t} = \frac{\partial u_n}{\partial t} - \frac{\partial u_{I,n}}{\partial t} \quad (\text{A.5})$$

Furthermore, for the linear elastic bedrock behavior hypothesis we can relate the motion of the incident wave at the interface to the motion at the  $u_0$  outcrop, obtaining the equation:

$$\frac{\partial u_0}{\partial t} = 2 \frac{\partial u_{I,n}}{\partial t} \quad (\text{A.6})$$

Substituting expressions (A.5) and (A.6) into equation (A.3), we arrive at equation (A.7), which expresses the sought-after link between motion at the outcrop and tangential stresses at the bedrock interface.

$$\tau_b(t) = \rho_b V_b \left( \frac{\partial u_0}{\partial t} - \frac{\partial u_n}{\partial t} \right) \quad (\text{A.7})$$

The tangential stress at the bedrock roof is composed of two contributions: the first represented by the term  $\rho_b V_b \frac{\partial u_0}{\partial t}$  which is due to the motion at the outcrop, while the second  $\rho_b V_b \frac{\partial u_n}{\partial t}$  is a function of the seismic motion at the interface between bedrock and loose soils and is a result of the analysis. At the base of the thin bedrock layer,

Lysmer & Kuhlemeyer absorbing barriers are applied according to the seismic wave polarization directions, thus two mutually orthogonal horizontals and one vertical, which are responsible for reproducing the stresses in equation (A.7). In fact, the viscous dampers at the boundary of the domain allow to reproduce the tension that would occur on that surface if the medium were undefined and inherit the mechanical properties of the medium to which they are in contact. Thus, the thin bedrock layer has the function of transmitting its mechanical properties to the dampers in order to have a proper implementation of the Joyner & Chen procedure. By virtue of the above considerations, from the design accelerograms we obtain, by integration, the velocigrams to be applied to the base of the subsurface model.



## Appendix B

# More refined 3D model elements

This appendix considers more refined modeling for the structural elements of the 3D model (see section 3.9) and how these changes affect the overall response of the system. In particular, the following are considered:

- Abutments modeling using *shell* elements,
- Bouc-Wen constitutive law coupled in the two directions  $x$  and  $y$  for soil-column elements.

### B.1 Abutments described with shell elements

In the section 3.9.2, the abutment is modeled using a grid of beams (along  $z$ ) and rigid elements (along  $y$ ). In this section we evaluate the difference, in terms of global system response<sup>1</sup>, with a model with a more advanced modeling using *shell* elements.

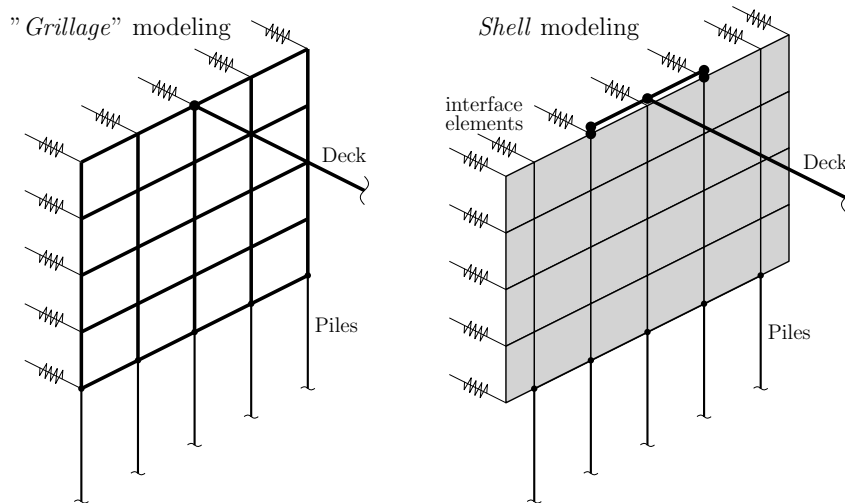


**Figure B.1.** Abutments alternative modeling using shell elements.

<sup>1</sup>Global system response in terms of bending moments at deck-abutments joints, piles head, and center span midpoint

The shell elements used are those implemented in `OpenSEES` under the name `ShellMITC4`, which uses a bilinear isoparametric formulation in combination with a modified shear interpolation to improve the bending performance of thin plates [37].

The modeling of the connection between the deck and the abutments was done through rigid elements that report the joints at the point where the main deck steel beams are supported (see figure B.1).

In the figure B.2 are shown the bending moments around  $y$  at the structure most stressed sections due to a ground motion taken from the set of signals used for the risk analysis. In particular a signal for the site of L'Aquila corresponding to a return period of 1000 years, i.e. for the sixth strip (see section 6.2.2).

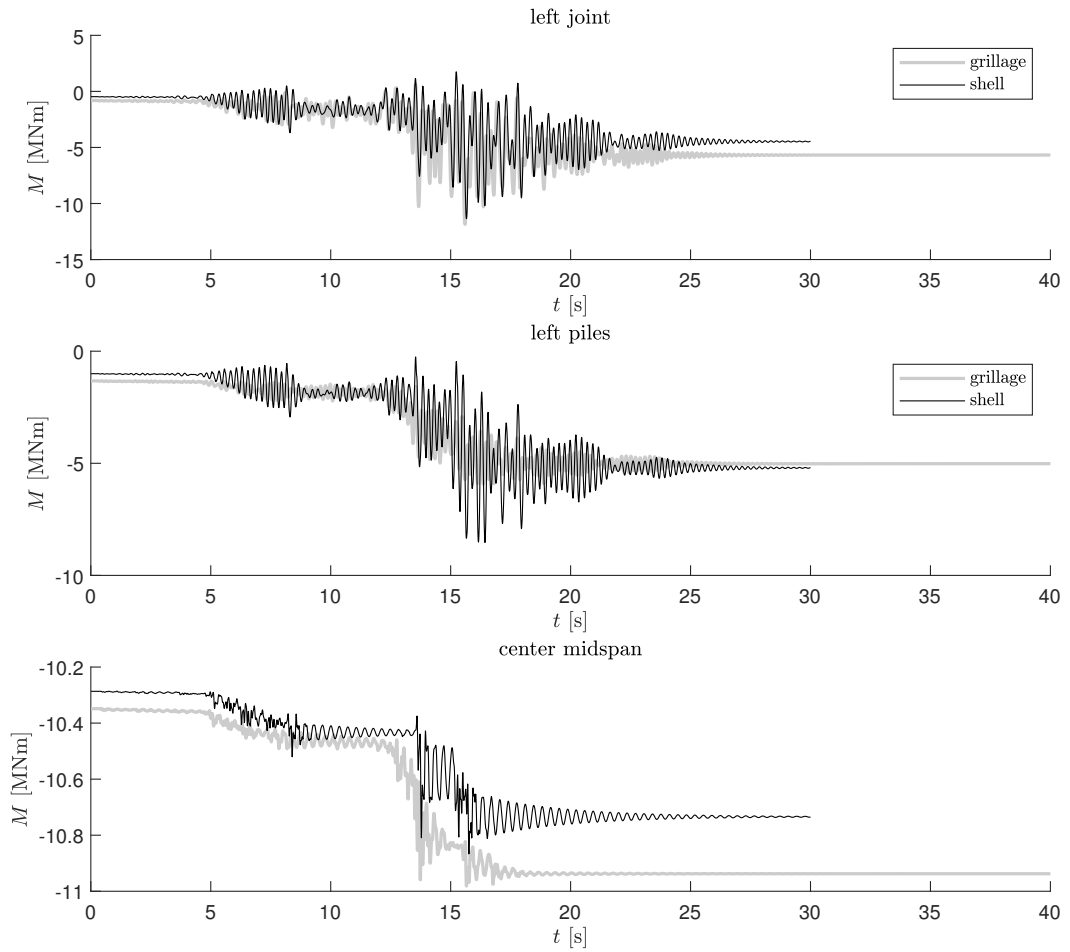


**Figure B.2.** Comparison of bending moments comparison around  $y$  (i.e. in the vertical  $xz$  plane) between grillage (black) and shell (red) abutment modeling.

As can be seen from the figure B.2 the two model responses are very similar. In terms of modal shapes and vibration periods, the two models (with beam grillage and with shell elements) also exhibit the same characteristics.

The analyses conducted with the model using shell elements took longer to complete. Given, therefore, that the result is substantially analogous for both



modeling strategies, for the 3D model (and in the seismic risk analysis) the grillage modeling was used for computational speed reasons.

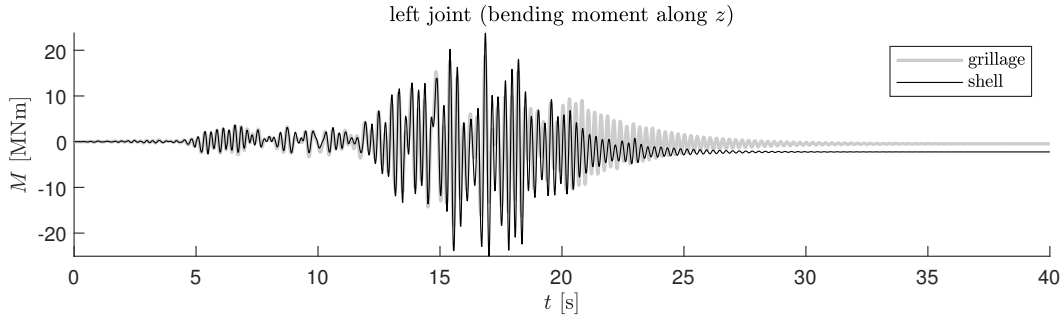


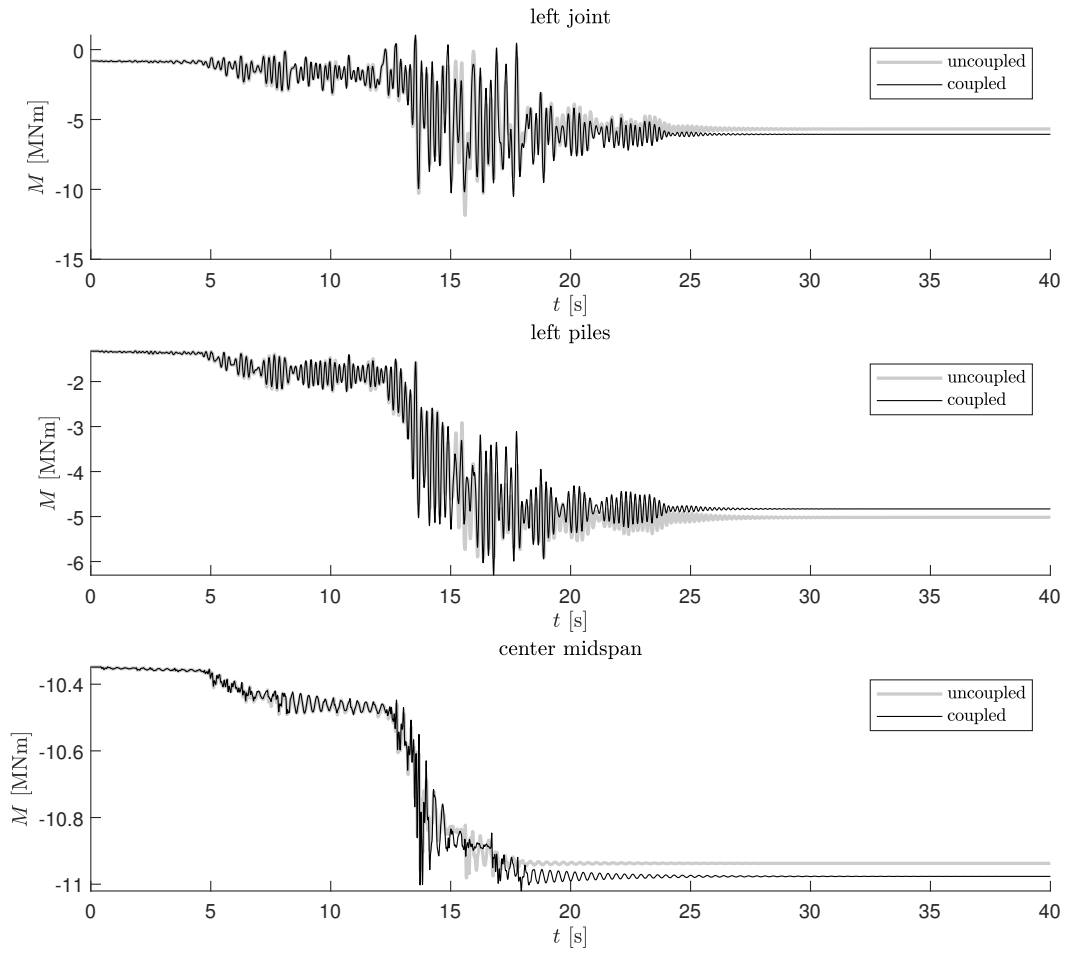
**Figure B.3.** Comparisons of bending moments around  $z$  (i.e. in the horizontal  $xy$  plane) between grillage (black) and shell (red) abutment modeling.

In the figure B.3 shows the comparison, in terms of bending moment around  $z$  for the section at the top of the left abutment. As can be seen from the response, the two models also exhibit a similar behavior in the transverse direction.

This result was however expected, since the abutment, in addition to being a very stiff element with respect to the underlying piles, is restrained at the top by the deck that prevents its deformation in the  $x$ - $y$  plane (the plane of inflection where the null deformability of the rigid elements of the grillage affects the model). For this reason, the responses of the two models are analogous.

## B.2 Coupled Bouc-Wen for soil-column elements

An analysis was also performed with a model that has, for the description of the soil columns, `elastomericBearingBoucWen` elements that have a coupled constitutive law in the two directions  $x$  and  $y$ . The analysis was performed with a seismic motion in its two components in  $x$  and  $y$ .



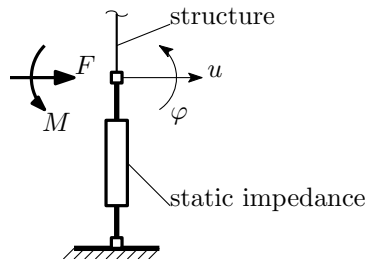
**Figure B.4.** Bending moments comparison (along  $y$ ) between uncoupled Bouc-Wen model (black) and the coupled one (red) in  $x$  and  $y$  direction for soil-column elements.

Figure B.4 shows that the response of the system, in terms of bending moment along  $y$ , does not change by considering a coupled law for the soil-column elements.

## Appendix C

# Static impedances implementation

The static impedances used to discretize the behavior of piles and the soil around them in static models (see chapter 5) can be modeled in various ways into finite-element softwares. Impedances are linear elastic elements<sup>1</sup> in which the stiffness is defined by means of a matrix, since there are coupling components between the translational and rotational degree of freedoms. In particular, since for the piles the behavior is mainly coupled in the horizontal component, the static impedances are defined through the following system of equations:



$$\begin{bmatrix} F \\ M \end{bmatrix} = \begin{bmatrix} K_{hh} & K_{hm} \\ K_{hm} & K_{mm} \end{bmatrix} \begin{bmatrix} u \\ \varphi \end{bmatrix} \quad (\text{C.1})$$

Decoupled from the horizontal-rotational behavior ( $u$ - $\varphi$ ) is also present the vertical<sup>2</sup> one, through the stiffness  $K_{vv}$ . The values of the impedances  $K_{hh}$ ,  $K_{mm}$  and  $K_{hm}$  are defined in the work of Gazetas [51] and recalled in the section 5.1.1. The evaluation of the stiffness  $K_{vv}$  is more complicated, since it is related to the vertical deformability of the soil-pile system, which depends on the friction between the lateral surface of the piles and the deformability of the soil under the piles tip. Detailed evaluations can be found in the section 3.2.3. Since the vertical stiffness is usually greater than the others, one can, in a very first approximation, consider  $K_{vv} \rightarrow \infty$ . Another approximation is to consider the piles as hinged at their tip:

<sup>1</sup>In general impedances depends also on the frequency content of the action, but, in this context, only the static part is considered.

<sup>2</sup>Defining the vertical force  $F_v$  and the vertical displacement  $v$  the complete system of equations is:

$$\begin{bmatrix} F \\ F_v \\ M \end{bmatrix} = \begin{bmatrix} K_{hh} & 0 & K_{hm} \\ 0 & K_{vv} & 0 \\ K_{hm} & 0 & K_{mm} \end{bmatrix} \begin{bmatrix} u \\ v \\ \varphi \end{bmatrix} \quad (\text{C.2})$$

that is, as if no friction is present between the side surface of the pile and the soil below it's infinitely stiff<sup>3</sup>. In that case the axial stiffness is given by the axial stiffness of the piles:

$$K_{vv} = n_p \frac{EA}{L_p} \quad (C.3)$$

Where  $n_p$  is the piles number.

In SAP2000 it is possible to define links with coupled stiffnesses in various degrees of freedom, while in OpenSEES (to date) this is not possible. In the following two equivalent systems are described that can be used to model static impedances with springs and linear elastic beam elements.

### C.1 Springs with a rigid element

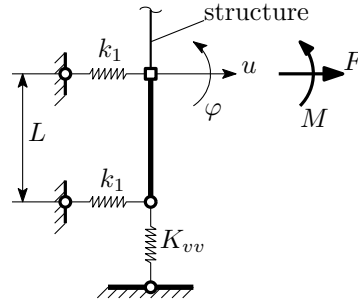


**Figure C.1.** Static impedances equivalent system with linear springs and a rigid element.

The system of equations governing this system is:

$$\begin{bmatrix} F \\ M \end{bmatrix} = \begin{bmatrix} (k_1 + k_2) & k_2 L \\ k_2 L & k_2 L^2 \end{bmatrix} \begin{bmatrix} u \\ \varphi \end{bmatrix} \quad \text{Parameters: } \begin{cases} k_1 = K_{hh} - k_2 \\ k_2 = \frac{K_{hm}^2}{K_{mm}} \\ L = \frac{K_{mm}}{K_{hm}} \end{cases} \quad (C.4)$$

The advantages of this system are that the equations are simple and it is easy conceptually. However, it has a rigid element<sup>4</sup>, which could give problems to the stiffness matrix inversion algorithm. It also has a relatively large number of nodes, elements and materials (5 nodes, 4 elements and 3 materials)<sup>5</sup>. For this reasons, in the next section, another equivalent system is proposed.

<sup>3</sup>This approximation is less acceptable for friction piles.

<sup>4</sup>The rigid element can be modeled through a beam element with a unit area and inertia and a large elastic modulus. Usually  $10^{12}$  kPa is enough; greater values can lead to numerical instabilities in the linear system solver.

<sup>5</sup>Number of nodes, elements and materials according to the implementation in OpenSEES.

## C.2 Euler-Bernoulli beam with a rotational spring

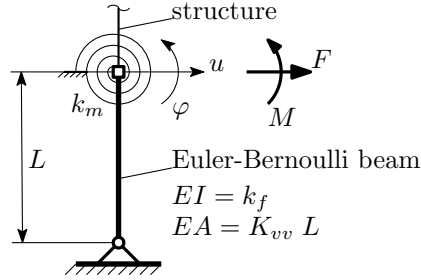


**Figure C.2.** Static impedances equivalent system with Euler-Bernoulli linear beam and a rotational spring.

The system of equations governing this system is:

$$\begin{bmatrix} F \\ M \end{bmatrix} = \begin{bmatrix} \frac{3k_f}{L^3} & \frac{3k_f}{L^2} \\ \frac{3k_f}{L^2} & \frac{3k_f}{L} + k_m \end{bmatrix} \begin{bmatrix} u \\ \varphi \end{bmatrix} \quad \text{Parameters: } \begin{cases} k_f = \frac{K_{hm}^3}{3K_{hh}^2} \\ k_m = K_{mm} - \frac{K_{hm}^2}{K_{hh}} \\ L = \frac{K_{hm}}{K_{hh}} \end{cases} \quad (\text{C.5})$$

This equivalent system has the same advantages of the previous one and, in addition, has a lower number of nodes, elements and materials (3 nodes, 2 elements and 1 material) and has no rigid elements. The flexural stiffness  $EI = k_f$  and the axial stiffness  $EA = K_{vv} L$  of the Euler-Bernoulli beam, assuming a unit cross-section rotational inertia ( $I = 1$ ), lead to the following definition of the beam parameters:

$$E = k_f \quad A = \frac{K_{vv} L}{k_f} \quad (\text{C.6})$$

It can be seen that, in the absence of the rotational spring, the equivalent system is free. Moreover, without the rotational spring, the system has only 2 parameters instead of 3 (there must be three parameters to correlate with the three static impedances).



## Appendix D

# Parameters sensitivity

The Input Parameters (IP) that are considered for sensitivity analyses are:

- exponent  $n$  of Bouc-Wen constitutive law for soil-column elements
- passive limit  $K_p$  for interface elements
- base damper coefficient  $C_b$
- stiffness ratio  $\hat{r}_{EI}$  between abutments, piles and deck

The analysis are done keeping all parameters to values of the single span benchmark case (*Gatteo* overpass described in section 4.2) and varying only the parameter of interest between the specified limits.

### D.0.1 Soil-column Bouc-Wen exponent $n$

The exponent  $n$  is defined in the Bouc-Wen internal equation (2.2). In the original model (described in section 2.4.2) this parameter was set equal to 2.0 and, in the modified model, is a function of the soil plasticity index and confining pressure and varies from 0.4 and 1.2. In this case the range is starting from 0.1 to further explore the variation in system response with small values of  $n$ . The range of this parameter is then set equal to:

$$n \in [0.1, 2.0] \quad (\text{D.1})$$

In the figures D.1 and D.2 results in terms of bending moments on the bridge structure are presented.

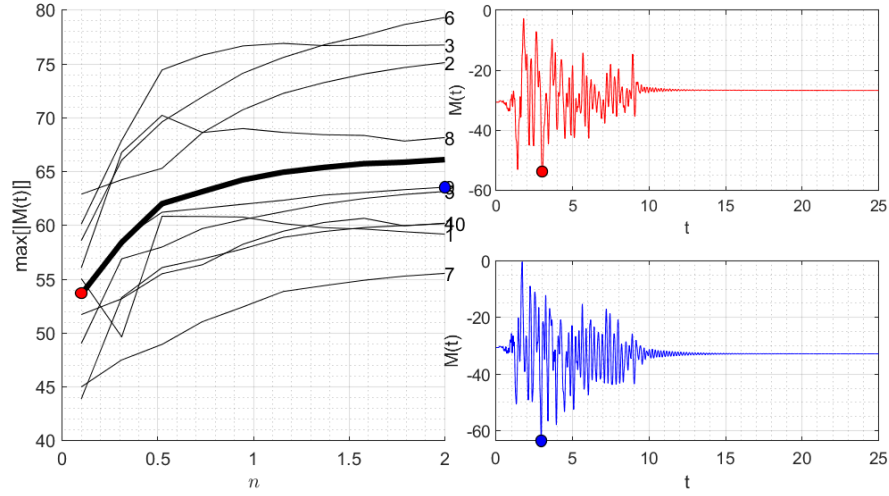


**Figure D.1.** Variation of bending moment at left deck-abutment joint versus parameter  $n$  of the Bouc-Wen constitutive law.

In the left part of the figure is plotted, varying the parameter  $X_i$ , the maximum of the absolute value of the bending moment  $EDP_m^{(j)}(X_i)$  (defined in equation 3.45) for every seismic signal ( $j$ ) (with thin lines). With the wider line is plotted the mean value  $\mu_{EDP_m}(X_i)$  over all the ( $j$ ) seismic signals. It can be noticed that, in terms of bending moments on the abutments, the lower the value of  $n$  the more system output change. Increasing  $n$  the bending moment also increase. This is because, increasing  $n$  in the Bouc-Wen model, the model itself becomes similar to an elasto-plastic model (with  $n = \infty$  the Bouc-Wen model is exactly an elasto-plastic model). So decreasing  $n$  the non-linear behavior of the model, for displacements smaller than the yielding one, also increase. Decreasing  $n$  increase nonlinear hysteretic behavior and also damping increase (due to hysteretic behavior).

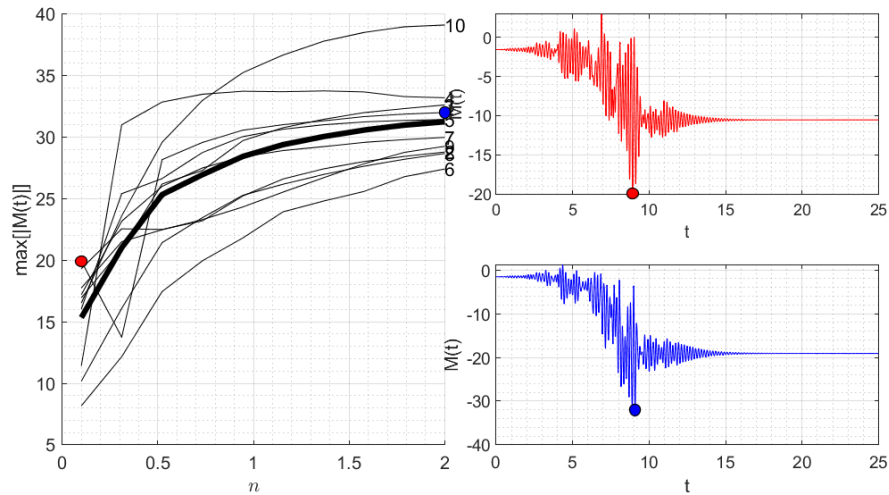


**Figure D.2.** Variation of bending moment at left piles head versus parameter  $n$  of the Bouc-Wen constitutive law.



The behavior described above is also visible for the bending moments at the piles head. The model is more sensible to  $n$  in range from 0.1 to 1.0 than in the range from 1.0 to 2.0. This is the same result described above and is even more visible in the local seismic site-response analysis, where only the soil-column is considered in the model. In this latter case an amplification is visible considering results in term of response spectra. The soil-response analysis presents higher spectral coordinates due to the lower hysteretic damping (see section 4.4).

### D.0.2 Interface elements passive limit

For the interface elements, the passive limit varies between that defined by Rankine [97] and that defined by Lancellotta [76]. In particular, for the particular soil deposit considered in the benchmark case described in section 4.2, a coefficient of passive stress  $K_p$  varying between 4 and 8 is taken.

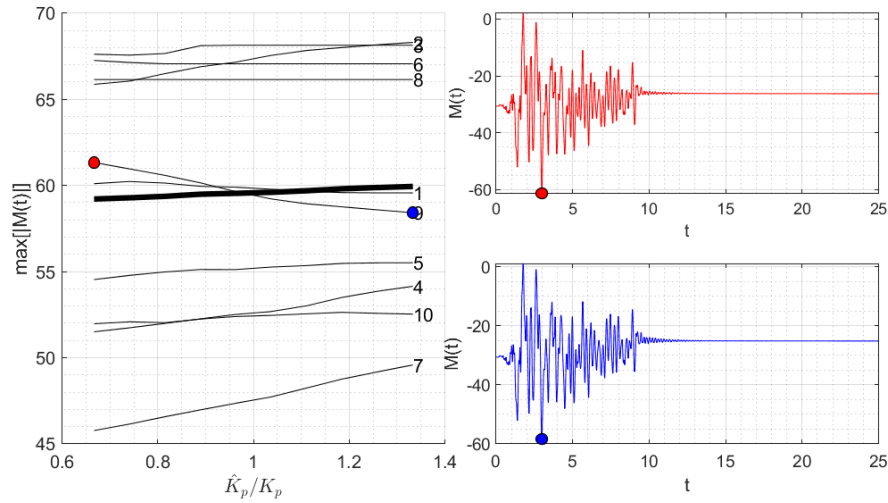


**Figure D.3.** Response in terms of bending moment at left deck-abutment joint varying  $K_p$  of interface elements.

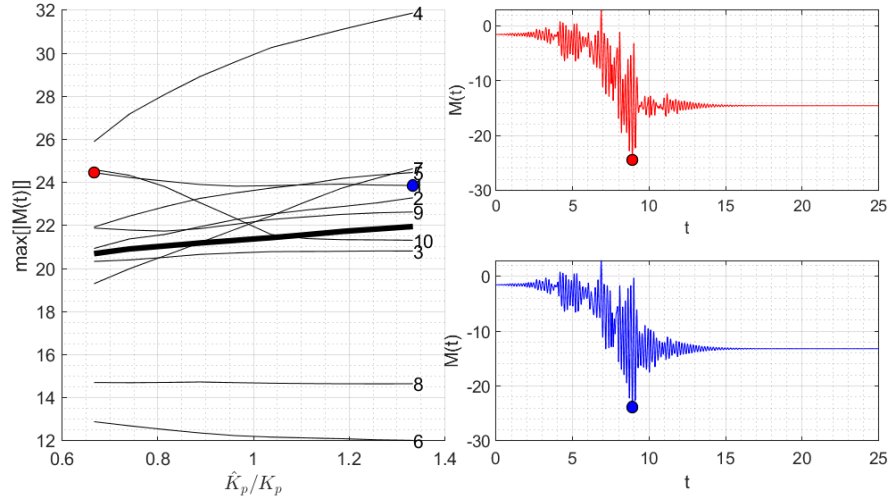


**Figure D.4.** Response in terms of bending moment at left piles head varying  $K_p$  of interface elements.

As can be seen from the results presented in the figures D.3 and D.4, as the passive limits for the interface elements change, the system response in terms of bending moment does not change much.

In the figure D.5 is shown the trend of the stresses on the structure varying the passive limit of the interface elements.

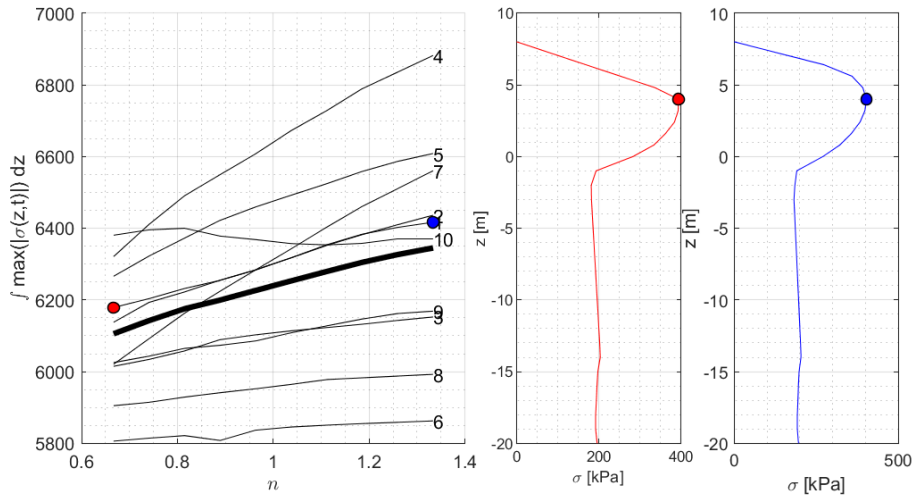


**Figure D.5.** Response in terms of soil stresses over the left abutment-piles alignment varying  $K_p$  of interface elements.

As simple output parameter indicative of the trend of maximum earth pressure on the structure, the total horizontal force (i.e., the integral along  $z$ ) was initially considered. This is the OP  $EDP_p^{(j)}$  defined in equation 3.50 for the  $(j)$ -th ground

motion. Greater variability can be noted with respect to soil stresses. Obviously, as the passive limit increases, the soil pressures on the structure also increase.

### D.0.3 Base damper coefficient

Varying the bedrock stiffness varies also the coefficient of the base damper

$$c_b = \rho_b V_{s,b} A_s(z_b) \quad (D.2)$$

where  $\rho_b$  is the bedrock density,  $V_{s,b}$  the bedrock shear-wave velocity and  $A_s(z_b)$  the area of the soil-column bottom element.

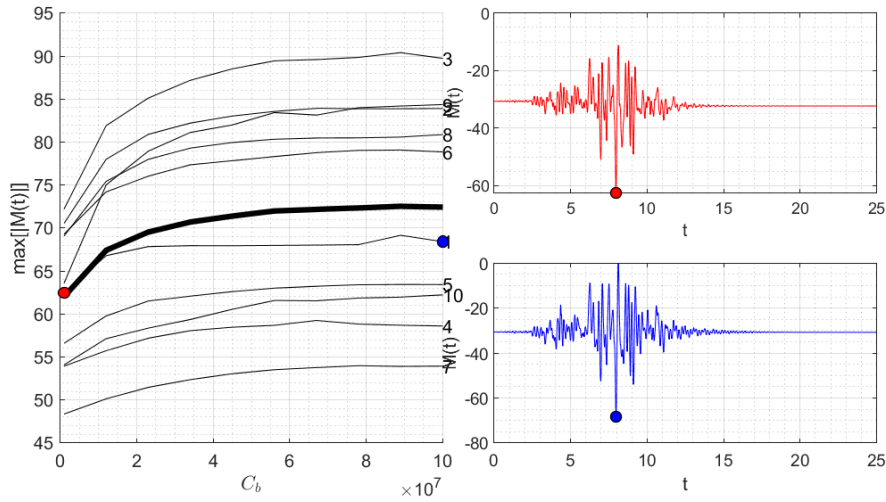


**Figure D.6.** Response in terms of bending moment at left deck-abutment joint varying base damper coefficient.

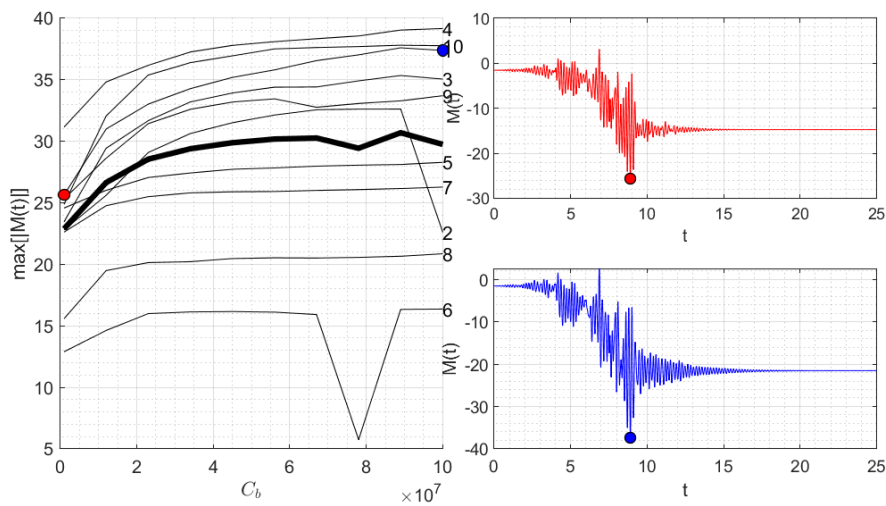


**Figure D.7.** Response in terms of bending moment at left piles head varying base damper coefficient.

Lower values of  $c_b$  means lower values for bedrock stiffness (calculated through the shear wave velocity  $V_{sb} = \sqrt{E_b/[2\rho_b(1+\nu)]}$ ). This leads to a change in the impedance between bedrock and soil-deposit. Also the relative large parameter variation interval causes a decrease in the force applied on the model and so a decrease in the bending moments in the structure decreasing  $c_b$ .

#### D.0.4 Abutment-deck and piles-deck stiffness ratios

The first generation of integral-abutment bridges (those built since the 1960s in the United States) were characterized by having foundations formed by steel piles with high flexibility along the longitudinal direction. This flexibility was used to accommodate the deck deformations caused by the temperature. The search for high flexibility of the foundation is the main reason why integral bridges have a single row of piles to support the abutments. In order to decrease the stiffness at the top of the piles, it was also usual to separate the pile from the surrounding soil by means of steel profiles with a circular hollow section. The typology of integral-abutment bridge mainly studied in the following thesis is the one with reinforced concrete foundations. This is the reason why, in this section, the global behavior of the system is studied varying the stiffness ratios between deck and substructure (abutments and piles). The individual elements present a modified flexural stiffness:

$$\hat{EI} = \hat{r}_{EI} EI \quad (D.3)$$

The range of variability of the parameter  $\hat{r}_{EI}$  was taken equal to:

$$\hat{r}_{EI} \in [0.5, 2.0] \quad (D.4)$$

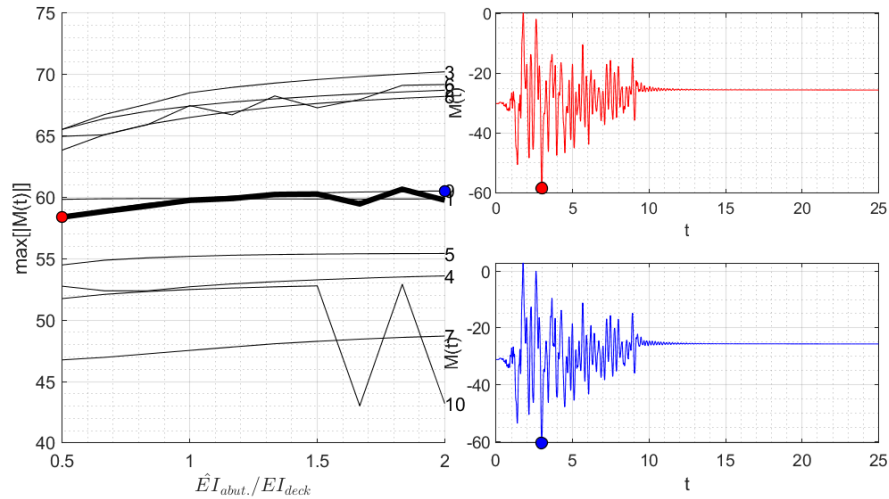


**Figure D.8.** Response in terms of bending moment at left deck-abutment joint varying ratio between abutment and deck stiffness.

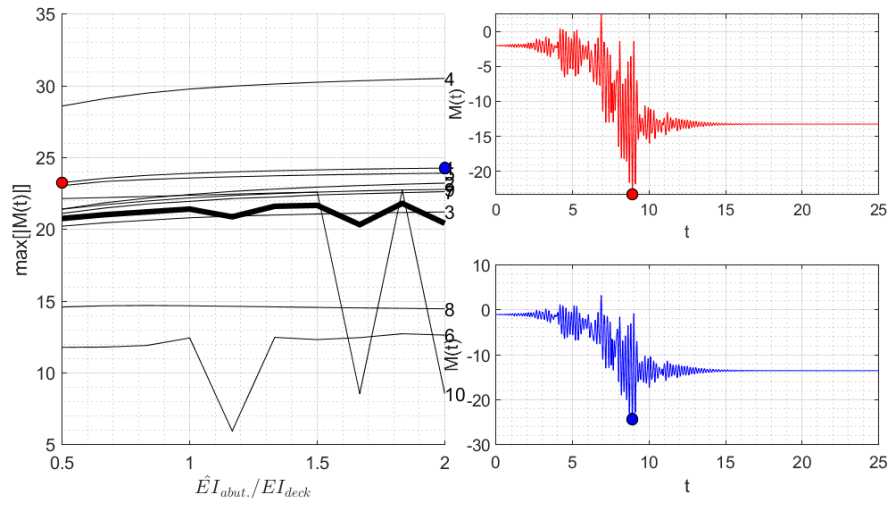


**Figure D.9.** Response in terms of bending moment at left piles head varying ratio between abutment and deck stiffness.

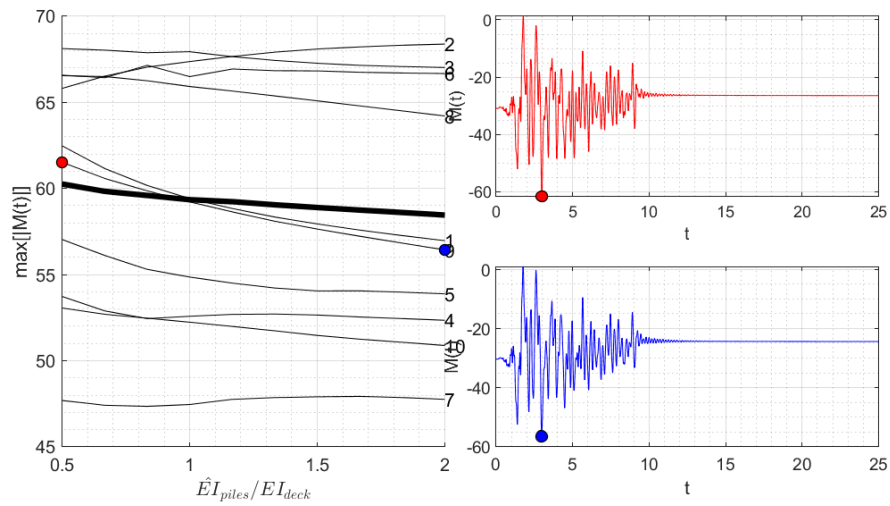


**Figure D.10.** Response in terms of bending moment at left deck-abutment joint varying ratio between piles and deck stiffness.

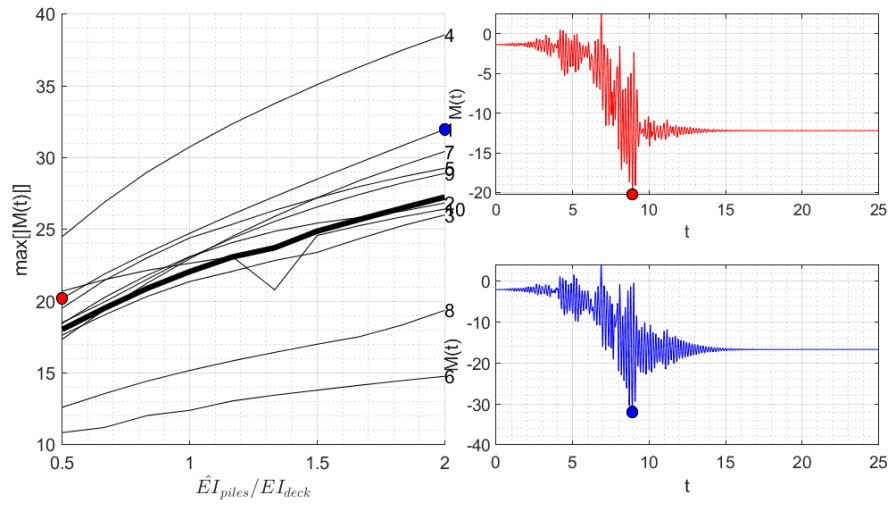


**Figure D.11.** Response in terms of bending moment at left piles head varying ratio between piles and deck stiffness.

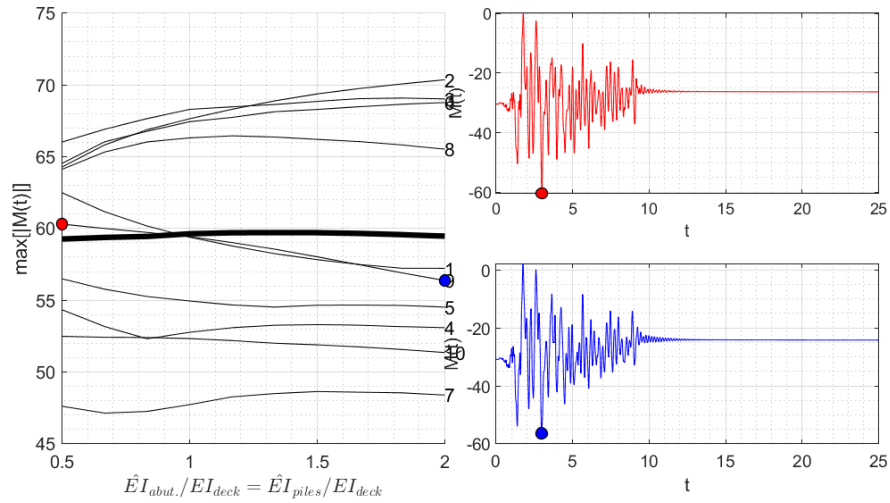


**Figure D.12.** Response in terms of bending moment at left deck-abutment joint varying abutment-deck and piles-deck stiffness ratios.

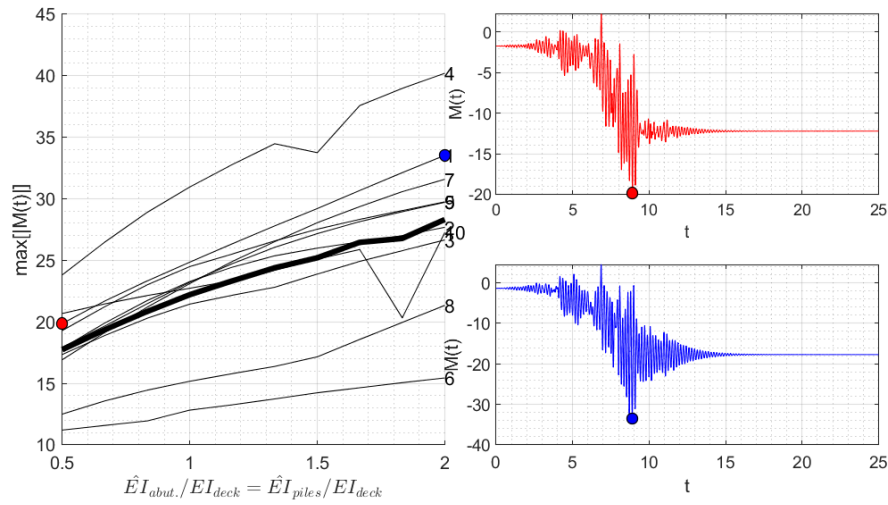


**Figure D.13.** Response in terms of bending moment at left piles head varying abutment-deck and piles-deck stiffness ratios.

As can be seen from the results presented in the figures, the parameters that most modify the response of the system in terms of bending moment at the piles head is the stiffness ratio between the piles and the deck. Lower stiffness brings lower stresses on the piles. It appears that the abutments-deck stiffness ratio does not affect the system response. Even the bending moment at top abutment cross-section is not affected by the piles stiffness variation. This can mainly be caused by the short length of these elements compared with the piles.

The soil stresses on the structure are not affected by the relative stiffness ratios.

Modifying the geometric ratios between the various structural elements, the system vibration modes clearly change. However, these are only slightly modified.





## Appendix E

# Seismic risk results

This appendix shows all results (time histories and global results) for the various strips for each site considered.

### E.1 Results summary

		L'AQUILA										NAPOLI										MILANO									
		IML1	IML2	IML3	IML4	IML5	IML6	IML7	IML8	IML9	IML10	IML1	IML2	IML3	IML4	IML5	IML6	IML7	IML8	IML9	IML10	IML1	IML2	IML3	IML4	IML5	IML6	IML7	IML8	IML9	IML10
RAPPORTI D/C USABILITY	RUN1	0.2	0.16	0.22	0.27	0.29	0.5	0.43	1.24	8.04	37.4	0.11	0.16	0.23	0.3	0.29	0.28	0.36	0.46	0.64	0.95	0.14	0.17	0.16	0.16	0.2	0.21	0.18	0.2	0.28	0.45
	RUN2	0.15	0.1	0.23	0.19	0.48	0.49	0.76	2.19	13.1	50.4	0.08	0.2	0.31	0.37	0.2	0.36	0.5	0.61	0.52	0.83	0.11	0.12	0.13	0.19	0.11	0.24	0.15	0.2	0.25	0.37
	RUN3	0.13	0.16	0.26	0.35	0.25	0.43	0.91	3.58	15.2	177	0.06	0.12	0.17	0.24	0.3	0.36	0.45	0.54	0.5	0.75	0.12	0.1	0.11	0.12	0.23	0.13	0.18	0.22	0.43	0.35
	RUN4	0.12	0.12	0.21	0.21	0.26	0.57	0.68	0.88	3.7	363	0.1	0.09	0.47	0.54	0.26	0.34	0.45	0.6	0.79	1.16	0.12	0.15	0.25	0.17	0.2	0.12	0.23	0.36	0.26	0.34
	RUN5	0.09	0.16	0.16	0.43	0.38	0.34	0.65	23.7	5.45	114	0.08	0.24	0.08	0.2	0.44	0.36	0.53	0.6	0.68	0.97	0.11	0.16	0.14	0.15	0.17	0.25	0.25	0.4	0.29	0.25
	RUN6	0.13	0.19	0.31	0.23	0.44	0.66	0.77	0.89	135	1107	0.07	0.11	0.19	0.28	0.49	0.4	0.34	0.69	1.07	1.3	0.09	0.12	0.1	0.13	0.17	0.25	0.28	0.29	0.3	0.44
	RUN7	0.12	0.17	0.2	0.27	0.26	0.36	0.63	1.1	3.55	69.1	0.07	0.38	0.2	0.11	0.4	0.32	0.51	0.3	0.84	1.27	0.09	0.12	0.19	0.16	0.23	0.18	0.32	0.22	0.37	0.4
	RUN8	0.11	0.14	0.17	0.3	0.3	0.48	0.83	0.55	0.79	46.3	0.1	0.08	0.22	0.24	0.35	0.59	0.87	0.84	1	1.15	0.12	0.11	0.15	0.18	0.16	0.22	0.22	0.39	0.38	0.4
	RUN9	0.12	0.14	0.24	0.31	0.71	0.79	0.76	0.68	15.2	7.64	0.13	0.13	0.25	0.25	0.32	0.34	0.42	0.71	1.18	1.3	0.13	0.13	0.2	0.15	0.19	0.23	0.21	0.31	0.28	0.36
	RUN10	0.07	0.17	0.21	0.35	0.48	0.55	0.73	4.08	14.1	160	0.07	0.11	0.35	0.26	0.34	0.45	0.57	1.03	0.85	2.73	0.09	0.19	0.15	0.2	0.13	0.28	0.24	0.25	0.34	0.25
	RUN11	0.08	0.2	0.25	0.37	0.34	0.49	0.47	1.51	7.46	14	0.09	0.13	0.15	0.3	0.49	0.51	1.43	0.51	0.72	0.68	0.09	0.12	0.12	0.2	0.12	0.23	0.29	0.32	0.29	0.43
	RUN12	0.1	0.09	0.16	0.28	0.23	0.85	0.68	0.77	12.7	23.8	0.09	0.12	0.42	0.44	0.38	0.41	0.6	0.69	0.62	1.31	0.1	0.14	0.16	0.16	0.16	0.22	0.21	0.24	0.33	0.47
	RUN13	0.09	0.21	0.11	0.37	0.4	0.47	0.8	0.84	2.6	67.3	0.08	0.13	0.26	0.35	0.51	0.5	0.8	0.7	0.73	1.06	0.13	0.13	0.18	0.14	0.22	0.12	0.25	0.24	0.28	0.28
	RUN14	0.09	0.12	0.2	0.2	0.39	0.35	0.66	0.89	22	36.2	0.09	0.22	0.19	0.31	0.4	0.63	0.62	1.21	0.51	0.83	0.11	0.13	0.12	0.11	0.16	0.16	0.32	0.3	0.2	0.63
	RUN15	0.09	0.1	0.21	0.29	0.26	0.63	0.78	1.07	2.13	58.9	0.11	0.28	0.16	0.37	0.39	0.26	0.97	0.38	1.11	1.09	0.09	0.12	0.12	0.14	0.11	0.15	0.17	0.23	0.38	0.32
	RUN16	0.12	0.13	0.2	0.41	0.4	1.37	0.44	5.32	5.19	40.5	0.09	0.09	0.17	0.17	0.24	0.66	0.31	0.89	1.27	1.1	0.12	0.09	0.24	0.12	0.18	0.22	0.19	0.23	0.22	0.27
	RUN17	0.1	0.12	0.22	0.2	0.44	0.68	0.65	8.1	1.1	76.7	0.11	0.23	0.13	0.23	0.29	0.46	0.81	0.9	1.15	4.23	0.09	0.14	0.16	0.17	0.18	0.27	0.29	0.33	0.43	0.63
	RUN18	0.09	0.14	0.16	0.23	0.31	0.41	0.71	0.6	47.3	90.5	0.13	0.16	0.2	0.27	0.36	0.31	0.71	0.54	0.72	2.73	0.09	0.11	0.1	0.25	0.15	0.22	0.34	0.17	0.2	0.42
	RUN19	0.1	0.14	0.16	0.29	0.31	0.48	0.78	0.81	10.5	13	0.05	0.12	0.34	0.25	0.2	0.45	0.42	0.77	0.83	1.24	0.14	0.09	0.16	0.18	0.2	0.25	0.14	0.22	0.27	0.31
	RUN20	0.15	0.2	0.27	0.19	0.54	0.37	0.71	1.59	1.41	63.1	0.1	0.22	0.12	0.45	0.63	0.75	0.59	0.71	1.01	1.07	0.09	0.09	0.11	0.18	0.21	0.22	0.15	0.22	0.18	0.24
RAPPORTI D/C SEVERE DAMAGE	RUN1	0.04	0.03	0.05	0.06	0.06	0.1	0.09	0.22	1.67	6.04	0.02	0.02	0.04	0.04	0.05	0.04	0.05	0.07	0.1	0.14	0.02	0.02	0.02	0.03	0.03	0.04	0.03	0.03	0.04	0.09
	RUN2	0.03	0.02	0.05	0.04	0.1	0.1	0.16	0.45	2.72	10.1	0.01	0.03	0.05	0.06	0.03	0.07	0.09	0.1	0.07	0.1	0.02	0.02	0.02	0.03	0.02	0.04	0.02	0.03	0.04	0.07
	RUN3	0.03	0.03	0.05	0.07	0.05	0.09	0.19	0.75	3.16	36.8	0.01	0.02	0.03	0.03	0.04	0.05	0.07	0.09	0.08	0.14	0.02	0.02	0.02	0.03	0.02	0.03	0.04	0.06	0.05	0.05
	RUN4	0.03	0.03	0.03	0.04	0.06	0.12	0.14	0.18	0.77	60.2	0.02	0.02	0.06	0.08	0.04	0.05	0.07	0.09	0.13	0.23	0.02	0.02	0.02	0.03	0.02	0.03	0.04	0.06	0.05	0.05
	RUN5	0.02	0.04	0.03	0.09	0.08	0.07	0.13	2.7	0.73	20.9	0.02	0.03	0.01	0.03	0.08	0.07	0.07	0.08	0.11	0.15	0.02	0.02	0.02	0.03	0.03	0.04	0.04	0.05	0.05	0.04
	RUN6	0.03	0.04	0.07	0.05	0.09	0.14	0.16	0.19	25.2	174	0.01	0.02	0.02	0.05	0.06	0.06	0.06	0.09	0.16	0.25	0.02	0.02	0.02	0.02	0.03	0.04	0.04	0.04	0.05	0.06
	RUN7	0.02	0.03	0.04	0.06	0.05	0.07	0.14	0.23	0.74	14.4	0.01	0.06	0.03	0.02	0.08	0.1	0.08	0.04	0.11	0.13	0.02	0.02	0.03	0.03	0.03	0.03	0.04	0.04	0.06	0.07
	RUN8	0.02	0.03	0.03	0.06	0.06	0.1	0.17	0.11	0.15	9.75	0.02	0.02	0.03	0.03	0.05	0.08	0.12	0.13	0.12	0.18	0.02	0.02	0.02	0.02	0.02	0.04	0.04	0.07	0.05	0.05
	RUN9	0.02	0.03	0.05	0.06	0.15	0.16	0.16	0.14	3.16	1.19	0.02	0.02	0.04	0.03	0.04	0.05	0.06	0.1	0.23	0.17	0.02	0.02	0.03	0.03	0.03	0.04	0.03	0.05	0.04	0.05
	RUN10	0.02	0.03	0.04	0.07	0.1	0.11	0.13	0.85	1.73	32.8	0.01	0.02	0.04	0.04	0.05	0.06	0.08	0.14	0.11	0.53	0.02	0.02	0.03	0.02	0.03	0.03	0.04	0.03	0.07	0.04
	RUN11	0.02	0.04	0.05	0.08	0.07	0.1	0.1	0.31	1.14	2.06	0.01	0.03	0.02	0.05	0.08	0.09	0.28	0.07	0.11	0.16	0.02	0.02	0.02	0.03	0.02	0.03	0.04	0.05	0.04	0.06
	RUN12	0.02	0.02	0.03	0.06	0.05	0.18	0.14	0.16	2.65	4.96	0.02	0.02	0.05	0.07	0.05	0.05	0.09	0.09	0.13	0.26	0.02	0.02	0.03	0.02	0.03	0.03	0.03	0.04	0.05	0.06
	RUN13	0.02	0.04	0.02	0.08	0.08	0.1	0.17	0.17	0.54	13.3	0.01	0.02	0.03	0.06	0.06	0.08	0.12	0.11	0.11	0.15	0.02	0.02	0.02	0.02	0.03	0.02	0.05	0.03	0.05	0.05
	RUN14	0.02	0.02	0.04	0.04	0.08	0.07	0.11	0.19	4.58	7.54	0.02	0.04	0.03	0.04	0.06	0.1	0.08	0.16	0.08	0.11	0.02	0.02	0.02	0.02	0.02	0.03	0.05	0.04	0.03	0.03
	RUN15	0.02	0.02	0.04	0.06	0.05	0.13	0.16	0.22	0.32	11.8	0.02	0.04	0.03	0.05	0.05	0.04	0.13	0.06	0.15	0.15	0.02	0.02	0.02	0.03	0.02	0.03	0.03	0.04	0.05	0.04
	RUN16	0.02	0.03	0.04	0.08	0.08	0.29	0.09	1.11	0.8	6.51	0.02	0.02	0.02	0.03	0.04	0.07	0.05	0.12	0.14	0.17	0.02	0.02	0.02	0.03	0.02	0.03	0.03	0.04	0.03	0.05
	RUN17	0.02	0.02	0.05	0.04	0.09	0.14	0.14	1.68	0.23	11.1	0.02	0.03	0.02	0.03	0.04	0.06	0.09	0.11	0.15	0.53	0.02	0.02	0.03	0.03	0.03	0.04	0.04	0.05	0.06	0.11
	RUN18	0.02	0.03	0.03	0.05	0.17	0.07	0.15	0.11	3.21	14.5	0.02	0.02	0.03	0.04	0.06	0.05	0.1	0.08	0.1	0.36	0.02	0.02	0.02	0.04	0.02	0.03	0.05	0.03	0.03	0.06
	RUN19	0.02	0.03	0.03	0.06	0.06	0.1	0.16	0.17	2.19	2.7	0.01	0.02	0.04	0.04	0.03	0.07	0.07	0.12	0.11	0.15	0.02	0.02	0.02	0.02	0.03	0.03	0.03	0.04	0.04	0.04
	RUN20	0.03	0.04	0.06	0.04	0.11	0.07	0.15	0.33	0.29	11.1	0.02	0.03	0.02	0.06	0.1	0.12	0.09	0.1	0.13	0.17	0.02	0.02	0.02	0.02	0.03	0.03	0.03	0		
3D 1PER	LS	IML1	IML2	IML3	IML4	IML5	IML6	IML7	IML8	IML9	IML10	IML1	IML2	IML3	IML4	IML5	IML6	IML7	IML8	IML9	IML10	IML1	IML2	IML3	IML4	IML5	IML6	IML7	IML8	IML9	IML10
	usability	0	0	0	0	0	1	0	11	19	20	0	0	0	0	0	0	1	2	7	14	0	0	0	0	0	0	0	0	0	0
source damage	0	0	0	0	0	0	0	3	11	20	0	0	0	0	0	0	0	0	0	0	0	0	0	0	0	0	0	0	0	0	0

## E.2 Time series

### E.2.1 MI

#### IML 3

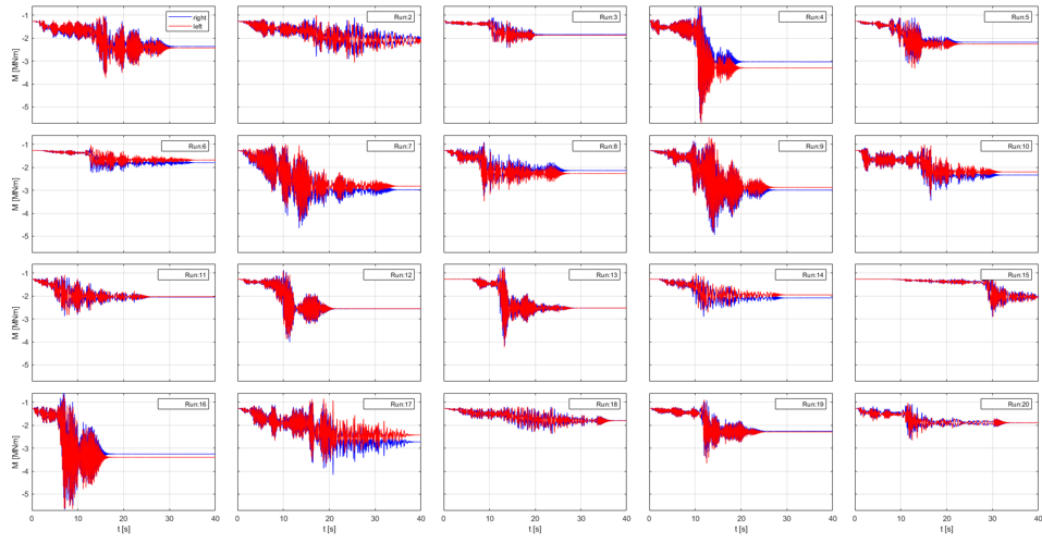


Figure E.2. Milano (IML3): bending moment at deck-abutments joints.

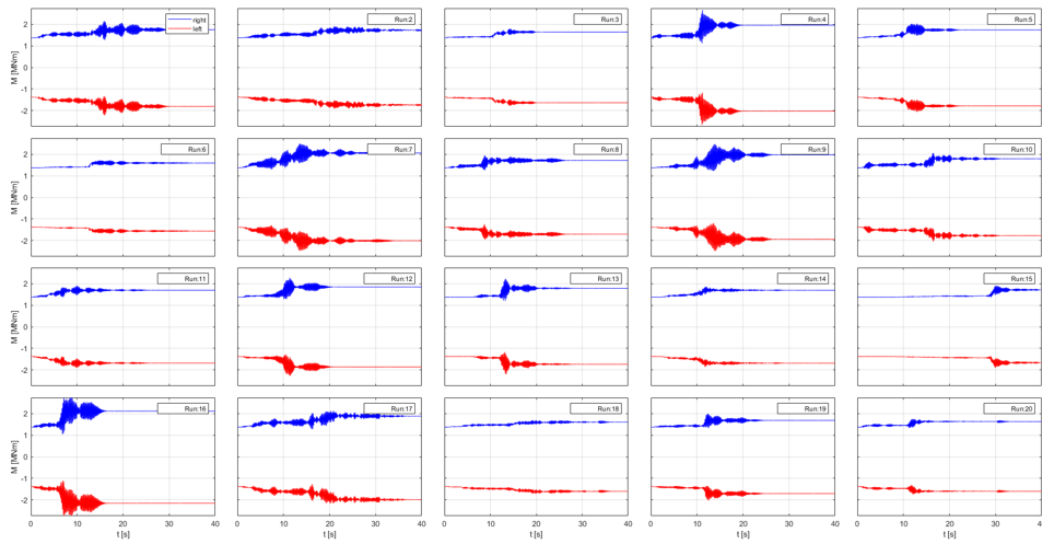


Figure E.3. Milano (IML3): bending moment at piles head.

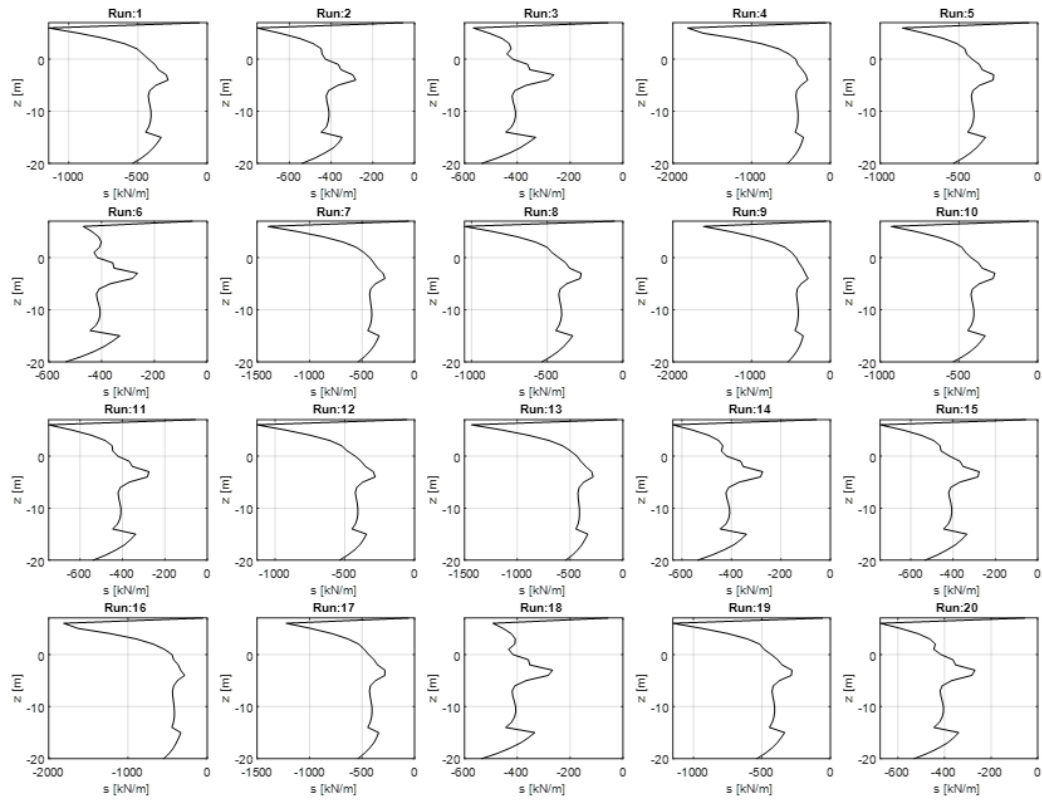


Figure E.4. Milano (IML3): earth pressures on left abutment-piles alignment.

## IML 6

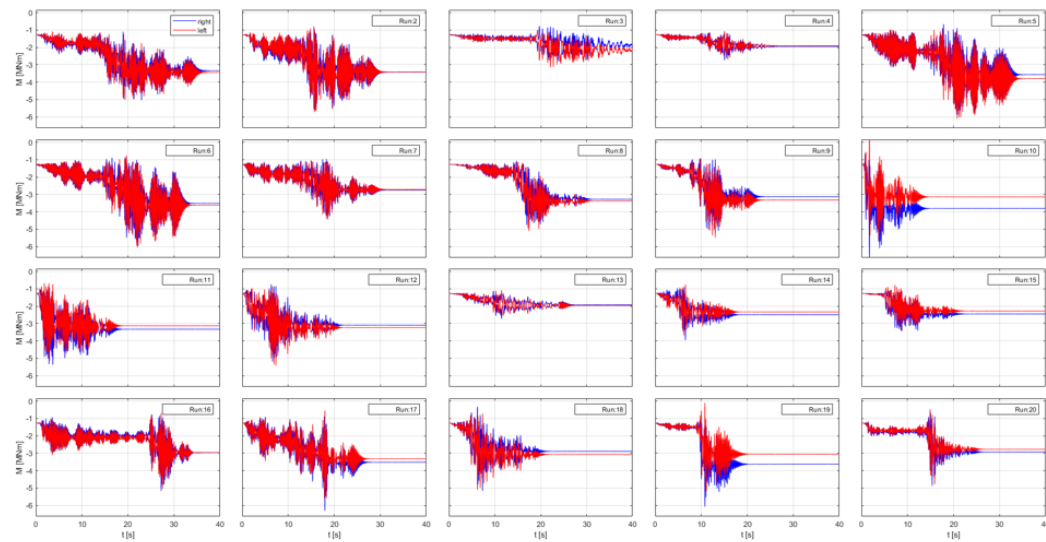


Figure E.5. Milano (IML6): bending moment at deck-abutments joints.

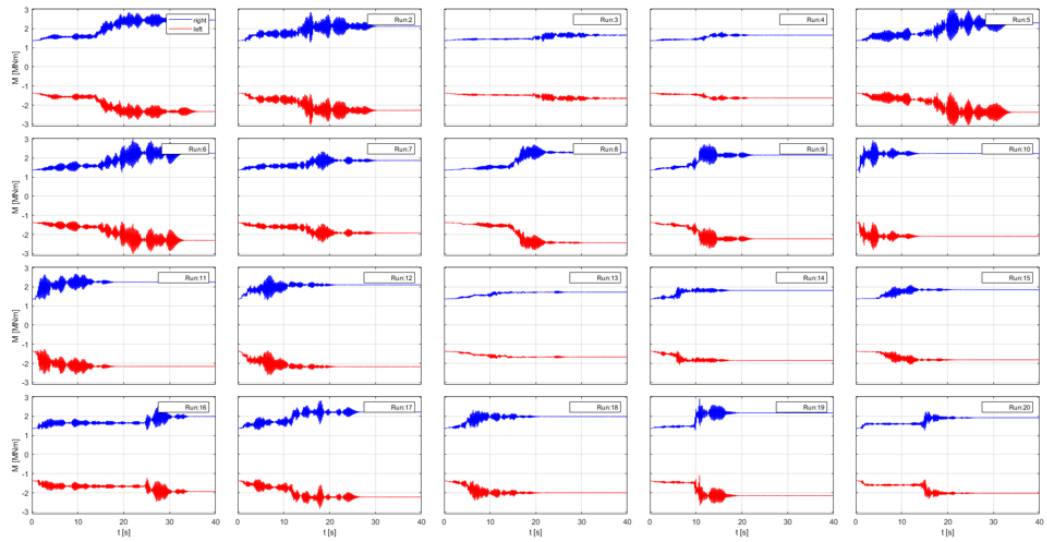


Figure E.6. Milano (IML6): bending moment at piles head.

### IML 9

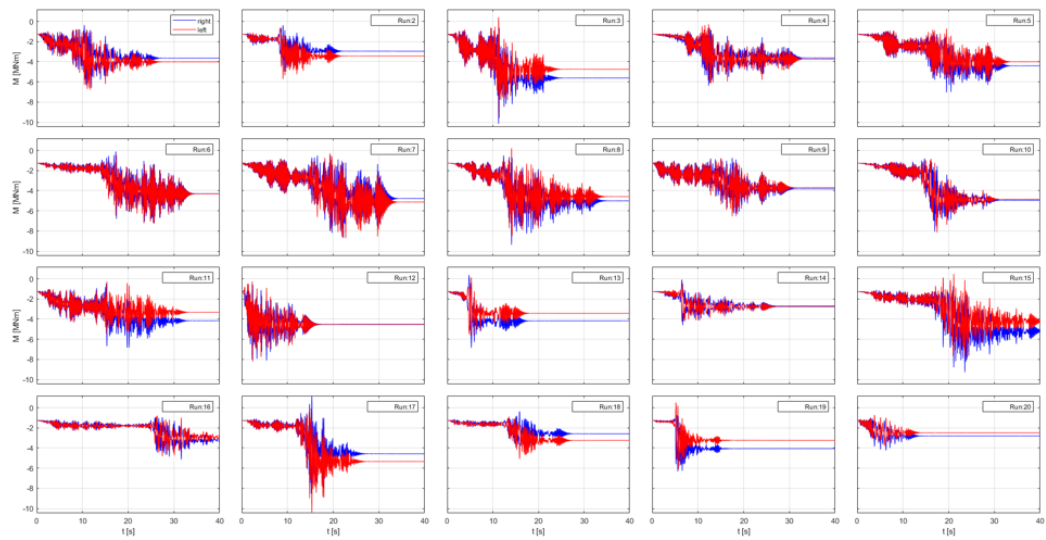


Figure E.7. Milano (IML9): bending moment at deck-abutments joints.

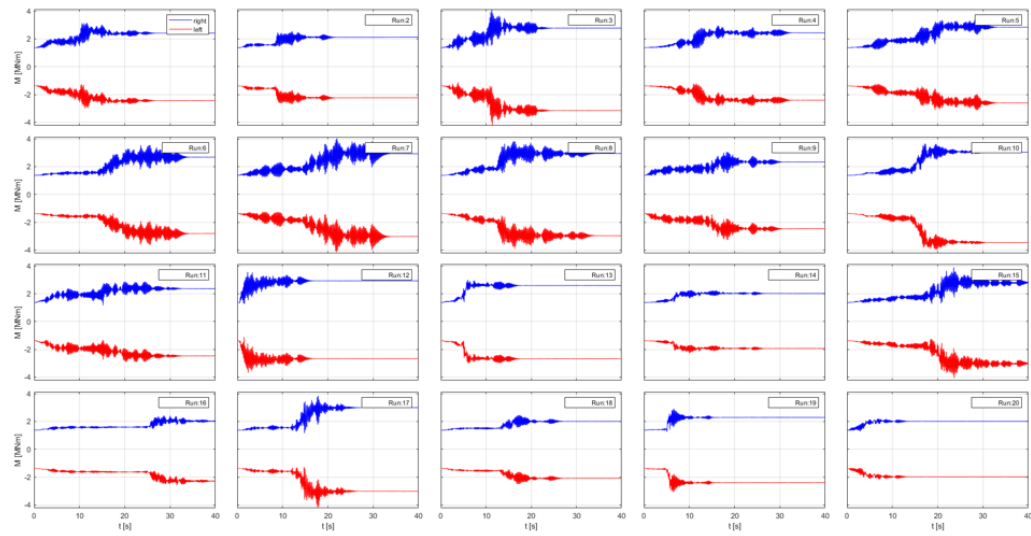


Figure E.8. Milano (IML9): bending moment at piles head.

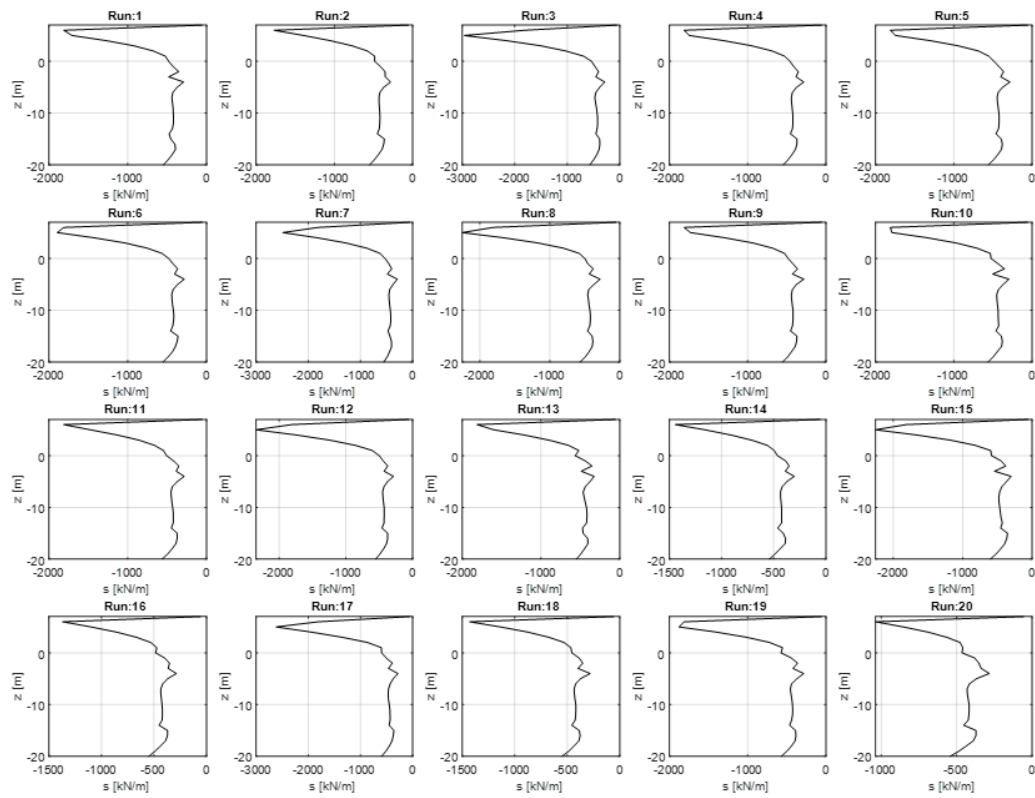
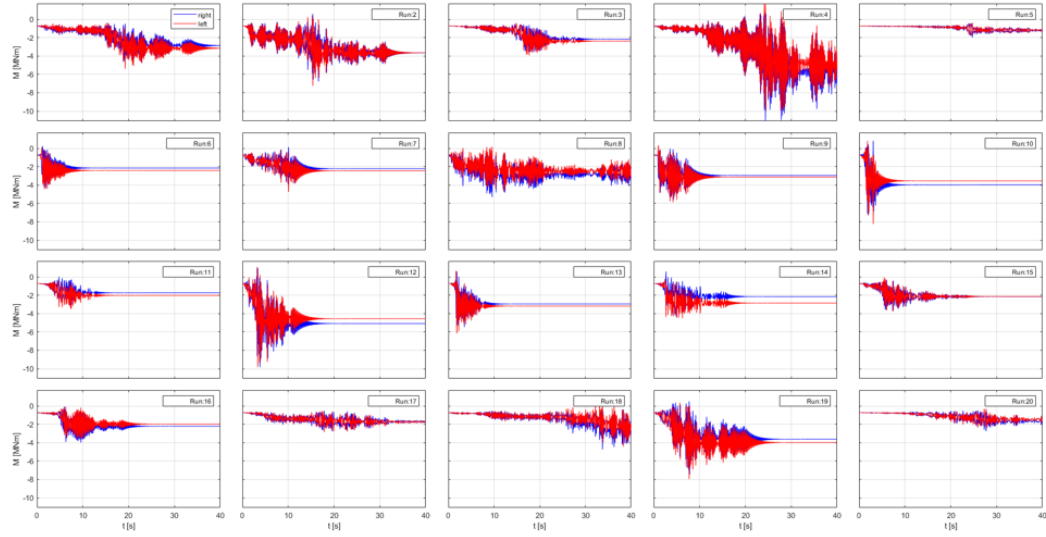


Figure E.9. Milano (IML9): earth pressures on left abutment-piles alignment.

## E.2.2 NA

## IML 3



**Figure E.10.** Napoli (IML3): bending moment at deck-abutments joints.

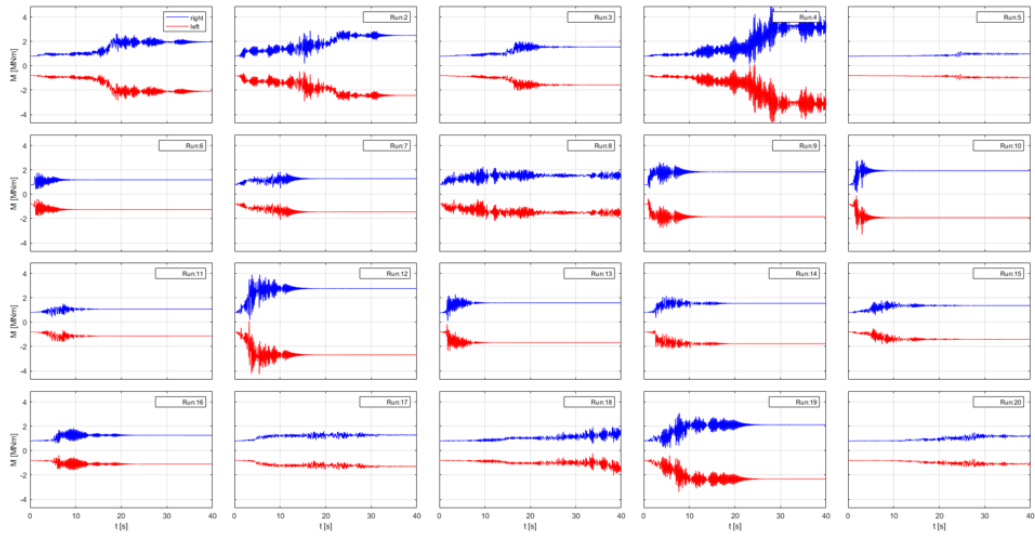


**Figure E.11.** Napoli (IML3): bending moment at piles head.

## IML 6

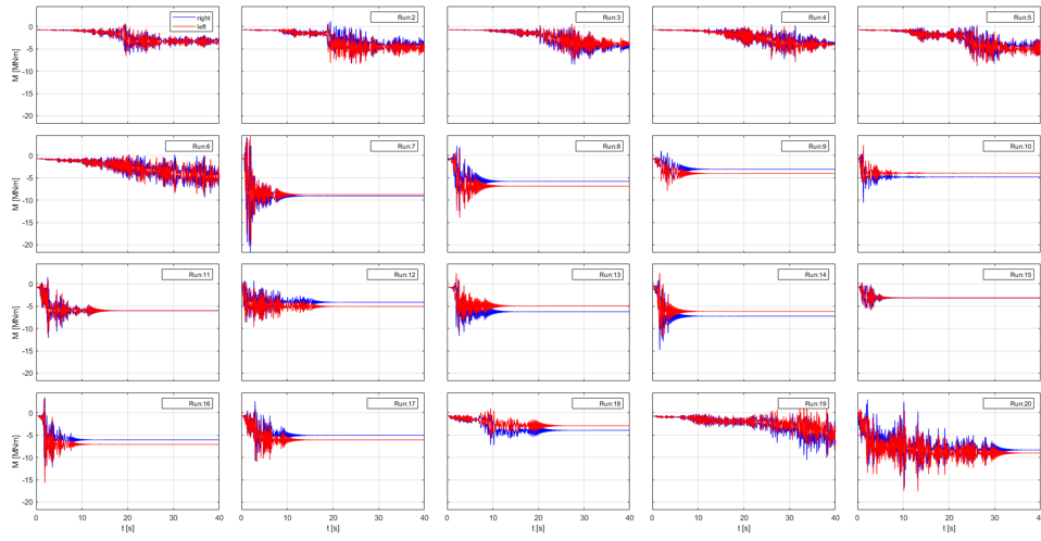


Figure E.12. Napoli (IML6): bending moment at deck-abutments joints.

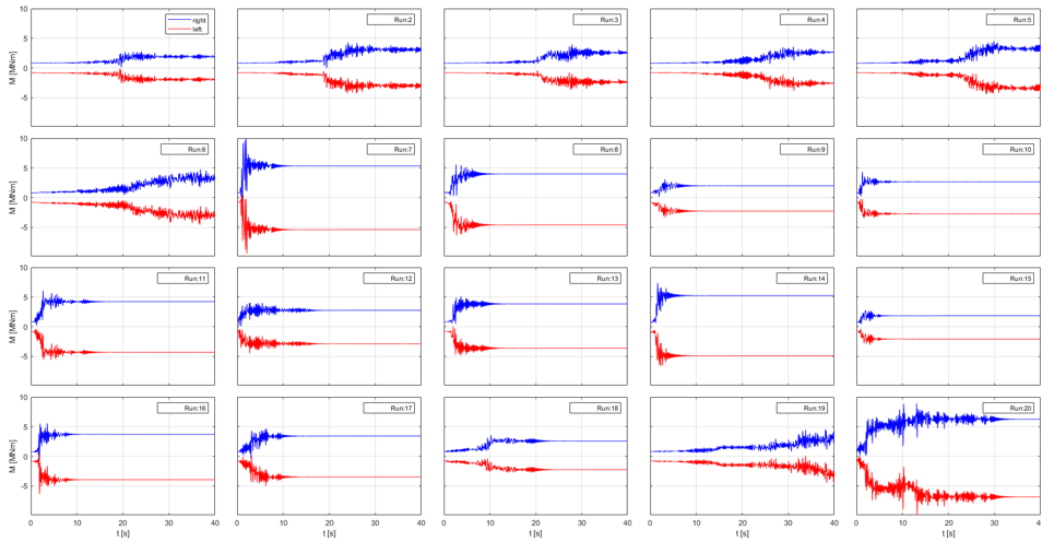
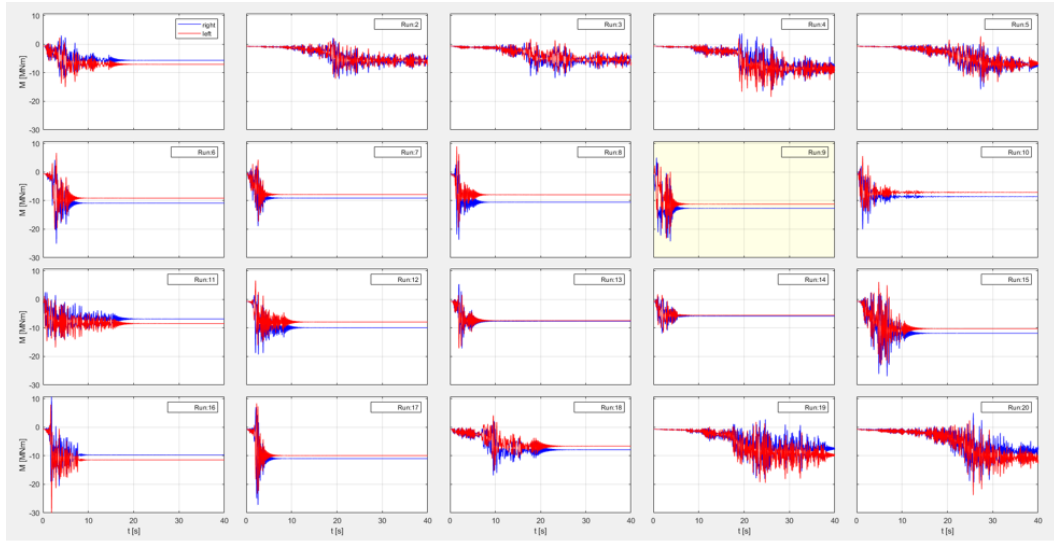
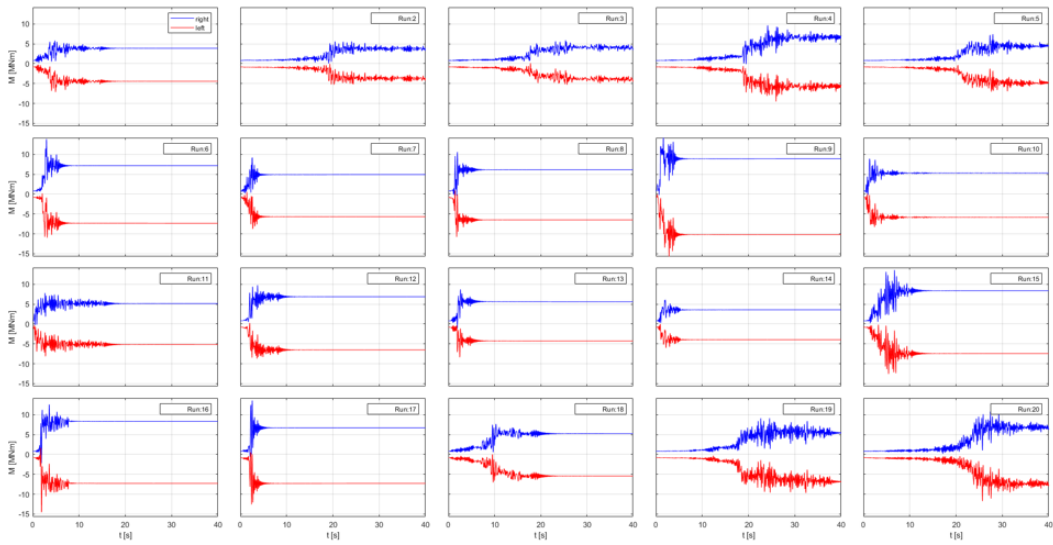


Figure E.13. Napoli (IML6): bending moment at piles head.

## IML 9



**Figure E.14.** Napoli (IML9): bending moment at deck-abutments joints.



**Figure E.15.** Napoli (IML9): bending moment at piles head.



## E.2.3 AQ

## IML 3

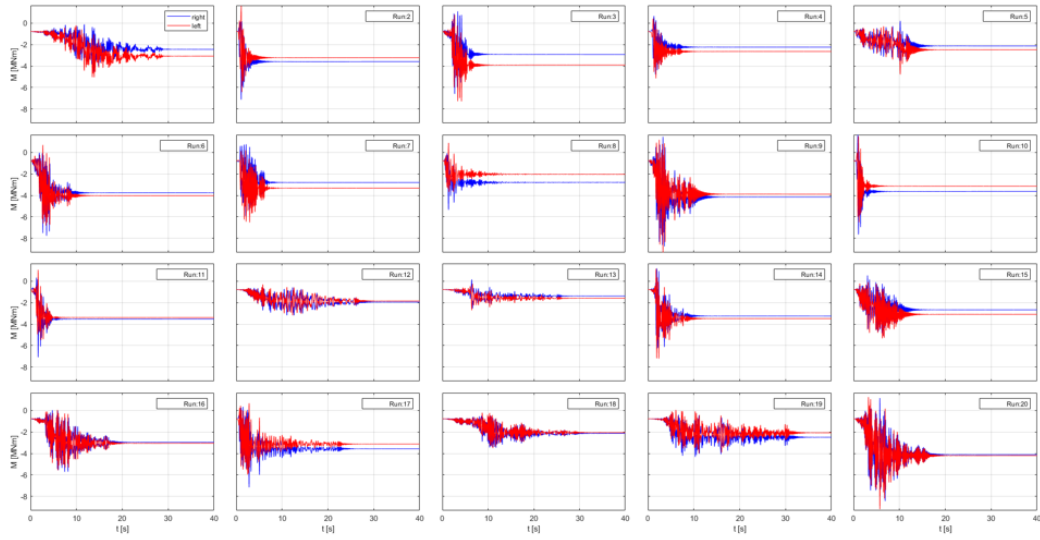


Figure E.16. L'Aquila (IML3): bending moment at deck-abutments joints.

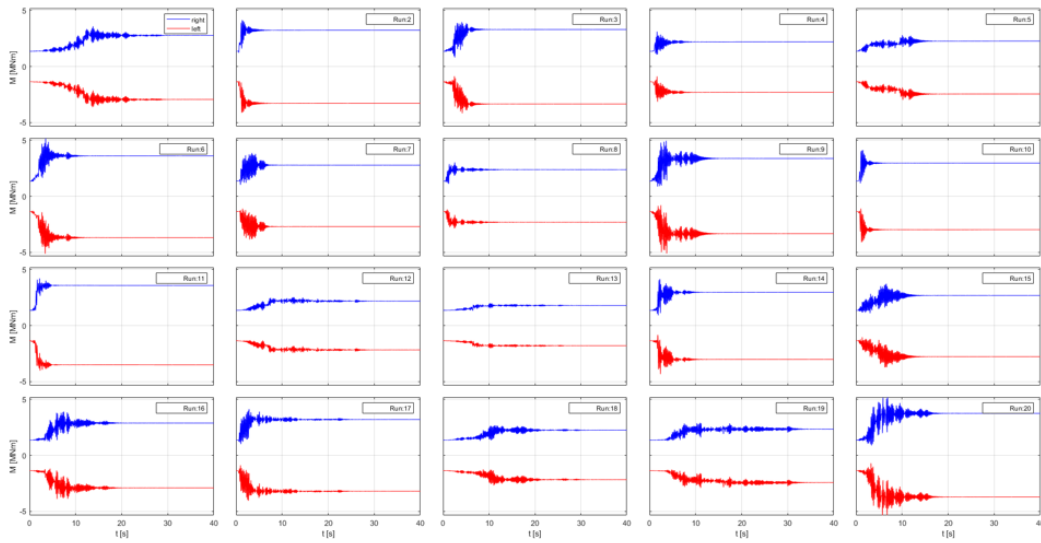


Figure E.17. L'Aquila (IML3): bending moment at piles head.

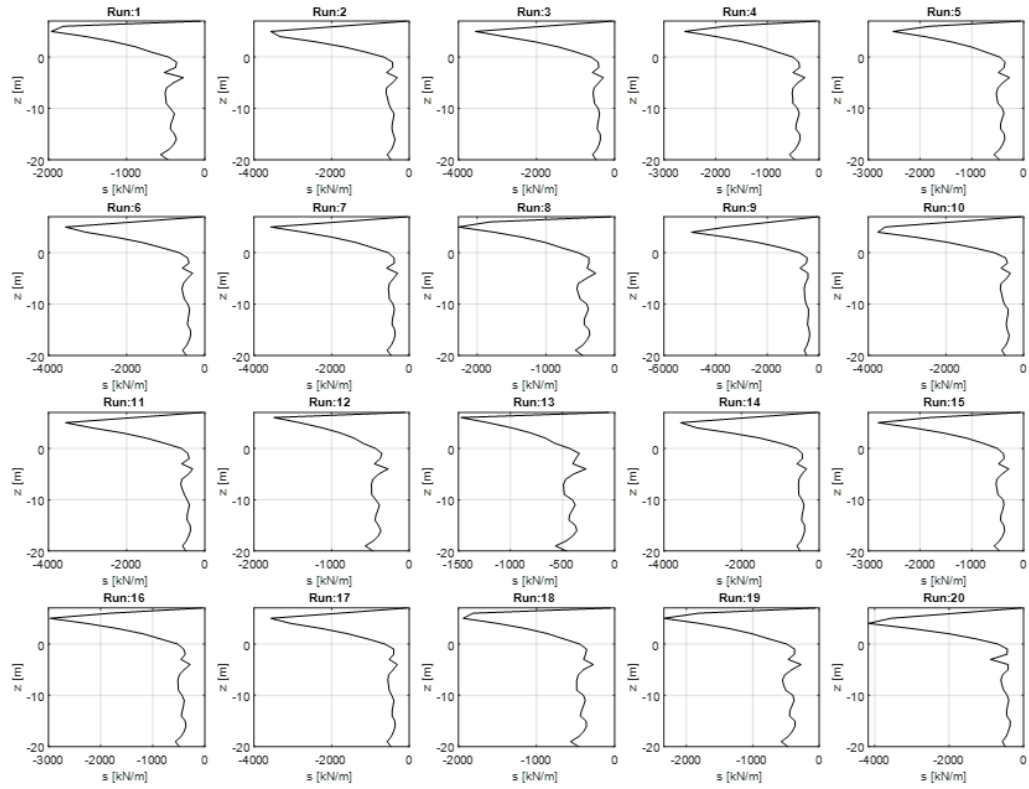


Figure E.18. L'Aquila (IML3): earth pressures on left abutment-piles alignment.

## IML 6

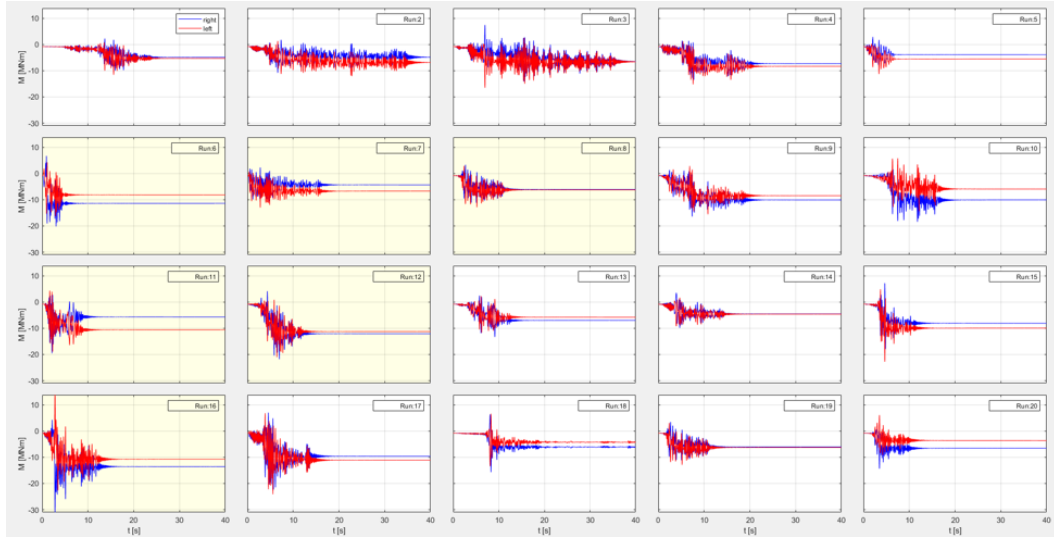


Figure E.19. L'Aquila (IML6): bending moment at deck-abutments joints.

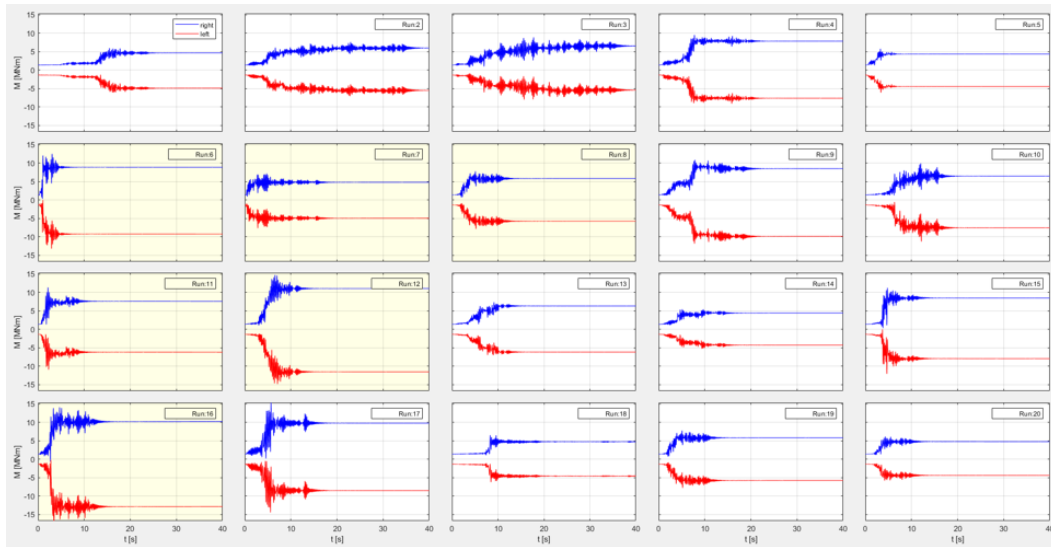


Figure E.20. L'Aquila (IML6): bending moment at piles head.

## IML 9

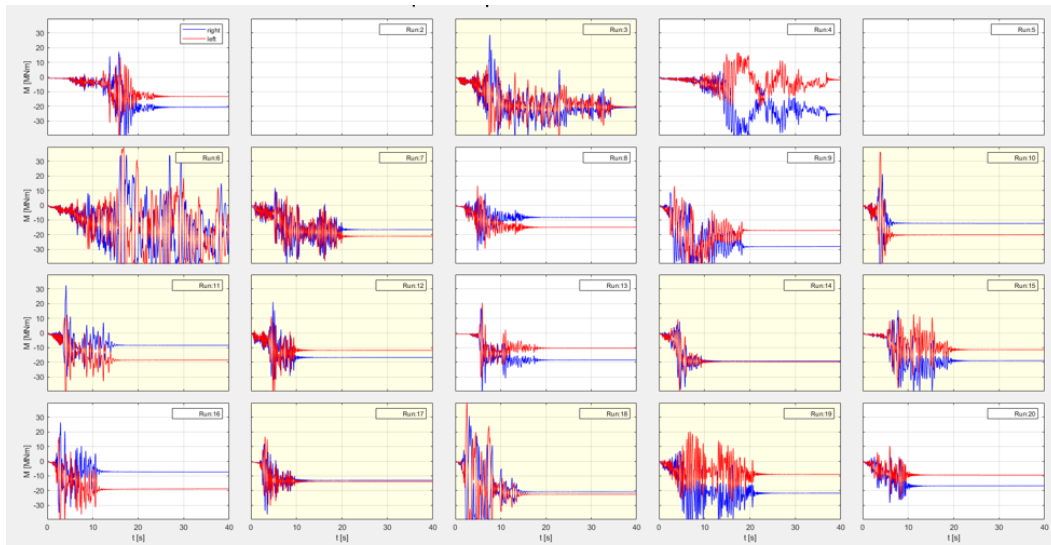


Figure E.21. L'Aquila (IML9): bending moment at deck-abutments joints.

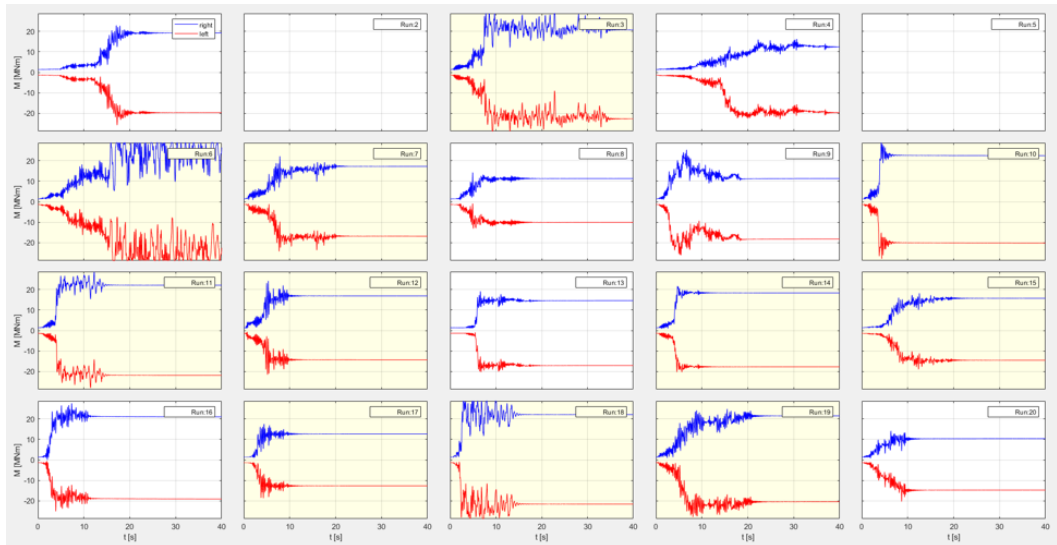


Figure E.22. L'Aquila (IML9): bending moment at piles head.

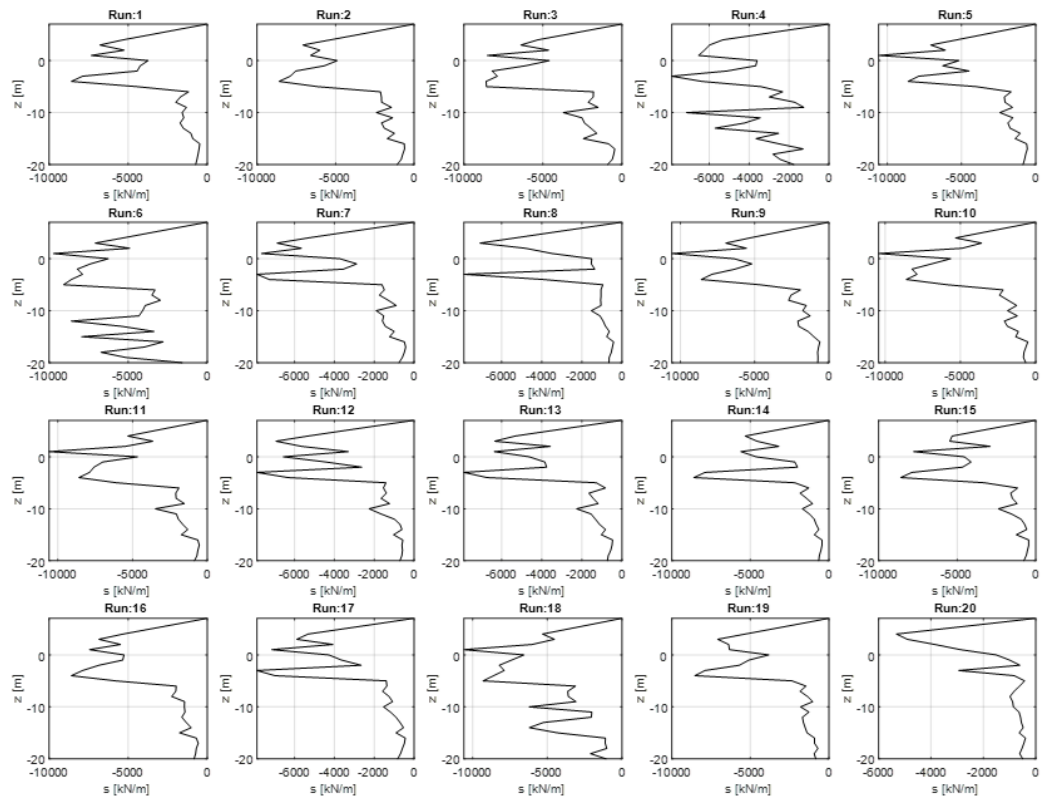


Figure E.23. L'Aquila (IML9): earth pressures on left abutment-piles alignment.

# Bibliography

- [1] CEN, Eurocode 1 - Actions on Structures. *Report EN1991:2005 by Technical Committee 250, Sub-Committee 1 of the European Committee for Standardization (CEN/TC250/SC1)*, (2005).
- [2] CEN, Eurocode 8 - Design of structures for earthquake resistance - Part 2: Bridges. *Report EN1998-2:2005 by Technical Committee 250, Sub-Committee 8 of the European Committee for Standardization (CEN/TC250/SC8)*, (2005).
- [3] Norme Tecniche per le Costruzioni (NTC). *Circolare 21 gennaio 2019, n. 7 C.S.LL.PP. Istruzioni per l'applicazione dell'Aggiornamento delle "Norme tecniche per le costruzioni" di cui al decreto ministeriale 17 gennaio 2018.*, (2018).
- [4] CEN, Eurocode 8 - Design of structures for earthquake resistance - Part 2: Bridges. *Report prEN1998-2:2022 by Technical Committee 250, Sub-Committee 8 of the European Committee for Standardization (CEN/TC250/SC8)*, (2022).
- [5] ABENDROTH, R. E., GREIMANN, L. F., AND EBNER, P. B. Abutment pile design for jointless bridges. *Journal of Structural Engineering*, **115** (1989), 2914. doi:10.1061/(ASCE)0733-9445(1989)115:11(2914).
- [6] AMBRASEYS, N. N., SIMPSON, K. A., AND BOMMER, J. J. Prediction of horizontal response spectra in europe. *Earthquake Engineering & Structural Dynamics*, **25** (1996), 371. doi:https://doi.org/10.1002/(SICI)1096-9845(199604)25:4<371::AID-EQE550>3.0.CO;2-A.
- [7] ANCHETA, T., DARRAGH, R., STEWART, J., AND AL. NGA-West2 database. *Earthq. Spectra*, pp. 989–1005. Available from: <http://peer.berkeley.edu/ngawest2/>.
- [8] ANOYATIS, G. AND LEMNITZER, A. Kinematic winkler modulus for laterally-loaded piles. *Soils and Foundations*, **57** (2017), 453. doi:https://doi.org/10.1016/j.sandf.2017.05.011.
- [9] AROCKIASAMY, M., BUTRIENG, N., AND SIVA KUMAR, M. State of the art-integral abutment bridges: Design and practice. *Journal of Bridge Engineering*, **9** (2004), 497.
- [10] ARSOY, S., BARKER, R. M., AND DUNCAN, J. M. The behavior of integral abutment bridges. Tech. rep., Virginia Polytechnic and State University, Blacksburg, Virginia (1999).

- [11] BADONI, D. AND MAKRIS, N. Nonlinear response of single piles under lateral inertial and seismic loads. *Soil Dynamics and Earthquake Engineering*, **15** (1996), 29. doi:[https://doi.org/10.1016/0267-7261\(95\)00027-5](https://doi.org/10.1016/0267-7261(95)00027-5).
- [12] BAKER, J. W. Efficient analytical fragility function fitting using dynamic structural analysis. *Earthquake Spectra*, **31** (2015), 579. Available from: <https://doi.org/10.1193/021113EQS025M>, arXiv:<https://doi.org/10.1193/021113EQS025M>, doi:10.1193/021113EQS025M.
- [13] BECCI, B. AND NOVA, R. A method for analysis and design of flexible sheetpiles. *Rivista Italiana di Geotecnica*, **87** (1987), 33.
- [14] BERGER, E., MAHI, S. A., AND PYKE, R. Simplified method for evaluating soil-pile-structure interaction effects. vol. All Days of *OTC Offshore Technology Conference* (1977). OTC-2954-MS. Available from: <https://doi.org/10.4043/2954-MS>, doi:10.4043/2954-MS.
- [15] BOUC, R. Forced vibration of mechanical systems with hysteresis. *Proceedings of 4th Conference Nonlinear Oscillation*, (1967), 315.
- [16] BRISEGHIELLA, B., SIVIERO, E., AND ZORDAN, T. An integral composite bridge in trento, italy: Design and analysis. In *Proc. IABSE Symposium Towards Metropolitan Habitats and Infrastructure, Shanghai, China* (2004).
- [17] BURKE, M. *Integral and Semi-Integral Bridges*. Wiley & Sons, 1 edn. (2009).
- [18] CALLISTO, L. MARTA: a computer program for the site response analysis of a layered soil deposit. Available from: <https://luigicallisto.site.uniroma1.it/attivita>.
- [19] CARISTO, A., BARNES, J., AND MITOULIS, S. A. Numerical modelling of integral abutment bridges under seasonal thermal cycles. *Proceedings of the Institution of Civil Engineers - Bridge Engineering*, **171** (2018), 179. doi:10.1680/jbren.17.00025.
- [20] CAVALIERI, F. AND FRANCHIN, P. Seismic risk of infrastructure systems with treatment of and sensitivity to epistemic uncertainty. *Infrastructures*, **5** (2020). Available from: <https://www.mdpi.com/2412-3811/5/11/103>, doi:10.3390/infrastructures5110103.
- [21] CHARALAMPAKIS, A. AND KOUMOUSIS, V. Parameters of Bouc–Wen model revisited. 9th HSTAM International Congress on Mechanics (2010).
- [22] CHEN, Y. Assessment on pile effective lengths and their effects on design—i. assessment. *Computers & Structures*, **62** (1997), 265. Available from: <https://www.sciencedirect.com/science/article/pii/S0045794996002015>, doi:[https://doi.org/10.1016/S0045-7949\(96\)00201-5](https://doi.org/10.1016/S0045-7949(96)00201-5).
- [23] COMISU, C. AND GHEORGHITA, B. Integral bridges and environmental conditions. In *Proceedings of the International Conference on Risk Management, Assessment and Mitigation*, pp. 164–169 (2010).

- [24] CONSTANTINOU, M. AND ADNANE, M. Dynamics of soil-base-isolated structure systems: evaluation of two models for yielding systems. Report to NSAF, Department of civil engineering, Drexel University, Philadelphia (1987).
- [25] CROSS, H. Analysis of continuous frames by distributing fixedend moments. *Proc., American Society of Civil Engineers*, (1930).
- [26] DAVID, T. K. AND FORTH, J. P. Modelling of soil structure interaction of integral abutment bridges. *World Acad Sci Eng Technol*, **78** (2011), 769.
- [27] DICLELI, M. *Innovative Bridge Design Handbook: Integral Bridges*. Butterworth-Heinemann, 1 edn. (2016).
- [28] DICLELI, M. AND ALBHAISI, S. M. Effect of cyclic thermal loading on the performance of steel h-piles in integral bridges with stub-abutments. *Journal of Constructional Steel Research*, **60** (2004), 161. Available from: <https://www.sciencedirect.com/science/article/pii/S0143974X03001767>, doi: <https://doi.org/10.1016/j.jcsr.2003.09.003>.
- [29] DICLELI, M. AND ALBHAISI, S. M. Estimation of length limits for integral bridges built on clay. *Journal of Bridge Engineering*, **9** (2004), 572. doi: 10.1061/(ASCE)1084-0702(2004)9:6(572).
- [30] DICLELI, M. AND ALBHAISI, S. M. Performance of abutment-backfill system under thermal variations in integral bridges built on clay. *Engineering Structures*, **26** (2004), 949. Available from: <https://www.sciencedirect.com/science/article/pii/S0141029604000641>, doi: <https://doi.org/10.1016/j.engstruct.2004.02.014>.
- [31] DICLELI, M., ENG, P., AND ALBHAISI, S. M. Maximum length of integral bridges supported on steel h-piles driven in sand. *Engineering Structures*, **25** (2003), 1491. Available from: <https://www.sciencedirect.com/science/article/pii/S0141029603001160>, doi: [https://doi.org/10.1016/S0141-0296\(03\)00116-0](https://doi.org/10.1016/S0141-0296(03)00116-0).
- [32] DICLELI, M. AND ERHAN, S. Low cycle fatigue effects in integral bridge steel h-piles under earthquake induced strain reversals. In *Advances in Structural Engineering* (edited by V. Matsagar), pp. 2505–2512. Springer India, New Delhi (2015). ISBN 978-81-322-2187-6.
- [33] DREIER, D., BURDET, O., AND MUTTONI, A. Transition slabs of integral abutment bridges. *Structural Engineering International*, **21** (2011), 144. doi: 10.2749/101686611X12994961034174.
- [34] DROSOS, V. A., GEROLYMOS, N., AND GAZETAS, G. Constitutive model for soil amplification of ground shaking: Parameter calibration, comparisons, validation. *Soil Dynamics and Earthquake Engineering*, **42** (2012), 255.
- [35] DUNCAN, J. AND ARSOY, S. Effect of bridge-soil interaction on behavior of piles supporting integral bridges. *Transportation research record*, **1849** (2003), 91.

- [36] DUNCAN, J. M. AND BUCHIGNANI, A. *An engineering manual for settlement studies*. University of California, Department of Civil Engineering (1976).
- [37] DVORKIN, E. AND BATHE, K.-J. A continuum mechanics based four-node shell element for general nonlinear analysis. *Engineering Computations*, **1** (1984), 77. doi:[10.1108/eb023562](https://doi.org/10.1108/eb023562).
- [38] ELGAMAL, A. AND WILSON, P. *Full Scale Testing and Simulation of Seismic Bridge Abutment-Backfill Interaction*, pp. 109–127. Springer Netherlands, Dordrecht (2012). ISBN 978-94-007-2060-2. Available from: [https://doi.org/10.1007/978-94-007-2060-2\\_4](https://doi.org/10.1007/978-94-007-2060-2_4), doi:[10.1007/978-94-007-2060-2\\_4](https://doi.org/10.1007/978-94-007-2060-2_4).
- [39] ERHAN, S. AND DICLELI, M. Effect of dynamic soil–bridge interaction modeling assumptions on the calculated seismic response of integral bridges. *Soil Dynamics and Earthquake Engineering*, **66** (2014), 42. Available from: <https://www.sciencedirect.com/science/article/pii/S0267726114001572>, doi:<https://doi.org/10.1016/j.soildyn.2014.06.033>.
- [40] ERHAN, S. AND DICLELI, M. Comparative assessment of the seismic performance of integral and conventional bridges with respect to the differences at the abutments. *Bulletin of Earthquake Engineering*, **13** (2015), 653.
- [41] FARAJI, S., TING, J. M., CROVO, D. S., AND ERNST, H. Nonlinear analysis of integral bridges: finite-element model. *Journal of Geotechnical and Geoenvironmental Engineering*, **127** (2001), 454.
- [42] FELDMANN, M., NAUMES, J., PAK, D., VELJKOVIC, M., ERIKSEN, J., HECHLER, O., POPA, N., SEIDL, G., AND BRAUN, A. INTAB DG eng 0 2 Design guide Integral bridges, Economic and Durable Design of Composite Bridges with Integral Abutments. *CEN/TC 250/SC 10, EN 1990 Basis of structural design*, (2010).
- [43] FERRETTI TORRICELLI, L. AND MARCHIONDELLI, A. *The Gatteo integral highway overpass*, pp. 2221–2229. Bridge Maintenance, Safety, Management and Life Extension (2014). ISBN 978-1-138-00103-9.
- [44] FERRETTI TORRICELLI, L., MARCHIONDELLI, A., PEFANO, R., AND STUCCHI, R. *Integral bridge design solutions for Italian highway overpasses*, pp. 2341–2348 (2012). ISBN 978-0-415-62124-3. doi:[10.1201/b12352-352](https://doi.org/10.1201/b12352-352).
- [45] FIORENTINO, G., ET AL. Integral abutment bridges: Investigation of seismic soil-structure interaction effects by shaking table testing. *Earthquake Engineering & Structural Dynamics*, **50** (2021), 1517. Available from: <https://onlinelibrary.wiley.com/doi/abs/10.1002/eqe.3409>, arXiv:<https://onlinelibrary.wiley.com/doi/pdf/10.1002/eqe.3409>, doi:<https://doi.org/10.1002/eqe.3409>.
- [46] FRANCHIN, P. AND CAVALIERI, F. Seismic performance-based design of flexible earth-retaining diaphragm walls. *Engineering Structures*, **78** (2014), 57. doi:<https://doi.org/10.1016/j.engstruct.2014.06.027>.



- [47] FRANCHIN, P. AND PINTO, P. E. Performance-based seismic design of integral abutment bridges. *Bull Earthquake Eng*, **12** (2014), 939. doi:10.1007/s10518-013-9552-2.
- [48] FRANCHIN, P., PINTO, P. E., AND NOTO, F. A simplified nonlinear dynamic model for seismic analysis of earth-retaining diaphragm-walls. *4th International Conference on Earthquake Geotechnical Engineering*, (2007).
- [49] FREYERMUTH, C. L. Design of continuous highway bridges with precast, prestressed concrete girders. (1969).
- [50] GALLESE, D., GORINI, D. N., AND CALLISTO, L. Effetti dell'interazione terreno-struttura sul comportamento sismico di ponti integrali a singola campata. *Incontro Annuale dei Ricercatori di Geotecnica 2021 - IARG2021*, (2021).
- [51] GAZETAS, G. *Foundation Vibrations*, pp. 553–593. Springer US, Boston, MA (1991). ISBN 978-1-4757-5271-7. Available from: [https://doi.org/10.1007/978-1-4757-5271-7\\_15](https://doi.org/10.1007/978-1-4757-5271-7_15), doi:10.1007/978-1-4757-5271-7\_15.
- [52] GAZETAS, G. AND DOBRY, R. Horizontal response of piles in layered soils. *Journal of Geotechnical Engineering*, **110** (1984), 20.
- [53] GEROLYMOS, N. AND GAZETAS, G. Constitutive model for 1-d cyclic soil behaviour applied to seismic analysis of layered deposits. *Soils and Foundations*, **45** (2005), 147.
- [54] GIRTON, D. D., HAWKINSON, T. R., AND GREIMANN, L. F. Validation of design recommendations for integral abutment piles. *Journal of Structural Engineering*, **117** (1991), 2117. doi:10.1061/(ASCE)0733-9445(1991)117:7(2117).
- [55] GORINI, D. N. AND CALLISTO, L. A coupled study of soil-abutment-superstructure interaction. *Springer Lecture Notes in Civil Engineering "Geotechnical Research for Land Protection and Development" (CNRIG2019)*, **40** (2020), 565. doi:[https://doi.org/10.1007/978-3-030-21359-6\\_60](https://doi.org/10.1007/978-3-030-21359-6_60).
- [56] GORINI, D. N., CALLISTO, L., AND WHITTLE, A. An inertial macroelement for bridge abutments. *Geotechnique*, (2020), 397. doi:<https://doi.org/10.1680/jgeot.19.P.397>.
- [57] GREIMANN, D. E. *An investigation of the responsibilities of secondary principals serving shared and nonshared superintendents*. Ph.D. thesis, University of Northern Iowa (1992).
- [58] GREIMANN, L. AND WOLDE-TINSAE, A. M. Design model for piles in jointless bridges. *Journal of Structural Engineering*, **114** (1988), 1354. doi:10.1061/(ASCE)0733-9445(1988)114:6(1354).
- [59] HOPPE, E. J., GOMEZ, J., ET AL. Field study of an integral backwall bridge. Tech. rep., Virginia Transportation Research Council (1996).

- [60] HORVATH, J. S. Integral-abutment bridges: problems and innovative solutions using EPS geofoam and other geosynthetics. *Res. Rpt. No. CE/GE-00*, **2** (2000).
- [61] HUMAR, J. L. *Dynamics of Structures*. CRC Press (2012). ISBN 978-0203112564.
- [62] IERVOLINO, I. Assessing uncertainty in estimation of seismic response for PBEE. *Earthquake Engineering & Structural Dynamics*, **46** (2017), 1711. Available from: <https://onlinelibrary.wiley.com/doi/abs/10.1002/eqe.2883>, arXiv:<https://onlinelibrary.wiley.com/doi/pdf/10.1002/eqe.2883>, doi:<https://doi.org/10.1002/eqe.2883>.
- [63] IERVOLINO, I., SPILLATURA, A., AND BAZZURRO, P. RINTC project: assessing the (implicit) seismic risk of code-conforming structures in Italy. *COMP-DYN*, (2017).
- [64] IERVOLINO, I., SPILLATURA, A., AND BAZZURRO, P. Seismic Reliability of Code-Conforming Italian Buildings. *Journal of Earthquake Engineering*, **22** (2018), 5. Available from: <https://doi.org/10.1080/13632469.2018.1540372>, arXiv:<https://doi.org/10.1080/13632469.2018.1540372>, doi: 10.1080/13632469.2018.1540372.
- [65] ILES, D. AND ASCOT, U. Integral bridges in the uk. In *International Workshop on the Bridges with Integral Abutments*, p. 13 (2006).
- [66] ISHIBASHI, I. AND ZHANG, X. Unified dynamic shear moduli and damping ratios of sand and clay. *Soils and Foundations*, **33** (1993), 182.
- [67] JALAYER, F. *Direct probabilistic seismic analysis: implementing non-linear dynamic assessments*. Ph.D. thesis, Department of Civil and Environmental Engineering, Stanford University, CA, USA (2003).
- [68] JALAYER, F. AND CORNELL, C. A. Alternative non-linear demand estimation methods for probability-based seismic assessments. *Earthquake Engineering & Structural Dynamics*, **38** (2009), 951. Available from: <https://onlinelibrary.wiley.com/doi/abs/10.1002/eqe.876>, arXiv:<https://onlinelibrary.wiley.com/doi/pdf/10.1002/eqe.876>, doi:<https://doi.org/10.1002/eqe.876>.
- [69] JOYNER, W. B. AND CHEN, A. T. F. Calculation of nonlinear ground response in earthquakes. *Bulletin of the Seismological Society of America*, **65** (1975), 1315. arXiv:<https://pubs.geoscienceworld.org/ssa/bssa/article-pdf/65/5/1315/2699824/BSSA0650051315.pdf>.
- [70] KARMANOS, S. A., ET AL. Optimising the seismic performance of steel and steel-concrete structures by standardising material quality control (OPUS). *Directorate-General for Research and Innovation (European Commission)*, **25** (2013). doi:10.2777/79330.

- [71] KOZAK, D., LAFAVE, J., AND FAHNESTOCK, L. Seismic modeling of integral abutment bridges in illinois. *Engineering Structures*, **165** (2018), 170. Available from: <https://www.sciencedirect.com/science/article/pii/S0141029618301044>, doi:<https://doi.org/10.1016/j.engstruct.2018.02.088>.
- [72] KRAMER, S. L. *Geotechnical Earthquake Engineering*. Prentice Hall, 1 edn. (1996). ISBN 978-0-133-74943-4.
- [73] KUNIN, J. AND ALAMPALLI, S. Integral Abutment Bridges: Current Practice in United States and Canada. *Journal of Performance of Constructed Facilities*, **14** (2000), 104. doi:10.1061/(ASCE)0887-3828(2000)14:3(104).
- [74] LAFAVE, J., FAHNESTOCK, L., JARRETT, M., WRIGHT, B., RIDDLE, J., AND SVATORA, J. *Numerical Simulations and Field Monitoring of Integral Abutment Bridges*, pp. 561–572 (2015). Available from: <https://ascelibrary.org/doi/abs/10.1061/9780784479117.049>, arXiv:<https://ascelibrary.org/doi/pdf/10.1061/9780784479117.049>, doi:10.1061/9780784479117.049.
- [75] LAFAVE, J. M., RIDDLE, J. K., JARRETT, M. W., WRIGHT, B. A., SVATORA, J. S., AN, H., AND FAHNESTOCK, L. A. Numerical simulations of steel integral abutment bridges under thermal loading. *Journal of Bridge Engineering*, **21** (2016), 04016061. doi:10.1061/(ASCE)BE.1943-5592.0000919.
- [76] LANCELLOTTA, R. Analytical solution of passive earth pressure. *Géotechnique*, **52** (2002), 617. doi:10.1680/geot.2002.52.8.617.
- [77] LEHANE, B., KEOGH, D., AND O'BRIEN, E. Simplified elastic model for restraining effects of backfill soil on integral bridges. *Computers & Structures*, **73** (1999), 303. Available from: <https://www.sciencedirect.com/science/article/pii/S0045794998002478>, doi:[https://doi.org/10.1016/S0045-7949\(98\)00247-8](https://doi.org/10.1016/S0045-7949(98)00247-8).
- [78] LEMNITZER, A., AHLBERG, E. R., NIGBOR, R. L., SHAMSABADI, A., WALLACE, J. W., AND STEWART, J. P. Lateral performance of full-scale bridge abutment wall with granular backfill. *Journal of Geotechnical and Geoenvironmental Engineering*, **135** (2009), 506. doi:10.1061/(ASCE)1090-0241(2009)135:4(506).
- [79] LIN, T., HARMSSEN, S. C., BAKER, J. W., AND LUCO, N. Conditional Spectrum Computation Incorporating Multiple Causal Earthquakes and Ground-Motion Prediction Models. *Bulletin of the Seismological Society of America*, **103** (2013), 1103. Available from: <https://doi.org/10.1785/0120110293>, arXiv:<https://pubs.geoscienceworld.org/ssa/bssa/article-pdf/103/2A/1103/3653433/1103.pdf>, doi:10.1785/0120110293.
- [80] LIN, T., HASELTON, C. B., AND BAKER, J. W. Conditional spectrum-based ground motion selection. part i: Hazard consistency for risk-based assessments. *Earthquake Engineering & Structural Dynamics*, **42** (2013), 1847. Available from: <https://onlinelibrary.wiley.com/doi/>

- abs/10.1002/eqe.2301, arXiv:<https://onlinelibrary.wiley.com/doi/pdf/10.1002/eqe.2301>, doi:<https://doi.org/10.1002/eqe.2301>.
- [81] LUZI, L., HAILEMIKAEL, S., BINDI, D., PACOR, F., MELE, F., AND SABETTA, F. ITACA (ITalian ACcelerometric Archive): a web portal for the dissemination of Italian strong-motion data. *Seismol. Res. Lett.*, (2008), 716. Available from: <http://itaca.mi.ingv.it/>.
- [82] LYSMER, J. AND KUHLEMEYER, R. Finite dynamic model for infinite media. *ASCE Jnl Eng. Mech. Div.*, **4** (1969), 859.
- [83] M. P. BURKE, J. The world's most expensive pavement expansion joints. Ohio Transportation Engineering Conference, pp. 65–68 (1972).
- [84] MCKENNA, F. AND FENVES, G. L. Using the OpenSees interpreter on parallel computers. *Network for earthquake engineering Simulations. Berkeley, CA*, (2008).
- [85] MCKENNA, F., SCOTT, M. H., AND FENVES, G. L. Nonlinear finite-element analysis software architecture using object composition. *Journal of Computing in Civil Engineering*, **24** (2010), 95. doi:10.1061/(ASCE)CP.1943-5487.0000002.
- [86] MELCHERS, R. E. AND BECK, A. T. *Structural reliability analysis and prediction*. John Wiley & Sons (2018). ISBN 978-1119265993. doi:10.1002/9781119266105.
- [87] MISTRY, V. C. *High Performance Steel for Highway Bridges*, pp. 301–308. doi:10.1061/40691(2003)26.
- [88] MITOULIS, S. A. Challenges and opportunities for the application of integral abutment bridges in earthquake-prone areas: A review. *Soil Dynamics and Earthquake Engineering*, **135** (2020), 106183. Available from: <https://www.sciencedirect.com/science/article/pii/S0267726120302566>, doi: <https://doi.org/10.1016/j.soildyn.2020.106183>.
- [89] NEUENHOFER, A. AND FILIPPOU, F. C. Evaluation of nonlinear frame finite-element models. *Journal of Structural Engineering*, **123** (1997), 958. doi:10.1061/(ASCE)0733-9445(1997)123:7(958).
- [90] NOVAK, D., TEPLÝ, B., AND SHIRAISHI, N. Sensitivity analysis of structures: A review. *5th International Conference on Civil and Structural Engineering Computing*, (1993), 201. doi:10.4203/ccp.19.8.1.
- [91] OOI, P. S. K., LIN, X., AND HAMADA, H. S. Numerical study of an integral abutment bridge supported on drilled shafts. *Journal of Bridge Engineering*, **15** (2010), 19. doi:10.1061/(ASCE)BE.1943-5592.0000037.
- [92] PRIESTLEY, M. J. N. Myths and fallacies in earthquake engineering: Conflicts between design and reality. *Bulletin of the New*

- Zealand Society for Earthquake Engineering*, **26** (1993), 329–341. Available from: <https://bulletin.nzsee.org.nz/index.php/bnzsee/article/view/671>, doi:10.5459/bnzsee.26.3.329–341.
- [93] PRIESTLEY, M. J. N. *Myths and fallacies in earthquake engineering, revisited: The ninth mallet Milne lecture*. IUSS press Pavia, Italy (2003).
- [94] PRÉVOST, J. H. Plasticity theory for soil stress-strain behavior. *Journal of the Engineering Mechanics Division*, **104** (1978), 1177. doi:10.1061/JMCEA3.0002411.
- [95] QUINN, B. H. AND CIVJAN, S. A. Parametric study on effects of pile orientation in integral abutment bridges. *Journal of Bridge Engineering*, **22** (2017), 04016132. doi:10.1061/(ASCE)BE.1943-5592.0000952.
- [96] RAMPELLO, S., CALLISTO, L., AND MASINI, L. Spinta delle terre sulle strutture di sostegno. *Dipartimento di Ingegneria Strutturale e Geotecnica, Università di Roma La Sapienza*, (2011).
- [97] RANKINE, W. On the stability of loose earth. *Philosophical Transactions of the Royal Society of London*, **147** (1857).
- [98] RHODES, S. AND MOSES, J. Integral bridges and the modelling of soil-structure interaction (2016).
- [99] ROESSET, J. AND ANGELIDES, D. Dynamic stiffness of piles. *Numerical Methods in Offshore Piling*, (1980), 75.
- [100] SANDBERG, J., ARGYLE, T., PETTY, R., PATEL, B., AND NOWAK, P. The design of integral bridges with bankseat, half-height and full-height abutments on the a14, uk. *Proceedings of the Institution of Civil Engineers - Bridge Engineering*, **171** (2018), 222. Available from: <https://doi.org/10.1680/jbren.17.00018>, arXiv:<https://doi.org/10.1680/jbren.17.00018>, doi:10.1680/jbren.17.00018.
- [101] SOLTANI, A. A. AND KUKRETI, A. R. Performance evaluation of integral abutment bridges. *Transportation Research Record 1371 (Oklahoma DOT)*, (1992).
- [102] SONG, J. AND KIUREGHIAN, A. D. Generalized Bouc-Wen Model for Highly Asymmetric Hysteresis. *Journal of Engineering Mechanics*, **132** (2006), 610. doi:10.1061/(ASCE)0733-9399(2006)132:6(610).
- [103] SPACONE, E., CIAMPI, V., AND FILIPPOU, F. Mixed formulation of nonlinear beam finite element. *Computers & Structures*, **58** (1996), 71. Available from: <https://www.sciencedirect.com/science/article/pii/004579499500103N>, doi:[https://doi.org/10.1016/0045-7949\(95\)00103-N](https://doi.org/10.1016/0045-7949(95)00103-N).
- [104] SPYRAKOS, C. AND LOANNIDIS, G. Seismic behavior of a post-tensioned integral bridge including soil-structure interaction (SSI). *Soil Dynamics*

- and *Earthquake Engineering*, **23** (2003), 53. Available from: <https://www.sciencedirect.com/science/article/pii/S0267726102001501>, doi: [https://doi.org/10.1016/S0267-7261\(02\)00150-1](https://doi.org/10.1016/S0267-7261(02)00150-1).
- [105] WEN, Y.-K. Method for random vibration of hysteretic systems. *Journal of the Engineering Mechanics Division*, **102** (1976), 249. doi:10.1061/JMCEA3.0002106.
  - [106] WHITE, H. *Integral abutment bridges: Comparison of current practice between European countries and the United States of America*. Transportation Research and Development Bureau, New York State Department of Transportation (2007).
  - [107] WHITE H, C. P., PÉTURSSON H. Integral abutment bridges: the european way. *Pract Period Struct Des Constr*, **15** (2010), 201.
  - [108] WOLDE-TINSAE, A. M. AND KLINGER, J. E. Integral abutment bridge design and construction. (1987).
  - [109] YANG, P.-S., WOLDE-TINSAE, A., AND GREIMANN, L. F. Effects of predrilling and layered soils on piles. *J Geotech Eng*, **111** (1985), 18.
  - [110] YANG, Z., ELGAMAL, A.-W., AND PARRA, E. Computational model for cyclic mobility and associated shear deformation. *Journal of Geotechnical and Geoenvironmental Engineering*, **129** (2003), 1119. doi:10.1061/(ASCE)1090-0241(2003)129:12(1119).
  - [111] YANNOTTI, A. P., ALAMPALLI, S., AND WHITE, H. New York State Department of Transportation's Experience with Integral Abutment Bridges. Tech. rep., Baltimore, Maryland (2005).
  - [112] ZAMBELLI, C., DI PRISCO, C., D'ONOFRIO, A., VISONE, C., AND DE MAGISTRIS, F. Dependency of the mechanical behaviour of granular soils on loading frequency: Experimental results and constitutive modelling. In *Soil Stress-Strain Behavior: Measurement, Modeling and Analysis* (edited by H. I. Ling, L. Callisto, D. Leshchinsky, and J. Koseki), pp. 567–582. Springer Netherlands, Dordrecht (2007). ISBN 978-1-4020-6146-2.
  - [113] ZHANG, J. AND MAKRIS, N. Kinematic response functions and dynamic stiffnesses of bridge embankments. *Earthquake Engineering and Structural Dynamics*, **31** (2002), 1933. doi:<https://doi.org/10.1002/eqe.196>.
  - [114] ZHANG, J. AND MAKRIS, N. Seismic response analysis of highway overcrossings including soil–structure interaction. *Earthquake Engineering and Structural Dynamics*, **31** (2002), 1967. doi:<https://doi.org/10.1002/eqe.197>.
  - [115] ZHAO, Q., VASHEGHANI-FARAHANI, R., AND BURDETTE, E. G. *Seismic Analysis of Integral Abutment Bridges Including Soil-Structure Interaction*, chap. 2201, pp. 289–303 (2011). doi:10.1061/41171(401)26.

- 
- [116] ZORDAN, T., BRISEGHIELLA, B., AND LAN, C. Parametric and pushover analyses on integral abutment bridge. *Engineering Structures*, **33** (2011), 502. Available from: <https://www.sciencedirect.com/science/article/pii/S0141029610004293>, doi:<https://doi.org/10.1016/j.engstruct.2010.11.009>.
- [117] ZORDAN, T., BRISEGHIELLA, B., AND LAN, C. Parametric and pushover analyses on integral abutment bridge. *Engineering Structures*, **33** (2011), 502. Available from: <https://www.sciencedirect.com/science/article/pii/S0141029610004293>, doi:<https://doi.org/10.1016/j.engstruct.2010.11.009>.